Acoustic characterization and imaging of Carrara marble degradation

Marie-Laure Chavazas

Aix Marseille Université

NNT : 0000AIXM0000

THÈSE DE DOCTORAT

Soutenue à Aix-Marseille Université
le 15 novembre 2024 par

Marie-Laure CHAVAZAS

Acoustic characterization and imaging of Carrara marble degradation

Discipline
Sciences pour l'ingénieur

Spécialité
Mécanique des solides

École doctorale
ED 353 Sciences pour l'ingénieur : mécanique, physique, micro et nanoélectronique

Laboratoire/Partenaires de recherche
Laboratoire de Mécanique et d'Acoustique
Centre Interdisciplinaire de Conservation et de Restauration du Patrimoine

Composition du jury

Ann BOURGÈS IR, C2RMF	Rapporteuse
Paul Allan JOHNSON DR, LANL	Rapporteur
Céline SCHNEIDER MCF, Université de Reims Champagne-Ardenne	Examinatrice
Livio DE LUCA DR, CNRS MAP	Président du jury
Cédric PAYAN PR, Aix-Marseille Université	Directeur de thèse
Philippe BROMBLET IR, CICRP	Co-directeur de thèse

Laboratoire de Mécanique et d'Acoustique

cnrs

Centrale Méditerranée

c!crp
Centre Interdisciplinaire de Conservation et Restauration du Patrimoine

Affidavit

I, undersigned, Marie-Laure Chavazas, hereby declare that the work presented in this manuscript is my own work, carried out under the scientific supervision of Cédric Payan and Philippe Bromblet, in accordance with the principles of honesty, integrity and responsibility inherent to the research mission. The research work and the writing of this manuscript have been carried out in compliance with both the French national charter for Research Integrity and the Aix-Marseille University charter on the fight against plagiarism.

This work has not been submitted previously either in this country or in another country in the same or in a similar version to any other examination body.

Place Marseille, date 09/09/2024

Liste de publications et/ou brevets et participation aux conférences

1) Liste des publications réalisées dans le cadre du projet de thèse :

1. **Marie-Laure Chavazas**, Philippe Bromblet, Jérémie Berthonneau, Jérémy Hénin, Cédric Payan, "Impact of relative humidity variations on Carrara marble mechanical properties investigated by nonlinear resonant ultrasound spectroscopy", *Construction and Building Materials* 431 (2024). DOI : 10.1016/j.conbuildmat.2024.136529
2. **Marie-Laure Chavazas**, Philippe Bromblet, Jérémie Berthonneau, Jérémy Hénin, Cédric Payan, "Progressive thermal decohesion in Carrara marble monitored with nonlinear resonant ultrasound spectroscopy", *Bulletin of Engineering Geology and the Environment* 83, 383 (2024). DOI : 10.1007/s10064-024-03875-8

2) Participation aux conférences et écoles d'été au cours de la période de thèse :

Conférences :

1. **Marie-Laure Chavazas**, Philippe Bromblet, Cédric Payan, "Caractérisation par acoustique non-linéaire des dégradations du marbre sous l'effet de cyclages thermiques pour la conservation du patrimoine", 16ème Congrès Français d'Acoustique, Marseille, France, 11-15 avril 2022, présentation orale.
2. **Marie-Laure Chavazas**, Philippe Bromblet, Jérémie Berthonneau, Cédric Payan, "Nonlinear acoustic characterization of Carrara marble degradation under thermo-hygric cycles", 5th International Conference on Innovation in Art Research and Technology, Paris, France, 28 juin – 1er juillet 2022, poster.
3. **Marie-Laure Chavazas**, Philippe Bromblet, Jérémie Berthonneau, Cédric Payan, "Non-destructive diagnosis of marble sculptures by 3D imaging coupled with acoustic tomography", Coopération franco-italienne sur les sciences du patrimoine, Marseille, 7-9 février 2024, présentation orale.
4. **Marie-Laure Chavazas**, Philippe Bromblet, Jérémie Berthonneau, Cédric Payan, "Thermo-hygric weathering of Carrara Gioia marble monitored with Nonlinear Resonant Ultrasound Spectroscopy", European Geoscience Union (EGU) General Assembly 2024, Vienne, Autriche, 14-19 avril 2024, présentation orale. DOI : 10.5194/egusphere-egu24-1312
5. **Marie-Laure Chavazas**, Philippe Bromblet, Jérémie Berthonneau, Cédric Payan, "Thermo-hygric weathering of Carrara Gioia marble monitored with

Nonlinear Resonant Ultrasound Spectroscopy", 26th International Conference on Nonlinear Elasticity in Materials, Prague, République Tchèque, 9-14 juin 2024, présentation orale.

Résumé

Cette thèse porte sur la caractérisation et l'imagerie des dégradations du marbre de Carrare à différentes échelles par des méthodes acoustiques.

La première partie de cette thèse s'intéresse aux dégradations du marbre de Carrare à l'échelle du matériau. Une étude de laboratoire est menée dans le but caractériser les effets des variations de température et d'humidité relative sur les propriétés mécaniques du marbre de Carrare. L'état mécanique de ce matériau est suivi de manière non-destructive par spectroscopie ultrasonore à résonance non-linéaire (NRUS) durant des cyclages thermiques, hygriques et thermo-hygriques. En outre, des caractérisations microstructurales (porosimétrie au mercure, isothermes d'adsorption, observations aux microscopes optique et électronique à balayage) et mécaniques destructives sont réalisées afin de relier l'évolution des propriétés mécaniques mesurées par NRUS aux changements de microstructure du marbre.

La deuxième partie de cette thèse porte sur les dégradations du marbre de Carrare à l'échelle d'œuvres. Les objets étudiés sont deux sculptures romaines antiques du Musée Départemental Arles Antique qui ont été exposées aux conditions climatiques naturelles pendant plusieurs siècles dans le théâtre antique d'Arles. Leur état mécanique est évalué *in situ* de manière non-destructive au moyen de la tomographie acoustique couplée à l'utilisation de modèles 3D photogrammétriques. Une image 3D de la vitesse de propagation des ultrasons dans les sculptures est reconstruite dans le but d'estimer leur cohésion interne, de localiser leurs zones de faiblesse et d'estimer l'étendue de certaines altérations visibles en surface.

Mots clés : Marbre de Carrare ; Résonance non-linéaire ; Imagerie acoustique ; Endommagement thermo-hygrique ; Mécanismes de dégradation ; Conservation du patrimoine.

Abstract

This thesis is focused on the characterization and imaging of Carrara marble degradation at different scales by means of acoustic methods.

The first part of this thesis deals with Carrara marble degradation at the material scale. It consists in a laboratory study aiming at characterizing the effects of temperature and relative humidity variations on Carrara marble mechanical properties. For this purpose, the mechanical state of this material is non-destructively followed during thermal, hygric and thermo-hygric cycling by means of nonlinear resonant ultrasound spectroscopy (NRUS). Additionally, microstructural (mercury intrusion porosimetry, adsorption isotherms, observation under optical and scanning electron microscopes) and destructive mechanical characterizations are carried out in order to link the evolution of the parameters measured by NRUS to the changes occurring in marble microstructure.

The second part of this thesis is focused on Carrara marble degradation at the sculpture scale. The objects under study are two Roman sculptures of the *Musée Départemental Arles Antique* which were exposed to natural weather conditions for centuries in the Roman theater of Arles, France. Their mechanical state is non-destructively assessed by applying acoustic tomography combined with 3D photogrammetric models. A 3D imaging of the ultrasound propagation velocity is reconstructed inside the sculptures in order to investigate their inner cohesion state, to locate their zones of weakness and to estimate the extent of some alterations visible at sculpture surface.

Keywords: Carrara marble; Nonlinear resonance; Acoustic imaging; Thermo-hygric weathering; Degradation mechanisms; Heritage conservation.

Acknowledgments

I would like to first thank my supervisors, Cédric Payan, Philippe Bromblet and Jérémie Berthonneau, for their implication, help and advice. It was a pleasure working with you over the last three years.

I would like to then thank the jury members. Thank you Ann Bourgès and Paul Allan Johnson for agreeing to act as reporters for this thesis. Thank you Céline Schneider for joining the jury as examiner and Livio De Luca for accepting the jury presidency.

I also thank my PhD committee members, Céline Schneider and Fabien Cherblanc, for accepting this role, evaluating my PhD progress and giving me advice on my work.

Working on real sculptures would not have been possible without the support of museums, so I sincerely thank the *Musée Départemental Arles Antique* and its curators Alain Charron and Soizic Toussaint for allowing me investigating some of their sculptures.

I would like to deeply thank Jérémy Hénin from the LRMH for performing mercury intrusion porosimetry experiments on my samples and welcoming me to the LRMH. I also thank Nicolas Chanut from KU Leuven CMACS for carrying out BET measurements.

I am grateful to all the LMA and CICRP staff for welcoming me over the past three years. More particularly, at the CICRP, I would like to thank Odile Guillon for her great help with photography and photogrammetry. I also thank Nathalie Gandolfo for preparing thin sections. At the LMA, I would like to thank Éric Debieu for his ideas, advice and help on the sculpture tomography, Laurent Sabatier for the mechanical tests and X-ray microtomography, and Philippe Lasaygues for his explanations and advice on tomography. I would also like to thank the administrative managers for their support in preparing the missions and the doctoral school secretariat.

Finally, I thank my parents, my sister and Adam for their support, encouragement and interest in my work.

Table of contents

General introduction

Carrara marble is an emblematic marble variety which is considered a prestigious material, associated to whiteness and durability. Quarried since Antiquity, Carrara marble has been employed in numerous buildings and sculptures all over the world and is therefore a prime cultural heritage stone. Yet, Carrara marble can develop various forms of alteration, either biological, chemical or physical, as it ages. Exposure to weather conditions can be one of the deterioration factors of Carrara marble. Indeed, marble exposure to temperature variations is known to result in expansion, cracks, bowing, reduction of mechanical strength. Yet, the actual temperature range triggering these phenomena remains unknown and the evolution of temperature impact during cycling is ill-understood. Additional relative humidity variations could also enhance these phenomena. However, the effects of sole relative humidity variations on marble degradation have not yet been investigated and the coupling between temperature and relative humidity variations is poorly understood. In this context, a better comprehension of these degradation mechanisms at marble microstructure level is essential for adequate conservation and restoration, as well as for a better detection of these alterations in cultural heritage artefacts.

Moreover, the characterization and detection of Carrara marble degradation by non-destructive techniques is crucial in the field of cultural heritage conservation. Indeed, conservation rules prohibit sampling in numerous cases or authorize it only in very limited quantity. Additionally, when working in laboratory on natural stones, non-destructive techniques avoid interpretation difficulties due to material heterogeneities since the same sample can be followed at different ageing stages. Thus, acoustic methods are particularly well-adapted to probe the mechanical properties of cultural heritage artefacts and to monitor decay evolution *in situ* or during laboratory studies. Among these techniques, the evaluation of the longitudinal wave propagation velocity is already commonly used in the field of cultural heritage conservation and has been related to marble decay degree. This technique is based on the measurement of a linear parameter (propagation velocity) only. Yet, other fields, such as civil engineering, have developed acoustic methods measuring on various materials both linear and nonlinear parameters, both probing different phenomena, at different material scales. Stones being intrinsically nonlinear materials, such methods could be particularly well-suited to study the evolution of mechanical properties of artificially aged Carrara marble samples. Non-destructive diagnostic techniques for sculpted objects are also needed to address concerns or questions raised by conservators. To this end, the potential of acoustic tomography applied to cultural heritage artefacts has been investigated in various studies over the last decades.

Thus, this thesis aims at studying Carrara marble degradation at multiple scales thanks to non-destructive acoustic methods. The objectives are on the one hand to understand further the degradation mechanisms occurring in Carrara marble at the microstructure scale under thermo-hygric weathering, and on the other hand to assess the degradation state of sculpted objects with a non-destructive diagnostic technique adapted to the requirements of the cultural heritage conservation field.

The first chapter will give an overview of marble degradation mechanisms. Firstly, marble as a material will be presented, describing its composition and presenting the Carrara varieties. Then, the different forms of marble alteration will be described. An overview of the main biological, chemical and physical alterations will first be given. Afterwards, thermal weathering and degradation induced by water transfers will be detailed. Finally, the techniques enabling the monitoring of marble decay will be addressed, with a focus made on acoustic methods.

In the second chapter, marble degradation at the material scale will be studied from laboratory experiments by means of nonlinear resonant ultrasound spectroscopy. Nonclassical nonlinearity and its indicators will first be explained, and an overview of nonclassical nonlinearity in rocks specifically will be given. Then, the impact of thermo-hygric cycling on marble decay will be experimentally investigated thanks to this nonlinear resonance technique and microstructural characterization. First the impact of heating temperature and relative humidity alone will be explored, then the influence of cycling for both parameters separately, and finally the impact of coupled thermo-hygric cycling.

In the final chapter, marble degradation at the sculpture scale will be investigated by applying acoustic tomography coupled to photogrammetry. The degradation state of two archaeological sculptures excavated in the Roman theater of Arles and exhibited in the *Musée Départemental Arles Antique* will be assessed by this means. The two sculpted objects will first be presented and the principles of photogrammetry and acoustic tomography explained. The experimental set-ups used for both sculptures will then be detailed. The degradation state of the two archaeological pieces will finally be discussed based on the results of apparent propagation velocities, on the 3D imaging of the propagation velocity and on crack depth measurements.

The laboratory study showed that marble is impacted by temperatures as low as 40 °C and by the very first stages of exposure to thermal and thermo-hygric cycling. Besides, NRUS was proven efficient to monitor marble mechanical properties during cycling. The *in situ* acoustic tomography on archaeological sculptures provided consistent 3D imaging in agreement with the degrees of exposure of each object to weather conditions during the Roman times.

Future works could use NRUS, which brought information on both the macroscopic cohesion and the microcracking state of the material, to study other conservation issues such as the effectiveness of consolidation treatments or the effects of soluble salt

crystallization-dissolution cycles. Moreover, the use of lasers for acoustic tomography could be explored to make this technique contactless and to reconstruct wave amplitude in addition to wave velocity.

1. Marble and marble degradation

1.1. Marble

Marble is a metamorphic rock formed when limestone (sedimentary rock) is subjected to increasing pressure and temperature. The original rock undergoes significant modifications, such as recrystallization, through metamorphic processes that last over millions of years [1]. Temperature and pressure increase can be due to burial beneath accumulating sediments or by crustal movements linked to plate tectonics [1]. Marble can be either calcitic or dolomitic. In the first case it is mainly composed of calcite ($CaCO_3$), and of dolomite ($CaMg(CO_3)_2$) in the second case.

Calcite is a carbonate mineral composed of calcium carbonate ($CaCO_3$). Its unit cell is rhombohedral with dimensions of a = 4.9896 Å and c = 17.0610 Å, and the crystal is hexagonal [2]. Calcite structure is illustrated in Fig. 1. Calcite exhibits a strong anisotropy of its thermal dilation coefficient. Parallel to crystallographic c-axis, a calcite crystal is subjected to a dilation upon heating as the thermal dilation coefficient along this axis is of $\alpha_{||} = 26 \times 10^{-6}\ C^{-1}$. In the other directions, the thermal dilation is of $\alpha_{\perp} = -6 \times 10^{-6}\ C^{-1}$ [3,4].

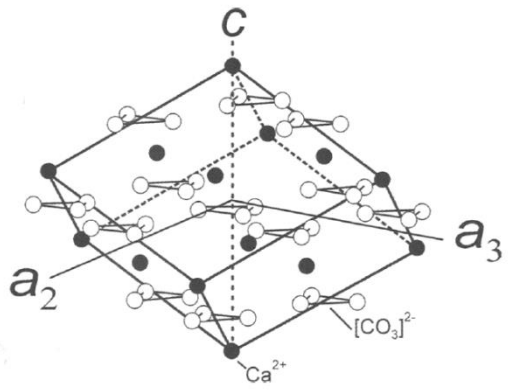

Fig. 1 Crystallographic structure of calcite (Weiss *et al.* 2002).

Dolomite ($CaMg(CO_3)_2$) is composed of calcium and magnesium carbonate. Like calcite, dolomite unit cell is rhombohedral and dolomite crystal is hexagonal. The unit cell dimensions of dolomite are a = 4.812 Å and c = 16.020 Å [2]. Dolomite and calcite have the same value of thermal dilation coefficient parallel to c-axis ($\alpha_{||} = 26 \times 10^{-6}\ C^{-1}$), whereas perpendicular to c-axis dolomite thermal dilation coefficient is positive ($\alpha_{\perp,dol} = 6 \times 10^{-6}\ C^{-1}$) [5].

The marble variety studied in this work is Carrara marble, and more precisely the Carrara Gioia variety. Carrara marble deposits are located in the Apuan Alps region, in

northwestern Tuscany, Italy. The area of occurrence of Carrara marble is shown in Fig. 2 (a). The Apuan Alps belong to the northern Apennines, which were formed during the Tertiary [6]. The metamorphism responsible for marble formation in the Apuan Alps was caused by two tectonic events occurring at the Oligocene/Miocene boundary and during Miocene [6,7]. Carrara marble quarries have been operating since the Roman Empire (1st century B.C.) and are still active nowadays [6,7]. A photograph of a modern Carrara marble quarry is displayed in Fig. 2 (b). Carrara marble refers to different marble varieties such as white Carrara marble, veined marble, Bardiglio marble, cloud-like marble, arabesque-like marble, statuary marble, Calacata marble, purple-violet marble, striped marble [6,7]. These varieties are distinguished based on the color, grain size distribution, orientation of the c-axes, or grain boundary shape [6]. The Carrara Gioia variety is a calcitic veined marble, has a granoblastic equigranular polygonal microstructure with straight to slightly curved grain boundaries meeting in triple points, has an unimodal grain size distribution with an average grain size between 200 and 350 µm and is not strongly oriented (type A microfabric in Meccheri *et al.* (2007)). Primavori (2015) gave some general technical properties for veined Carrara marble, to which Carrara Gioia marble belongs: apparent density of 2710 kg/m^3, open porosity of 0.40%, uniaxial compressive strength of 101.4 MPa [7].

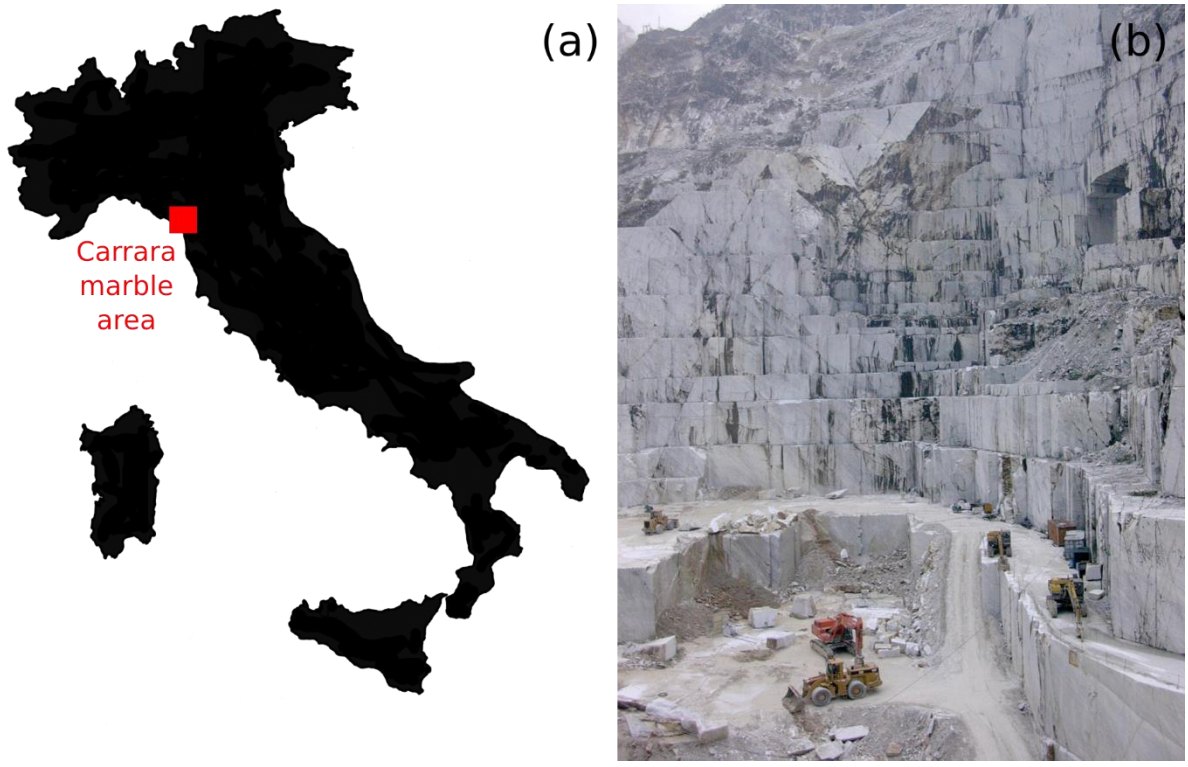

Fig. 2 Carrara marble quarries. (a) Location of Carrara marble deposits in Italy, and (b) photograph of a Carrara marble quarry in 2009 (picture by Philippe Bromblet).

1.2. Marble alterations

When used in sculptures or buildings, marble is subjected to diverse alteration factors and agents. Its intrinsic properties can make it more sensitive to some deterioration patterns. Marble alterations can be either biological, chemical or physical.

Like other stones, marble can be affected by biological colonization. Stones can be colonized, on surface or in cavities, by plants or various micro-organisms such as bacteria, cyanobacteria, algae, fungi, and lichen [8]. An example of such alteration on marble is shown in Fig. 3. The penetration depth of biological colonization inside the stone depends on the nature of the organisms [8]. The colonization is influenced by the environment of the stone as well as by its properties [9].

Fig. 3 Biological colonization. Lichen colonization on a marble statue in the Cemetery of Pontresina, Switzerland (ICOMOS Glossary 2008).

Calcite, the main component of calcitic marble, can also be subjected to different chemical weathering through the processes of dissolution, hydrolysis, hydration. Indeed, calcite is vulnerable to dissolution in water (solubility of 0.014 g/L in pure water at 25 °C [10]), according to the following reaction [11]:

$$CaCO_3 + CO_2 + H_2O \leftrightarrow 2HCO_3^- + Ca^{2+}$$

Besides, calcite hydration with atmosphere pollutants plays a significant role in the formation of black crusts on marble, as sulfur trioxide (SO_3) and calcite ($CaCO_3$) react with water to form gypsum ($CaSO_4 \cdot 2H_2O$):

$$CaCO_3 + SO_3 + 2H_2O \rightarrow CaSO_4 \cdot 2H_2O + CO_2$$

The resulting gypsum matrices absorb carbonaceous particles, which leads to the formation of black crusts on the stone. Fig. 4 shows an example of black crusts on marble. Black crusts generally develop on surfaces sheltered from rainfall and water runoff. As black crusts adhere firmly to the substrate, their detachment results in loss of stone substrate [8,12–15].

Fig. 4 Black crust. Black crusts on marble sculpture exposed in Beijing Stone Carving Art Museum (Wang *et al.* 2002).

Salts are another type of stone damaging agents. They can come from the ground, sea spray, chemical treatments, or natural constituents of the stone [1]. Salts can deteriorate sculptures and buildings through efflorescence and subflorescence. Efflorescence consists in the formation of whitish, powdery or whisker-like salt crystals on the material surface [8]. When salt crystallization occur beneath the material surface, it is called subflorescence [8]. Salts can damage stones by several means such as crystallization, hydration, differential thermal expansion. During crystallization, salts that were originally dissolved in water crystallize in the pores of the stone. This phenomenon is accompanied by a crystallization pressure applied by the growing crystals, and by a volume expansion of the salts that can lead to the cracking of the material [1]. During hydration, water is absorbed into the salt crystal lattice leading to an increase of the salt volume and thus to a pressure exerted against the pore walls [1]. Moreover, salts can have a stronger thermal expansion than the surrounding stone, which can result in thermal disruption when the stone surface is exposed to heating-cooling cycles [1]. Salt action on a marble block from Delos Island, Greece, is shown in Fig. 5. The presence of salt from the marine environment resulted in dissolution and in crack and cavity formation in Delos marble [16].

Frost is another damaging element for marble. Frost action on stones depends on various factors such as pore size distribution, relative humidity, water saturation, presence of salts [17,18]. Deterioration caused by frost can result from ice crystallization, hydrostatic pressure, or expansion of unfrozen water [1]. Indeed, the volume of unfrozen water strongly increases between +4 °C to -9 °C, which can cause bursting in smaller pores [1]. Ice crystallization during freezing can also be damaging as it induces pressure in the pore network [19]. The forming ice can also induce pressure on unfrozen water still present in the pore network. Reduction of marble mechanical properties (Young's modulus, ultrasonic pulse velocity) has been observed after freeze-thaw cycles [20–23].

Fig. 5 Salt decay. Small cavities on a marble block in Delos Island, Greece (modified from Chabas and Jeannette 2001)

Exposure to climatic conditions also induces weathering in marble artefacts. The specific impact of temperature and water on marble degradation will be discussed in the next sections (1.3, 1.4).

1.3. Marble thermal weathering

Marble artefacts exposed outdoors are subjected to temperature variations. These variations may occur due to daily as well as seasonal temperature fluctuations. Temperature variations are known to have a great impact on marble degradation state according to a phenomenon called thermal weathering.

The sensitivity of marble to thermal weathering is generally explained by the anisotropy of calcite thermal dilation coefficient (see section 1.1). Indeed, the thermal elongation Δl induced in a material of initial length l_0 by a temperature variation ΔT is related to the material thermal dilation coefficient α_{th}:

$$\frac{\Delta l}{l_0} = \alpha_{th}\,\Delta T$$

In calcite, the value of the thermal dilation coefficient is strongly dependent on the crystallographic orientation ($\alpha_{||} = 26 \times 10^{-6}\ C^{-1}$ and $\alpha_{\perp} = -6 \times 10^{-6}\ C^{-1}$ parallel and perpendicular to c-axis, see section 1.1). Thus, for example, a thermal variation of 40 °C on a crystal with a length of 300 µm along the c-axis theoretically leads to an elongation of 0.3 µm along this axis. The thermal behavior of a calcite grain during a heating-cooling cycle is schematized in Fig. 6. This figure shows that calcite grains do not regain their initial position after cooling down, leading to the creation of intergranular spaces in marble and therefore to a loss of grain contacts [24–26].

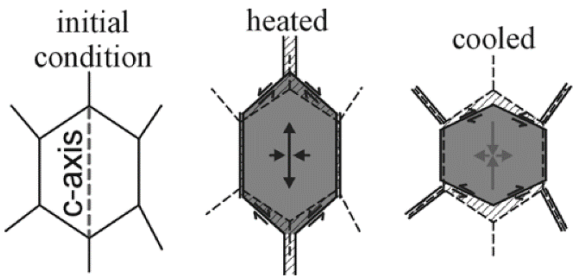

Fig. 6 Calcite thermal behavior. Scheme of calcite crystal behavior during a heating-cooling cycle (Grelk *et al.* 2004).

At the macroscopic scale, the thermal behavior of a marble sample also depends on the grain orientation and their arrangement. Neighbor grains with a different orientation have different dilation/contraction directions, which can lead to internal stress at grain contacts. Thus, the residual thermal expansion depends on the specific microstructure of a sample. Marble thermal expansion have been quantified in several studies as shown in Fig. 7 [24,25,27]. In natural conditions, temperature variations also generate a thermal gradient, controlled by thermal conductivity, in marble artefacts. As temperature is not uniform inside the stone (surface directly exposed to solar radiation compared to side against a wall or in the shadow), it can lead to a thermal stress field [28].

The loss of cohesion due to calcite anisotropic thermal behavior results in an important reduction of marble mechanical properties after heating, which has been noticed in many studies. For example, Mahmutoğlu (1998, 2006) observed a reduction of 50% in compressive strength and of 60% in tensile strength in Carrara marble heated 16 times up to 600 °C, and a reduction of 44% in compressive strength for Muğla marble heated 8 times at 400 °C [29,30]. Ferrero and Marini (2001) noted a drop of 60% and 66% in Young's modulus for black marble heated at 600 °C and white marble heated at 500 °C, respectively [31]. Furthermore, thermal treatments are also used as an artificial weathering procedure to produce modifications in marble porosity and mechanical properties that resemble alterations found in the field on naturally weathered marble [32,33].

However, the temperature ranges chosen in the previously presented studies are not representative of marble natural exposure conditions. Indeed, Schouenborg *et al.* (2007) concluded from an onsite monitoring campaign and a comprehensive literature review that the maximum temperature reached on white Carrara marble surface was about 60 °C [34]. Besides, the environmental monitoring made on marble in the central Namib desert for three years by Viles (2005) showed that marble surface temperature reaches 55 °C, with a maximum air temperature of 37 °C [35].

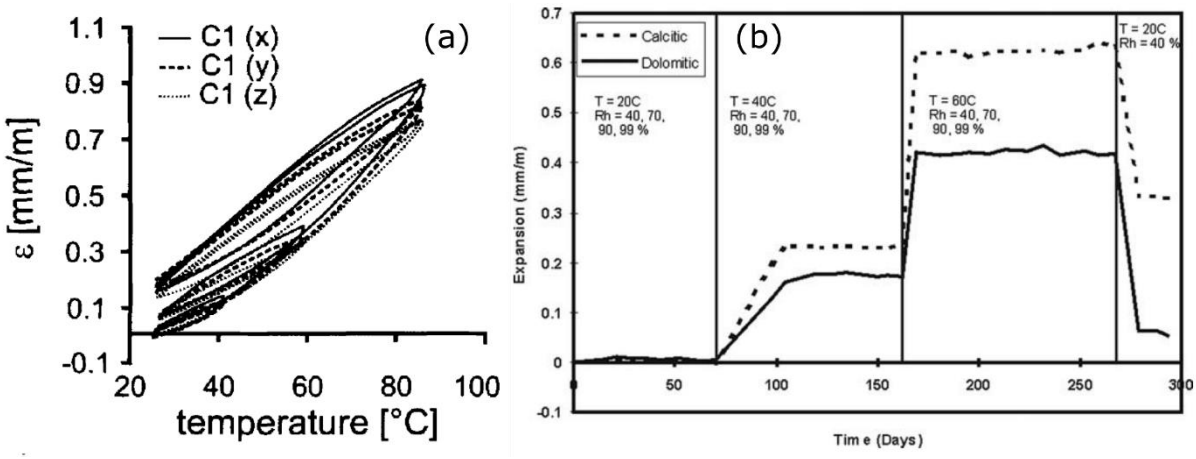

Fig. 7 Marble thermal expansion. Expansion upon heating of (a) Carrara marble in three directions (Zeisig *et al.* 2002) and of (b) a calcitic and a dolomitic marble (Malaga-Starzec *et al.* 2006). In both subfigures a residual strain is observed when the initial temperature is again reached, in agreement with the loss of grain contacts at the microscopic scale.

Therefore, thermal cycling in the mild temperature range reproduces more closely the natural impact of temperature on marble. Some studies already indicate marble deterioration in this temperature range. For instance, Schouenborg *et al.* (2007) recommended to condition marble at 40 °C rather than 70 °C since a considerable loss of mechanical strength was observed for temperatures lower than 70 °C [34]. Moreover, Malaga *et al.* (2002) suggested that intergranular decohesion could occur between 40 and 50 °C for some marble varieties, based on porosity measurements on calcitic and dolomitic marbles heated between 40 and 200 °C [36]. In Malaga-Starzec *et al.* (2006), a calcitic and a dolomitic marble were thermally cycled 50 times between -15 °C and +80 °C [24]. Ultrasonic pulse velocity (UPV) is about 65% lower for the thermally cycled calcitic samples than the reference fresh samples, whereas it is similar for all dolomitic samples. Waragi (2023) subjected Carrara marble samples to 144 thermal cycles from 4 to 84 °C [37]. UPV decreases in the first four cycles, then increases between the 4th and 80th cycle, and finally reaches a plateau until the 144th cycle. The hypothesis made by the author for the increasing values of UPV above 4 thermal cycles is a healing effect through the re-strengthening of calcite grain contacts.

Exposure to temperature variations can result in several alteration patterns on marble artefacts such as sugaring, bowing, microcracking. The bowing of marble slabs was extensively studied during the early 2000s [5,26,34,38–42]. Marble bowing appears on slabs covering facades or cemetery vaults. This phenomenon is illustrated in Fig. 8 (a) [5,43]. Slabs can bow inward or outward, and bowing creates serious security issues as the slab mechanical strength is greatly reduced, which can result in panels falling off from building facades (Zagrepcanka business tower, Zagreb, Croatia [38]). For instance, Marini and Bellopede (2007, 2009) observed a 50% drop in UPV and flexural strength on Tuscan marbles subjected to bowing [41,42]. Sugaring consists in marble granular disintegration. An example of such alteration is shown in Fig. 8 (b). In case of sugaring, cohesion between calcite grains is completely lost and single grains or grain aggregates are detached from the stone [8,44]. Thermally induced microcracks can also develop

inside marble upon heating. Ferrero and Marini (2001) noted an increase in the number and density of microcracks with increasing heating temperature of marble [31]. Peng *et al.* (2019) observed an increase in the number, width and length of microcracks with increasing number of heating-cooling cycles (up to 600 °C) [45].

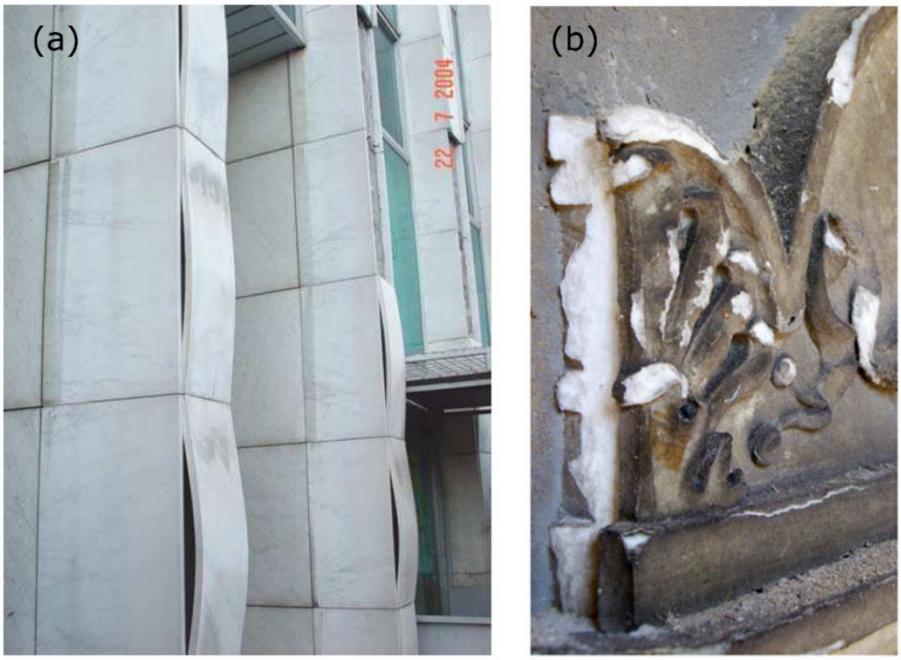

Fig. 8 Marble bowing and sugaring. (a) Bowing of marble slabs on Zagrepcanka business tower in Zagreb, Croatia (Grelk *et al.* 2007), and (b) sugaring on gravestones in the Monumental Cemetery in Bologna, Italy (Sassoni *et al.* 2014).

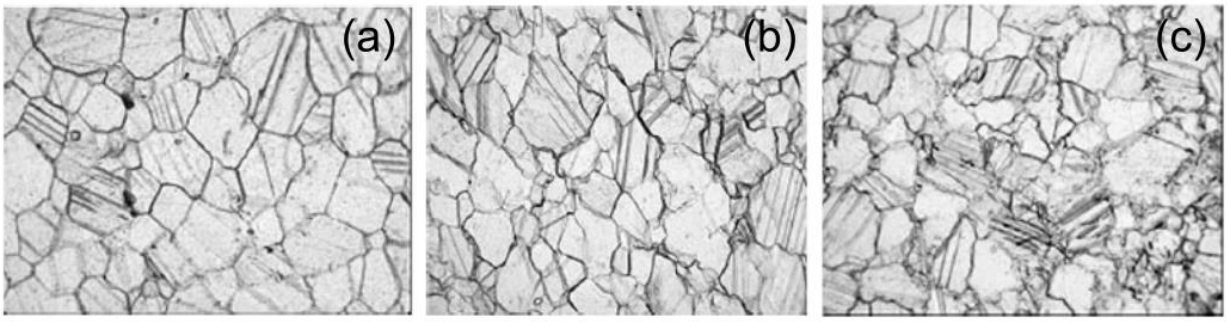

Fig. 9 Marble microstructures. (a) Equigranular, (b) intermediate (between equigranular and seriate interlobate) and (c) seriate interlobate microstructures in three Tuscan calcitic marbles (Marini and Bellopede 2009)

Marble sensitivity to thermal damage can be enhanced by intrinsic and extrinsic factors. Regarding intrinsic factors, some microstructures are more favorable than others for the development of thermal damage. Indeed, Åkesson *et al.* (2005) and Marini and Bellopede (2009) showed that marbles with equigranular or intermediate microstructures exhibit more bowing than marbles with seriate interlobate microstructure [39,41]. These three microstructure types are illustrated in Fig. 9. Additionally, dolomitic marble tends to be less sensitive to thermal weathering than

calcitic marble [5,24,34,41,42]. Regarding extrinsic factors, the presence of moisture in marble can increase thermal expansion [40].

Therefore, even though marble thermal weathering has been well-studied, this phenomenon is not yet completely understood. The actual temperature range triggering this weathering remains unknown, especially in the mild temperature range. Yet, Malaga *et al.* (2002) suggest temperatures as low as 40 °C for intergranular decohesion initiation [36]. Such temperatures are frequently reached on the surfaces of marble exposed outdoors, thus a better insight on the impact of this temperature range on marble weathering would be enlightening. Additionally, the effects of prolongated thermal cycling in the mild temperature range have been little investigated. For instance, Waragi (2023) suggests that calcite grains have the ability of re-strengthening their contacts when subjected to several thermal cycles. Yet, so far this hypothesis is not supported by other works and some studies draw contrary conclusions with evidence of mechanical property reduction during long-term cycling [24]. Besides, the temperature range that could trigger such re-strengthening is unknown, as well as microstructural phenomena resulting in such a mechanism.

1.4. Marble degradation induced by water transfers

As porous materials, stones are subjected to water transfers in gaseous, liquid or simultaneously both states. The location of these water transfers is the pore network which is composed of the voids between and inside grains. Porosity (classically expressed by the percentage by volume, vol. %) is the physical quantity defined as the ratio of the volume of these voids to the total apparent volume of the stone. For example, marble is known to have a very low porosity (between 0.3 and 0.4 % of open porosity in Carrara marble varieties [7]). The stone pore volume may be further defined by its size distribution. Indeed, a pore network can be made of micropores, mesopores or macropores (with width < 2 nm, between 2 and 50 nm, and > 50 nm, respectively, according to IUPAC (International Union of Pure and Applied Chemistry) [46]), and the pore size distribution can be unimodal or multimodal if one or several pore sizes dominate in the stone. This pore size distribution eventually governs water transfers.

A model of the gaseous and liquid water transfers in the pore network was developed by Rose in the 1960s (Fig. 10) [47]. The first stages of water transfer correspond to the hygric interactions. In hygric interactions, gaseous water movements dominate over liquid water movements. These stages occur from a few % up to 100% relative humidity. Relative humidity (RH) is defined as the ratio of the partial pressure of water vapor P_w in air to the saturation vapor pressure $P_{w,sat}$: $RH = P_w/P_{w,sat}$. Saturation vapor pressure corresponds to the maximum value that can be reached by partial pressure at a given temperature. Absolute humidity represents the amount of gaseous water molecules in

dry air. With increasing water saturation degree, water transfers are dominated by liquid water movements and correspond to hydric interactions.

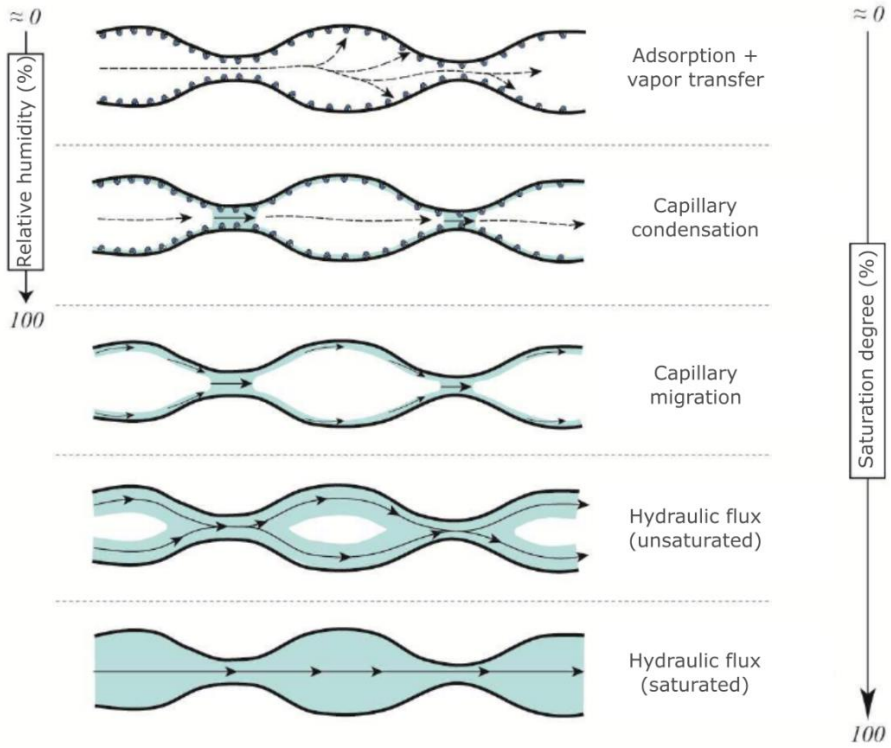

Fig. 10 Water transfers in the pore network. The different stages of water transfers in porous materials (modified from Berthonneau 2013). Dashed lines correspond to gaseous water movements and solid lines to liquid water movements.

1.4.1. Adsorption

At low relative humidity, the first stage of water transfers consists in adsorption. Adsorption results from the interactions between a gas and a solid surface. In the context of water transfers in stones, adsorption corresponds to gaseous water molecules binding to pore walls. As relative humidity increases, molecules aggregate to form mono- and pluri-layers of water molecules. Adsorption can be classified in two types: it can be either physical (physisorption) or chemical (chemisorption) [49]. Different bonding is formed in each type of adsorption. In physisorption, water molecules adhere to the surface thanks to Van Den Waals bonds that have a bonding energy of a few $kJ.mol^{-1}$ [49]. In chemisorption, water molecules adhere to electrically charged surfaces of minerals. Chemisorption involves ionic and covalent bonds whose bonding energy is superior to 41.8 $kJ.mol^{-1}$ [49]. As calcite grain surfaces are rather chemically inert under ambient conditions, marble is mainly subjected to physisorption.

1.4.2. Capillary condensation

When relative humidity increases, water molecules form more stable arrangements and films of bound water appear in the smallest pores. This phenomenon is called capillary condensation. It does not occur simultaneously in the whole pore network as it is governed by pore size. Indeed, the largest pore size in which capillary condensation can occur at a given relative humidity RH and temperature T is defined by Kelvin's radius r_K [50]:

$$r_K = -\frac{2\,\gamma\,V_M\cos\theta}{R\,T\ln(RH)} \qquad (1)$$

where γ is the surface tension at the liquid/gas interface, V_M is the molar volume of the liquid condensate, θ is the contact angle, R is the ideal gas constant. For water at T = 25 °C, the values of the parameters of Eq. (1) are R = 8.314 J.mol^{-1}.K^{-1}, θ = 0°, γ = 71.99 × 10^{3} N.m^{-1}, V_M = 1.807 × 10^{-5} m^{3}.mol^{-1} [49], and Eq. (1) becomes:

$$r_K[\mu m] = -\frac{1.05007\ \cdot\ 10^{-3}}{\ln(RH)} \qquad (2)$$

Kelvin's radius evolution with relative humidity for water at T = 25 °C is displayed in Fig. 11 (a). As capillary condensation does not affect the whole pore network simultaneously, air and liquid water coexist in pores and menisci are formed at their interfaces. These menisci are subjected to microscopic capillary pressure as a result of the different pressures in air and in liquid water. Microscopic capillary pressure in water films leads to microscopic contraction pressure in the solid matrix as a reaction force [51]. These phenomena are schematically represented in Fig. 11 (b).

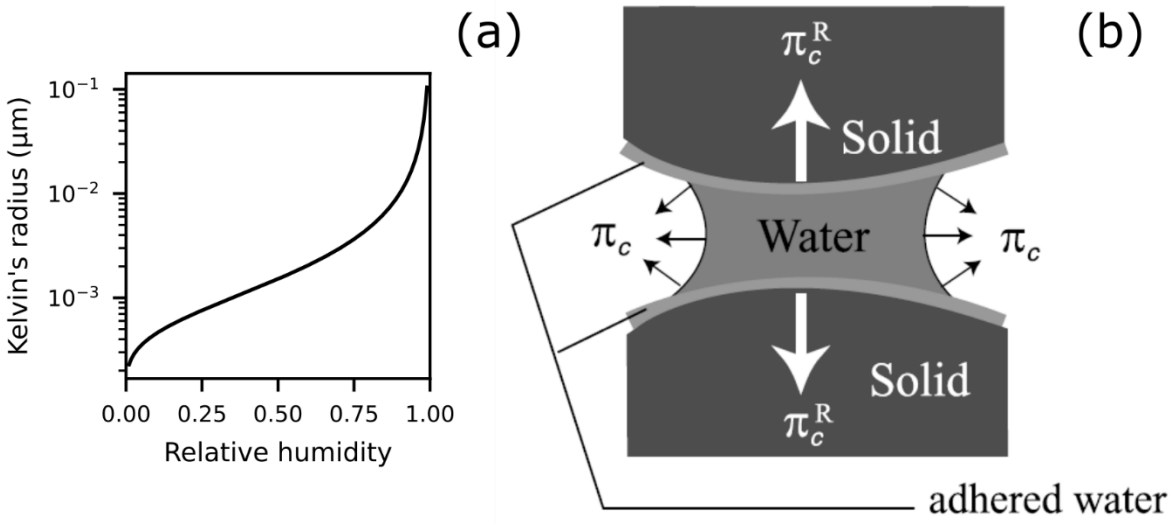

Fig. 11 Capillary condensation. (a) Evolution of Kelvin's radius with relative humidity, and (b) scheme of the microscopic capillary pressure and microscopic contraction pressure resulting from menisci formation during capillary condensation (Van Den Abeele *et al.* 2002).

1.4.3. Desorption

If relative humidity then decreases, water molecules progressively move towards the exterior of the pore network: this is the desorption phase. Desorption and adsorption are not perfectly symmetrical processes as the progressive decrease in water content during desorption does not follow the exact path of the water uptake during adsorption. This results in a hysteretic phenomenon in sorption curves calculated for an adsorption-desorption cycle [50]. The four types of hysteresis loops identified by IUPAC are presented in Fig. 12. Various reasons can explain the adsorption-desorption hysteresis such as a difference in contact angle value during adsorption and desorption, the presence of ink-bottle pores [52], or fluid being more structured during desorption [53].

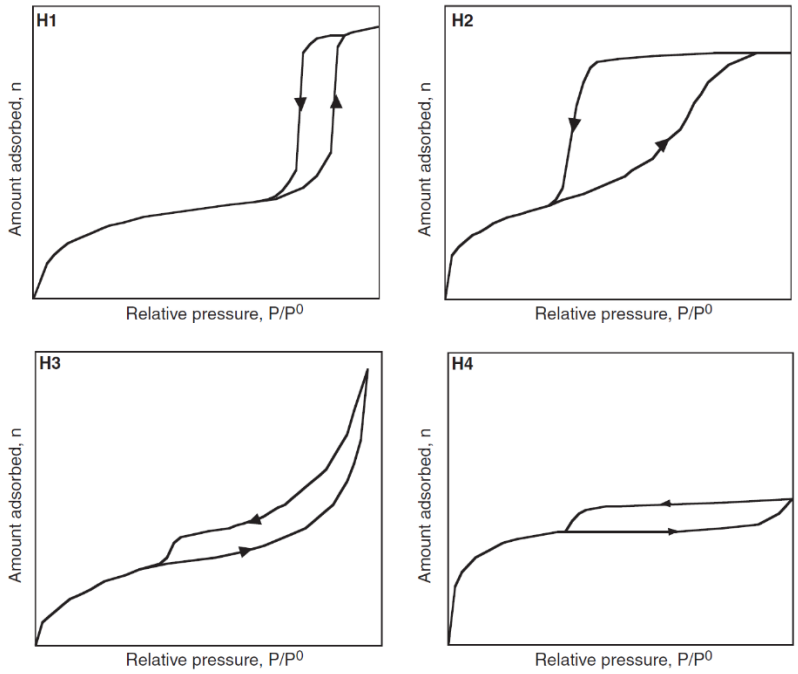

Fig. 12 Sorption hysteresis. The four types of hysteresis loops identified by IUPAC (Sing and Williams 2004).

1.4.4. Hydric transfers

If water saturation then increases, water transfers now correspond to hydric interactions and are dominated by liquid water movements in the pore network. Hydric interactions are characterized by different phenomena such as capillary imbibition, drainage, evaporation. Capillary imbibition corresponds to the spontaneous migration of water in a capillary when its base is introduced in a fluid. Drainage is not spontaneous and requires the application of an external force. It corresponds to the displacement of the most wetting fluid by the least wetting fluid. The maximum height reached by water in a capillary through capillary imbibition is given by Jurin's law [49]. The flux and the maximum velocity of an incompressible and viscous fluid in a capillary is given by

Poiseuille's law [49]. Evaporation corresponds to the transition from liquid to gaseous state and occurs when relative humidity decreases or when temperature or air agitation increases. Evaporation goes hand in hand with the diffusion of gaseous water molecules in the air which is governed by Fick's laws [49].

1.4.5. Marble degradation due to hydric transfers

Comparably to thermal dilation upon temperature increase, stones are also subjected to hydric dilation upon water saturation increase (Fig. 13) [54]. During events of humidification and drying, hydric dilation and shrinkage generate mechanical stress in stones and can lead to significant alterations such as spalling decay [55]. Hydric dilation is particularly pronounced in clay-bearing stones as clay minerals possess a significant swelling ability [55]. On the contrary, marble shows very little sensitivity to hydric dilation, with length change of less than 0.1% [56,57].

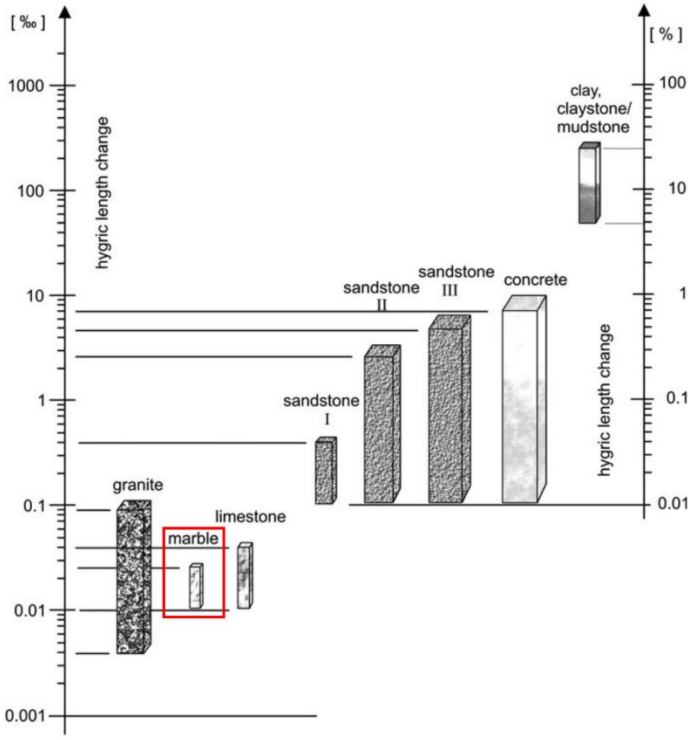

Fig. 13 Hydric dilation in stones. Hygric length change in various stone types. Marble domain is squared in red (modified from Siegesmund and Snethlage 2014)

Stone mechanical properties can also be impacted by hydric transfers. Indeed, mechanical properties of various stone types, such as sandstones [58–61], limestones [55,62–66], igneous rocks [67], shales [68], are significantly changed in presence of liquid water. Different mechanisms can be at stake depending on the stone type: fracture energy reduction, capillary tension decrease, pore pressure increase, frictional reduction, chemical and corrosive deterioration [11,68]. Various studies have shown that marble is mechanically affected by water saturation. Vásárhelyi *et al.* (1999) found that Young's modulus decreases by 4%, compressive strength by 7% and tensile

strength by 1% between air-dry and saturated samples of Sivac marble [23]. Mahmutoğlu (2006) showed that peak strength of Muğla marble diminishes between dry and saturated samples subjected to the same strain rate [30]. Cai *et al.* (2019) compared the water-weakening effects on the mechanical behavior of sandstone, granite and marble and found that marble is the rock type least affected by water saturation [11]. Cai *et al.* (2019) also presented pore pressure and calcite dissolution to be the causes of uniaxial compressive strength reduction in water-saturated marble. In Zhu *et al.* (2020), a Chinese white marble exhibits a 29% reduction in average uniaxial compressive strength and a 23% reduction in average Young's modulus between dry and water-saturated samples [69]. Therefore, the water-induced softening of different marble types has been extensively investigated. Yet, marble artefacts are more frequently subjected to relative humidity variations than episodes of water imbibition.

1.4.6. Marble degradation due to moisture

There are very few studies focused on the sole impact of moisture on marble decay. Siegesmund *et al.* (2021) investigated the influence of air relative humidity level on UPV of Blanco Macael marble samples in different weathering states [70]. On average in the three directions of space, UPV increases by 8% for the fresh Blanco Macael sample and the sample heated up to 200 °C and then subjected a freeze-heat cycle, by 6% for the sample heated at 150 °C and by 12% for the sample heated at 60 °C, between dry state and 90% RH. Therefore, Siegesmund *et al.* (2021) concluded on a small influence of relative humidity level on marble UPV and on a lower influence with higher weathering state [70]. However, moisture plays a role in various alterations previously presented (see section 1.2). For instance, variation in moisture content inside stones can enhance the damage caused by salt crystallization if relative humidity and temperature conditions lead salts to change of stability domain. Moisture uptake in stones can also activate alteration due to frost, dissolution, and hydration. Besides, the presence of moisture is thought to enhance thermal expansion in marble exposed to temperature fluctuations [40].

Therefore, the sole impact of relative humidity variations on marble mechanical properties has been very little studied so far while marble artefacts are very often exposed to relative humidity variations in natural environment. For a better understanding of marble degradation due to climatic conditions, it would be important to study marble decay under similar conditions in laboratory. Controlled laboratory experiments focusing on the mild temperature range and on relative humidity variations could thus improve knowledge on marble degradation mechanisms. To follow such degradation processes on long-term experiments, nondestructive monitoring techniques are needed.

1.5. Monitoring marble decay

Various techniques are employed to evaluate marble decay. By collecting small samples of matter directly on buildings or sculptures, microstructural analyses can be carried out. Microstructural analyses include porosimetry, capillarity or water adsorption measurements, chemical composition, observations under scanning electron and optical microscopes. Mechanical properties are usually monitored by means of destructive mechanical tests such as compressive, tensile and flexural strength test [5,29,31,41,42]. These tests require larger samples (e.g., core samples of about 100 cm^3) than microstructural analyses and are therefore ill-suited for decay evaluation of cultural heritage artefacts. Moreover, due to their destructive nature, these methods are also ill-adapted to laboratory monitoring of stone properties all along weathering cycling. Indeed, they do not allow following properties of the same samples at different cycling stages while stone samples exhibit a lot of variability between one another, even within a same stone block.

Nondestructive techniques based on electromagnetic or acoustic waves have been developed to investigate degradation in cultural heritage artefacts. Electromagnetic wave-based methods include ground-penetrating radar and infrared thermography, for instance. Ground-penetrating radar uses the reflection of high-frequency electromagnetic waves to determine structure layer thickness, estimate continuity of materials, locate and determine depth of structural anomalies [71]. Infrared thermography consists in detecting the infrared electromagnetic radiation of an object. It has been applied for various conservation issues: assessment of stone cleaning [72,73] and of stone consolidation [72], nondestructive testing of mural paintings [74], monitoring of water diffusion [75] and of failure modes [76].

Table 1 Marble damage classes (after Weiss *et al.* 2002).

Damage class	Ultrasonic pulse velocity (m/s)	Marble condition
0	> 5,000	Fresh
I	3,000 – 5,000	Increasingly porous
II	2,000 – 3,000	Granular disintegration
III	1,500 – 2,000	Fragile
IV	< 1,500	Crumbling rock

Contrary to ground-penetrating radar and infrared thermography, acoustic techniques are physically linked to the material mechanical properties. Therefore, they can overcome the limitations of destructive mechanical testing while probing the same properties. Acoustic techniques are based on the study of propagation, attenuation, diffraction, reflection of acoustic waves. The most popular of such methods in the field of cultural heritage conservation is the measure of ultrasonic pulse velocity (UPV) which consists in evaluating propagation velocity of longitudinal waves in a sample. UPV is widely used to assess marble damage. Five damage classes were defined by Köhler in

the 1990s to link UPV values to marble degradation state [77]. These classes are presented in Table 1.

As UPV measurement is nondestructive, it allows evaluating the state of marble under investigation in laboratory. For instance, Sena da Fonseca *et al.* (2021) compared UPV before and after consolidation, Siegesmund *et al.* (2021) followed the evolution of UPV with heating temperature, water saturation and under different air relative humidity, Waragi (2023) monitored UPV of Carrara marble during 144 thermal cycles [33,37,70]. UPV is also well-adapted to decay diagnosis of cultural heritage artefacts. Wave propagation inside objects is impacted by the inner defects, the weak areas, or the heterogeneities that acoustic waves may cross. Therefore, UPV can probe inner degradation state of an artefact without sampling it. For instance, Pascale and Lolli (2015) studied the degradation state of the left foot of the Michelangelo's David by measuring UPV in various directions (Fig. 14) [78]. Fais *et al.* (2018) used this technique on a pillar of the Palazzo di Città of Cagliari [79].

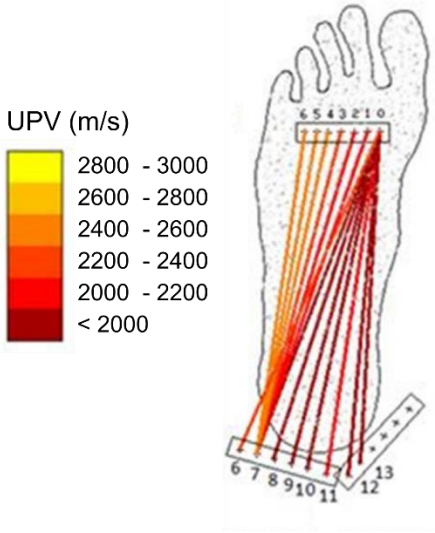

Fig. 14 UPV measurements carried out in the left foot of Michelangelo's David (modified from Pascale and Lolli 2015).

Authors have been interested not only in having global UPV measurements on various segments across sculptures but also in producing UPV cartographies in the volume of the object from the UPV measurements on the segments. To this end, ultrasound tomography can be used to generate a mapping of the inner degradation state of objects without damaging them. Siegesmund *et al.* (2021) explored acoustic tomography on marble laboratory samples and presented planar UPV cartographies (Fig. 15 (a)) [70]. Ruedrich *et al.* (2013) obtained similar planar UPV cartographies on the marble sculpture "Athena Arms the Warrior" situated in Berlin, Germany, by carrying out acoustic tomography in three cross-sections in the chest and the right leg of the warrior (Fig. 15 (b)) [80]. A step further in the use of acoustic tomography for decay diagnosis is the generation of not only planar UPV cartographies but also of UPV cartographies in the whole volume of sculpted objects. Colombero *et al*. (2022) provided such 3D cartography of UPV on a diorite statue of Ramses II [81]. By means of a 3D lasergrammetric model of the statue and of several hundreds of UPV measurements

covering the whole volume of the sculpture (Fig. 16 (a)), the authors were able to reconstruct a 3D cartography of UPV inside the statue (Fig. 16 (b)). Their 3D acoustic tomography results were then combined with results of ground-penetrating radar scans to define a damage index which is effective in locating superficially visible fractures of the statue. However, the application of this method, linking surveys of sculpture inner state to surface decay, remains limited by the fact that the use of ground-penetrating radar requires the presence of flat surfaces, which excludes a large number of sculpted objects.

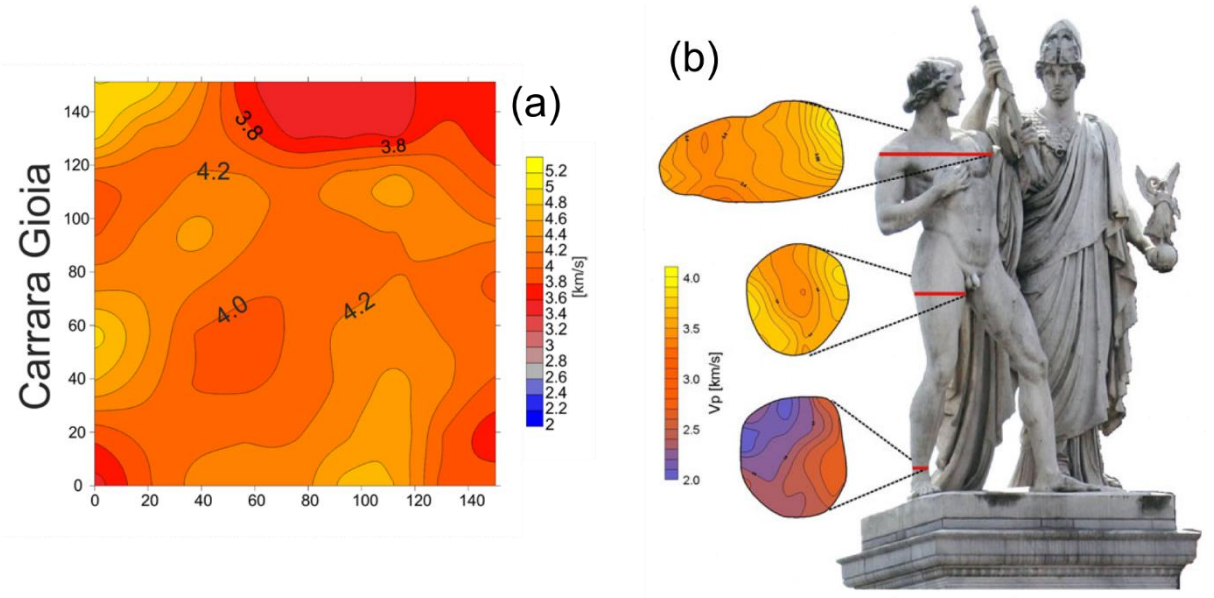

Fig. 15 Planar UPV tomographs. (a) Tomograph in a Carrara marble laboratory sample (Siegesmund *et al.* 2021), and (b) three tomographs in "Athena Arms the Warrior" marble sculpture (Ruedrich *et al.* 2013).

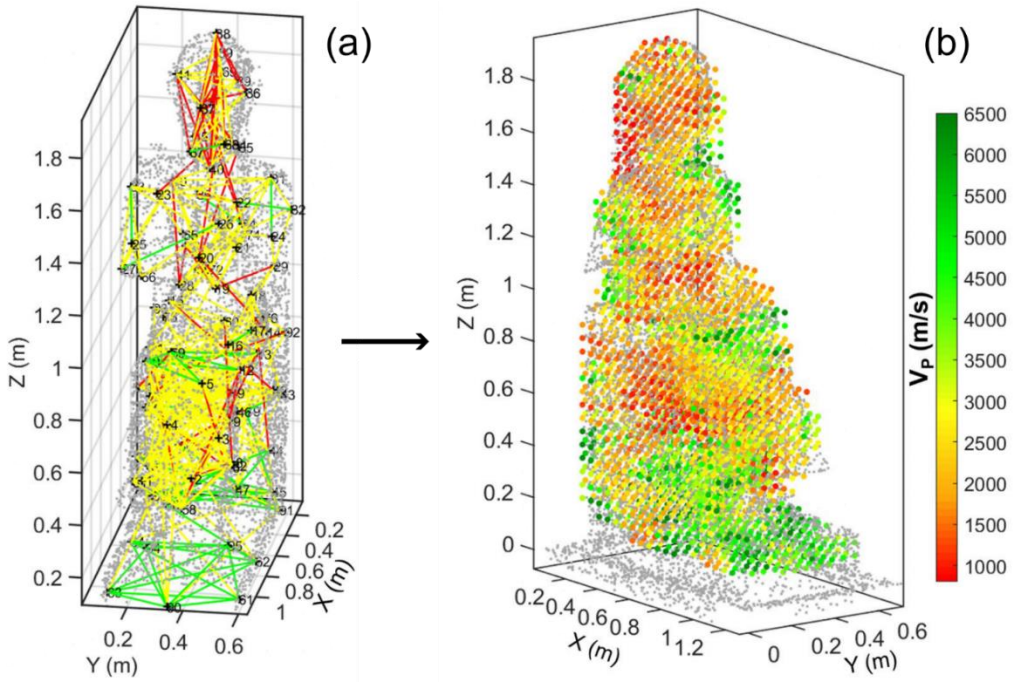

Fig. 16 3D acoustic tomography. (a) Punctual UPV measurements carried out on Ramses II statue and (b) the resulting 3D UPV cartography (modified from Colombero *et al.* 2022).

1.6. Conclusion on marble degradation

Thus, marble used in architectural or sculpted works can be subjected to diverse biological, chemical or physical alterations as it ages. Among all deterioration phenomena, marble microstructure makes this material particularly sensitive to thermal weathering. Indeed, the anisotropic thermal dilation behavior of calcite, the main marble component, leads to intergranular decohesion in this material during heating-cooling cycles. Exposure to relative humidity variations can enhance thermal weathering, as well as other decay processes such as salt crystallization or freeze-thaw cycles.

Yet, the phenomena at stake during thermal and hygric weathering are still not fully understood. For instance, the actual temperature range, especially in the mild temperature range, triggering thermal weathering is still not clearly defined. Besides, the sole impact of relative humidity variations on marble, not coupled with any other degradation factor, has not been studied so far.

The evaluation of the degradation state of cultural heritage artefacts must respect strict requirements for their integrity preservation. The great variability of natural stone properties also has to be taken into account. Therefore, the methods best adapted to this field are nondestructive techniques. Acoustic methods fall into this category and can probe and monitor mechanical properties. UPV measurement is already widely used in the field of cultural heritage conservation to assess marble decay, either by means of punctual measurements across the sculpture or by means of ultrasound tomography.

Other fields, such as civil engineering, employ nondestructive acoustic methods suitable for decay monitoring that are not yet used in the field of cultural heritage conservation. For instance, resonance techniques also enable probing and monitoring material mechanical state and are largely employed in civil engineering. More specifically, the resonant ultrasound spectroscopy (RUS) method [82] was developed in the early 2000s and successfully applied for rock characterization [83,84]. In the same period, the nonlinear resonant ultrasound spectroscopy (NRUS) method was also developed, based on noticeable nonlinearity found in rocks when increasing vibration amplitude. NRUS is already commonly used for concrete damage monitoring [85–87]. One major asset of nonlinear techniques, such as NRUS, is that they exhibit a greater sensitivity to damage than linear methods such as UPV measurement, thus allowing probing the early stages of material deterioration [85,88,89].

The next chapters will be focused on the characterization of Carrara marble degradation at the material and sculpture scales. Mechanical properties will be followed during weathering processes and imaged in degraded sculpted objects by means of nondestructive acoustic methods, suitable for long-term monitoring of properties and for working on cultural heritage artefacts. First, the phenomena at stake in marble

during temperature and relative humidity variations will be studied by evaluating thermal and hygric weathering of Carrara marble samples with NRUS and by carrying out microstructural characterization on thermally damaged samples. Then, the decay of two Carrara marble sculptures, exposed to natural weather conditions for several centuries, will be investigated with ultrasound tomography to image their inner degradation state and thus to evaluate their conservation issues.

2. Degradation at the material scale

Two publications associated with this chapter were published : Chavazas *et al.* JCBM 2024 (see Annex B) and Chavazas *et al.* BOEG 2024 (see Annex C).

As shown in the previous chapter, temperature fluctuations play a key role in Carrara marble degradation. Marble thermal degradation can even be enhanced when temperature variations are coupled with relative humidity variations. Yet, the mechanisms at stake are still not fully comprehended. It is not yet understood if these alterations are triggered at a certain threshold temperature or by prolongated cyclic. In both cases, the actual temperature range activating these weathering phenomena remains unknown. Moreover, the sole impact of relative humidity variations on Carrara marble decay has been very little studied so far. Besides, some authors suggest a healing ability of marble upon heating at high temperatures or after several thermal cycling [37,92]. This healing would result from a re-strengthening of calcite grain contacts. Yet, in both studies this hypothesis is not compared with microstructural analyses and observations. The temperature range that would trigger such a mechanism is also unknown, as well as the microstructural phenomena at stake in this re-strengthening.

In this chapter, the impact of temperature and relative humidity on the decay of Carrara marble is thus studied at the material scale. The aim is to understand further the effects of temperature and relative humidity variations on Carrara marble, as well as the mechanisms at stake at the microstructural level. First, nonclassical nonlinear behavior of materials will be described, with a focus on nonlinear resonant ultrasound spectroscopy (NRUS) and on the nonclassical nonlinearity in rocks. Then, the experimental methodologies used for the resonant spectroscopy tests and for the material characterization will be explained. The impact of heating on marble physical properties will be presented. Finally, the impact of heating temperature, relative humidity and thermo-hygric cycling on Carrara marble decay will be evaluated with NRUS and discussed.

2.1. Nonclassical nonlinearity

2.1.1. Constitutive laws

In the case of a linear elastic unidimensional isotropic solid, Hooke's law gives the constitutive relation between the stress σ and the strain ε:

$$\sigma = K\varepsilon \qquad (3)$$

where K is the elastic modulus. In the unidimensional case, the three physical quantities of Eq. (3) are scalar. In the linear elastic case, the modulus K is an intrinsic constant property of the material. Yet, in some cases, the modulus K is itself dependent on the material strain ε: this is the nonlinear elastic regime. In this regime, the constitutive relation becomes:

$$\sigma = K_0(1 + \beta\varepsilon + \delta\varepsilon^2 + \cdots)\varepsilon \qquad (4)$$

Therefore, the modulus of classical nonlinear materials depends on the level of stress undergone by the solid. The classical nonlinearity is related to the nonlinearity of the force-displacement relationship at the atomic scale of the material.

In other cases, the modulus does not only depend on the strain level but also on the strain history of the material. This regime is known as the nonclassical nonlinear elastic behavior. In the nonclassical nonlinear case, the constitutive law takes the following form [51,92–94]:

$$\sigma = K_0\big(1 + \beta\varepsilon + \delta\varepsilon^2 + \cdots + \alpha(\Delta\varepsilon, \dot{\varepsilon})\big)\varepsilon \qquad (5)$$

In this case, the modulus also depends on the strain amplitude $\Delta\varepsilon$ and on the time derivation of the strain ε. The form of the function $\alpha(\Delta\varepsilon, \dot{\varepsilon})$ remains unknown, even though phenomenological models of nonclassical nonlinearity exist. Nonclassical nonlinear behavior accounts for nonlinear phenomena occurring at the mesoscopic scale of the material such as opening/closing of microcracks, capillary effects, friction, contacts, dislocations, etc. [85,95,96]. Nonclassical nonlinear materials comprise granular materials such as rocks (limestones, sandstones, granites, etc.), concrete, mortar. These materials are characterized by elastically soft constituents, called the "bond system" by Johnson and Sutin (2005), distributed within a rigid matrix (Fig. 17) [94]. Moreover, linear elastic materials can exhibit nonclassical nonlinearity once they are damaged: this is the case of metals [97,98], bones [99,100], or composite materials [101,102].

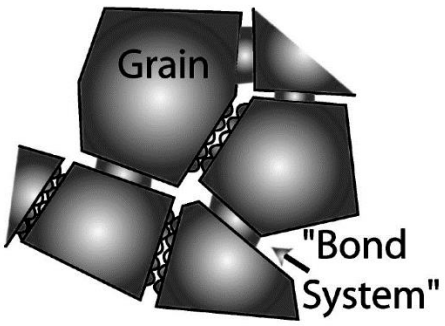

Fig. 17 The hard/soft paradigm defined by Johnson and Sutin (2005)

In the 1990s, a phenomenological model for nonclassical nonlinearity was developed based on the work of Preisach and Mayergoyz [103–105]. It was called the Preisach-Mayergoyz (PM) space model. In this model, a rock is represented by an ensemble of

classical and nonclassical elastic units. Classical units correspond to the material grains and are associated to a classical nonlinear stress – strain relation in the form of Eq. (4). Nonclassical units represent rock features contributing to nonclassical nonlinearity: cracks, joints, voids, contacts. Each nonclassical unit is associated with two stresses $\sigma_o < \sigma_c$ and two lengths $L_o > L_c$ representing the two states in which the unit can be: open or closed. The behavior of a single nonclassical unit is illustrated in Fig. 18. The unit is initially open with length L_o and the stress is below σ_c. As the stress increases up to σ_c, the unit length is not modified. When the stress reached σ_c, the nonclassical unit closes to a length L_c and remains at this length if stress increases further. In the case of a stress decrease, the nonclassical unit opens back to length L_o when the stress reaches σ_o and it remains at this length if the stress decreases further. To model a nonclassical nonlinear material, a large number of nonclassical units are assigned to different values of $(\sigma_o, \sigma_c, L_o, L_c)$. The PM space uses the stress σ_o and σ_c as the nonclassical unit coordinates to display the density of these units (visible in gray scale in Fig. 18). The PM space can be used to simulate nonclassical nonlinear material behavior under varying stress by keeping track of open and closed nonclassical units and adding their resulting strain to the one of the classical units [51].

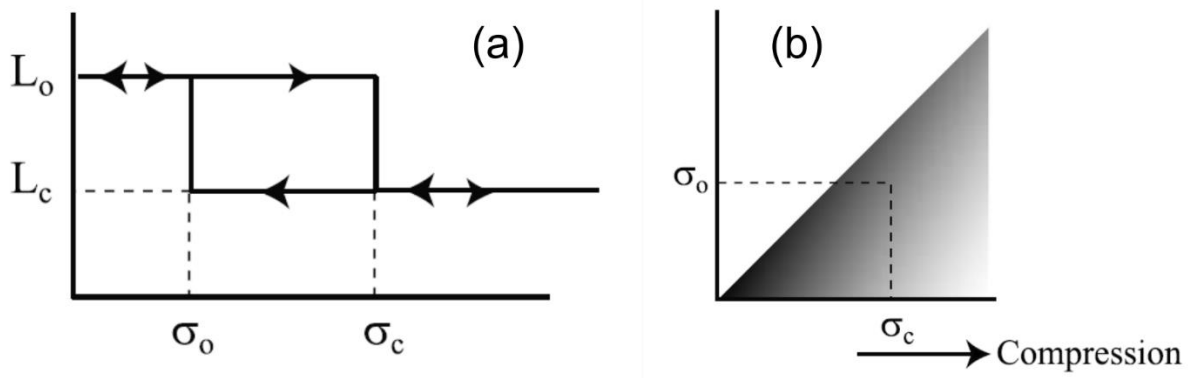

Fig. 18 PM space model. (a) Graphical representation of a nonclassical unit, and (b) example of PM space density in gray scale (Van Den Abeele *et al.* 2002).

2.1.2. Indicators of nonclassical nonlinearity

Nonclassical nonlinearity can be differentiated from classical nonlinearity by various experimental indicators. Nonclassical nonlinear features comprise hysteresis, endpoint memory, slow dynamics, harmonic generation, wave modulation, shift in resonant frequency [93,95,96,106,107].

The constitutive law of nonclassical nonlinear materials (Eq. (5)) highlights that they are characterized by a hysteretic phenomenon, contrary to classical nonlinear materials (Eq. (4)). Strain – stress relation depends on the loading history, which is pointed out by the presence of the time derivative of strain $\dot{\varepsilon}$ in the modulus formula. The hysteresis phenomenon is observed experimentally as shown for Berea sandstone in Fig. 19.

Endpoint memory also characterized nonclassical nonlinearity. It is the memory of the last strain extremum. The phenomenon appears during internal hysteresis loops as illustrated by Fig. 19 (b): the strain continues its initial trajectory after it goes out of the internal loop when σ_3 is reached again.

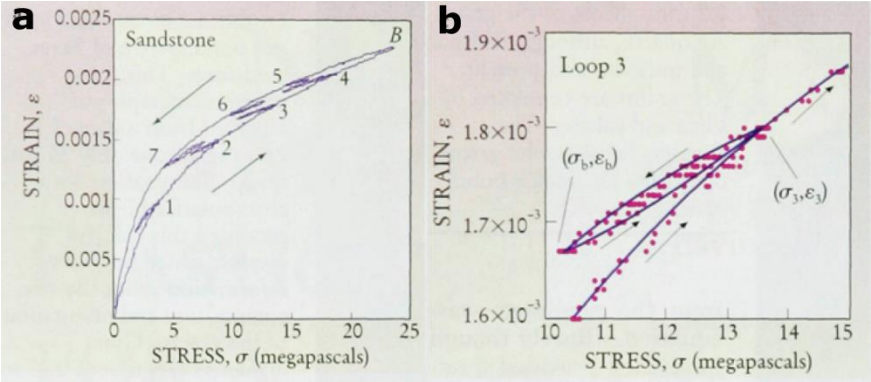

Fig. 19 Strain – stress relationship in Berea sandstone. Curves show (a) hysteretic and (b) endpoint memory phenomena (Guyer and Johnson 1999).

Slow dynamics is also a specific behavior of nonclassical nonlinear materials. When a nonclassical nonlinear solid is subjected to a strong wave excitation, its modulus decreases. It is the conditioning phase. Once the excitation is stopped, the decrease in modulus is reversible but not immediate. The modulus recovery to initial value takes about 10^3-10^4 s and is linear with $\log(t)$ [94,95]. This is the slow dynamics phenomenon. Slow dynamics is illustrated for several rock types and concrete in Fig. 20.

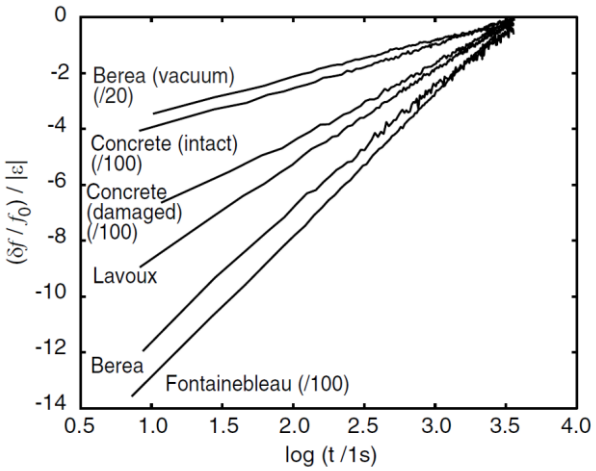

Fig. 20 Slow dynamics in rocks and concrete. Recovery of the relative shift in resonant frequency per unit driving strain $|\varepsilon|$. Some data were scaled: scaling factors are bracketed (Ostrovsky and Johnson 2001).

Nonlinearity is also characterized by harmonic generation. When a single-frequency wave propagates in a nonlinear material, the nonlinear medium distorts the wave, which generates initially absent harmonic frequencies [96]. The nature of nonlinearity (classical or nonclassical) can be discriminated from the slopes of the second and third

harmonic amplitudes. The third harmonic amplitude has a cubic dependance on the main one in classical nonlinear materials, while the dependance is quadratic for the second and third harmonic amplitudes in nonclassical nonlinear materials [106].

A phenomenon of wave modulation also appears in nonlinear materials. When two single-frequency ($\omega_1 < \omega_2$) waves propagates in a nonlinear material, not only harmonics ($2\omega_1$, $2\omega_2$, $3\omega_1$, ...) are generated but also the sum- and difference-frequency waves ($\omega_2 \pm \omega_1$, $\omega_2 \pm 2\omega_1$, ...) (sidebands). Besides, if the drive amplitude of one input frequency is increased during the experiment, the sideband amplitude increases as well. A linear dependence of the sideband amplitude with the amplitude of the increased fundamental frequency denotes nonclassical nonlinearity [95]. Wave modulation and harmonic generation are illustrated in Fig. 21.

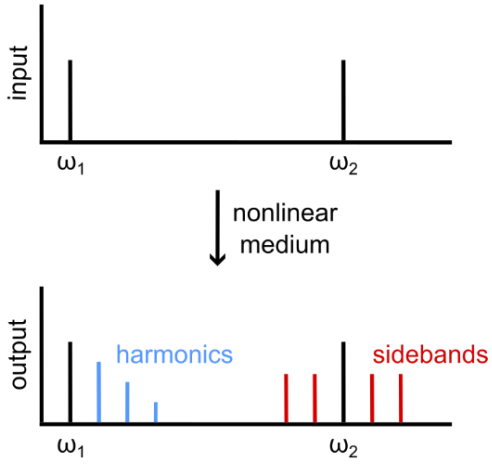

Fig. 21 Harmonic generation and wave modulation. Excitation of a nonlinear material with two single-frequency waves creates harmonics (blue frequency peaks) and sidebands (red frequency peaks) in the output response (modified from Ostrovsky and Johnson 2001)

Shift in resonant frequency is another indicator of nonlinearity. In nonlinear materials, the resonant frequency is dependent on the amplitude of the driving excitation. Resonant frequency shifts towards low frequencies when driving amplitude of excitation increases. Typical resonant curves acquired at increasing excitation amplitudes are shown in Fig. 22. In nonclassical nonlinear materials, hysteresis is also visible in resonant curves as their shape depends on the sweep direction (increasing or decreasing frequencies) (Fig. 22 (a)).

2.1.1. Nonlinear resonant ultrasound spectroscopy

Various nondestructive methods were developed to investigate experimental indicators of nonclassical nonlinearity. These nonlinear methods proved to be particularly sensitive to the detection of microstructural damage, and their sensitivity is greater than the one of linear methods [85,88,89]. Specifically, such techniques are sensitive to crack density and orientation [88,89,107,108], early stages of damage [88,99], thermal damage [85,88,109], water saturation [51,110,111].

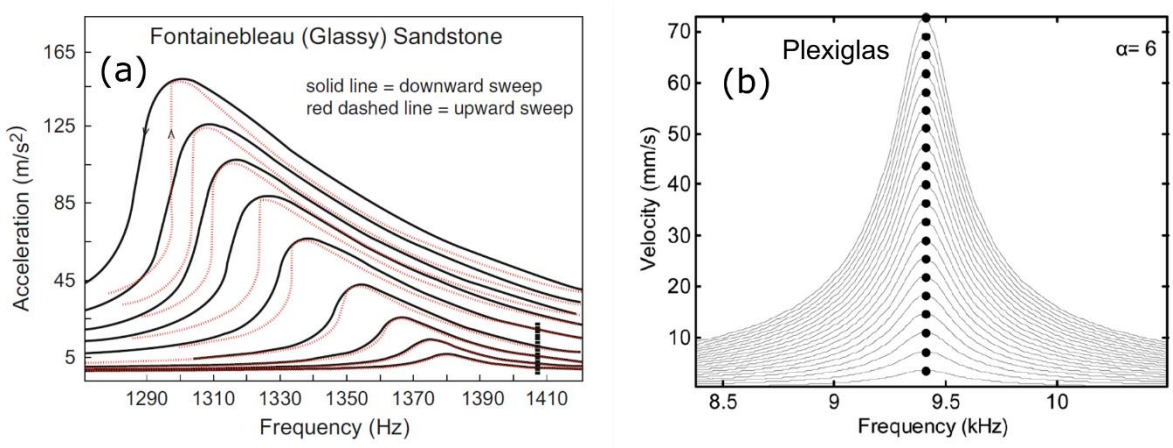

Fig. 22 Resonant curves. (a) Nonclassical nonlinear material (Fontainebleau sandstone) exhibiting shift in resonant frequency (TenCate and Johnson 2019) and (b) linear material (Plexiglas) with resonant frequency independent of excitation amplitude (Payan *et al.* 2014). Hysteresis induces different responses between downward and upward sweeps in (a).

One of these nondestructive techniques is the nonlinear resonant ultrasound spectroscopy (NRUS) method. NRUS consists in exciting a sample at several increasing drive amplitudes to study the evolution of the resonant modes. Samples generally approach the one-dimension geometry for an easier detection of the vibrational modes: rods or bars with a large height over section ratio. The most commonly studied vibrational mode is the longitudinal mode but some studies also use torsional, shear or flexural modes [92,112,113]. In this work, only the first longitudinal resonant mode is studied. As shown in Fig. 22, a shift towards low frequencies is observed in the resonant frequency of nonclassical nonlinear materials. From a certain level of strain, this shift is proportional to the strain amplitude $\Delta\varepsilon$ reached at resonance by the sample:

$$\Delta f / f_0 = \alpha \, \Delta\varepsilon \qquad (6)$$

In this equation, $\Delta f = f_0 - f$ with f_0 the linear resonant frequency extracted for the lowest drive amplitude and f the resonant frequency for higher drive amplitudes, and the coefficient of proportionality is the nonlinear parameter α introduced in Eq. (5). The strain amplitude $\Delta\varepsilon$ at resonance is evaluated by dividing the particle velocity amplitude A by the longitudinal wave velocity [113,114]:

$$\Delta\varepsilon = A \,/\, (2 * L * f_0) \qquad (7)$$

where L is the sample length and f_0 the linear resonant frequency.

Fig. 23 (a) shows a typical NRUS scan obtained on a fresh core sample of Carrara Gioia marble with a resonant frequency f_0 of 6.42 kHz and a nonlinear parameter α of 4990. Each curve corresponds to a different drive amplitude level. Fig. 23 (b) displays the relative shift in resonant frequency as a function of the amplitude strain reached at resonance. When a sufficient strain level is reached, the proportionality of Eq. (6) is verified in Fig. 23.

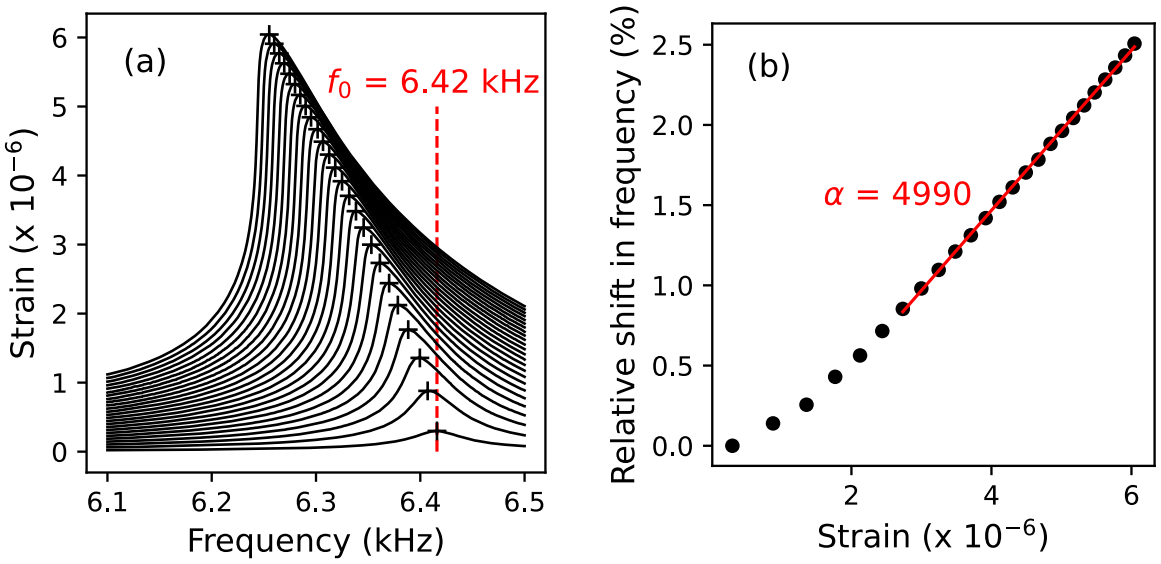

Fig. 23 NRUS curves. (a) NRUS scans and (b) evolution of relative shift in resonant frequency as a function of amplitude strain at resonance for a fresh Carrara Gioia marble sample. The sample exhibits a resonant frequency of 6.42 kHz and a nonlinear parameter of 4990.

Linear and nonlinear parameters extracted from NRUS scans provide information on the mechanical state of a sample. The resonant frequency f_0 is related to the stiffness and density ρ of the macroscopic sample. Young's modulus E and UPV v are directly related to the resonant frequency f_0 of the longitudinal mode [51]:

$$E = (2\,L\,f_0)^2\,\rho \qquad (8)$$

$$v = 2\,L\,f_0 \qquad (9)$$

The nonlinear parameter α originates from nonlinear phenomena occurring at the mesoscopic scale of the material, such as opening/closing of microcracks, capillary effects, friction, contacts, dislocations, etc. [85,95,96]. The mesoscopic scale is ranging between grain contacts and grain assemblage. Therefore, these two parameters account for different phenomena occurring at different scales in the material.

NRUS thus provides two useful parameters to characterize any nonclassical nonlinear material such as marble:

- The resonant frequency f_0 (linear resonant frequency extracted for the lowest drive amplitude) which is related to the stiffness of the macroscopic sample,
- The nonlinear parameter α which is highly sensitive to any change (microcrack generation, capillary effects, friction, etc.) occurring at the microstructural scale.

NRUS can probe damage in a large variety of materials. For instance, it is sensitive to the stage of loading-fatigue microdamage in bones [99,100,115]. Various alterations of concrete can be assessed by NRUS: carbonation results in a decrease of the nonlinear parameter α [116], thermal and mechanical damage lead to an increase of the nonlinear

parameter α [85–87,117]. The nonlinear parameter α is also sensitive to the fracture process zone in concrete [118], and to alkali-silica reactivity in mortar [119]. Thermal damage results in an increase of the nonlinear parameter α not only in concrete [85,86] but also in mortar [109] and in carbon fiber reinforced plastic [88]. In steel, NRUS can monitor strength and hardness reduction due to incoherent copper-rich precipitates [97] and is also sensitive to dislocation density [120], precipitate size [120], stress corrosion cracking [98]. Besides, NRUS has been used to evaluate fatigue damage in copper [121] and fatigue crack growth in aluminum [122]. NRUS has also been applied on carbon fiber reinforced plastic to detect thermal and fatigue damage [88,101,102].

The presence of fluid in the material also impacts NRUS measurements [95]. Yet, there are relatively few NRUS measurements for varying water saturation conditions in the literature [51,92,110–112,123]. Payan *et al.* (2010) found that nonclassical nonlinearity decreases with water saturation in concrete [123]. On the contrary, Gao *et al.* (2022, 2023) showed that the nonlinear parameter α increases with relative humidity in glass beads [110,111]. However, the same authors also found that the nonclassical nonlinearity of sand remains steady when relative humidity increases and hypothesized that this difference in behavior comes from more grain interlocking in sand which prevents adsorbed water from weakening/dilating the sample, unlike in glass beads [110]. Van Den Abeele *et al.* (2002), Johnson *et al.* (2004) and Averbakh *et al.* (2017) studied the evolution of the nonlinear parameter α with water saturation in different rocks (see section 2.1.2) [51,92,112].

Thus, NRUS is a nondestructive resonant technique able to probe various forms of damage (thermal, mechanical, chemical) in a wide range of materials (concrete, metals, bones, composites). Rock behavior has also been studied by means of this technique, and the next section will present the nonclassical nonlinearity of rocks specifically.

2.1.2. Nonclassical nonlinearity in rocks

Nonclassical nonlinearity has been investigated in diverse rock types such as sandstones [51,92,124–129] and carbonate rocks like marble, limestone and chalk [51,92,94,112,126].

Nonlinear phenomena have been particularly investigated in sandstones. The slow dynamics of nonclassical nonlinearity was studied in Berea sandstone by TenCate and Shankland (1996) [124]. TenCate *et al.* (2004) and Pasqualini *et al.* (2007) investigated the strain domains of the linear, classical nonlinear and nonclassical nonlinear behaviors in Berea and Fontainebleau sandstones [127,128]. Renaud *et al.* (2013) detected nonclassical nonlinear in Berea sandstone at low dynamic strain [129]. Other rock types have been studied as well. For instance, Johnson *et al.* (2004) measured the nonlinear parameter α under room conditions for Estaillades limestone and Fontainebleau sandstone, and found that the nonlinear parameter α strongly increases between Berea sandstone samples heated at 65 and 100 °C (from 1130 to 104,450) [92]. Rivière *et al.*

(2015) carried out NRUS and dynamic acoustoelastic testing in four sandstones (Berea, Meule, Sander, Pietra Serena), a soapstone (Grunnes Nidaros) and a granite (Berkeley Blue) to try to classify rock nonlinear elastic behavior [125].

Regarding the influence of water saturation on nonclassical nonlinearity in rocks, Johnson *et al.* (2004) showed that the nonlinear parameter α increases with water saturation in St. Pantaleon limestone and that it increases for saturation below 30% and then slowly decreases in Meule sandstone [92]. In Averbakh *et al.* (2017), the nonlinear parameter α increases with water saturation for an unspecified limestone (3 saturation states: dry, air-dry and water-saturated) [112]. Van Den Abeele *et al.* (2002) found that the nonlinear parameter α first increases with water saturation in Lavoux limestone and Berea and Meule sandstones, and then levels off at highest saturations [51]. Van Den Abeele *et al.* (2002) explained the increase in nonclassical nonlinearity with water saturation by the presence of capillary condensation. As explained in section 1.4.2, capillary condensation does not appear simultaneously in the whole pore network as it depends on the pore radius via Kelvin's law (see section 1.4.2). Menisci formed at the air/liquid water interfaces are subjected to microscopic capillary pressure because of the different pressures in air and liquid water. Microscopic capillary pressure then results in a microscopic contraction pressure in the solid matrix. These microscopic forces occurring in the pore network can lead to additional nonlinearity when samples are subjected to an increasing relative humidity.

However, specific studies on the impact of heating and relative humidity on marble nonlinear response are very limited and present very few data. Johnson and Sutin (2005) presented one nonlinear parameter measurement on marble under ambient conditions: $\alpha = 149$ [94]. Johnson *et al.* (2004) studied the nonclassical nonlinearity in a white Asian marble (from Turkey) under varying conditions [92]. In their work, the nonlinear parameter α was first measured in ambient conditions, then after the sample was heated at 200 °C, and finally in three different saturation state (100%, unknown between 100 and 1%, <1%) after heating at 200 °C. The 44% drop of the nonlinear parameter value (from 27,006 to 15,251) after heating at 200 °C was interpreted by the authors as an ability of Asian marble to heal itself during the heating process. The same hypothesis was made recently by Waragi (2023) in the case of thermal cycling between 4 and 84 °C. Yet, this hypothesis has not been supported by microstructural characterization so far and the temperature at which this mechanism may be triggered is unknown. Johnson *et al.* (2004) also found that the nonlinear parameter α increases with decreasing water saturation in Asian marble (from 19,747 to 44,381, 3 saturation degrees).

Thus, the literature on the influence of heating and relative humidity on marble nonlinearity is very limited. The impact of exposure to mild temperatures can be critical for marble artefact preservation. Yet, this temperature range has not been investigated by NRUS even though this technique can bring further information on the underlying degradation mechanisms compared to traditional techniques such as destructive mechanical tests and UPV. Indeed, NRUS does not only probe the macroscopic scale of

materials as traditional methods but also the mesoscopic scale, and accounts for other phenomena. Moreover, thermo-hygric cycling has not been yet followed in marble by NRUS while it is a nondestructive technique, therefore suitable for evaluating the mechanical state of the same samples all along cycling.

That is why this study aims at understanding further the impact of temperature and relative humidity variations on Carrara marble by means of NRUS. The evolution of the resonant frequency f_0 and of the nonlinear parameter α is followed as a function of heating temperature, relative humidity level, and all along thermal, hygric and thermo-hygric cycling. Besides, through various microstructural characterizations, the evolution of the NRUS parameters is linked to the changes occurring at the Carrara marble microstructure level upon heating and moisture uptake.

2.2. Experimental methodology

Carrara marble sample preparation is detailed in this section and the NRUS experimental set-up and the microstructural and mechanical characterizations are also presented.

2.2.1. Sample preparation

In this subsection, the characterization carried out on the fresh Carrara marble block are described. Then, the procedures used for the thermal ageing and the thermal, hygric and thermo-hygric cycling of the marble samples are explained.

2.2.1.1. Fresh marble characterization

A block (45 cm x 45 cm x 20 cm) of fresh Carrara Gioia marble (provided by Logica SRL, Carrara, Italy) was used for all the experiments presented in this chapter (Fig. 24 (a)). Carrara Gioia variety is a calcitic white veined marble and has a granoblastic equigranular polygonal microstructure [5,130–132]. This microstructure was chosen for this work as it is expected to be particularly sensitive to thermal weathering [26,39,133]. The microstructure of the Carrara Gioia marble block used here is shown in Fig. 24 (b). This marble is mainly composed by equigranular monocrystals of calcite. The average size of calcite grains is ca. 300 µm, grain boundaries are mostly straight, and calcite grains meet at triple points. The condition and isotropy of the whole block were first checked by measuring UPV, at different points, in the three orthogonal directions. The mean velocities were 3.9 ± 0.1 km.s^{-1}, 4.4 ± 0.2 km.s^{-1}, and 3.8 ± 0.4 km.s^{-1}, respectively in the X-, Y-, and Z-directions. The block can therefore be considered as a class I marble in Köhler classification (see Table 1) and is characterized by an anisotropy

of 14%.

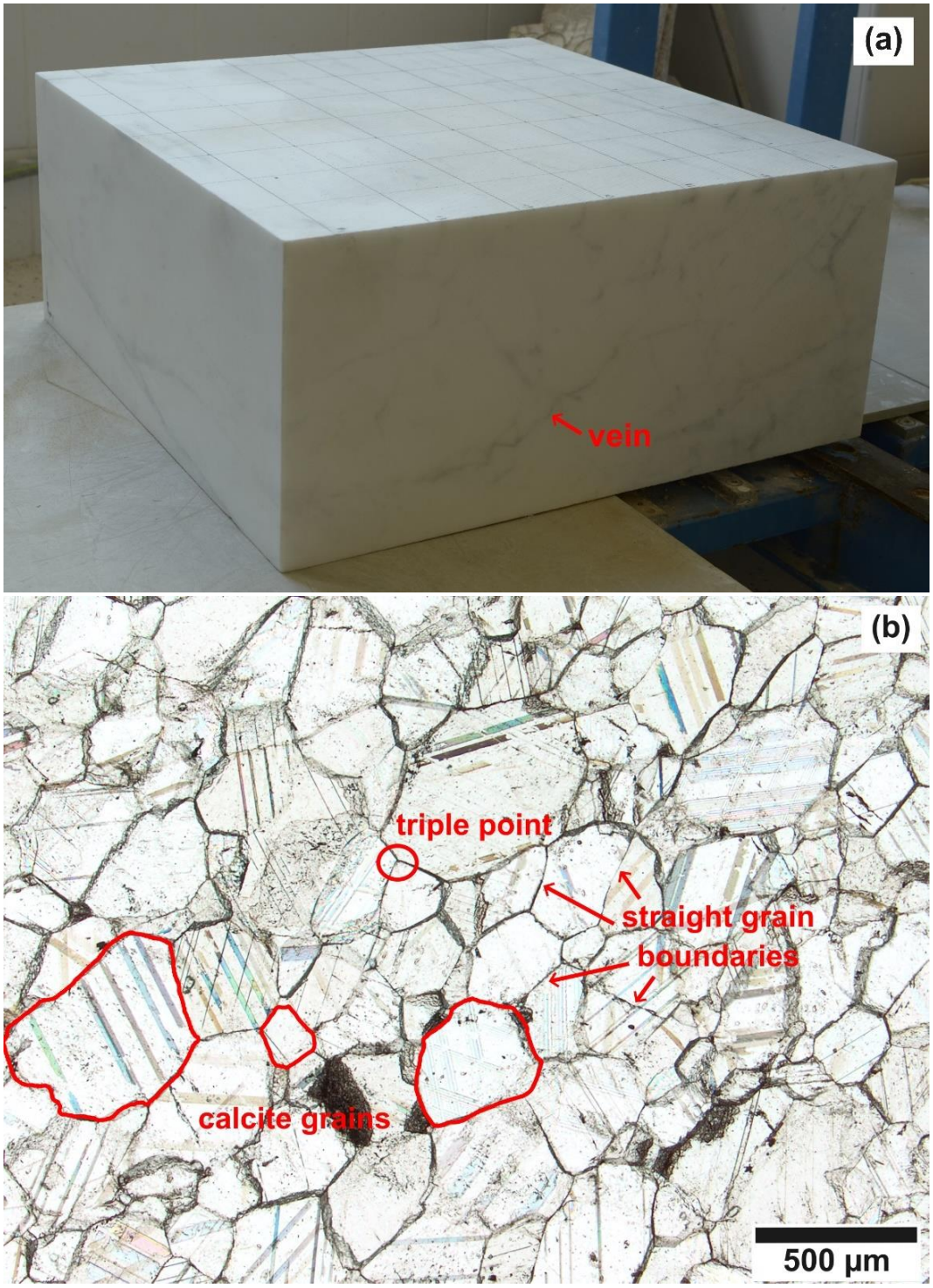

Fig. 24 Carrara Gioia marble. (a) Entire block with veins visible on the lateral sides. (b) Optical microscope image of a thin section of a fresh sample, magnification x25, plane polarized light.

41 core samples of 20 cm in height and 4 cm in diameter were then drilled from the block (all along the Z-direction), their faces polished to ensure flat and parallel surfaces for NRUS measurements, and the samples were stocked in a temperature-controlled oven maintained at 23 °C. This height over diameter ratio of the core samples was

chosen to mimic a one-dimension geometry, which is favorable for the NRUS testing. Before any thermal or hygric treatment, reference NRUS measurements were carried out on every fresh core sample. Results are displayed in Fig. 25 and show some variability among the samples in both resonant frequency f_0 and nonlinear parameter α. Minimum and maximum values for the resonant frequency f_0 are 4.5 ± 0.2 and 6.9 ± 0.2 kHz, respectively. The resonant frequency f_0 tends to decrease along the X-axis. Minimum and maximum values for the nonlinear parameter α are (4.4 ± 0.7) × 10^3 and (14 ± 2) × 10^3, respectively. The variability in nonlinear parameter α does not seem to follow a spatial pattern in the block. Comparable value, α = 27,006, of nonlinear parameter α was found in Asian white marble by Johnson *et al.* (2004) and significantly lower value, α = 149, was found in Carrara marble by Johnson and Sutin (2005) [92,94]. The relatively high nonlinearity levels in the fresh core samples lead to think that nonclassical nonlinearity features (linked to the quality of grain contacts) were present in the fresh marble block prior to thermal and hygric weathering.

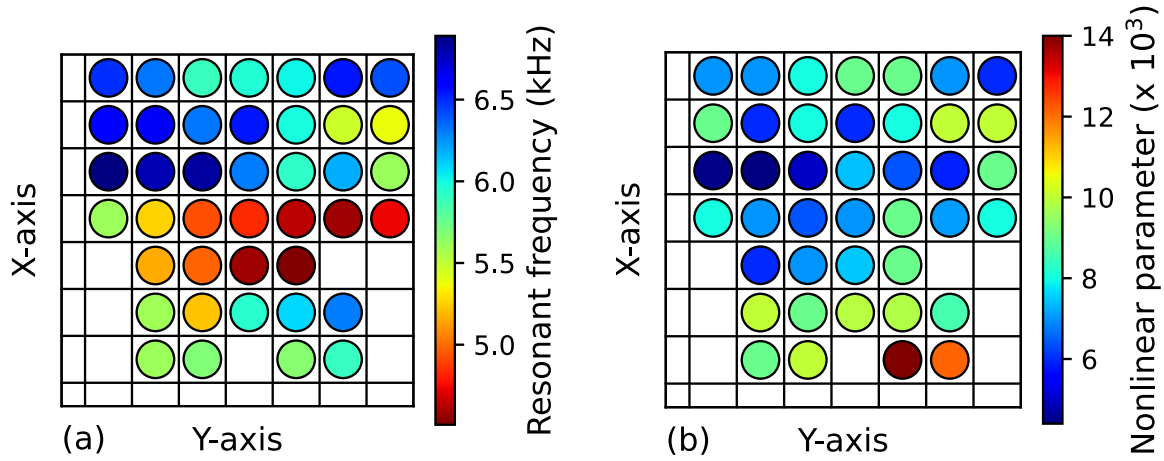

Fig. 25 Reference measurements of the NRUS parameters. (a) Resonant frequency f_0 and (b) nonlinear parameter α prior to any hygric or thermal treatment. The grid schematizes the top view of the marble block and each square corresponds to the initial position of a core sample in the block.

2.2.1.2. Thermal ageing

The protocol followed for the thermal ageing is schematized in Fig. 26: the heating rate was set to 1 °C.min^{-1} to allow a homogeneous heating of the material [3,44,70], the setpoint temperature was maintained for 6 h [70], and the cooling down to room temperature was left free. Firstly, 32 samples were heated once up to 8 different setpoint temperatures (four samples per temperature): 40, 65, 85, 105, 150, 200, 250, and 500 °C. Four fresh unheated samples (23 °C) were used as reference. This temperature set was chosen to explore the impact of natural exposure conditions (40 – 85 °C) [34,35], and the evolution of marble state until its complete granular decohesion (105 – 500 °C). The drilled samples were randomly assigned to each setpoint temperature to account for variability in the resonant frequency f_0 and the nonlinear

parameter α in the fresh marble block (Fig. 25) and to avoid any influence of sample original location. No experimental data is presented for the samples heated at 500 °C as they suffered complete disintegration after heating. Among the fresh and heated samples, one sample per temperature was used for microstructural and mechanical characterization.

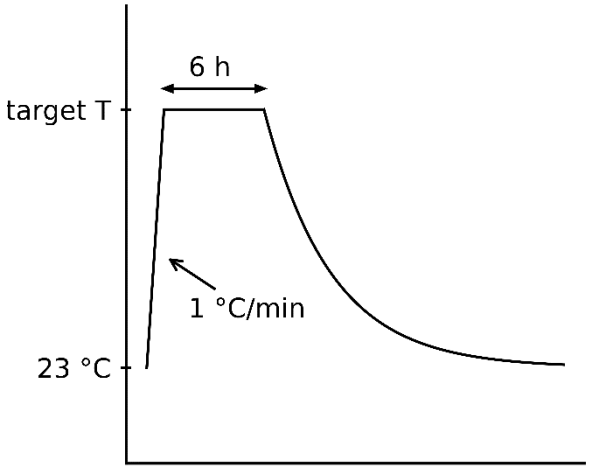

Fig. 26 Thermal cycle. Carrara Gioia marble samples were first subjected once to this cycle up to 40, 65, 85, 105, 150, 200, 250, or 500 °C. Then some samples were subjected 135 times to this cycle up to 40, 65, 85, or 105 °C.

2.2.1.3. Thermal cycling

Two samples out of the four heated up to 40, 65, 85, and 105 °C were thermally cycled at the same temperatures with the same heating protocol repeated 135 times. Only these temperatures were kept to study the impact of thermal cycling as they correspond to natural exposure conditions and thus allow simulating outdoor conditions. Between each heating phase, samples were always stocked in a temperature-controlled oven maintained at 23 °C.

2.2.1.4. Hygric cycling

The remaining sample for setpoint temperatures 40, 65, 85, 105 °C and one fresh sample were used for hygric cycling. They were placed on the two middle racks of a four-level desiccator cabinet (1 in Fig. 27). The desiccator was itself placed in the temperature-controlled oven (2 in Fig. 27) maintained at 23 °C. On the lowest and highest racks of the desiccator, two containers with supersaturated salt solutions (3 in Fig. 27) were placed to control relative humidity inside the desiccator. The following salts were used throughout the experiments (equilibrium relative humidity is bracketed): LiCl (12%), $MgCl_2$ (33%), K_2CO_3 (44%), $Mg(NO_3)_2$ (52%), $NaNO_2$ (66%), NaCl (76%), KCl (86%), K_2SO_4 (96%).

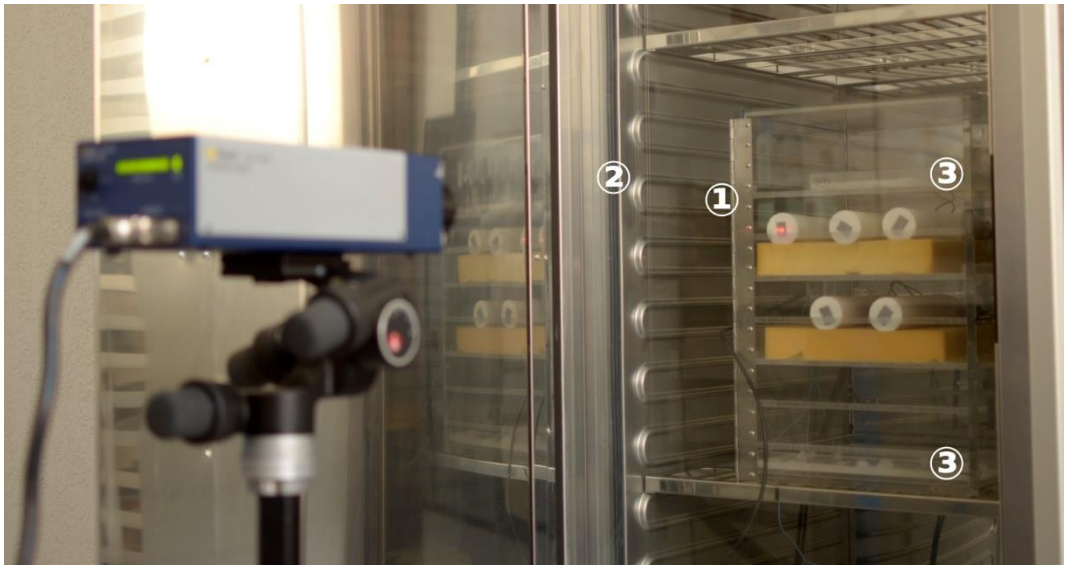

Fig. 27 Experimental set-up used for the experiments on the relative humidity influence. (1) Plexiglas desiccator cabinet, (2) temperature-controlled oven, (3) supersaturated salt solutions.

This experimental configuration was kept even during the NRUS measurements as the laser vibrometer used in the NRUS set-up (see section 2.2.2) allows conducting measurements through the interior glass door of the temperature-controlled oven and through the Plexiglas wall of the desiccator. NRUS measurements were made only after samples have been exposed under a specific relative humidity for at least 48 h to ensure stabilization of equilibrium humidity inside the desiccator (controlled by an iButton® temperature-humidity logger).

2.2.1.5. Thermo-hygric cycling

Five fresh samples were used for thermo-hygric cycling. They were subjected 450 times to the thermo-hygric cycle displayed in Fig. 28 in a climatic chamber. This cycle mimics one day of outdoor exposure in 8 h. The plateau at (85 °C, 30% RH) and at (10 °C, 60% RH) both lasted 3 h. The temperature and relative humidity ramps lasted 1 h. The lower temperature bound of 10 °C was chosen to avoid freeze-thaw phenomena. The upper temperature bound of 85 °C was chosen to simulate the maximum temperature reached on marble surface even though it is somewhat higher than what is found in the literature [34,35]. The relative humidity values were chosen as they fall in the range of the annual mean values near Marseille, France [134].

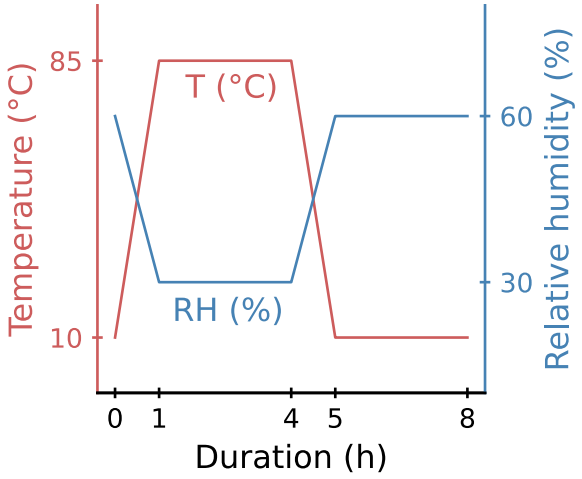

Fig. 28 Thermo-hygric cycle. Five Carrara Gioia marble samples were subjected 450 times to this weathering cycle.

2.2.2. NRUS experimental set-up

Fig. 29 illustrates the experimental set-up for the NRUS experiments. The signal generation was managed by RITA© software coupled with a generator (NI PXIe-5406) and an amplifier (NF Electronic Instruments 4005 High Speed). The input signals sent to the transducer are schematized in Fig. 30. A series of sine signals with successively different frequency values (from the chosen initial f_1 value to the chosen final value, with a constant frequency step Δf) and at a constant amplitude is sent to the transducer. The sine series is then sent again with a constant amplitude increment ΔA.

The vibrations were generated in the core sample thanks to an ultrasonic piezoelectric transducer (Beijing Ultrasonic, resonant frequency of 40 kHz) placed at one sample extremity. The transducer was either non-permanently glued to the sample with phenyl salicylate (also called salol) and unglued between each NRUS scan (impact of one heating cycle between 40 and 250 °C, corresponds to section 2.4), or permanently glued with epoxy Araldite® 2020 (impact of relative humidity and of cycling, corresponds to sections 2.5 and 2.6). During experiments on the influence of relative humidity and during hygric cycling, the piezoelectric devices and the unsheathed wires were wrapped in stretch film to avoid deterioration due to high humidity levels.

The out-of-plane velocity was measured at the other sample extremity with a Polytec laser vibrometer (OFV-505 Single Point Sensor Head and OFV-5000 Controller, λ = 633 nm (He-Ne), power < 1 mW). The signal acquisition was also managed by RITA© software coupled with a digitizer (NI PXIe-5122). For each driving amplitude, the output signal is given as the received amplitudes against the drive frequencies.

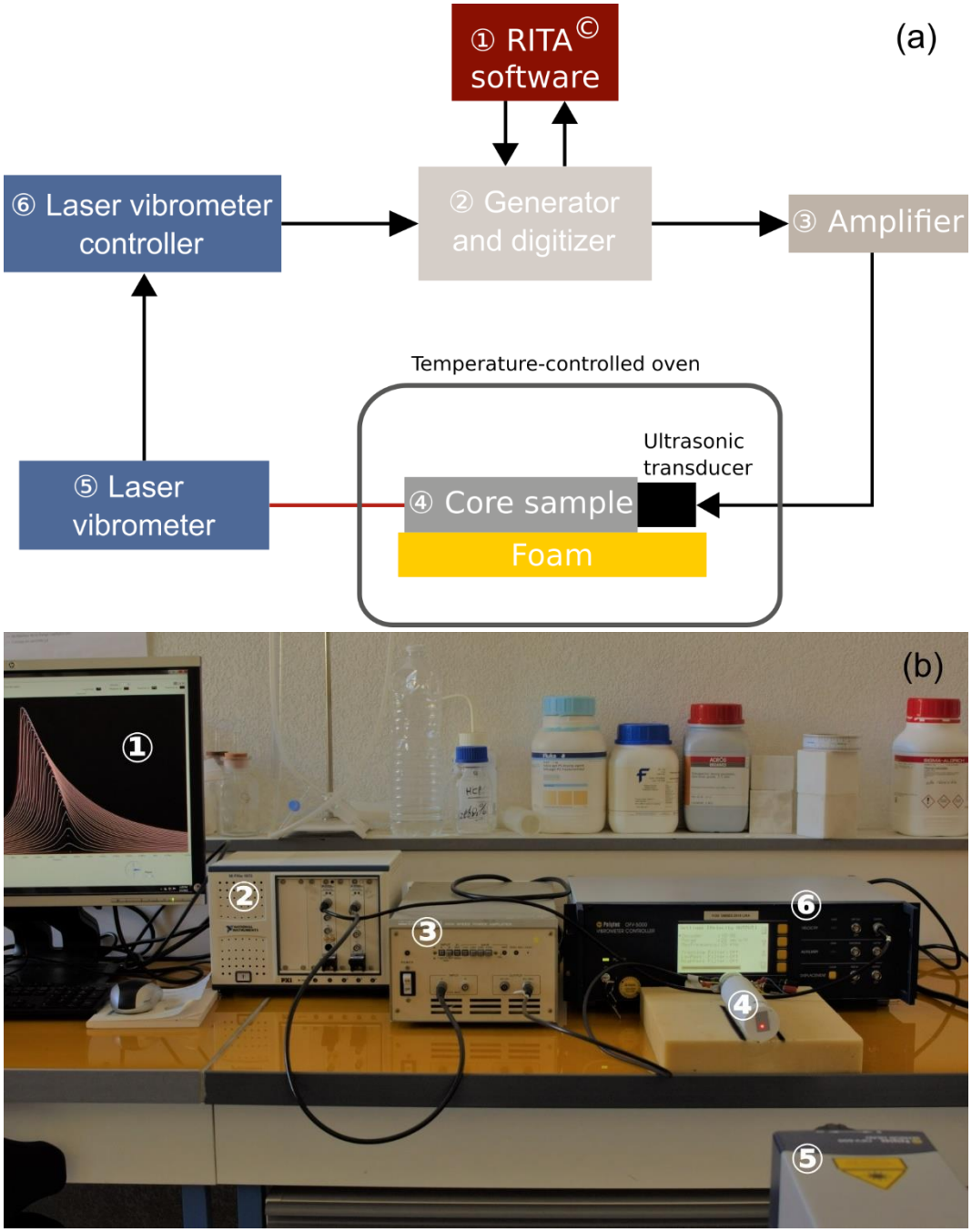

Fig. 29 NRUS experimental set-up. (a) Scheme of the NRUS experimental set-up. (b) Picture of the NRUS experimental set-up (the sample and the foam are out of the temperature-controlled oven for the convenience of picture taking).

During signal recording, the tested sample was placed on foam to minimize the attenuation or modification of the vibration modes due to the rigid support. Ambient temperature was also controlled and maintained at 23 °C during the NRUS tests as the samples remained in a temperature-controlled oven. Indeed, the use of the laser vibrometer allows carrying measurements through the interior glass door of the temperature-controlled oven (and through the desiccator Plexiglas wall during the experiments on the impact of relative humidity and during hygric cycling). The exterior steel doors of the temperature-controlled oven were left open during measurements to allow the laser to go through. At least three NRUS scans were performed on each sample

in a specific thermo-hygric state, waiting at least 3 h between two scans on the same sample in order to avoid slow dynamic processes influence [92,94,124,135]. Samples were also provided sufficient time to reach equilibrium at ambient temperature (23 °C) after each heating phase, so that measurements are not affected by temperature changes [136].

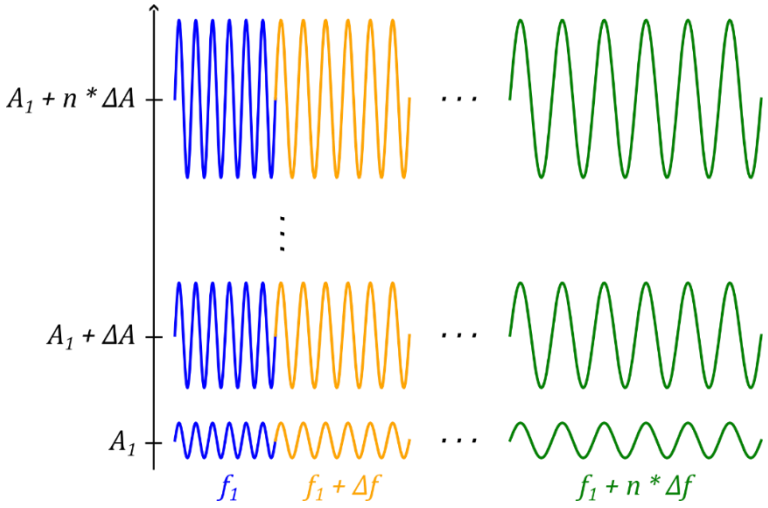

Fig. 30 Scheme of the input signals. At each step, a series of sine signals with successively different frequencies and at a constant amplitude is sent. In the next step, the same frequencies are kept and the amplitude is increased by a constant increment.

2.2.3. Microstructural characterization

Microstructural characterization was carried out on seven Carrara Gioia marble samples heated once respectively at 40, 65, 85, 105, 150, 200, 250 °C and on one fresh sample. These tests were used to follow the microstructure evolution of the marble samples with heating temperature.

One fragment of each sample was used to characterize marble porosity and pore size distribution with mercury intrusion porosimetry (MIP) using an AutoPore IV 9500 (Micromeritics) working with a maximal pressure of 210 MPa, thus probing pores between 0.01 and 360 µm. Mercury intrusion was measured at 111 increasing pressure points. The data acquisition for MIP was kindly performed by Jérémy Hénin at the Laboratoire de Recherche sur les Monuments Historiques (LRMH).

Another part of each sample was impregnated in epoxy resin under vacuum and glued on a glass slide. Once hardened, the preparation was thinned down to 30 µm with a diamond-coated saw and several polishing pads of decreasing grain sizes. A petrographic description of the produced thin sections was performed using a polarized light microscope (Olympus BX-51).

The thin sections as well as remaining freshly cut fragments were also characterized under Scanning Electron Microscope (SEM, Zeiss Evo 15).

Adsorption isotherms were determined for one fresh sample and four samples respectively heated at 40, 65, 85, and 105 °C. Vapor adsorption behavior was characterized only for these heating temperatures as they are the only ones used to study the impact of relative humidity. For adsorption isotherm measurements, one disc of 1 cm in thickness and 4 cm in diameter was used per sample. The experiment was carried out in a temperature-controlled oven maintained at 23 °C. First, the discs were all put in an airtight container with a relative humidity of 3% imposed by silica gel to measure their dry mass. Then, the discs were successively put in eight airtight containers in which eight different relative humidities were imposed by the supersaturated salt solutions listed in section 2.2.1. Samples were weighted between their stay in each airtight container.

2.2.4. Mechanical characterization

Uniaxial Compressive Strength (UCS) test was performed on seven Carrara Gioia marble samples heated once respectively at 40, 65, 85, 105, 150, 200, 250 °C and on one fresh sample. The UCS test set-up is shown in Fig. 31. Two 8 cm long cylinders (1 in Fig. 31) per sample were tested. The tests were carried out on an MTS 809 Axial / Torsional Test System (2 in Fig. 31), at a constant displacement rate of 0.24 $mm.min^{-1}$. Two discs of Teflon™ (3 in Fig. 31) of 1 mm in thickness and 5.4 cm in diameter were placed on the top and bottom of the sample to correct the lack of strict parallelism of the sample faces and to limit edge effect. This test was used in addition to NRUS testing to quantify the mechanical strength evolution of the marble samples with heating temperature.

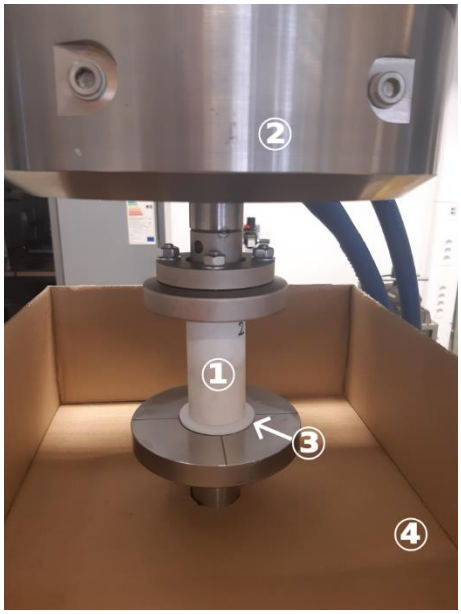

Fig. 31 UCS test set-up. (1) Carrara marble sample, (2) torsional test system, (3) disc of Teflon™, (4) cardboard box to avoid splinters from the sample.

2.3. Impact of heating temperature on marble physical properties

Microstructural and mechanical characterization was carried out on Carrara Gioia marble samples heated up to seven different temperatures (40, 65, 85, 105, 150, 200, and 250 °C) and on one fresh sample in order to study the evolution of marble properties with heating temperature. No characterization could be made on the samples heated up to 500 °C as they disintegrated after heating.

The evolution of porosity and pore size distribution with temperature was probed through MIP. Fig. 32 presents the total porosity accessible to mercury as a function of the sample heating temperature. Data point for the fresh sample is positioned at 23 °C. Fig. 33 indicates the contribution of five different porosity classes to the total porosity of each sample: radius of pore access between 0.01 and 0.1 µm, between 0.1 and 1 µm, between 1 and 10 µm, between 10 and 100 µm, and above 100 µm. It can be noted that the total porosity accessible to mercury increases with heating temperature, from 0.81% for the fresh sample to 3.39% for the sample heated at 250 °C. This is interpreted as the consequence of the creation of intergranular spaces due to calcite dilation anisotropy (see section 1.3). Moreover, as heating temperature increases, the contribution of the smaller pores, with access radius between 0.01 and 1 µm, to the total porosity exhibits a tendency to decrease for the benefit of larger pores with access radius between 1 and 10 µm. The contribution of pores with access radius between 10 and 100 µm is relatively steady for samples heated at 65 °C and above, and is lower for the fresh and heated at 40 °C samples. The contribution of pores with access radius above 100 µm is quite variable with heating temperature but does not show a clear evolution pattern. The decrease of the contribution of smaller pores (radius between 0.01 and 1 µm) can also be explained by the thermal behavior of calcite as dilation of calcite grains parallel to crystallographic c-axe is more important for higher temperatures. Waragi (2023) found a similar shift in pore access radius of Carrara marble between fresh samples and samples subjected to five thermal cycles between 4 and 84 °C [37].

Thin sections of heated Carrara Gioia marble samples were observed under optical microscope. Images for the fresh sample and the sample heated at 200 °C are presented in Fig. 34. Images of the other samples can be found in Annex A. In Fig. 34 (b), widths of the intergranular spaces are given in red. The optical microscope images show the progressive decohesion of Carrara marble with heating temperature. At magnification x25, no intergranular spaces are visible in samples heated up to 85 °C while intergranular spaces of a few microns can be detected in samples heated at 105 °C and above. These observations corroborate MIP results, as it also illustrates a widening of marble intergranular spaces with heating temperature and thus a higher porosity at higher temperatures.

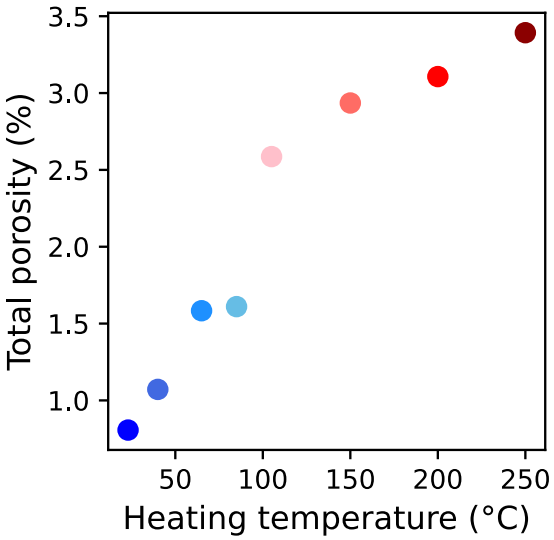

Fig. 32 Porosity. Total porosity (accessible via mercury intrusion) of Carrara Gioia marble samples heated at different temperature. Data point at 23 °C corresponds to the fresh sample.

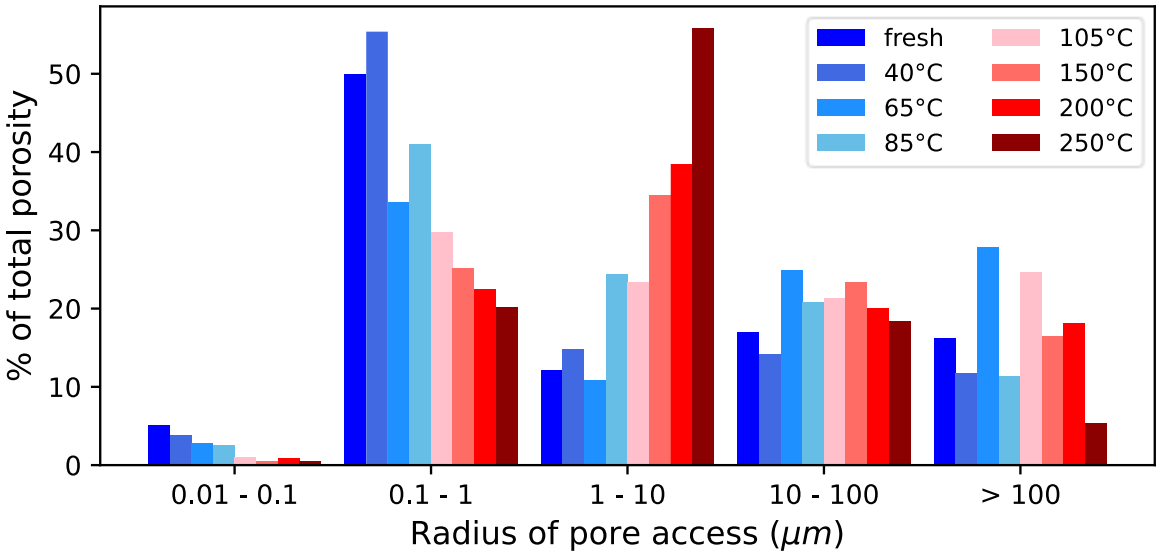

Fig. 33 Pore size distribution. Contribution of five porosity classes to the total porosity of Carrara Gioia marble samples heated at different temperatures.

SEM images show that even at low temperatures intergranular spaces are present between calcite grains in Carrara Gioia marble. They can be observed in Fig. 35 on a fracture plan of the fresh sample. Moreover, SEM observations on thin sections show that localized microcracking can be found along some calcite grain edges. The localized microcracking is already observable in the fresh sample (Fig. 36 (a)) and is also found in every heated samples (example for the sample heated at 105 °C in Fig. 36 (b)). This localized microcracking could be explained by friction between calcite grains during the heating phase. Indeed, when calcite grains expand parallel to crystallographic c-axe, neighbor grains could enter in contact and undergo friction from shear stress as they do not have the same crystallographic orientation. The presence of this localized

microcracking in the fresh sample, that was not heated in the laboratory, could be explained by the fact that the Carrara marble block was not immediately maintained at constant temperature after it was quarried.

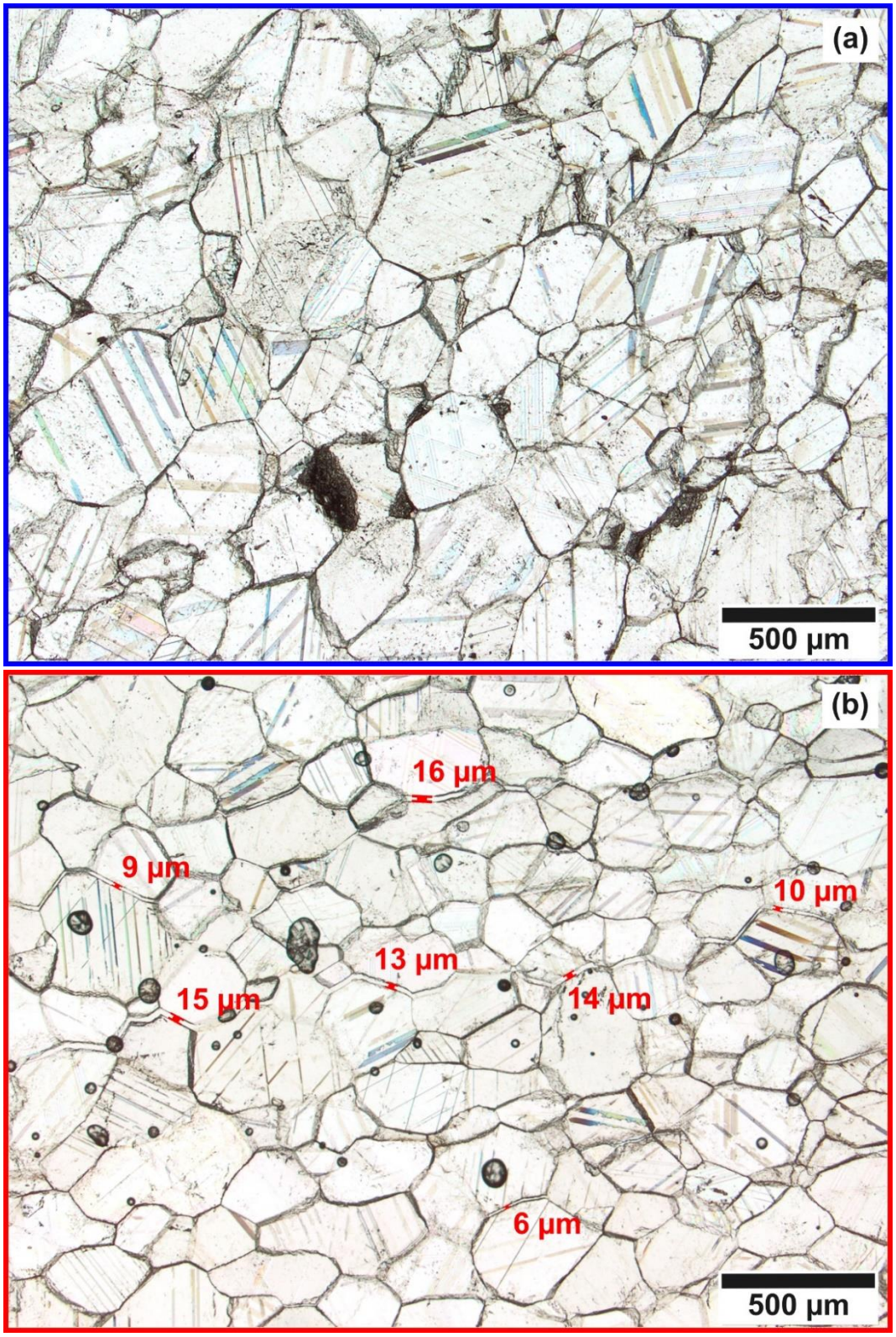

Fig. 34 Thin sections. Optical microscope images, at magnification x25, under plane polarized light, of thin sections of Carrara Gioia marble for (a) a fresh sample and (b) a sample heated at 200 °C. Widths of the intergranular spaces are given in red.

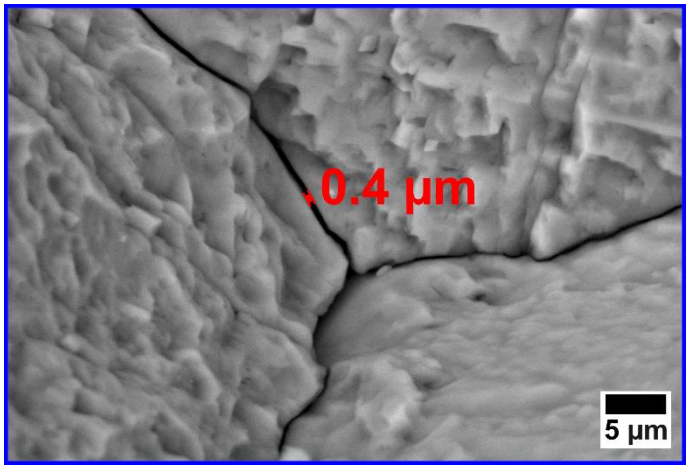

Fig. 35 Fracture plan. SEM images on a fracture plan of Carrara Gioia marble on a fresh sample. The image shows that intergranular spaces are already present in the samples at low temperatures, even in the fresh sample. The width of the intergranular space in this sample is given in red.

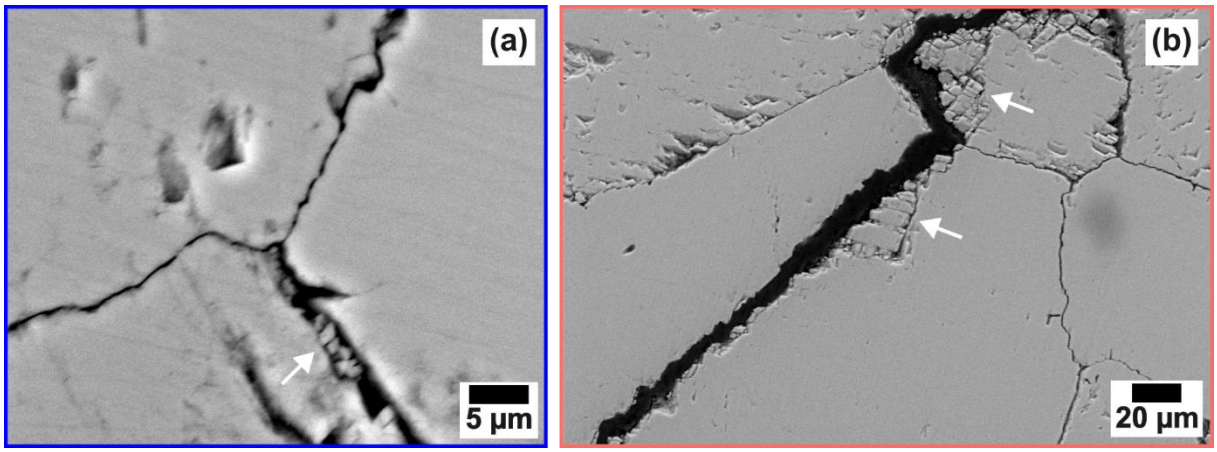

Fig. 36 Localized microcracking along calcite grain edges. SEM images on thin sections of Carrara Gioia marble for (a) a fresh sample and (b) a sample heated at 105 °C. The microcracked zones are pointed by white arrows.

Mechanical properties of Carrara Gioia marble samples were destructively probed with UCS tests. Fig. 37 shows the evolution of UCS values with heating temperature. Black circle data points correspond to the UCS values extracted from two measurements at each heating temperature. The average value and one standard deviation associated with these two measurements are also given as the square data points. UCS exhibits an overall tendency to decrease with heating temperature, from 57 MPa for the fresh sample (data point at 23 °C) to 45 MPa for the sample heated at 250 °C, in average. Only one of the two measurements made on the sample heated at 85 °C does not follow this trend. No specific reason for this behavior was found: NRUS measurements on this sample did not give scattered values of resonant frequency f_0 or nonlinear parameter α compared to the three other samples heated at 85 °C. This decrease in UCS with heating temperature can also be attributed to the progressive thermal decohesion of marble until its complete disintegration at 500 °C.

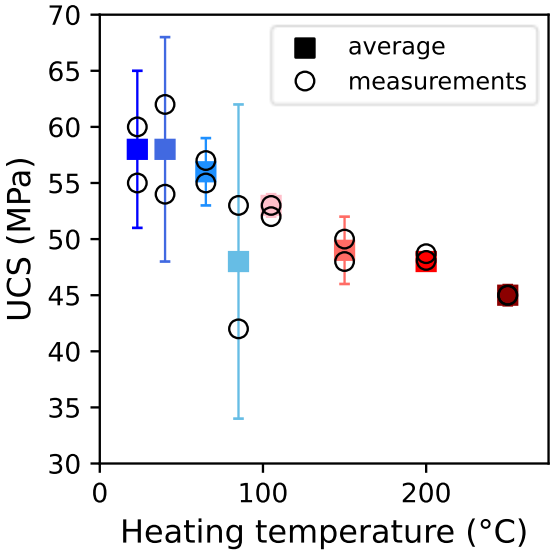

Fig. 37 Uniaxial compressive strength. Values of two UCS measurements (black circles) made on Carrara Gioia marble samples heated at different temperatures, and their average values (squares). Data points at 23 °C correspond to the fresh sample.

The adsorption isotherms for a fresh Carrara Gioia marble sample and samples heated at 40, 65, 85, and 105 °C are displayed in Fig. 38. The experimental water contents (empty circles) were fitted with the GAB theoretical modeling (solid lines). The water uptake is the lowest for the sample heated at 105 °C and the highest for the unheated sample and the sample heated at 40 °C, with the samples heated at 65 and 85 °C in between. The increase in water content with relative humidity at a given heating temperature can be explained by the capillary condensation occurring at the highest relative humidities. One can note that, for a given value of relative humidity, water content tends to decrease with heating temperature. It can be linked to the widening of pores access radius when heating temperature increases (Fig. 33). Indeed, at a certain relative humidity level, capillary condensation occurs only in pores below the Kelvin radius (Fig. 11). In this study, marble samples heated at the lowest temperatures exhibit a larger proportion of small pores (Fig. 33) and therefore are more subjected to capillary condensation, which results in higher water contents in these marble samples compared to the samples heated at higher temperatures.

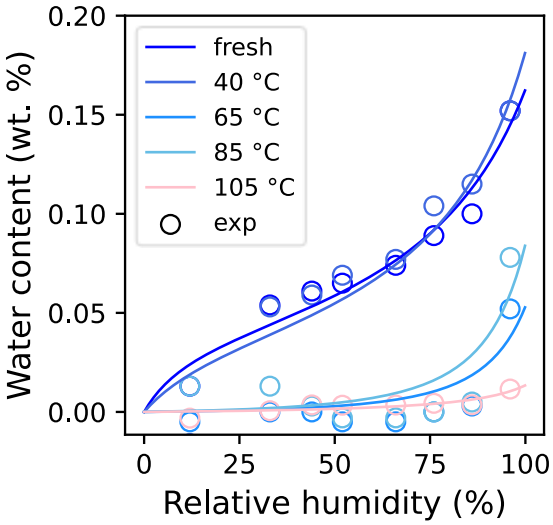

Fig. 38 Adsorption isotherms at 23 °C for Carrara Gioia marble samples heated at different temperatures. Empty circle data points correspond to the experimental measurements, and the solid lines to the fitting.

2.4. Impact of heating temperature evaluated by NRUS

Fig. 39 shows the NRUS results for the Carrara Gioia marble samples heated once at 40, 65, 85, 105, 150, 200, 250 °C and for fresh samples. The values of resonant frequency f_0 and nonlinear parameter α given in Fig. 39 correspond to the average values for all NRUS measurements made on all four samples heated at a given temperature. Uncertainties (shaded areas in Fig. 39) correspond to one standard deviation. In Fig. 39 (a), the resonant frequency f_0 exhibits a clear decrease with increasing heating temperature. It ranges from an average of 6.2 ± 0.5 kHz for the fresh samples to an average of 1.9 ± 0.3 kHz for the samples heated at 250 °C, thus displaying a global decrease of 69%. The evolution of the nonlinear parameter α differs from the one of the resonant frequency f_0 (Fig. 39 (b)). For heating temperatures between 23 and 85 °C, the nonlinear parameter α increases from an average of $(6 \pm 2) \times 10^3$ to an average of $(13 \pm 4) \times 10^3$. Then, it decreases down to an average of $(7 \pm 2) \times 10^3$ for the samples heated at 250 °C.

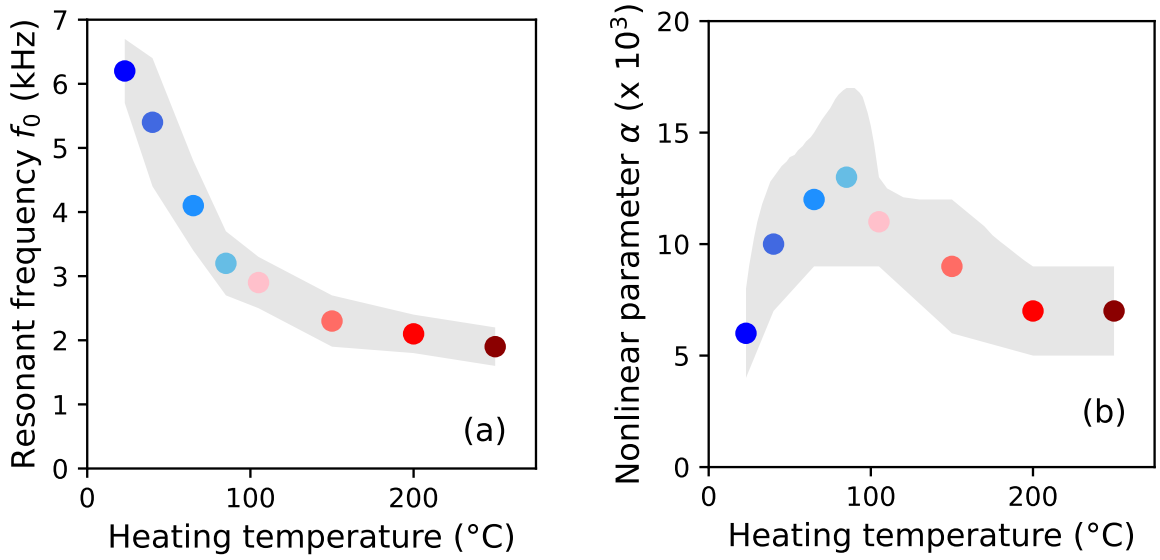

Fig. 39 Evolution of NRUS parameters with heating temperature. (a) Resonant frequency f_0 and (b) nonlinear parameter α as a function of heating temperature for Carrara Gioia marble. Data points at 23 °C correspond to fresh samples. Shaded areas denote one standard deviation.

Overall, the collected data display significant uncertainties, especially for the nonlinear parameter α. This could be explained by diverse factors. The uncertainties are calculated on measurements made on four different samples and these samples exhibited a significant variability in resonant frequency f_0 and nonlinear parameter α prior to thermal treatment as shown by reference measurements (Fig. 25). Moreover, the use of reversible glue (phenyl salicylate) and the reattachment of the piezoelectric transducers between each NRUS scan in these experiments could have brought more variability in the results. Additionally, relative humidity was not controlled during these NRUS scans and the nonlinear parameter α is very sensitive to ambient relative humidity (see section 2.5). Nonetheless, the global tendency of these evolutions seems robust.

The progressive decrease of resonant frequency f_0 may be explained by the creation of intergranular spaces in marble due to the anisotropic thermal dilation of calcite grains. Indeed, MIP and optical microscope results highlight the progressive thermal decohesion occurring in Carrara Gioia marble as heating temperature increases: higher porosity (Fig. 32, Fig. 34) and wider pores (Fig. 33) at higher temperatures. This increase in porosity induces a loss of cohesion in the material. The loss of cohesion is supported by the UCS measurements: mechanical strength of Carrara marble decreases as the heating temperature increases (Fig. 37). In Fig. 40, resonant frequency f_0 is displayed as a function of total porosity and of UCS. The resonant frequency f_0 decreases as porosity increases and increases as UCS increases. This behavior is consistent with the fact that resonant frequency is related to the material stiffness: the loss of contacts between calcite grains at the microscopic scale leads to a loss of cohesion at the sample macroscopic scale.

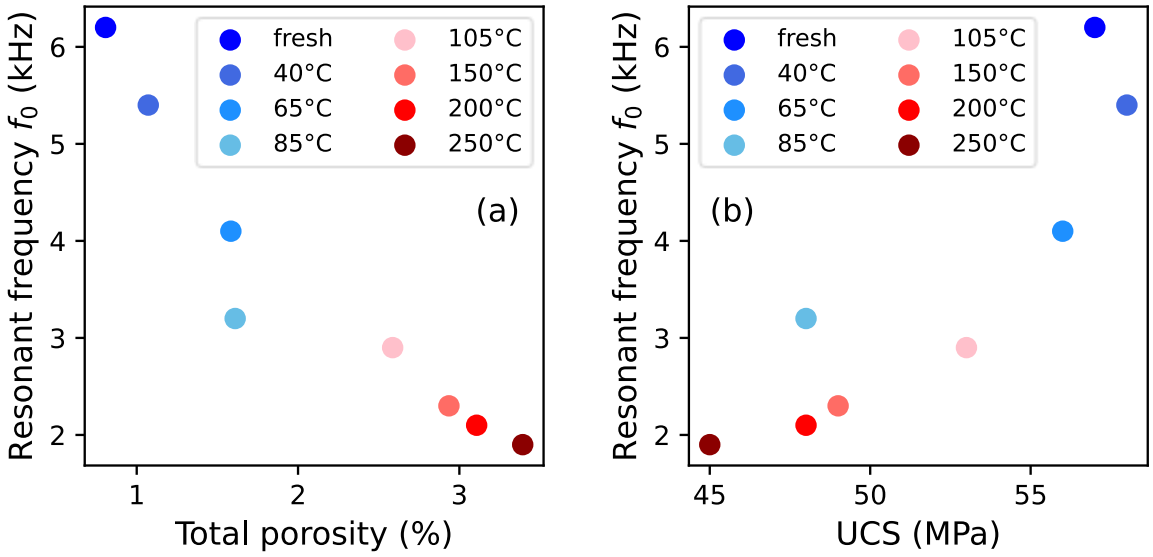

Fig. 40 Resonant frequency f_0 as a function of (a) total porosity and of (b) UCS for Carrara Gioia marble samples heated at different temperatures.

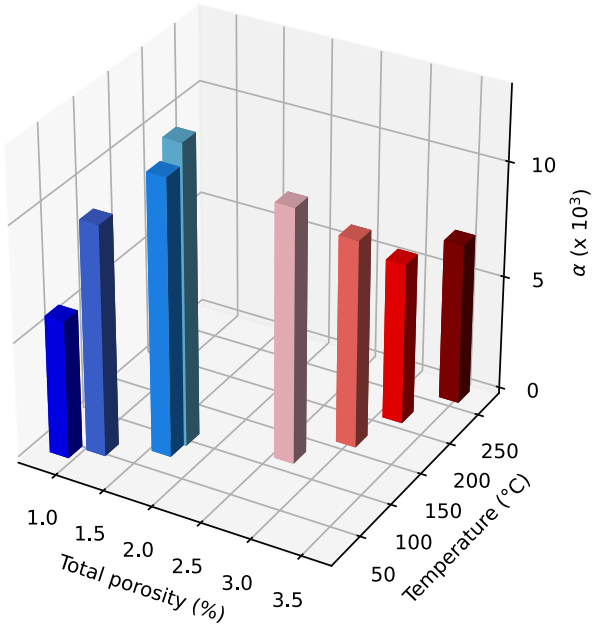

Fig. 41 Nonlinear parameter α as a function of total porosity and heating temperature for Carrara Gioia marble samples heated at different temperatures.

As presented in sections 2.1.1 and 2.1.2, the nonlinear parameter α increases with increasing thermal damage for several granular materials such as concrete, mortar or sandstone [85,92,109]. Unlike other granular materials, marble is composed of only one mineral (calcite) and has no cemented material in between grains, which can result in a different nonlinear behavior. In fact, this study shows that the nonlinear parameter α increases for heating temperatures between 23 and 85 °C, and then diminishes from 85 °C onwards (Fig. 39 (b)). The initial increase in the nonlinear parameter α could be explained by phenomena occurring at intergranular contacts between calcite grains

such as the closing/opening of the intergranular spaces created by heating (Fig. 34) and the friction between adjacent grains (Fig. 36). A hypothesis for the subsequent diminution of the nonlinear parameter α is the loss of these intergranular contacts. Indeed, intergranular spaces between calcite grains widen as heating temperature increases, and contacts between adjacent grains could thus be gradually lost and with them the local nonlinear phenomena occurring at grain contacts. This hypothesis is supported by the porosimetry data as the total porosity jumps from 1.6% to 2.6% between 85 and 105 °C, and as the radius of pore access shifts from between 0.01 and 1 µm to between 1 and 10 µm with increasing heating temperature (Fig. 32 and Fig. 33). Besides, **Erreur ! Source du renvoi introuvable.** shows that the nonlinear parameter α starts decreasing after the jump of total porosity situated between the samples heated at 85 and 105 °C. This hypothesis allows decoupling the thermal degradation affecting Carrara Gioia marble at the mesoscopic scale for the mild heating temperatures (40 – 85 °C), and at progressively higher scale above 85 °C.

Thus, the results presented here are not consistent with an ability of marble to heal itself during the heating process. This hypothesis, presented by Johnson *et al.* (2004) to explain a diminution of the nonlinear parameter α between measurements at ambient temperature and after heating at 200 °C for Asian white marble, falls short to explain the decrease of the resonant frequency f_0 (Fig. 39), the microstructural evolution (Fig. 34), mechanical tests (Fig. 37), and observations made previously. Specifically, more porosity is created (Fig. 32) in the form of microcracks visible in SEM (Fig. 35 and Fig. 36) when heating temperature increases, which invalidates the idea of a healing of the grain contacts during the heating process. On the contrary, this study evidences a progressive decohesion of marble until complete disintegration occurring at 500 °C with sample breakage.

Overall, the resonant frequency f_0 and the nonlinear parameter α exhibit, respectively, a significant decrease and increase in the mild temperature range (40 – 85 °C). These results point out that weathering already starts in Carrara marble in the natural exposure conditions. It is consistent with the studies of Malaga *et al.* (2002) and Schouenborg *et al.* (2007) which respectively suggested that marble intergranular decohesion occurred between 40 and 50 °C and recommended marble conditioning at 40 °C to avoid mechanical loss occurring at 70 °C [24,34]. The evolution of both NRUS parameters with heating temperature confirmed from laboratory testing that exposure to temperatures as low as 40 °C can initiate damage in Carrara Gioia marble. Such temperatures are often reached on facades or objects exposed outdoors even in temperate climatic areas [34,35]. This extreme sensitivity of marble to thermal weathering could therefore easily affect marble heritage subjected to climatic variation. Furthermore, the induced increasing porosity and loss of stiffness make this originally non-porous, compact and hard material much more sensitive to any degradation processes which are responsible for stone degradation (see section 1.2) including chemical dissolution, sulphation, soluble salt crystallizations, freezing-thaw cycles. Only an efficient protection against insolation or even an indoor exposure could be able to

preserve Carrara Gioia marble artworks from the first stages of intergranular decohesion induced by temperature.

2.5. Impact of relative humidity evaluated by NRUS

The impact of relative humidity (RH) on Carrara Gioia marble was also studied with NRUS. For these experiments, samples with different degrees of thermal damage were used: one fresh marble sample and four samples heated respectively at 40, 65, 85 and 105 °C. The previous temperature range was narrowed to these four temperatures to be closer to the mild temperature range reached in the outdoor environments.

2.5.1. Adsorption

The first experiment consisted in the study of the adsorption phase. Carrara Gioia marble samples were successively exposed to the relative humidities listed in section 2.2.1 in increasing order (from 12% RH to 96% RH).

The evolution of the NRUS parameters during the adsorption phase are displayed in Fig. 42. Data points correspond to the average values of the studied parameter for all NRUS scans performed at a given relative humidity on the sample. The uncertainties (shaded areas in Fig. 42) correspond to one standard deviation. Uncertainties are smaller than those obtained in the former experiment on thermal ageing (Fig. 39) as in the current experiment the piezoelectric transducers are permanently glued with epoxy to the samples and temperature and relative humidity are both controlled during the NRUS scans. Relative changes in resonant frequency f_0 and in nonlinear parameter α as a function of relative humidity and of relative change in water content are shown respectively in Fig. 43 and Fig. 44, the reference value being the parameter value at 12% RH. Water content at each relative humidity for each sample was obtained from the adsorption isotherms (Fig. 38).

The results for the fresh sample (blue circles in Fig. 42 and Fig. 43) show that the resonant frequency f_0 tends to slightly decrease as relative humidity increases. It decreases from 6.4801 ± 0.0007 kHz at 12% RH to 5.909 ± 0.008 kHz at 96% RH for this sample (Fig. 42 (a)). This decrease corresponds to a global decrease of 9% between 12% and 96% RH (Fig. 43 (a)). This decrease in the resonant frequency f_0 is not in agreement with the results of Siegesmund *et al.* (2021) which found an increase in UPV with increasing relative humidity in Blanco Macael marble (resonant frequency and UPV are linked by Eq. (9)) [70]. The relative humidity level has a significant impact on the nonlinear parameter α of the fresh sample. Indeed, the nonlinear parameter α of the

fresh sample is evaluated at (3.8 ± 0.5) × 10^3 at 12% RH and reaches (16 ± 1) × 10^3 at 96% RH (Fig. 42 (b)). This evolution corresponds to an increase of 320% between 12% and 96% RH (Fig. 43 (b)).

The NRUS parameters of the thermally damaged samples exhibit the same patterns than the ones of fresh sample: a slight decrease in the resonant frequency f_0 and a significant increase in the nonlinear parameter α (Fig. 42, Fig. 43). The global decrease in the resonant frequency between 12% and 96% RH is of 7%, 16%, 13%, and 11%, respectively for the samples heated at 40, 65, 85, and 105°C (Fig. 43 (a)). The global increase in the nonlinear parameter α between 12% and 96% RH is of 280%, 350%, 350%, and 300%, respectively for the samples heated at 40, 65, 85, and 105°C (Fig. 43 (b)). At a given relative humidity level, the absolute values of the NRUS parameters of all the samples follow the same order than in the previous experiment on the heating temperature impact (Fig. 39). The values of the resonant frequency f_0 rank correspondingly to the thermal damage level: the highest value for the fresh sample and the lowest for the sample heated at 105 °C. The values of the nonlinear parameter α at a certain relative humidity level are ranked as follow: the fresh sample (lowest value), the samples heated at 40, 65, 105 and 85 °C (highest value).

The relative changes in resonant frequency f_0 and in nonlinear parameter α with relative humidity are quite similar for all the samples (Fig. 43). For a given increase in water content, samples exhibit comparable relative changes in resonant frequency f_0 (Fig. 44 (a)). However, they do not reach the same levels of increase in nonlinear α at a given increase in water content: the highest is reached for the fresh sample and the sample heated at 40 °C, followed by the samples heated at 65, 85, and 105 °C (Fig. 44 (b)).

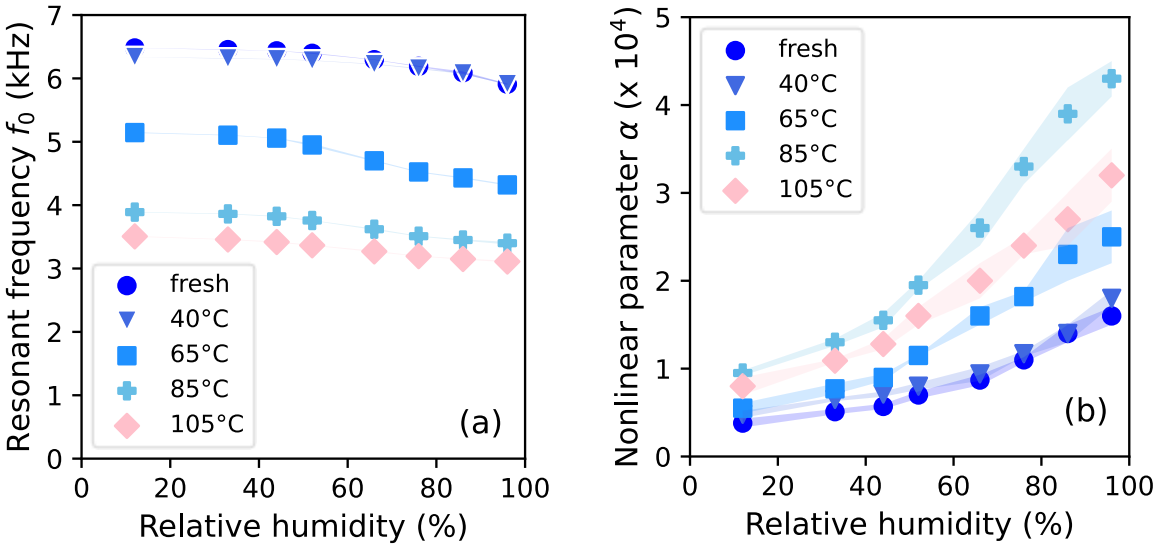

Fig. 42 Evolution of NRUS parameters during adsorption. (a) Resonant frequency f_0 and (b) nonlinear parameter α as a function of relative humidity for Carrara Gioia marble samples previously heated at various temperatures. Shaded areas denote one standard deviation.

One can first note the difference in sensitivities of the resonant frequency f_0 and the nonlinear parameter α to relative humidity changes (Fig. 42, Fig. 43). This observation is consistent with previous studies on granular materials. Siegesmund *et al.* (2021) found a low influence in marble of air humidity on ultrasonic velocity, which is closely linked to the resonant frequency f_0 (see Eq. (9)) [70]. Moreover, Ostrovsky and Johnson (2001) emphasized that the nonlinear parameter α is more dependent on water presence than linear parameters in geomaterials [95]. It is also in agreement with findings on a glass bead medium in which linear wave velocity is not affected by relative humidity changes while all the classical and nonclassical nonlinear parameters (β, γ, α) (see Eq. (5)) increase with increasing relative humidity [111].

The resonant frequency f_0 of Carrara marble samples decreases by between 7% and 16% as RH increases between 12% and 96% regardless of the thermal damage degree, even in the fresh sample (Fig. 43 (a)). This decrease of the resonant frequency f_0 could be explained by the moisture-induced softening which reduces stone mechanical strength in presence of water [137]. Studies have shown that mechanical properties of marble are reduced in water-saturated samples [23,30,69]. While generally considered as a result of liquid water, this work shows that this reduction occurs even along relative humidity changes corresponding to very low water content (between 0.01 and 0.18 wt. %). This diminution of resonant frequency f_0 at low water content could correspond to the onset of moisture-induced softening in Carrara marble: water inside pores can weaken friction between grains, thus inducing sliding between them and reducing mechanical properties.

Besides, the nonlinear parameter α exhibits a significant increase (by between 280% and 350%) with increasing relative humidity (between 12% and 96% RH). This increase corroborates observations made on others granular materials (see sections 2.1.1 and 2.1.2) [51,92,110,112]. As explained in section 2.1.2, Van Den Abeele *et al.* (2002) related an increasing nonclassical nonlinearity with increasing water saturation to the action of capillary condensation and the subsequent microscopic forces occurring in the pore network [51]. Microscopic forces due to capillary condensation could also explain the increase of nonlinearity with relative humidity in this work as water molecules can penetrate the intergranular space which are present in all the studied samples (Fig. 35). Moreover, the sorption isotherms highlight that less capillary condensation occurs in the samples heated at 65, 85 and 105 °C than in the fresh sample and the sample heated at 40 °C (Fig. 38). The fresh sample and the sample heated at 40 °C are also the ones in which the nonlinear parameter α exhibits the highest increase for a given increase in water content (Fig. 44). This corroborates the impact of capillary condensation in the nonclassical nonlinearity of granular materials.

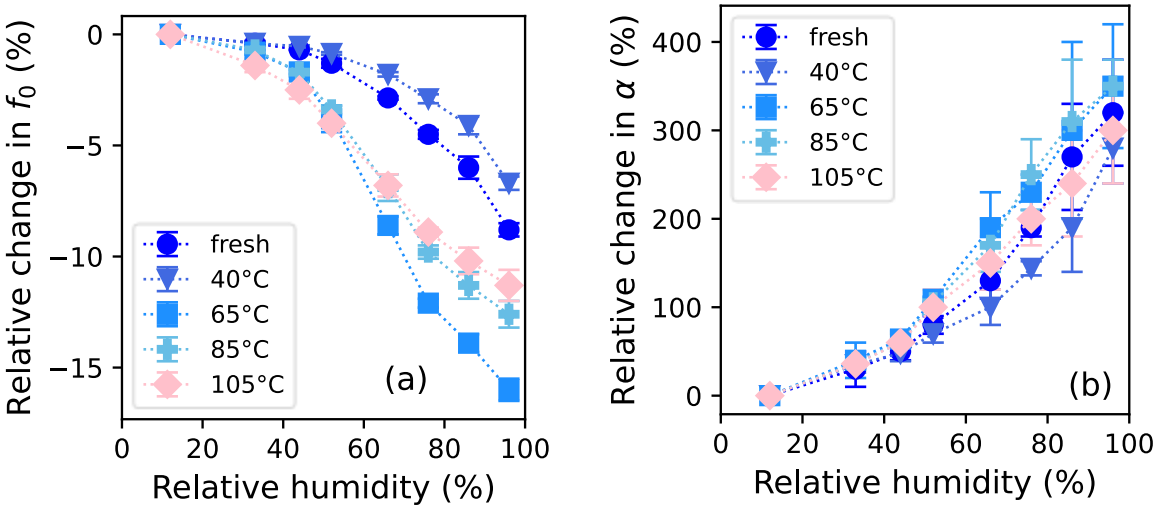

Fig. 43 Variation of NRUS parameters during adsorption. Relative change in (a) resonant frequency f_0 and (b) nonlinear parameter α with relative humidity for Carrara Gioia marble samples previously heated at various temperatures.

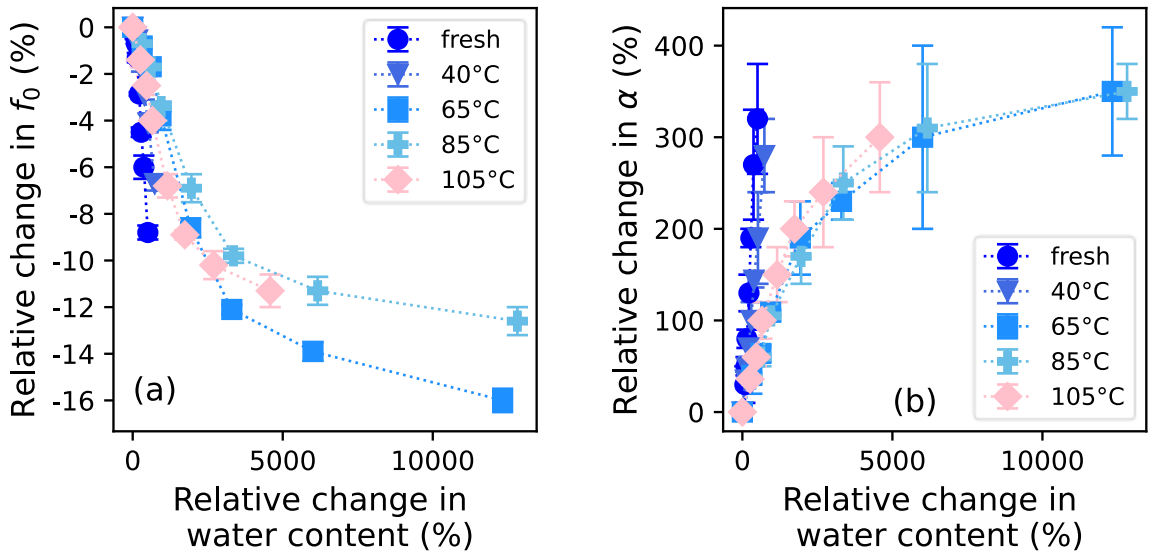

Fig. 44 Variation of NRUS parameters during adsorption. Relative change in (a) resonant frequency f_0 and (b) nonlinear parameter α as a function of relative change in water content for Carrara Gioia marble samples previously heated at various temperatures.

However, it can be noted that relative changes in the nonlinear parameter α (Fig. 43) do not seem correlated with total amount of porosity in sample (Fig. 32) or pore size distribution (Fig. 33). Indeed, relative changes with relative humidity level are of the same order of magnitude for all the samples regardless of their thermal damage degree (Fig. 43), whereas one could have expected that some samples exhibit larger relative variations of nonlinearity than others due to their different pore network (Fig. 32, Fig. 33). As capillary condensation is conditioned by Kelvin's law, a study of pore proportion below and above Kelvin's radius in the studied marble samples could have been

insightful. Unfortunately, for water as the fluid and at 25 °C, Kelvin's radius ranges from 4.95×10^{-4} to 2.57×10^{-2} µm for relative humidity between 12% and 96% (Fig. 11 (a)), which is below the pore radius detected by MIP on the studied samples.

When comparing the relative changes in NRUS parameters as a function of relative humidity (Fig. 43) to water content at the same relative humidity levels from the sorption isotherms (Fig. 38), it can be noted that the relative changes in NRUS parameters are extremely dissimilar between each sample for the same water content. Nonetheless, more comparable increases of the nonlinear parameter α and very similar decreases of the resonant frequency f_0 are reached for a given relative change in water content (Fig. 44). Therefore, the NRUS parameters could be more affected by variations occurring in water content than by the absolute water content amount within the samples.

2.5.2. Adsorption-desorption cycle

The evolution of the NRUS parameters was also investigated during desorption for the fresh and 85 °C heated samples to study a complete adsorption-desorption cycle. Carrara Gioia marble samples were successively exposed to the relative humidities listed in section 2.2.1 in decreasing order (from 96% RH to 12% RH).

The results of the evolution of the NRUS parameters during a full adsorption-desorption cycle are presented in Fig. 45 for the fresh sample and the sample heated at 85 °C. Data points correspond to the average values of the studied parameter for all NRUS scans performed at a given relative humidity on the sample. The uncertainties (shaded areas in Fig. 45) correspond to one standard deviation. The results for the adsorption phase are taken from the previous section (2.5.1). For a given relative humidity level, the resonant frequency f_0 values are extremely similar during adsorption and desorption phases for the two samples. They only differ at 12% and 33% RH for the sample heated at 85 °C.

In contrast, the nonlinear parameter α values do not coincide during the two phases for intermediate relative humidities for none of the samples. This parameter seems affected by a hysteresis phenomenon during adsorption-desorption. As explained in section 1.4.3, hysteresis loop are a well-known feature of sorption isotherms and can result from mechanisms such as a difference in contact angle value during adsorption and desorption or the presence of ink-bottle pores. These mechanisms occur at the microscopic scale. They could thus affect the nonlinear parameter α and lead to the presence of a hysteresis loop between adsorption and desorption phases. The presence of a hysteresis in the nonlinear parameter curve for an adsorption-desorption cycle is consistent with an influence of capillary condensation on the evolution of the nonlinear parameter α with moisture uptake (see section 2.1.2) as hysteresis in sorption isotherms occurs during the capillary condensation step (Fig. 46) [49]. Therefore, the

value of the nonlinear parameter α measured at a given relative humidity depends on the sample history regarding moisture uptake or release.

Except for the resonant frequency f_0 of the sample heated at 85 °C, the NRUS parameters reach the same value at the beginning and at the end of the adsorption-desorption cycle (data superimpose at 12% RH in Fig. 45). One could thus wonder whether the changes caused in the resonant frequency f_0 and the nonlinear parameter α by relative humidity variations are reversible. The evolution of both parameters was followed during hygric cycling to verify this hypothesis of reversibility on a longer-term experiment (see section 0)

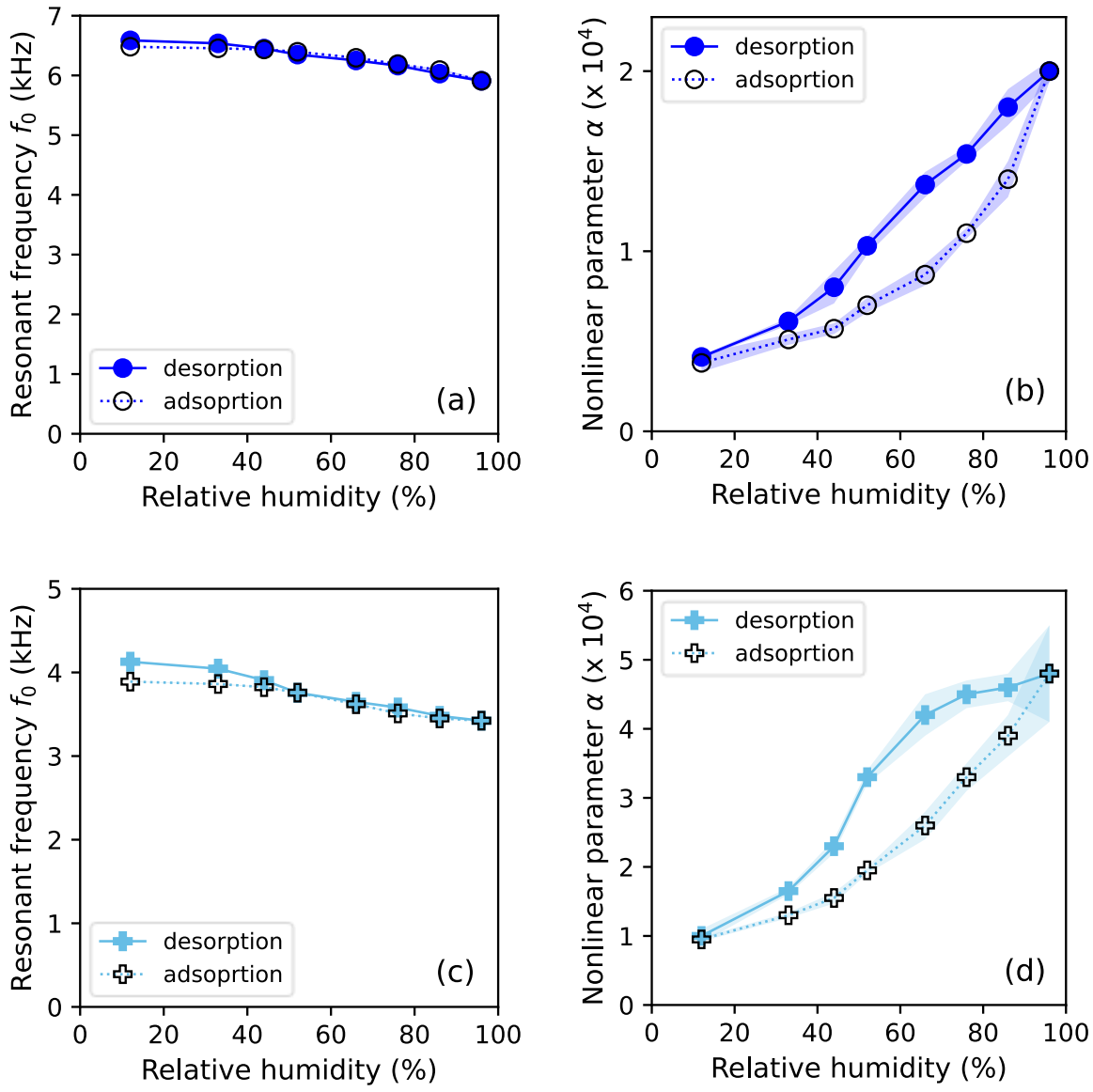

Fig. 45 Adsorption-desorption cycle. Evolution of the resonant frequency f_0 (on the left) and of the nonlinear parameter α (on the right) with relative humidity during adsorption (empty symbols) and desorption (filled symbols) for the (a, b) fresh (circles) and (c, d) 85 °C heated (crosses) Carrara Gioia marble samples. Shaded areas correspond to one standard deviation.

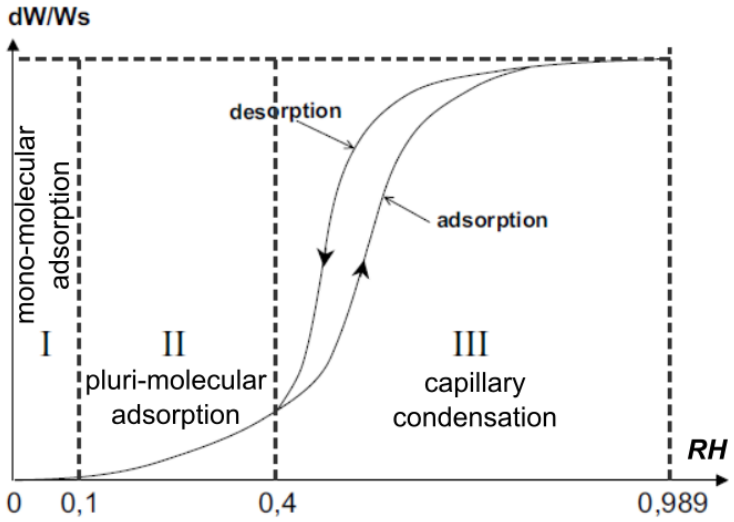

Fig. 46 Adsorption-desorption isotherm. Schematic representation of the adsorption processes during an adsorption-desorption cycle (modified from Rousset-Tournier 2001). Hysteresis occurs during the capillary condensation phase.

Carrara marble mechanical properties are therefore strongly impacted by relative humidity variations, especially at the mesoscopic scale. Yet, relative humidity changes have similar influence upon fresh samples and samples with different thermal damage degrees. Therefore, the effect of the sole relative humidity fluctuations on Carrara marble cultural heritage could be decorrelated from the degradation state of the artefacts. Moreover, exposure to cyclical relative humidity variations alone might not lead to permanent weakening or deformation of Carrara Gioia marble: this hypothesis is further tested in the next section (0).

2.6. Impact of cycling evaluated by NRUS

Under natural exposure conditions, marble artworks are not subjected only once to a temperature or humidity fluctuations. These phenomena are cyclical and marble heritage is exposed to daily as well as to seasonal variations of temperature and relative humidity. Therefore, thermal, hygric and thermo-hygric cycling were used to simulate outdoor exposure conditions in laboratory. The temperature amplitude studied in this section was narrowed compared to the one used to investigate the impact of heating temperature (see section 2.4) to be closer to temperatures reached under natural exposure.

2.6.1. Hygric cycling

After one adsorption-desorption cycle, changes in the resonant frequency f_0 and in the nonlinear parameter α caused by relative humidity fluctuations seemed reversible (see section 2.5.2). The evolution of the NRUS parameters at 12% and 96% RH was therefore followed during 10 adsorption-desorption cycles on Carrara Gioia marble samples with five different thermal damage degrees (fresh and heated at 40, 65, 85, and 105 °C) to verify this hypothesis on a longer-term experiment.

The NRUS results during 10 adsorption-desorption cycles are displayed in Fig. 47. Evolutions of the resonant frequency f_0 and of the nonlinear parameter α are displayed in Fig. 47 (a, b) at 12% RH and in Fig. 47 (c, d) at 96% RH. Data points correspond to the average values of the studied parameter for all NRUS scans performed at a given hygric state on the sample. Error bars correspond to one standard deviation. Data for the second cycle lack for samples heated at 40, 65 and 105 °C because they were not measured. Overall, the results tend to validate the hypothesis of reversibility. The resonant frequency f_0 at 12% RH displays a slight increase during cycling (up to 13% for the sample heated at 85 °C). However, it remains constant at 96% RH for all the samples. The nonlinear parameter α at 12% and 96% RH does not remain completely steady during cycling. Nevertheless, it does not exhibit any overall tendency to increase or decrease. It varies around the average value while remaining within the uncertainty range.

Therefore, both NRUS parameters (resonant frequency f_0 and nonlinear parameter α) do not seem permanently affected by relative humidity variations: same values are reached when returning to the initial relative humidity level. Thus, under stable temperature conditions, microstructural phenomena at stake in Carrara Gioia samples subjected to relative humidity variations could be reversible. This reversible behavior is observed for fresh marble and marble samples with four increasing degrees of thermal deterioration, meaning that relative humidity cycling does not permanently impact Carrara marble regardless of its degradation state. Therefore, climatic relative humidity fluctuations alone do not seem able to lead to a permanent weakening or deformation (see section 1.3) of Carrara Gioia marble. Nevertheless, relative humidity variations could play a role in the initiation or enhancement of some alterations when they are coupled to other agents (salt crystallizations, thermal variation, etc.) (see section 1.4.6).

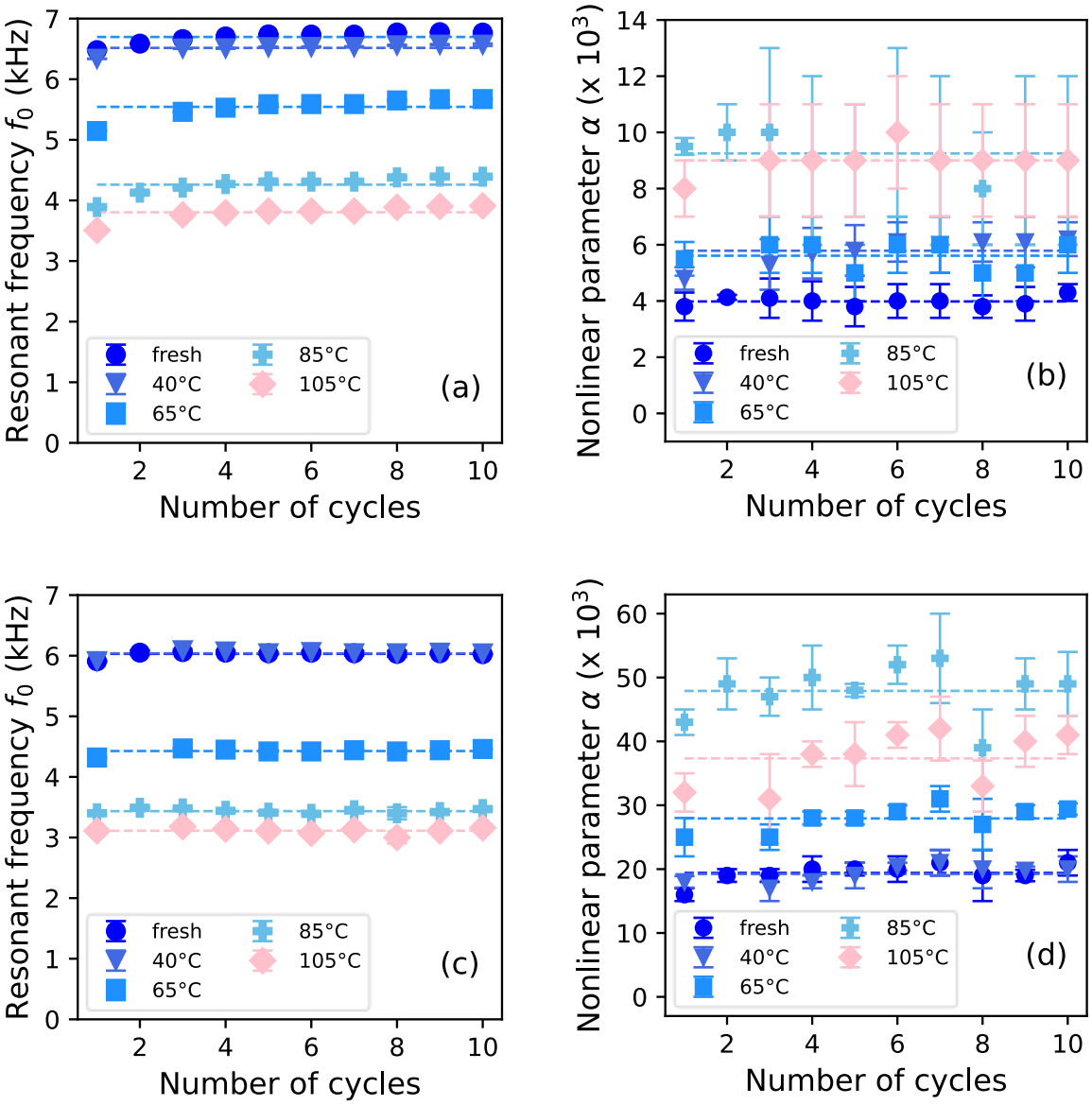

Fig. 47 Hygric cycling. Evolution of the resonant frequency f_0 (on the left) and of the nonlinear parameter α (on the right) at (a, b) 12% RH and (c, d) 96% RH during 10 adsorption-desorption cycles for Carrara Gioia marble samples previously heated at various temperatures. Dashed lines correspond to average values of the parameter and are given for information.

2.6.2. Thermal cycling

The impact of thermal cycling is studied for heating temperatures of 40, 65, 85, and 105 °C. The effects of cycling are investigated only in the mild temperature range to simulate natural exposure conditions. Two Carrara Gioia marble samples are used per temperature and NRUS measurements are made before cycling and after 1, 2, 3, 4, 5, 15, 25, 35, 45, 55, 65, 75, 85, 95, 105, 115, 125, and 135 cycles. Data is missing for the 115th thermal cycle of the samples heated at 65 °C because they were not measured.

The evolution of the resonant frequency f_0 and of the nonlinear parameter α are displayed in Fig. 48 and a focus on the data for the first 15 thermal cycles that are difficult to read in Fig. 48 is presented in Fig. 49. Data points correspond to the average values of the studied parameter for all NRUS scans performed on the two samples used at a given temperature. Error bars correspond to one standard deviation. The results highlight that the resonant frequency f_0 varies almost only between the fresh state and the first thermal cycle and levels off onwards. It decreases by 9%, 30%, 43%, and 44% for the sample heated at 40, 65, 85, and 105 °C, respectively. The nonlinear parameter α increases up to the 2nd or 3rd thermal cycle depending on the sample heating temperature, then decreases until the 15th cycle almost down to its original value in the fresh state. It then slightly increases again before staying relatively steady, except between about the 65th and 95th cycles where it reaches higher values.

First of all, one can note that the resonant frequency f_0 exhibits almost no variation after the first thermal cycle. This could be related to the behavior of marble permanent expansion under dry thermal cycles. Indeed, Koch and Siegesmund (2004) showed that under dry conditions marble residual strain is primarily affected by the first thermal cycle (between 20 and 90 °C) and then stays relatively steady in absence of water [40]. Intergranular spaces between calcite grains could therefore mainly be created during the first thermal cycle and might not further widen onwards. Marble decohesion could thus be mainly conditioned by the first thermal cycle and could stay relatively constant onwards.

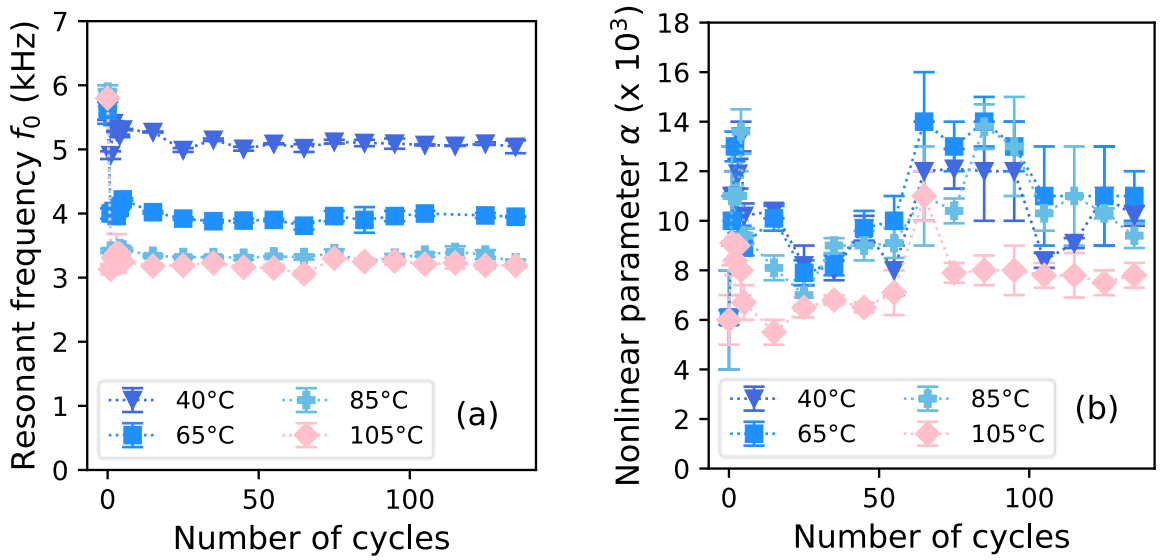

Fig. 48 Thermal cycling. Evolution of (a) the resonant frequency f_0 and of (b) the nonlinear parameter α of Carrara Gioia marble samples during 135 thermal cycles up to four different temperatures.

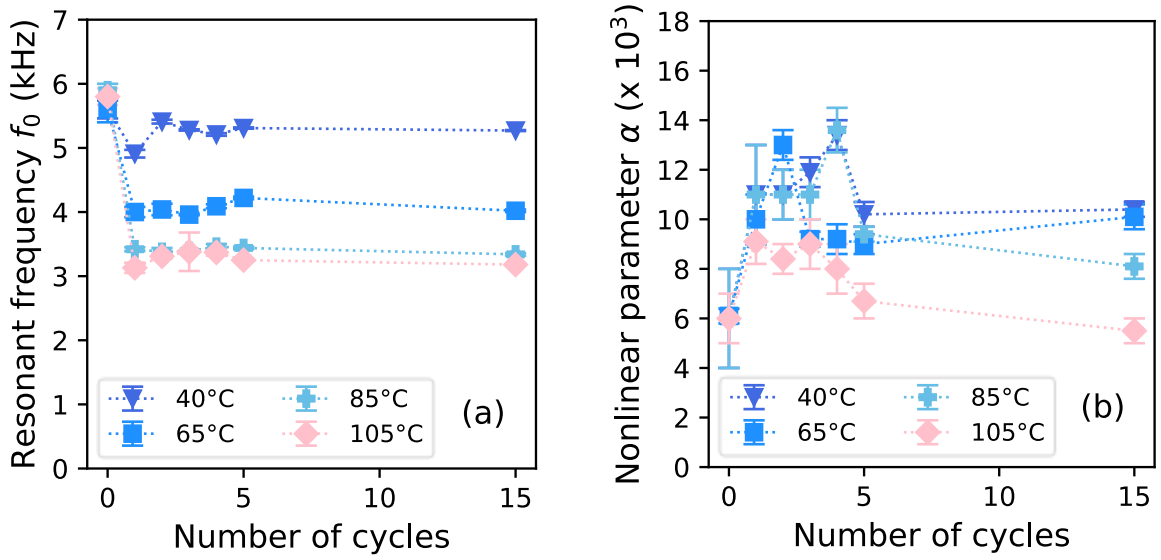

Fig. 49 Focus on the first 15 thermal cycles. Evolution of (a) the resonant frequency f_0 and of (b) the nonlinear parameter α during the first 15 thermal cycles.

Besides, the results for the resonant frequency f_0 (Fig. 48 (a)) are not consistent with the results of Waragi (2023) on the evolution of UPV during 144 thermal cycles between 4 and 84 °C [37]. Indeed, Waragi (2023) found that UPV decreases between the fresh state and the 4th thermal cycle, then increases and reaches a plateau at a higher value than the one for the fresh state. UPV is related to the resonant frequency by Eq. (9). In the results presented here, the resonant frequency f_0 only decreases over 135 thermal cycles and is therefore lower after 135 thermal cycles than it was in the fresh state.

The nonlinear parameter α exhibits more variations than the resonant frequency f_0. Therefore, the anisotropic dilation of calcite grains at each heating cycle may generate some microstructural changes, such as slight grain displacements or friction between adjacent grains. But these changes should be small enough not to impact the macroscopic cohesion of the samples.

Thus, the initial exposure to temperature variations seems the most harmful to Carrara Gioia marble artworks. However, one limit of this experiment in simulating outdoor exposure of marble artefacts is that the core samples used here are unconstrained and do not present zones of stress concentration, unlike masonries or statues. The samples are free to expand during thermal cycling and do not present geometries unfavorable to loading, which is not the case of most marble cultural heritage artefacts [34,78]. This difference most probably impacts the results provided here and has therefore to be born in mind when drawing conclusions.

2.6.3. Thermo-hygric cycling

After studying the impact of hygric and thermal cycling separately, the two parameters were combined. Five initially fresh Carrara Gioia marble samples were subjected 450 times to the thermo-hygric cycle presented in Fig. 28. The NRUS parameters are measured before cycling and after 42, 60, 90, 114, 135, 165, 228, 276, 303, 327, 360, 390, 420, and 450 cycles. The samples had to be taken out of the climatic chamber to perform the NRUS scans. Only one NRUS scan was made per sample. The samples were always taken out at the same point of the thermo-hygric cycle: during the plateau at 10 °C and 60% RH (see Fig. 28). The samples were left in a temperature-controlled oven maintained at 23 °C for 2 h before carrying out the NRUS scans so that they could recover from temperature and relative humidity changes.

The effects of thermo-hygric cycling on the resonant frequency f_0 and the nonlinear parameter α are displayed in Fig. 50. The results are presented for each sample individually. The results show that for all five samples the resonant frequency f_0 decreases by about 70% between the fresh state and the 42nd thermo-hygric cycle and exhibits less variation afterwards. The nonlinear parameter α initially increases by about 300% between the fresh state and around the 100th cycle for all five samples, then it decreases until the 200th cycle, and finally either stays relatively steady onwards or exhibits sawtooth-like variations without showing a global tendency to increase or decrease.

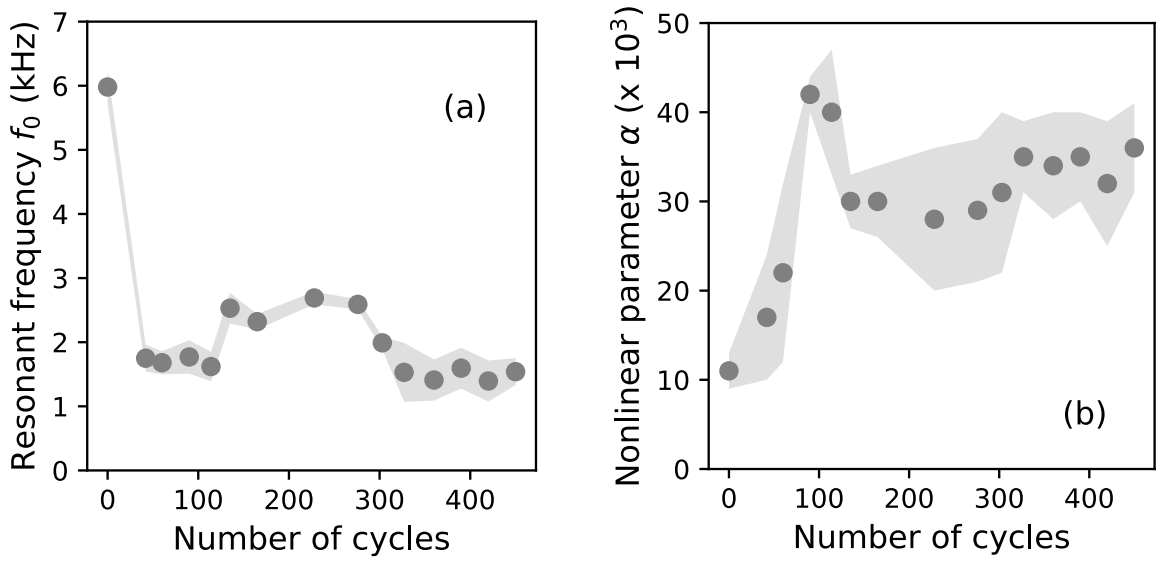

Fig. 50 Thermo-hygric cycling. Evolution of (a) the resonant frequency f_0 and of (b) the nonlinear parameter α of five Carrara Gioia marble samples during 450 thermo-hygric cycles (see Fig. 28 for a scheme of one thermo-hygric cycle).

It can be highlighted that, as for the thermal cycling (Fig. 48 (a)), the thermo-hygric cycling induces almost no variation in the resonant frequency f_0 after the first cycles, similarly to what is observed in thermal cycles. However, the decrease is stronger than during thermal cycling alone. During thermal cycling, the decrease in resonant frequency f_0 was of 43% for the same maximum temperature (85 °C) and of 44% for a similar temperature variation (samples heated at 105 °C: $\Delta T = 105\ °C - 23\ °C = 82\ °C$). The decrease is of about 70% during thermo-hygric cycling. It is similar to the decrease in resonant frequency f_0 between the fresh state and after one heating at 200 °C (66% reduction) or 250 °C (69% reduction) (Fig. 39 (a)). This stronger decrease in the resonant frequency f_0 could result from the coupling of thermal decohesion and moisture-induced softening. One must also bear in mind that the temperature evolutions differ during the thermal and thermo-hygric cycling. The stable temperature phase is shorter and the cooling quicker in the latter, which could have also impacted the resonant frequency f_0 differently in the two cases.

In the previous subsection (2.6.2), the resonant frequency behavior during thermal cycling was compared to marble permanent expansion behavior. The same pattern between the two evolutions is not found for thermo-hygric cycling. Indeed, Koch and Siegesmund (2004) showed that under wet conditions marble residual strain continuously increases during thermal cycles between 20 and 90 °C [40]. Yet, in the results presented here, the resonant frequency f_0 does not exhibit much variation after the first measurement. Nevertheless, Koch and Siegesmund (2004) presented results over 10 wet thermal cycles while the first measurement in this work was performed after the 42nd thermo-hygric cycle, therefore the initial evolution of the resonant frequency f_0 over the first cycles (< 42) was missed out. More measurements should be performed during the very first thermo-hygric cycles so that the initial variations of the resonant frequency f_0 could be observed.

The evolution of the nonlinear parameter α follows a similar pattern than during thermal cycling (Fig. 48 (b)) but on larger spans. It goes through the same steps of increase, then decrease, and finally relative steadiness. However, the nonlinear parameter α exhibits such variations over 135 cycles during thermal cycling while it only continuously increases over the first 100 thermo-hygric cycles.

The nonlinear parameter variations and absolute values are higher during thermo-hygric cycles than during thermal cycling. During thermal cycling, the nonlinear parameter α increased by 130% and reaches $(14 \pm 1) \times 10^3$ at most during the initial increase while it increases by about 300% and reaches 46×10^3 during thermo-hygric cycling. These levels are also higher than those reached during adsorption at 60% RH (Fig. 42), therefore they cannot only be explained by the fact that the samples are taken out the climatic chamber for NRUS measurement during the 60% RH part of the thermo-hygric cycle. The levels reached here correspond more to the ones reached at 96% RH during adsorption phase (Fig. 42). Therefore, thermo-hygric variations have a stronger influence on nonlinearity in Carrara marble than thermal or hygric fluctuations alone. Perhaps, nonclassical nonlinearity is enhanced in Carrara marble during thermo-hygric

cycling because of the combined effects of grain dilation due to temperature variation and of microscopic pressures due to capillary condensation.

While the resonant frequency f_0 does not vary much after the first NRUS measurement, the nonlinear parameter α progressively increases over the first 100 thermo-hygric cycles. An increasing micro-damage is thus probed over a larger number of thermo-hygric cycles than macro-damage. Therefore, changes due to exposure to cyclical temperature and humidity variations could occur in Carrara marble microstructure but not lead to further degradation at the macroscopic scale after the first cycles.

Overall, the results showed that thermo-hygric cycling has a greater impact on Carrara Gioia marble than thermal cycling alone. This stronger influence is found both at the macroscopic and mesoscopic level. Thermo-hygric cycling is at the same time the most encountered situation by marble artefacts exposed outdoors. Indeed, sole fluctuations of temperature or relative humidity do not represent natural weather conditions. These two factors vary simultaneously over daytime/nighttime and seasons. Besides, even a very limited outdoor exposure is able to induce significant deterioration in Carrara marble artworks as the macroscopic decohesion is mainly impacted by the very first thermo-hygric cycles. Therefore, only an indoor exposure from the very beginning of the artwork life seems able to preserve Carrara Gioia marble from the initial stages of thermal-hygric degradation. Similarly to what was previously stated in section 2.6.2, this experiment is also limited in simulating real artefact behavior by the unconstrained state and the geometry of the samples.

2.7. Conclusion on the degradation at the material scale

The thermal and hygric degradation of Carrara Gioia marble at the material scale was followed through NRUS, combined with microstructural and mechanical characterization. The mechanical state of Carrara marble was assessed by means of two parameters. The resonant frequency f_0 is related to sample stiffness and probes damage at the macroscopic scale. The nonlinear parameter α is related to phenomena occurring at the mesoscopic scale.

As a non-destructive method, NRUS overcomes the limitations of traditional destructive mechanical testing in monitoring the mechanical properties of natural stones during cycling. Indeed, such materials exhibit a significant property variability from one sample to another, even inside the same stone block. Besides, the results presented above show that NRUS is much more sensitive to marble decay than other non-destructive methods such as UPV measurements. Lastly, NRUS does not only

provide information on stiffness, which is classically studied, but also on the material microcracking state.

The results presented above highlight the progressive thermal decohesion of Carrara Gioia marble from 40 °C to complete disintegration at 500 °C. This work showed from laboratory experiments that thermal damage is already detected in Carrara marble after only one exposure to temperatures as low as 40 °C. This temperature range is easily reachable on marble surface under natural exposure conditions. This material is therefore particularly vulnerable to outdoor exposure. Moreover, during thermal cycling Carrara marble is mainly impacted by the first thermal cycle, therefore thermal degradation state of Carrara marble is primarily conditioned by the very initial stages of exposure to cyclical temperature variations. The results on the impact of heating temperature and thermal cycling contradict the hypotheses of a healing of Carrara marble upon heating at high temperatures and upon thermal cycling in the mild temperature range. Indeed, microstructural characterization on thermally weathered samples shows that more porosity is created and intergranular spaces widen when increasing heating temperature. These observations are in contradiction with a re-strengthening of calcite grain contacts.

Relative humidity has a considerable impact on Carrara marble nonlinearity level, even for fresh samples. However, contrary to temperature variations, relative humidity fluctuations do not induce permanent weakening of Carrara marble, and this regardless of the thermal damage degree of the samples. Therefore, exposure to sole relative humidity variations, uncoupled with thermal fluctuations, soluble salts, frost, or other alteration factors, is unharmful to Carrara marble artefacts.

Thermo-hygric cycling induces greater damage in Carrara marble than both thermal and hygric cycling alone. For comparable maximum temperatures and temperature variations, marble decohesion is more pronounced during thermal cycles combined with relative humidity variations than in absence of relative humidity variations. Similarly to thermal cycling, Carrara marble decohesion is primarily impacted by the very first thermo-hygric cycles. This highlights once more the significant vulnerability of Carrara Gioia marble to outdoor exposure. A prolongated exposure to cyclical variations of temperature and relative humidity is not necessary for Carrara marble to reach a considerable degradation state, a very limited exposure duration is sufficient to do so. Such phenomena could be worsened in the future due to climate change and global warming. A global warming (relative to 1850-1900) limited to +3 °C is projected for intermediate greenhouse gas emissions scenario (+1.1 °C over 2011-2020), with even larger temperature increases inland where cultural heritage is located [138]. In fact, an increase of the risk of Carrara marble thermal weathering has been projected in the Mediterranean area [139].

Nevertheless, all these experiments are limited in simulating real artefact behavior under outdoor exposure by several factors. Indeed, in this work samples were not constrained during cycling. Their thermo-hygric expansion was not limited by

surrounding stone blocks for instance as it is the case in real masonry. Therefore, samples were free to deform and were not subjected to contraction stress on their edges. Besides, the sample geometry was quite simple (cylinders) and did not present zones more favorable for stress concentration, contrary to statues which have complex geometries and weaker zones such as elbow crease. Additionally, the impact of other factors and agents was left out of this study in order to simplify the data interpretation by decomposing the degradation sources. Thermo-hygric cycling can have a different impact on Carrara Gioia marble degradation in the presence of soluble salts, pollutants, or frost.

In the next section, the degradation state of Carrara marble sculptures will be assessed by means of another ultrasound-based method. Acoustic tomography will be combined with photogrammetry to probe the inner degradation state of two archaeological pieces which had been exposed to natural weather conditions for centuries. 3D imaging of the propagation velocity inside the objects will be used to try answering related conservation issues.

3. Degradation at the sculpture scale

In the previous chapter, the significant sensitivity of Carrara Gioia marble to exposure to cyclical thermo-hygric fluctuations was highlighted on artificially weathered laboratory samples. This chapter is focused on Carrara marble degradation at the sculpture scale, in objects exposed under natural weather conditions over a large time span. The results of the previous chapter showed from linear (resonant frequency f_0) and nonlinear (nonlinear parameter α) parameters that such outdoor exposure could lead to considerable material degradation. Therefore, this chapter intends to image the potential degradation in Carrara marble sculptures resulting from their conservation history. This time, only a linear parameter (propagation velocity of longitudinal waves) is mapped in the volume of the sculpted objects.

The two archaeological sculptures under study are a Roman altar devoted to the god Apollo and a Roman statue of the Emperor Augustus. They both belonged to the Roman theater of Arles, France, and were exhibited in different parts of the theater, resulting in different exposures to weather conditions. The two sculptures are now displayed in the *Musée Départemental Arles Antique*. The study of such archaeological pieces was made possible thanks to the kind cooperation of the museum and its curators Alain Charron and Soizic Toussaint.

The inner degradation state of these archaeological pieces was assessed by means of acoustic tomography coupled with 3D photogrammetric imaging. This technique is non-destructive, thus it is well-suited to study cultural heritage artefacts. Since the 1990s, acoustic tomography has been applied on various cultural heritage artefacts [80,81,140–150]. When dealing with real artefacts having sometimes complex shapes, one of the issues of acoustic tomography is the distance measurement between ultrasound emitters and receivers. On artefacts with simple geometries, such as pillars [142,147–149], slabs [140], walls [150], or on cross-sections [80,144], acoustic tomography can be carried out without using 3D models since the distance are relatively easy to measure. However, when investigating the conservation state of sculptures with complex geometries, acoustic tomography is usually coupled to the use of 3D photogrammetric or lasergrammetric models [81,141,143,145]. When using 3D models, the transducer positions are generally tracked thanks to markers sticked on the sculpture surface [81,143,145,146,151]. Here, the transducer positions were located in an innovative way by projecting the 3D models onto the sculptures. The transducer positions were tracked and saved on the 3D models during the measurement campaigns. By applying acoustic tomography on two archaeological sculptures, this work aims at evaluating their inner cohesion state, at highlighting potential weaker areas and at answering specific conservation issues raised by the curators. It is also aimed at investigating the extent of cracks visible on the sculpture surface.

The Roman theater of Arles and the studied objects will be first presented. The methodology and the experimental set-ups will then be described. The apparent velocity results, the 3D imaging of velocity and the crack depth measurements will finally be discussed.

3.1. Studied sculptures

The degradation state of two sculptures from the Roman theater of Arles will be assessed in this chapter. One is an altar devoted to the god Apollo, the other is a statue representing the Emperor Augustus. They are both nowadays exhibited in the *Musée Départemental Arles Antique*, in Arles, France. The Roman theater and both sculptures will be presented in this section.

3.1.1. Roman theater of Arles

A Roman colony was founded in Arles (Fig. 51) by Julius Caesar in 46 BC under the name of Colonia Iulia Paterna Arelate Sextanorum and veterans of the 6th Roman legion settled in Arles [152]. Public monuments (theater, forum) were built under Augustus reign (27 BC – 14 AD) when an urban plan was implemented [152].

Fig. 51 Location of the city of Arles in France.

The Roman theater of Arles was built at the end of the 1st century BC on the top of the Hauture hill, contrary to most Roman theaters which were built upon a hillside [153]. A model of the theater in the Roman times is shown in Fig. 52. The current remains of the theater of Arles are shown in Fig. 53. 10,000 spectators could seat in the *cavea* (1 in Fig. 52 and Fig. 53) [153]. The wooden scene (2 in Fig. 52 and Fig. 53) measured 50 m in length and 6 m in width. Behind it, the three-level *scaenae frons* (3 in Fig. 52 and Fig. 53) was richly decorated with columns and statues [153,154]. The Roman theater of Arles is

believed to have been in activity until 5th century AD when its materials were reused in religious buildings, therefore the building and the decorative columns and sculptures may have been in place for four centuries (A. Charron, personal communication, May 21st, 2024). The south part of the theater was integrated to the rampart built in the 5th century and the Roland tower was added to the south side of the theater building [153,155]. The theater was later buried in order to build over it (A. Charron, personal communication, May 21st, 2024). A Jesuit school and the convent of Mercy were successively built over the theater site [153]. The remains of the theater started to be excavated during the 19th century [153]. Today, the remains of the Roman theater (Fig. 53) comprise the *cavea*, the *orchestra* (5 in Fig. 52 and Fig. 53) and some columns or column parts from the *scaenae frons*. Besides, sculptures from the *scaenae frons* are displayed in the *Musée Départemental Arles Antique*.

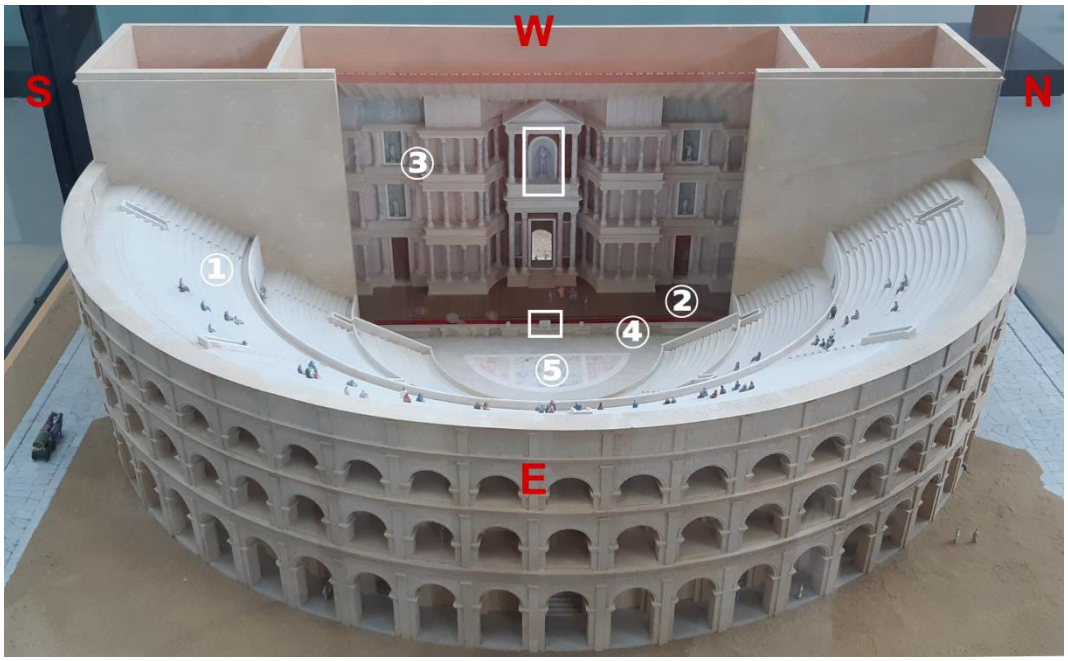

Fig. 52 Model of the Roman theater of Arles, *Musée Départemental Arles Antique*. (1) C*avea*, (2) wooden scene, (3) *scaenae frons*, (4) *pulpitum*, (5) *orchestra*. The locations of the Apollo altar and the Augustus statue are indicated by white boxes, respectively at the bottom and top. The cardinal directions are indicated in red.

The respective locations of the Apollo altar and the Augustus statue are indicated in Fig. 52 by white boxes (Apollo altar on the bottom in front of the scene, Augustus statue on the top in a niche inserted in the *scaenae frons*). The front sides of both sculptures were facing east in Roman times. Both sculptures could have spent several centuries in this disposition. The Roman theater is an open building, therefore decorative sculptures were continuously subjected to the natural outdoor weather conditions. Due to their arrangement, the Augustus statue should have been less exposed to some weather conditions: it had probably been more protected from rain and insolation than the altar thanks to the recess. However, the burying conditions of both sculptures are unknown and could have also influenced their current degradation state. Moreover, while both

objects are made of Carrara marble, their alteration could have been impacted by their precise origin (quarry) and type (microstructure), which are also unknown.

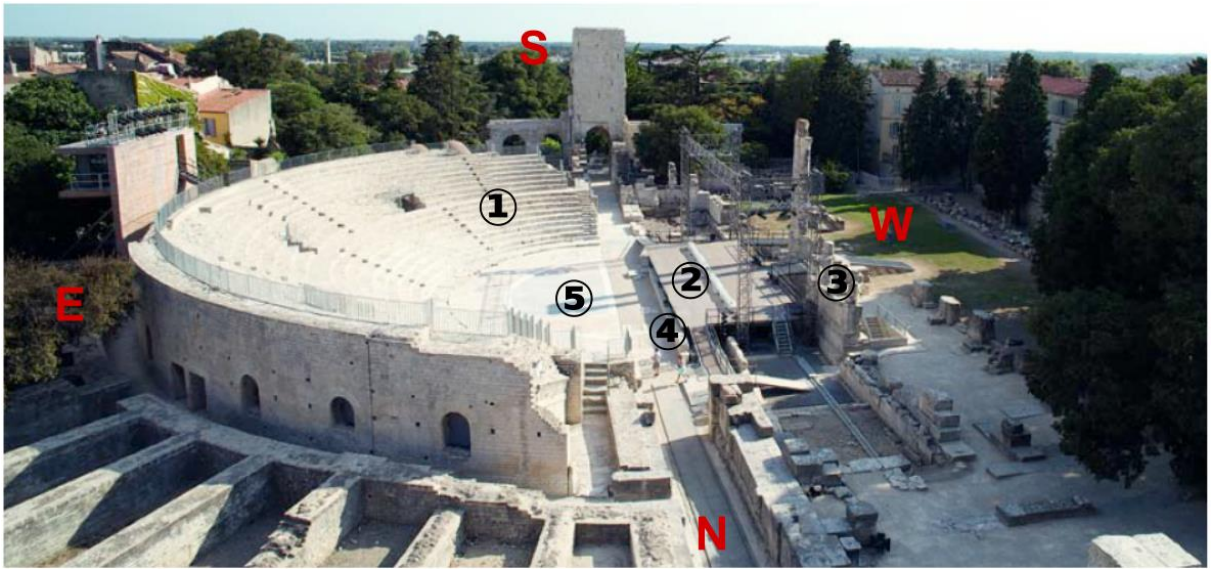

Fig. 53 Remains of the Roman theater of Arles. (1) C*avea*, (2) wooden scene, (3) *scaenae frons*, (4) *pulpitum*, (5) *orchestra*. The cardinal directions are indicated in red (modified from Botton 2009).

Therefore, weather conditions in Arles are important to summarize as the Apollo altar and the Augustus statue were exposed to climatic conditions for centuries. The data presented hereafter correspond to averages on the period from 1980 to 2016 [156]. In Arles, the lowest average temperature fluctuates between 4 and 19 °C, and the highest average temperature between 11 and 30 °C. The weather is mainly clear, with at most 45% of cloudy days during winter. The rainiest time of the year in Arles is between September and November, with 187 mm of rain cumulated during those three months. The main wind direction is north all over the year. The second main wind direction is east during winter and south during summer.

3.1.2. Apollo altar

The Apollo altar was located at the base of the *pulpitum* of the Roman theater of Arles (small wall supporting the front of the scene, 4 in Fig. 52). It is made of a fine-grained Carrara marble and dates from the end of the 1st century BC [157]. The altar was discovered during archaeological digs in 1823 [153,157]. It measures about 150 cm in length, 60 cm in width and 95 cm in height. On the front side of the altar, the god Apollo is represented with a lyre under his left arm (Fig. 54 (a)). Behind him, a Delphic tripod is visible. Apollo's head is missing: it might have been removable to put the current emperor face on the god's body [157]. Two laurels with birds are sculpted on the lateral parts of the front side. The lateral sides of the altar represent the punishment of Marsyas [154,157]. Marsyas, a double flute player, claimed to be a better musician than the god Apollo. As a punishment, Apollo sentenced him to be skinned alive. On the right lateral

side of the altar, Marsyas is hanging from a tree by his hands, waiting for his execution (Fig. 54 (b)). On the left lateral side of the altar, the executioner is sharpening his knife before skinning Marsyas alive (Fig. 54 (c)).

Fig. 54 Apollo altar displayed in the *Musée Départemental Arles Antique*. Carrara marble, end of the 1st century BC. (a) Front side, (b) lateral left side and (c) lateral right side.

On the top of the Apollo altar, two long cracks are visible. They are located at the interfaces between the middle and the lateral parts of the altar. Both cracks go through the entire width of the top of the altar (Fig. 55). They are both visible from the front side of the altar (Fig. 56 (a) and (b)) and the crack on the right side also emerges at the back of the altar (Fig. 56 (c)). The depth of these cracks in the volume of the altar is yet unknown and the curators of the *Musée Départemental Arles Antique* do not move the Apollo altar anymore fearing that its right side could break away from the rest of the altar. Thus, a better knowledge on the extent of the right-side crack in the altar volume would help the curators for the conservation of this object.

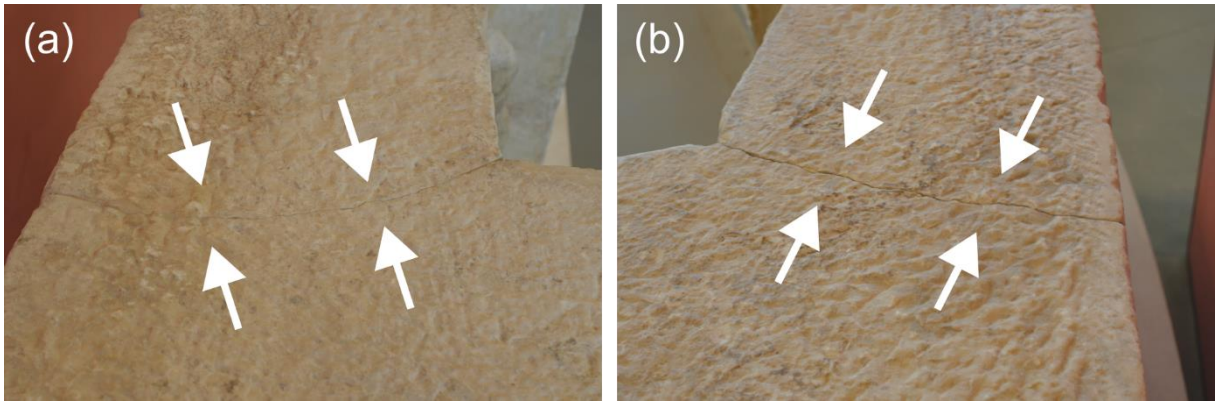

Fig. 55 Cracks on the (a) left and (b) right sides on the top of the Apollo altar. The cracks are indicated between white arrows.

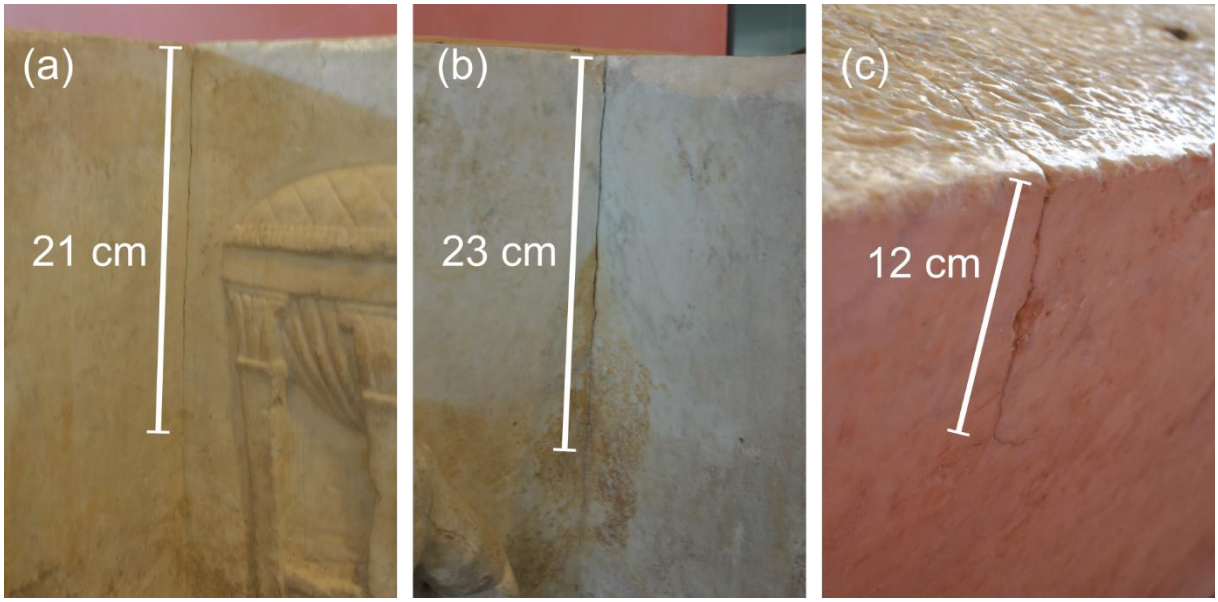

Fig. 56 Cracks from the (a, b) front (a: left-side crack, b: right-side crack) and (c) back (right-side crack) sides of the altar. The approximative length of the superficially visible parts of the cracks is indicated near the cracks in white.

3.1.3. Augustus statue

The Augustus statue (Fig. 57) was located in the upper part of the *scaenae frons* (three-level wall behind the scene, 3 in Fig. 52) in a niche. It dates from the last quarter of the 1st century BC [158]. The statue was originally a sculpture from head to feet. The only remaining parts are the head and chest of Augustus and the drapery. They were all excavated separately (in 1750 for the chest, in 1834 for the head and the drapery) and were later associated and put back together [154]. The total height of the current statue is of 2.40 m [154]. The head and chest are both made of fined-grained Carrara marble and the drapery is made of limestone from the Bois de Lens (Nîmes area, Fance) [154]. Only the marble chest was investigated in this study.

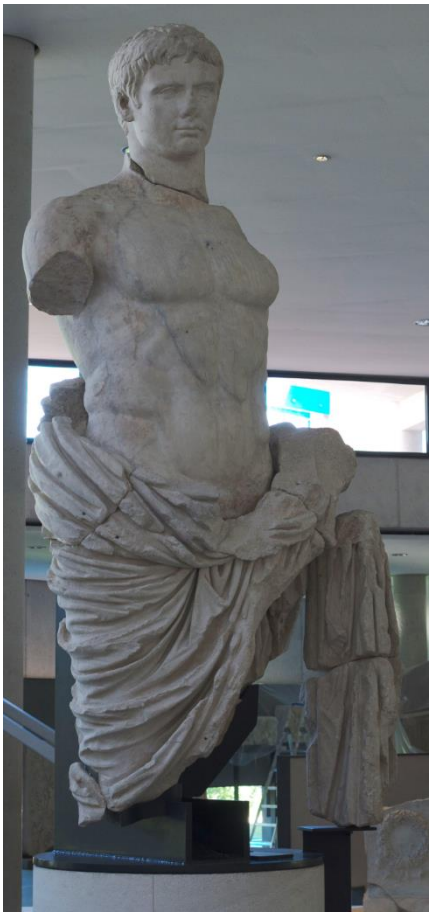

Fig. 57 Augustus statue displayed at the *Musée Départemental Arles Antique*. Carrara marble (head and chest) and limestone (drapery), last quarter of the 1st century BC.

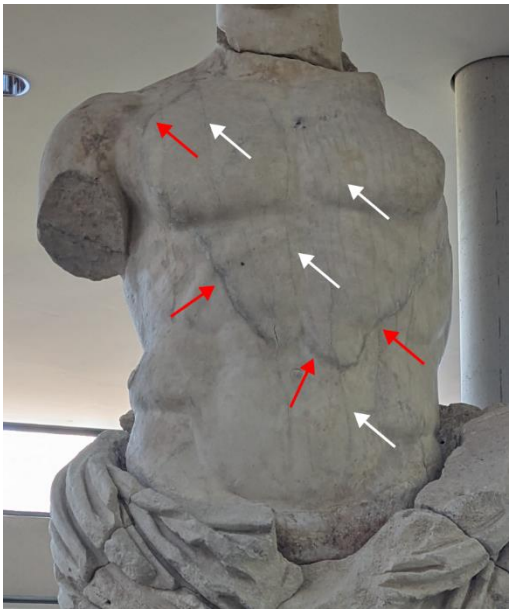

Fig. 58 Cracks and vein on Augustus statue. Some vertical cracks are indicated by white arrows and a circling vein is indicated by red arrows on the chest of the Augustus statue. Original picture by Éric Debieu (cropped and annotated).

From visual inspection, the Augustus statue appears to have a better conservation state than the Apollo altar. Indeed, the sculpture only exhibits a thick vein circling on the chest and cracks along the vertical direction that seem to be very superficial. The vein and some cracks are shown in Fig. 58. This could be the first indication of a better conservation of the Augustus statue and coincides with the relative degrees of exposure to weather conditions of both sculptures due to their relative positions in the Roman theater of Arles.

3.2. Methodology

The inner degradation state of the Apollo altar and the Augustus statue was assessed by coupling acoustic tomography to 3D photogrammetric imaging of the sculptures. The 3D photogrammetric models were used for distance measurement between transducers. The transducer positions were tracked during data acquisition in an innovative way by directly projecting the 3D photogrammetric models onto the sculptures. Indeed, the use of any markers to locate the transducers was prohibited during the study of these two archaeological objects. The transducer positions were used for distance measurements during data processing as distances on such sculptures with complex geometries cannot be accurately measured with traditional techniques, such as rule, tape measure or compass.

3.2.1. Photogrammetry

Photogrammetry is a technique enabling measurements of features of interest thanks to the use of trigonometry on overlapping photographs [159]. The technique has been developed since the mid-19th century [159]. First, photogrammetry used stereo pairs of images, which allowed performing measurements and generating models on facades for instance but not on complex buildings and objects [160]. Indeed, photogrammetric reconstruction of buildings or objects requires larger photograph datasets. In order to build a 3D model, photographs need to be taken all around the object or building of interest from different positions and angles. Nowadays, the photograph datasets are then usually analyzed by a software with automatic processes for camera calibration, feature matching and reconstruction of 3D models.

The first step in the photogrammetry process is image acquisition. An example of acquisition strategy and acquisition set-up is given in Fig. 59 (a) and (b). Nowadays, the image acquisition can be managed with a common (non-metric) camera and it is not necessary to precisely know the camera locations (1 in Fig. 59) as they are calculated afterwards by the photogrammetry software. An overlap of 60% between two spatially successive photographs is required. Control points are mandatory in order to perform measurements as they enable the future model (Fig. 59 (c)) to be scaled and a

coordinate system to be created [159,161]. Geometric control can be done with vertical and horizontal features that are already present in the object or building of interest and that have been measured precisely, or targets (3 in Fig. 59) can also be used to define the coordinate system and scale the model. The recommendations of the CIPA (International Committee of Architectural Photogrammetry) for image acquisition with non-metric cameras are the following [160,161]:

- The inner geometry has to be constant: fixed optics, no zoom, fixed focus distance,
- A homogeneous illumination of the whole object is required,
- The best quality, highest resolution, most stable and largest format camera available are recommended.

Once the acquisition is completed, the photograph dataset is processed in a photogrammetry software. The first step in software workflow is the feature matching in which each image is compared with every other image taken with a different scale and orientation to identify their common features. The most used algorithm for this procedure is the Scale-Invariant Feature Transform (SIFT) algorithm [159,162]. The relative camera positions are then calculated based on the feature matches and using trigonometry and iterative testing [159]. At this point, a sparse 3D point cloud (2 in Fig. 59) can be produced, with color values included in the point attributes. Then, a denser point cloud can be generated and wireframed or textured models (Fig. 59 (c)) can also be created.

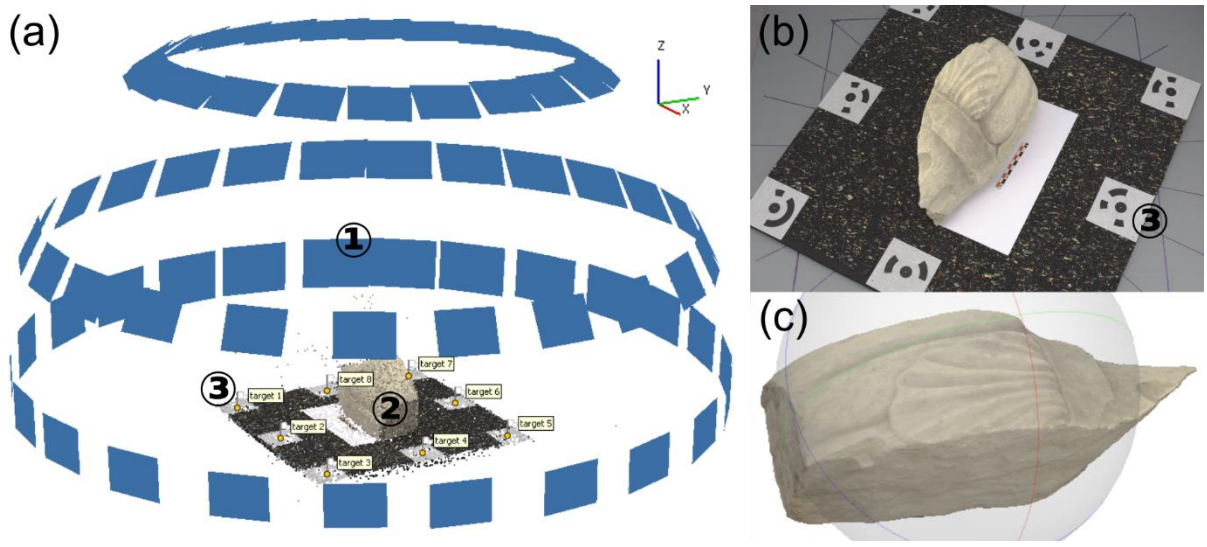

Fig. 59 Example of a photogrammetric acquisition and reconstruction. (a) Camera positions during acquisition, recalculated by the software (1, blue rectangles), and the generated point cloud (2). Here, three circular acquisitions were made around the object, at different heights and different angles. This procedure was repeated after returning the object to capture all its sides. (b) Acquisition set-up with targets (3) for coordinate system definition and scaling. (c) 3D textured model obtained after merging the point clouds for all the object configurations.

Provided that control points have been used during image acquisition, the 3D photogrammetric model of an object strictly respects its geometry. This is why photogrammetric models can be used for precise distance measurements in various fields such as archaeology, civil engineering, medicine [163–165]. 3D photogrammetric models are also used to improve data integration and graphical representation of analysis in the field of cultural heritage conservation [81,143]. The texture of the object or building of interest can also be rendered on the 3D models based on the original photographs as points from the 3D clouds are associated to color values.

In this work, photogrammetric models were used for both distance measurement and graphical representation. Distance measurement was the primary reason for using photogrammetric models as distances between ultrasound emitters and receivers are needed to perform acoustic tomography. The sculptures presented complex geometrical shapes and complex sculpted surfaces, which made it difficult to use rule, tape measure or compass for precise measurements. Other studies have used 3D photogrammetric (or lasergrammetric) models to carry out acoustic tomography [81,143,145,146]. The transducers are usually located by putting markers on the studied object [81,143,145,146,151]. However, application of stickers on the Apollo altar and the Augustus statue was prohibited due to conservation rules. Therefore, an innovative way of locating the transducer positions was tested: the 3D models were directly projected onto the sculptures in order to track and save the transducer positions on the 3D model during the measurement campaigns (see section 3.3).

3.2.2. Acoustic tomography

Acoustic tomography allows imaging the inner structure of an object. Here, travel-time tomography is used to estimate the variations of the apparent propagation velocity of longitudinal waves inside the sculptures. Inner structure and defects can be deduced from apparent velocity variation as it is influenced by the inner features crossed by ultrasonic waves: the presence of a fracture, a defect, or of fractured areas on the ultrasound path will result in a decrease of apparent velocity compared to sound zones of the object. Acoustic tomography has successfully linked low velocity zones to superficially visible features in various studies on stone cultural heritage artefacts [79,81,144,145,166]. Some studies have combined acoustic tomography and ground-penetrating radar on Egyptian sculptures and could identify fractures (filled or not with mortar) on the combined radar and tomography maps [81,144]. Other works have compared acoustic tomography results to 3D terrestrial laser scans on pillars [79]. Zones with anomalies evidenced by the laser scanning corresponded to low velocity zones and could be related to the presence of cracks or mortar-filled junctions. Studies using only acoustic tomography could also link low velocity areas to the presence of cracks [145,166].

To perform acoustic tomography, numerous positions for ultrasonic emitters and receivers are defined on the object under study and times of flight between each of them are measured. It is important to carry out a great number of measurements all around the object to maximize the object coverage by the ultrasound paths in order to accurately reconstruct propagation velocity everywhere in the object. The object is then virtually discretized into voxels. The global times of flight correspond to the sum of the partial travel-times in each voxel along the propagation path, which can be converted in terms of travelled distance and local propagation velocity:

$$t_i = \sum_{j=1}^{n} t_{ij} = \sum_{j=1}^{n} d_{ij} \frac{1}{v_j} \qquad (10)$$

where t_i is the global time of flight of the i^{th} path, t_{ij} is the partial time of flight of the i^{th} path in the j^{th} voxel, d_{ij} is the travelled distance by the i^{th} path in the j^{th} voxel, v_j is the local propagation velocity in the voxel j. The following linear system is obtained when the equations for all the emitter – receiver pairs are combined:

$$\begin{pmatrix} t_1 & t_2 & \cdots & t_m \end{pmatrix} = \begin{pmatrix} d_{11} & d_{12} & \cdots & d_{1n} \\ d_{21} & \ddots & \ddots & \vdots \\ \vdots & \ddots & \ddots & \vdots \\ d_{m1} & \cdots & \cdots & d_{mn} \end{pmatrix} \begin{pmatrix} 1/v_1 \\ 1/v_2 \\ \vdots \\ 1/v_n \end{pmatrix} \qquad (11)$$

where the t_i vector of the global times of flight and the d_{ij} matrix of distances are known and the $1/v_j$ vector of the inverse propagation velocities has to be estimated. The different components are represented graphically in two dimensions in Fig. 60.

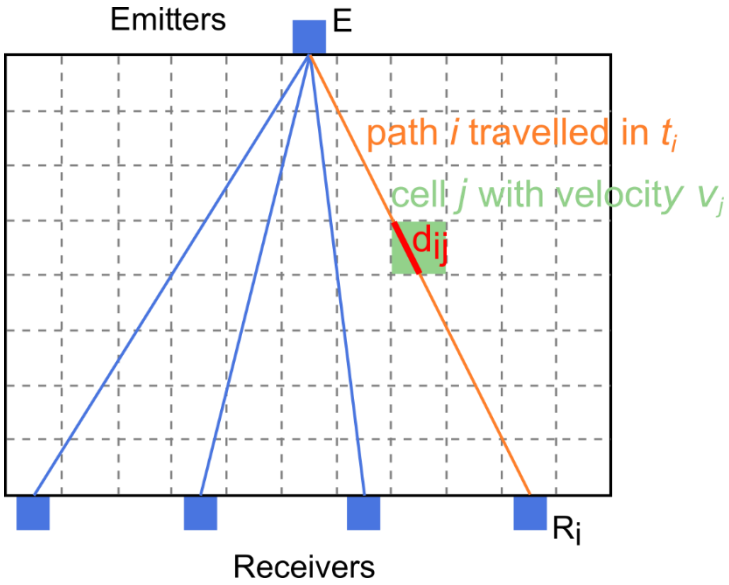

Fig. 60 2D graphical representation of the components of the system (11).

In this work, the inversion of the system (11) was managed by a simultaneous iterative reconstruction technique (SIRT). The Air Tools II Matlab package, in which several algebraic (ART) and simultaneous iterative (SIRT) reconstruction techniques are implemented, was used [167,168]. SIRT methods have been employed for various

tomography problems: cultural heritage objects [79,81,140,143–145], concrete structures [169–172], 3D distribution of water vapor [173], ionospheric electron density [174]. SIRT can solve linear systems of the following form, where the matrix A and the vector b are known, and the vector x has to be estimated:

$$A\,x = b, \qquad A \in \mathbb{R}^{m\times n}, b \in \mathbb{R}^{1\times m}, x \in \mathbb{R}^{n\times 1} \tag{12}$$

In SIRT, all the equations from the system (12) are used simultaneously in one iteration. An iteration k of these methods has the general form of:

$$x^{k+1} = x^k + \lambda_k N A^T M (b - A x^k) \tag{13}$$

where x^k and x^{k+1} are the current and new iteration of the vector x, λ_k is a relaxation parameter, A^T is the transpose of the matrix A, and M and N are symmetric positive definite matrices. Different methods can be implemented depending on the choice of the matrices M and N. Five methods are implemented in the Air Tools II Matlab package: Landweber's, Cimmino's, component averaging (CAV), diagonally relaxed orthogonal projections (DROP) and simultaneous algebraic reconstruction technique (SART) methods [167,168]. In Landweber's method, the matrices M and N are defined as the identity matrices of order m and n. In the SART method, the matrices M and N are diagonal matrices where:

$$M_{ii} = \frac{1}{\sum_{j=1}^{n} a_{ij}}, \qquad N_{jj} = \frac{1}{\sum_{i=1}^{m} a_{ij}} \tag{14}$$

In Ciminno's method, the matrix N is the identity matrix of order n. The matrix M is a diagonal matrix defined by:

$$M_{ii} = \frac{1}{m}\,\frac{1}{\sum_{j=1}^{n} a_{ij}^2} \tag{15}$$

The CAV and DROP methods are extensions of Cimmino's method. In the CAV method, the matrix N is still the identity matrix of order n. The matrix M is modified as follows:

$$M_{ii} = \frac{1}{\sum_{j=1}^{n} a_{ij}^2\, nnz_j} \tag{16}$$

where nnz_j is the number of nonzero coefficients of the column j of the matrix A. In the DROP method, the matrices M and N are in the form:

$$M_{ii} = \frac{1}{\sum_{j=1}^{n} a_{ij}^2}, \qquad N_{jj} = \frac{1}{nnz_j} \tag{17}$$

In the current case, the voxel edge size for the sculpture discretization was defined as the half of the wavelength (3 cm for both sculptures). A straight-ray tracing was assumed to compute the d_{ij} matrix of distances. This approximation is adequate for uniform materials with moderate heterogeneities. However, in materials exhibiting significant variations of propagation velocities and higher degree of heterogeneity and wave refraction, ray bending can become significant, and curved-ray tracing can be more appropriate to take these effects into account [170,175]. Nevertheless, a straight-ray tracing has allowed identifying and locating some inner defects in previous studies

[171,172,176]. Moreover, SIRT does not take diffraction into account [177], which could be a limitation in the present case considering the UPV range typical found in marble (1.5 – 5.0 km.s^{-1} for not crumbling marble), the frequency used (54 kHz) and that the studied objects are expected to contain heterogeneities. The SIRT method that was used is the CAV method as it integrates information about sparsity of the matrix A from the system (12), that is the d_{ij} matrix of distances, and this matrix is very sparse in this case.

3.3. Experimental set-ups

The experimental set-ups used for the measurement campaigns on the Apollo altar and the Augustus statue are detailed in this section. The 3D photogrammetric models had been already acquired by the *Musée Départemental Arles Antique* and were kindly provided by the curators for this work.

In both cases, times of flight were measured with a Proceq Pundit PL-2 200 device (1 in Fig. 61) combined with flat Proceq transducers of 54 kHz which have a flat circular surface contact with the object of about 4 cm in diameter. Due to their relatively large surface contact, both transducers had to be placed on sufficiently flat zones of the sculptures to enable good ultrasound emission and reception. This has sometimes limited the positioning that could be considered for both transducers, particularly on the front and lateral sides of the Apollo altar which have a lot of relief elements. The exponential Proceq transducers, which have a smaller contact surface, were not employed as they have sharp edges that could have damaged the sculptures. The measurements were carried out in direct and semi-direct transmission configurations. The travel times were manually picked on the apparatus screen by the same operator to ensure consistency. Ultrasonic gel could not be employed for ultrasound transmission between the transducers and the sculptures. Indeed, the use of such gel is not in agreement with the conservation rules of the museum as it could leave permanent visible stains on the marble surface. Instead, supple polymer films and membranes were used to improve contact between the transducers and the surface and also to protect the sculptures from direct contact with the transducers.

During both measurement campaigns, the transducer positions were not indicated by stickers on the sculpted objects, as it has been usually done in similar studies [81,143,145,146,151]. Instead, it was decided to project the 3D models of the sculptures onto them to instantaneously locate the transducer positions. During the measurement campaigns, the projection allowed replacing the emitter and the receiver back to the same positions as measurements progressed since their positions were saved and marked by points on the 3D model. During the data processing, the saved positions were used to measure distances between emitters and receivers. This new way of locating transducer positions directly on the projected 3D model was successful. Direct projection of a 3D model can be an adequate solution when markers cannot be used on sculptures to locate the transducer positions.

3.3.1. Apollo altar

The experimental set-up used during the measurement campaign on the Apollo altar is presented in Fig. 61. The wall at the back of the Apollo altar did not allow projecting the 3D model on this side of the sculpture. Therefore, a Melinex® sheet was used to locate the emitter positions at the back of the altar (2 in Fig. 61). On the front side, the 3D model was projected thanks to a projector (3 in Fig. 61). The projection gives a blurry aspect to the altar in Fig. 61. One position is marked by a combination (circled in white in Fig. 61) of a pink circle and three red, blue and green squares. The pink circle corresponds to the point location on the model and the squares are the values of the three coordinates associated automatically to the point.

Fig. 61 Experimental set-up for the measurement campaign on the Apollo altar. (1) Time-of-flight measurement apparatus, (2) Melinex® sheet to locate emitter positions at the back of the altar, (3) projector, (4) projected 3D model (gives a blurry aspect to the alter) with each position marked by a combination (circled in white) of a pink circle (point location) and red, blue and green squares (point coordinates).

The flat Proceq transducers used for the time-of-flight measurement were not directly put in contact with the Apollo altar to avoid inducing surface deterioration. In addition, finely carved surfaces were avoided as a precaution. The Melinex® sheet was used as an interface between the emitter and the altar. An Olympus polymer membrane was put between the receiver and the altar. The Proceq Pundit measuring device was calibrated with the interfaces. The transducer positions during the measurement

campaign are shown in Fig. 62 and Fig. 63: 38 positions were defined for the emitter and 36 for the receiver. In total, 560 measurements were made through the altar.

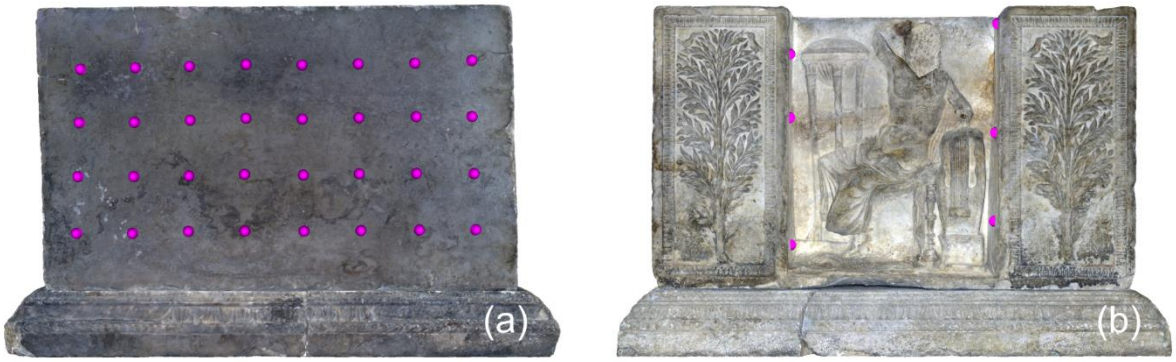

Fig. 62 Emitter positions (pink circles) on the (a) back and (b) front sides of the Apollo altar.

Fig. 63 Receiver positions (pink circles) on the (a) lateral left, (b) front and (c) lateral right sides of the Apollo altar.

3.3.2. Augustus statue

The experimental set-up used for the measurement campaign on the Augustus statue is presented in Fig. 64. The disposition of the Augustus statue in the museum room allowed projecting the 3D model on every side of the sculpture. Two projectors (1 in Fig. 64) were used simultaneously to project the model (2 in Fig. 64) on the two opposite sides. Only the state of chest of the statue was probed with acoustic tomography. The chest, which is elevated, was reached with the acoustic transducers thanks to a ladder and an elevating platform (3 and 4 in Fig. 64).

The flat Proceq transducers were once again not directly put in contact with the sculpture to avoid any surface deterioration. One Olympus polymer membranes was put between each transducer and the chest. The Proceq Pundit measuring device was calibrated with the interfaces. The transducer positions during the measurement campaign are shown in Fig. 65 and Fig. 66: 21 positions were defined for the emitter and 20 for the receiver. In total, 270 measurements were made through the sculpture.

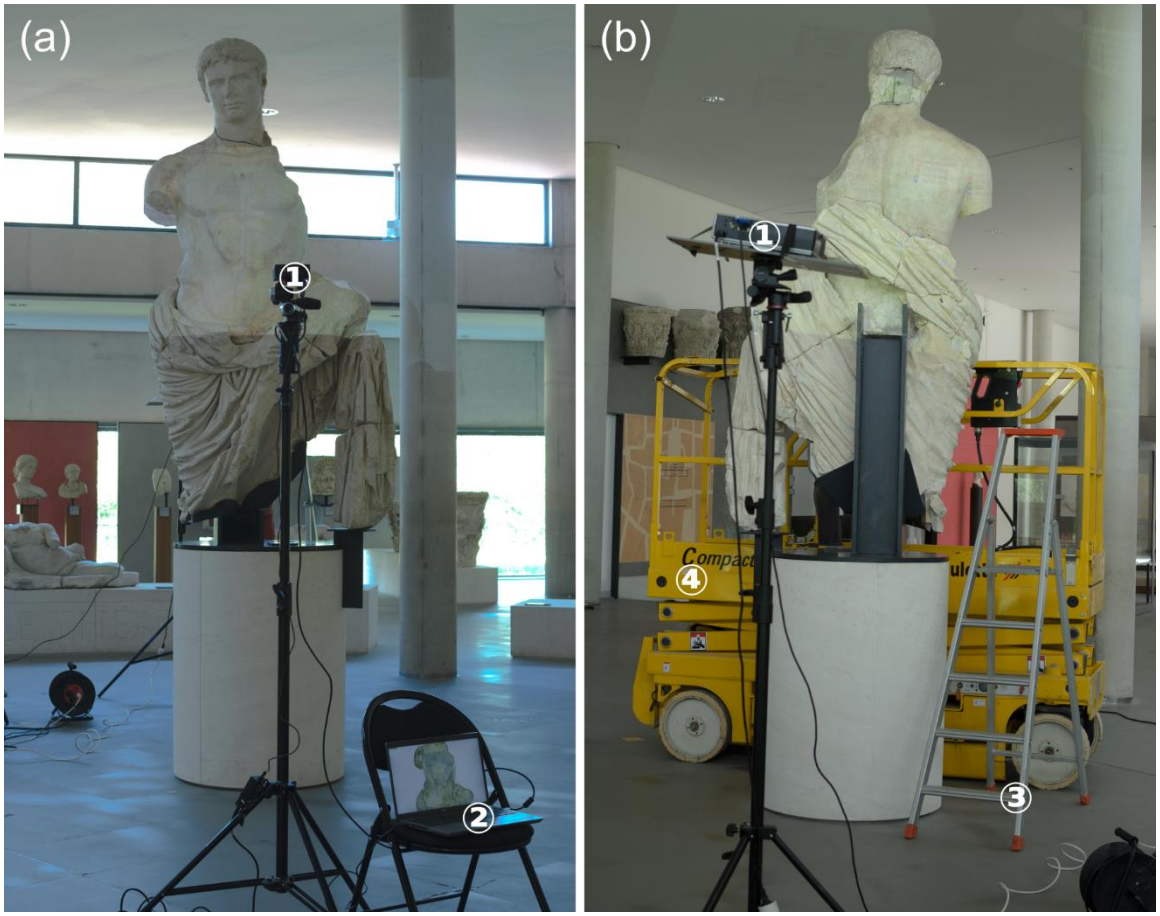

Fig. 64 Experimental set-up for the measurement campaign on the Augustus statue from the (a) front and (b) back sides. (1) Projectors, (2) computer with the 3D model, (3) ladder to access the back side, (4) elevating platform to access the front side.

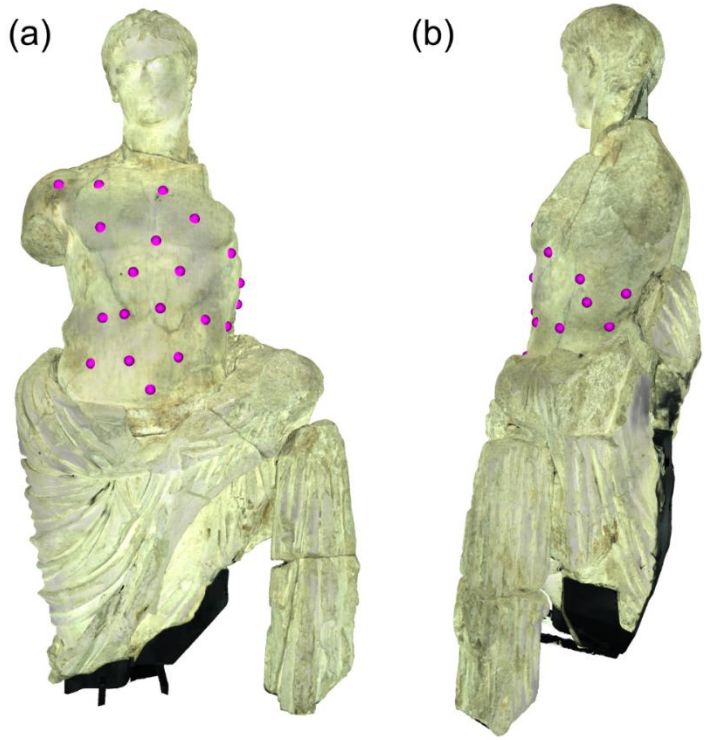

Fig. 65 Emitter positions (pink circles) on the (a) front and (b) lateral sides of the Augustus statue.

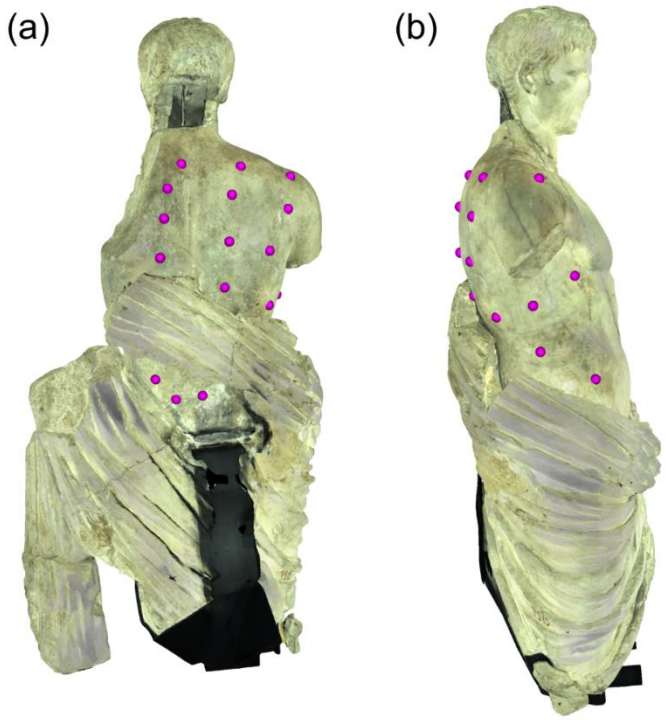

Fig. 66 Receiver positions (pink circles) on the (a) back and (b) lateral sides of the Augustus statue.

3.4. Results and discussions

The plotting of the acoustic results on the 3D models and the inversion part of the acoustic tomography were managed on Matlab (The MathWorks Inc., version: 9.12.0 (R2022a), Natick, Massachusetts, 2022). The Air Tools II Matlab package was used for the inversion (see section 3.2.2) [167,168]. The reading and plotting of the 3D model files were managed with the readObj and display_obj functions by Bernard Abayowa [178,179], and by the dispObj function by Alutsyah Luthfian modified from display_obj [180].

Different results are discussed in this section. The global degradation state of the sculptures is first evaluated through the measured apparent propagation velocities. The reconstructed 3D imaging of the propagation velocity is then examined to identify inner weaknesses. Finally local crack depth measurements are presented.

3.4.1. Apparent propagation velocities

The global apparent velocities between each emitter – receiver pair are first analyzed to assess the global cohesion state of Carrara marble in the two studied sculpted objects. The apparent velocity results are represented under two forms for both sculptures: a

histogram (Fig. 67) and a spatial representation in which every emitter – receiver pair is linked with a line colored according to Köhler UPV classes for marble (see Table 1) (Fig. 68 for the Apollo altar, Fig. 69 for the Augustus statue). These results highlight that the Augustus statue exhibits a better cohesion state compared to the Apollo altar. The apparent velocity values measured in the Augustus statue belong to damage classes 0 (fresh state) to II (granular disintegration), whereas the ones measured in the Apollo altar belong to classes I (increasing porosity) to III (fragile). The average apparent velocity of the Augustus statue is of 3.6 ± 0.6 km.s^{-1} and thus belongs to class I, while it is of 2.9 ± 0.5 km.s^{-1} in the Apollo altar and therefore belongs to the upper limit of class II. Nevertheless, none of the global apparent velocities on both sculptures belongs to class IV and only 14 measurements in the Apollo altar out of 560 belong to class III. Therefore, both objects display an acceptable cohesion state.

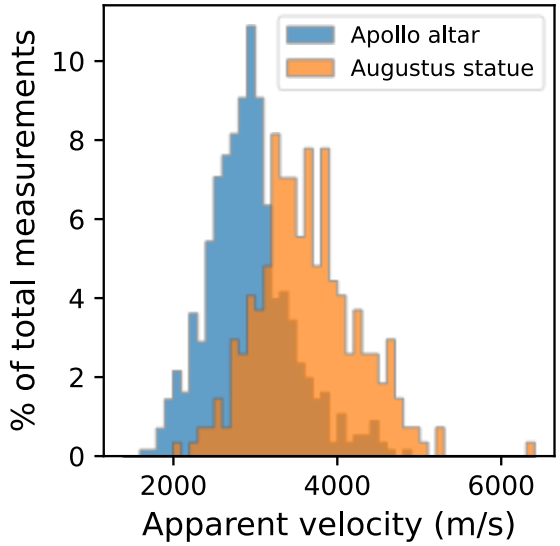

Fig. 67 Histograms of the apparent velocities in the Apollo altar (blue) and in the Augustus statue (orange).

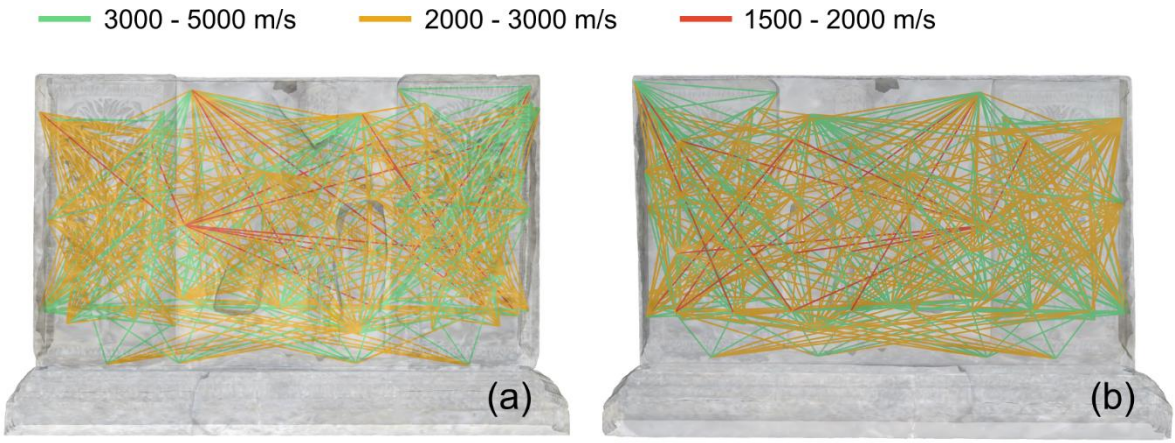

Fig. 68 Spatial representation of the apparent velocities in the Apollo altar from the (a) front and (b) back sides.

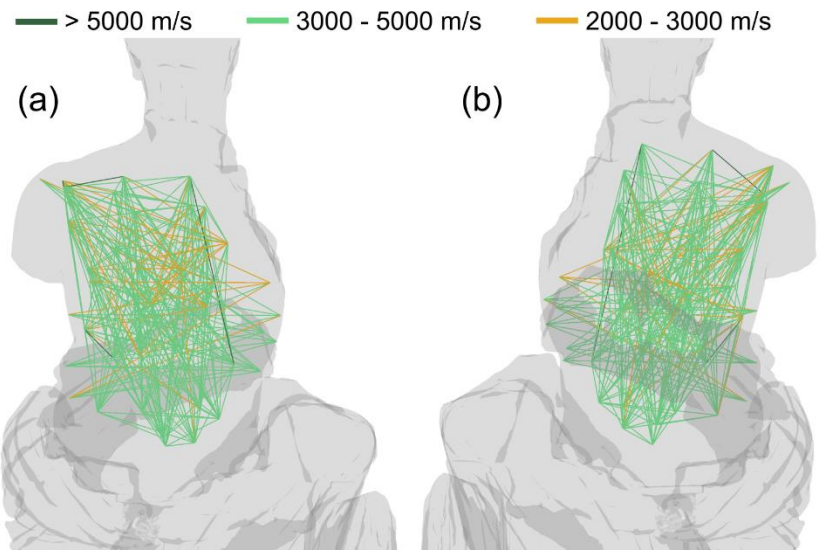

Fig. 69 Spatial representation of the apparent velocities in the Augustus statue from the (a) front and (b) back sides.

The apparent velocity results corroborate the outer visual inspections of the sculptures. The Augustus statue displays numerous cracks on its chest, but they seemed very superficial from the visual observations. On the contrary, the Apollo altar displays a lesser number of cracks on its surface but the two that cross it from back to front seemed deeper and more concerning. The apparent velocity results show that the Apollo altar is indeed more degraded in its volume than the Augustus statue.

The globally worse cohesion state of the Apollo altar compared to the Augustus statue could reflect the better disposition of the Augustus statue in the Roman theater of Arles in terms of protection against weather conditions (Fig. 52). Indeed, the Augustus statue was located in a niche that partially protected it from weathering, whereas the Apollo altar, put on ground in front of the stage, was wholly exposed to insolation and rain. Both sculptures were facing east (Fig. 52), therefore their front sides were both exposed to direct sun radiations in the morning. However, the back and lateral sides of the Augustus statue were always protected against insolation and rain by the *scaenae frons*. The back of the Apollo altar was less protected against insolation, although it must have benefited from the shade of the *scaenae frons* which was behind it. Besides, the Apollo altar was fully exposed to rain, regardless of wind direction, while the Augustus statue was only subjected to rain from the east and even in this case the impact might have been lessened by the niche. East is only the second main wind direction during the rainiest season in Arles, the main one being north. Nevertheless, no information exists on the burying conditions of the sculptures, and the precise varieties and microstructures of the Carrara marble employed in each of them are unknown. These factors could have also impacted the degradation state of these objects.

3.4.2. 3D imaging of the propagation velocity

From the global times of flight measured on the Apollo altar and the Augustus statue, a 3D imaging of the propagation velocity was reconstructed with SIRT (see section 3.2.2). The half of the wavelength was used as voxel edge size. It corresponds to approximately 3 cm for both sculptures: $\frac{2924\ m/s}{2*54\ kHz}$ for the Apollo altar and $\frac{3635\ m/s}{2*54\ kHz}$ for the Augustus statue. The entire volumes of the altar and of Augustus' chest were first discretized into cubic voxels, however only the voxels crossed by at least one emitter – receiver path were later kept for the inversion, which correspond to 7,081 voxels for the Apollo altar and to 3,533 voxels for the Augustus statue.

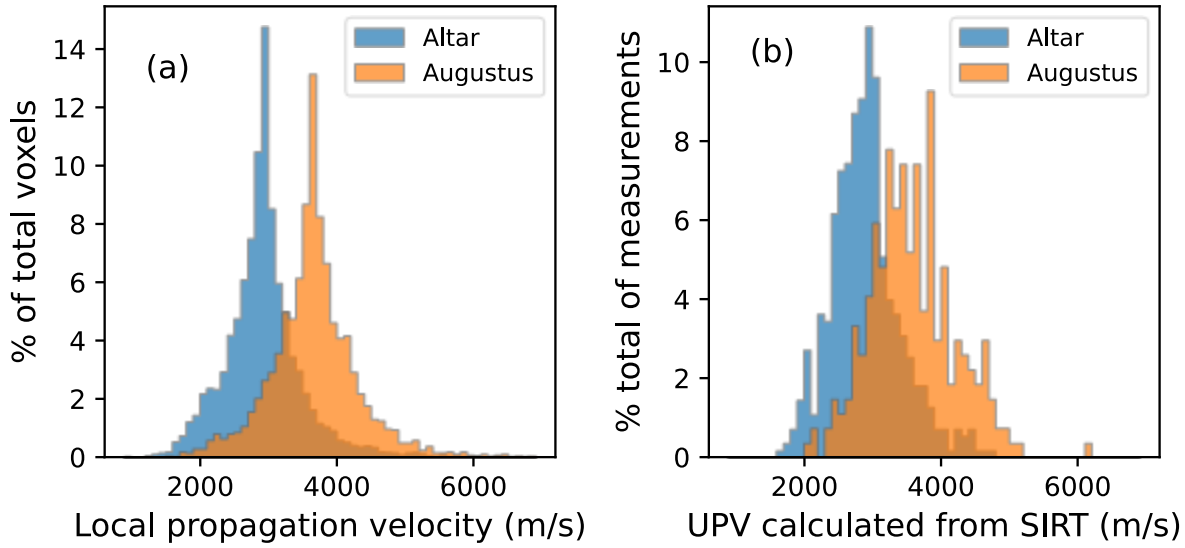

Fig. 70 Histograms of the reconstructed (a) local and (b) global propagation velocities in the Apollo altar (blue) and in the Augustus statue (orange).

The reconstructed local propagation velocities exhibited some abnormal values. Indeed, the lowest and highest calculated velocities are of 0.9 km.s^{-1} and 242.2 km.s^{-1} in the Apollo altar, and of 1.3 km.s^{-1} and 63.8 km.s^{-1} in the Augustus statue. While the lowest velocities are utterly realistic for measurements made in Carrara marble, the highest velocities do not correspond to physically reachable propagation velocities. In the plots presented in this section, the abnormal velocity values were deleted so that velocity variations can be readable on the figures. 7.0 km.s^{-1} was chosen as the upper limit for velocity values in the plots. Voxels with velocity values above this limit correspond to 0.6% and 0.8% of total voxels associated with a velocity value (voxels crossed by at least one emitter – receiver path) for the Apollo altar and the Augustus statue, respectively. Therefore, most of the reconstructed local velocities lie in a physically realistic range. The histograms of the reconstructed local velocities are given in Fig. 70 (a) for both sculpted objects. Average velocities are similar to the ones of the apparent velocity: 2.9 ± 0.6 km.s^{-1} in the Apollo altar and 3.7 ± 0.6 km.s^{-1} in the Augustus statue (without taking velocities above 7.0 km.s^{-1} into account). Thus, the tendencies

observed in the global apparent velocities of both objects (Fig. 67) are preserved in the 3D velocity reconstruction.

If the distributions from Fig. 67 and Fig. 70 (a) are compared, it can initially seem that the SIRT algorithm affects significantly the velocity distribution. However, one must bear in mind that both data do not correspond to the same kind of velocities. Fig. 70 (a) presents the local propagation velocities applying to each voxel in which the sculptures are discretized. The velocity data presented in Fig. 67 can be recalculated from the local velocities estimated with SIRT (Fig. 70 (a)) with Eq. (10). In that case, as it is shown by Fig. 70 (b), the recalculated global apparent velocities exhibit a distribution very similar to the one of the experimentally measured apparent velocities, as it could be expected considering the way the SIRT algorithm works (Eq. (11)).

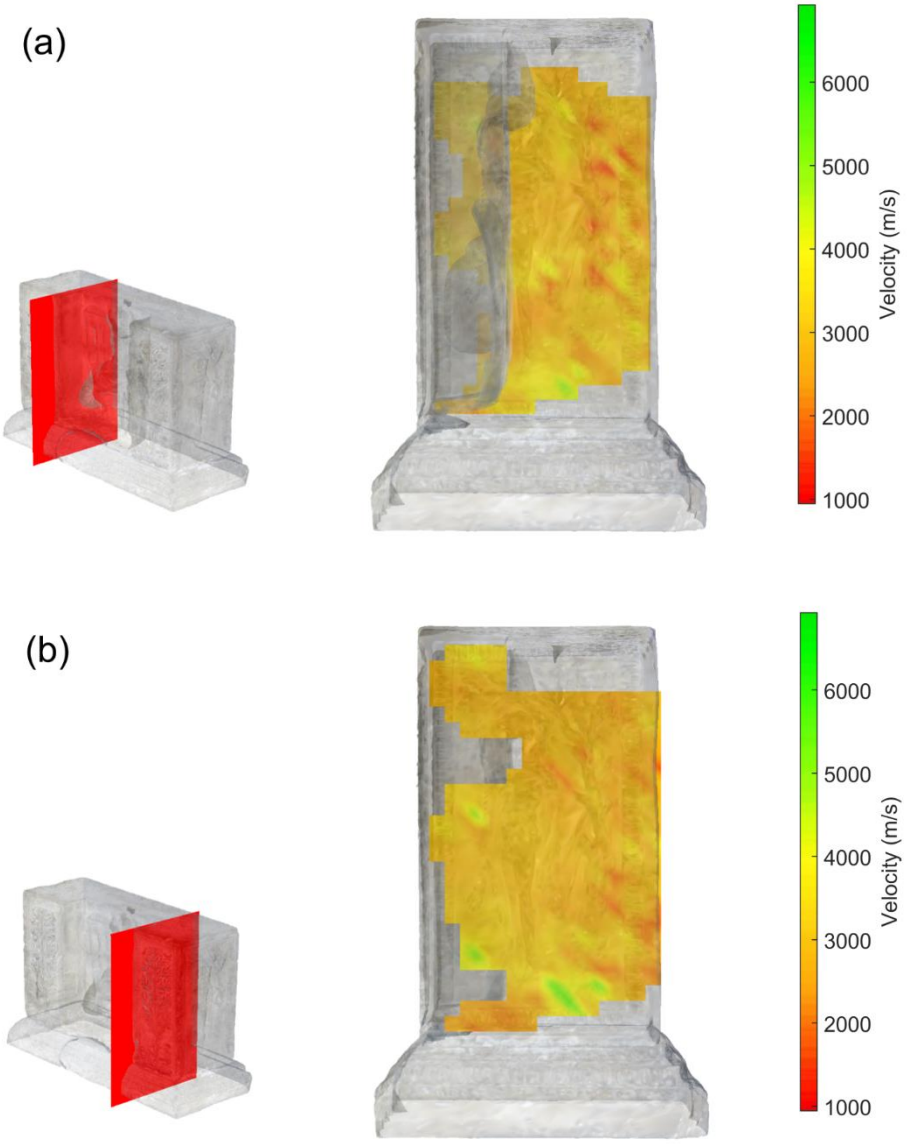

Fig. 71 Two slices in the 3D imaging of the velocity in the Apollo altar. Slice positions in the altar are indicated by the red planes on the left side. The lowest velocity values are predominantly situated at the back of the altar.

The 3D imaging of the velocity in the Apollo altar tends to indicate that the weakest zones of the sculpture are located at the back of the altar. This is visually illustrated for two slices in Fig. 71: zones with the lowest velocities prevail in the back area of the sculpture. Statistically, 57% of the velocities from class III and IV (see Table 1) are situated at the back of the altar, in the part colored in red in Fig. 72, which represents only 37% of the total altar volume. The location of the weakest areas does not coincide with the zones most exposed to weather conditions. Indeed, the front side of the altar was exposed towards the east (Fig. 52), without any protection against insolation, whereas the back of the altar was exposed towards the west but with the stage and the *scaenae frons* behind it as protections against sun radiations. Moreover, the main wind directions during the rainiest periods of the year are north and east, therefore the front and the lateral right sides of the altar should have more been exposed to rain than its back. Yet, the local propagation velocity results do not show a worse conservation of the front or lateral sides. Therefore, although the global cohesion state of the Apollo altar compared to the one of the Augustus statue can be explained by a higher degree of exposure to weather conditions, the local cohesion variations inside the altar are more difficult to grasp from this perspective. Nevertheless, the complete history of the altar is mostly unknown and the local variations of its degradation state can originate from other events.

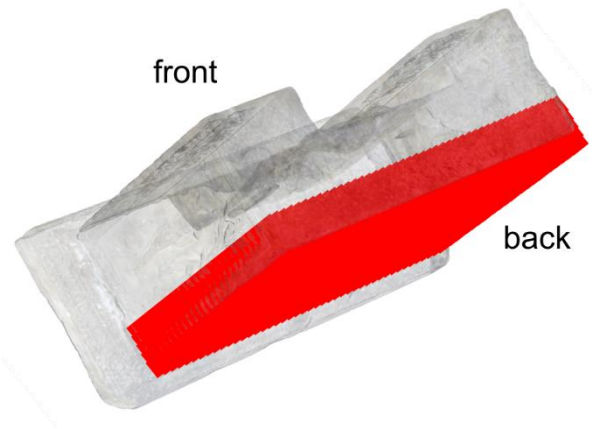

Fig. 72 Back of the altar. The zone defined as the back of the altar is colored in red.

The two long surface cracks of the Apollo altar are not highlighted by the 3D imaging of the velocity. Indeed, the crack zones presented in Fig. 55 and Fig. 56 do not coincidence with low velocity areas in the velocity cartographies. Fig. 73 shows the velocity cartography in the crack zones for the slice situated at 12 cm from the altar top surface. This slice is the nearest reconstructed slice to the top of the altar. The crack profiles at the surface are indicated in red. The lack of correlation between velocity reconstruction and crack location could be due to the presence of shallow cracks combined with the lack of measurements very near the top surface (see the emitter and receiver positions in Fig. 62 and Fig. 63). Moreover, the averaging effects of the velocity reconstruction and interpolation could have erased very local velocity variations, and the wavelength could be too high for crack detection.

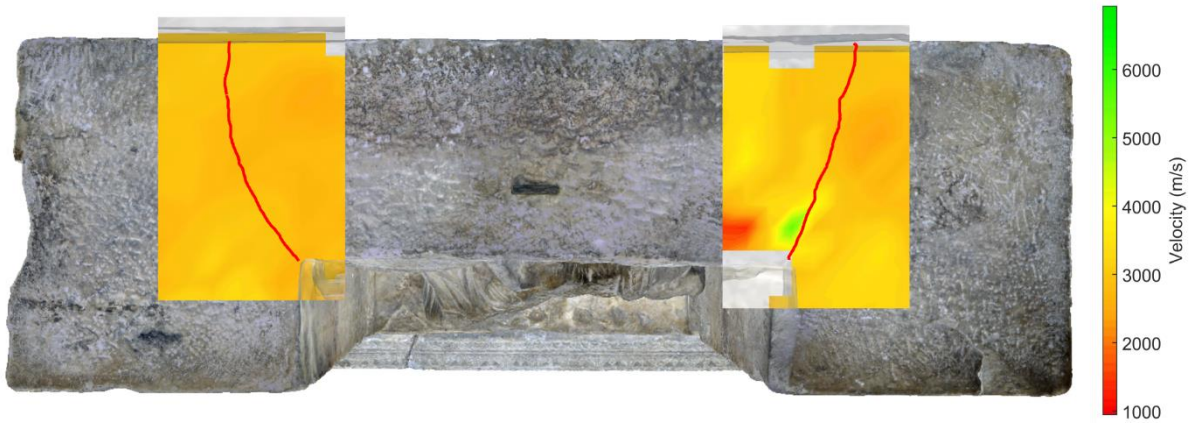

Fig. 73 Velocity values at the crack locations, 12 cm below the Apollo altar top surface. The profile of the cracks at the top surface is indicated in red.

The 3D imaging of propagation velocity in the Augustus statue does not exhibit very clear patterns of weak areas. Nevertheless, the upper part of the chest seems to contain more low velocity values than the lower part. This is illustrated in Fig. 74 on two slices made along the vertical axis. Calculations show that the upper half of the chest, which represents 57% of the reconstructed volume, comprises indeed less class 0 velocities (44%) and more class II velocities (75%) than the lower half. The upper part of the chest comprises the most part of the thick vein evidenced in Fig. 58 as well as the areas of breakage of the left arm and the head. This could explain that a higher proportion of lower velocities and a smaller proportion of higher velocities are found in this zone. Besides, more velocities from classes II and III (22% of class III velocities in the front quarter of the chest which represents 11% of the reconstructed volume) are found in the front part of the chest. This part was more subjected to weather conditions than the back of the statue since the back was protected from insolation and rain by a niche in the *scaenae frons* (Fig. 52). In addition, a lot of small cracks and a circling vein (Fig. 58) can be found on the front side of Augustus statue and could contribute to the higher proportion of low velocities in the front part of the chest. Although the cracks seem quite superficial and have not necessarily affected the sculpture deeply under the surface, they could contribute to a lesser cohesion in that part of the statue.

Therefore, this approach allows investigating the inner degradation state of marble sculptures. Tomography has provided 3D images of the velocity that are physically consistent with UPV values generally found in Carrara marble. Besides, the reconstructed 3D images of the velocity are in agreement with the tendencies observed in the punctual UPV measurements. The 3D images also correspond to the original hypotheses made on the global cohesion state of each sculpture according to their location in the Roman theater of Arles. Some uncertainties on the reconstruction accuracy still remain since the actual inner state of both sculpted objects is mostly unknown. Moreover, surface cracks do not stand out in the 3D imaging, which could indicate a lack of accuracy but also result from a lack of sufficient inner extent of these defects.

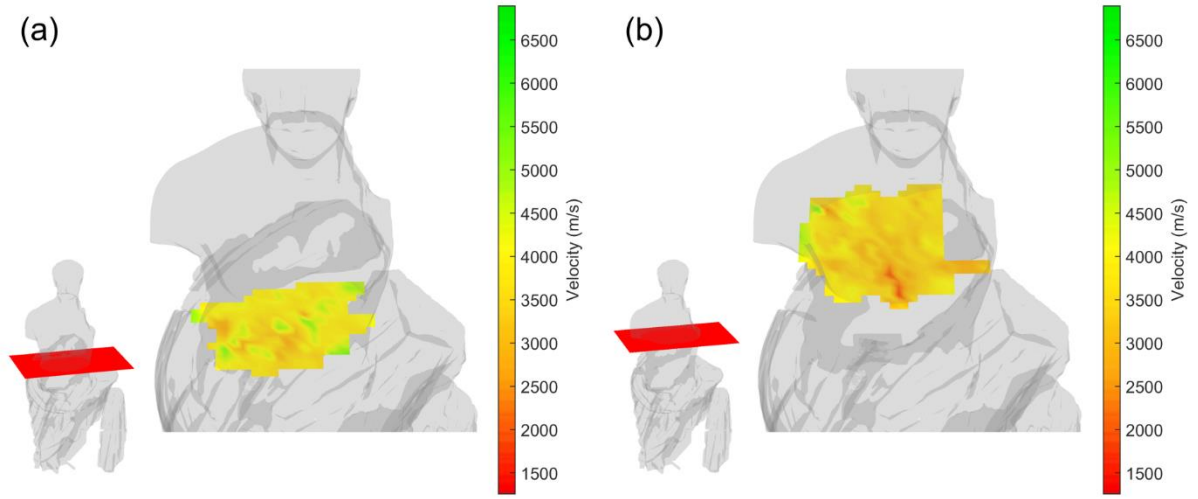

Fig. 74 Two slices in the 3D imaging of the velocity in the Augustus statue. Slice positions in the statue are indicated by the red planes on the left sides. A higher proportion of low velocity zones are noticeable on the (b) subfigure and a higher proportion of high velocity zones on the (a) subfigure.

3.4.3. Crack depth

As stated in the previous section (3.4.2), the cracks noticeable on the top surface of the Apollo altar (see section 3.1.2) are not highlighted in the 3D imaging of the velocity. The crack zones do not coincide with significantly lower propagation velocity values. Therefore, crack depths were estimated independently, with another ultrasonic technique.

The crack depth measurement method is illustrated in Fig. 75. It consisted in measuring the times of flight between a fixed emitter (E in Fig. 75) and a receiver (R in Fig. 75) placed at increasing distances from the emitter, before and after the crack [78,181]. The relationship between the time of flight and the emitter – receiver distance is linear when the receiver is placed before the crack as ultrasonic waves propagate in a homogenous material (green curve in Fig. 75). At the crack position, the time of flight generally suddenly increases, and when the receiver is placed beyond the crack the relationship between the time of flight and the distance can be approximated by a polynomial law (orange curve in Fig. 75). The crack depth h is estimated by the following equation:

$$h = \frac{L}{2}\left(\frac{T_2}{T_1} - \frac{T_1}{T_2}\right) \quad (18)$$

where L is the distance between the emitter and the crack, T_1 and T_2 are the times of flight obtained at the crack position L from the linear and the polynomial fits. It can be assumed that this method allows crack depth detection for depths above the diffraction limit (half of the wavelength) which is of approximately 3 cm in this case.

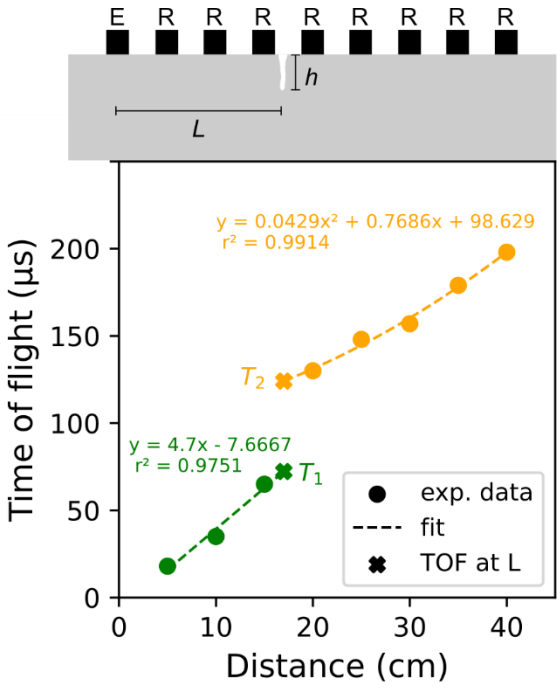

Fig. 75 Method for the estimation of the crack depth *h*. T_1 and T_2 are the times of flight obtained at the crack position *L* (here, *L* = 17 cm) from the linear and polynomial fits, respectively before and after the crack. Here, a depth *h* of 10 cm may be deduced.

Here, crack depths were evaluated at different points along the cracks, thus crack profiles could be estimated. The different positions at which the depth was measured on both cracks are shown in Fig. 76. The deduced crack geometries are schematized in Fig. 77. The first three experimental data of the left-side crack and the experimental data of the right-side crack were fitted with polynomial laws.

The crack depth profiles show that the right-side crack is more concerning than the left-side crack. Indeed, on the left-side crack a jump in the time of flight was only measured at the first measurement position. The relationship between the time of flight and the distance was always linear at the other measurement positions, which points out that this crack is very superficial far from the front of the altar (probably shallower than 3 cm).

The estimated depth profile of the right-side crack has an asymmetrical bell shape with local extrema reached at the front and back sides of the altar. Thus, the crack depth measurements show that the right-side crack has not yet propagated through the entire height of the altar. Therefore, the altar parts on both sides of the crack remain linked to each other. Nevertheless, moving the altar could increase the crack propagation and result in fracture. Numerical simulation of the crack mechanical behavior in different displacement situations could provide a clearer view on the risks associated to these altar displacements.

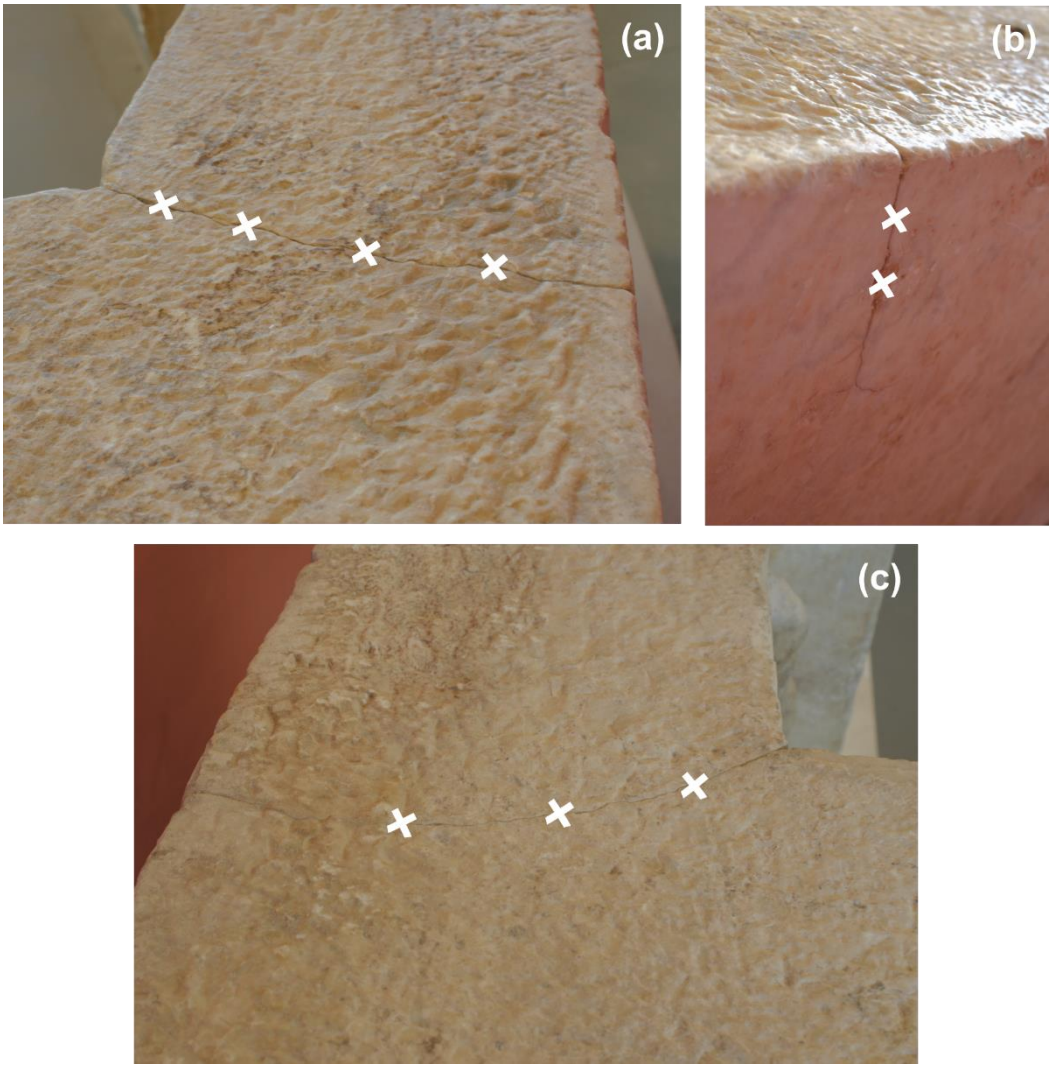

Fig. 76 Measurement positions. Positions on the Apollo altar at which the depths of the (a), (b) right-side and (c) left-side cracks were estimated. The right-side crack depth was estimated (a) on the top and (b) at the back of the Apollo altar.

When comparing the estimated crack depths (Fig. 77) with the velocity cartography at the crack zones (Fig. 73), it can be noticed that at 12 cm from the top surface both cracks should be present at the front of the Apollo altar according to the estimated depth profiles. However, the front part of the right-side crack coincides with a high velocity zone on the velocity cartography and the velocity in the zone of the left-side crack is very uniform. Therefore, the presence of both cracks cannot be correlated to the variations of the reconstructed local propagation velocities. This lack of correlation may be due to the acquisition, reconstruction or interpolation procedures, or it could reflect that the cracks do not significantly impact the mechanical integrity of the altar.

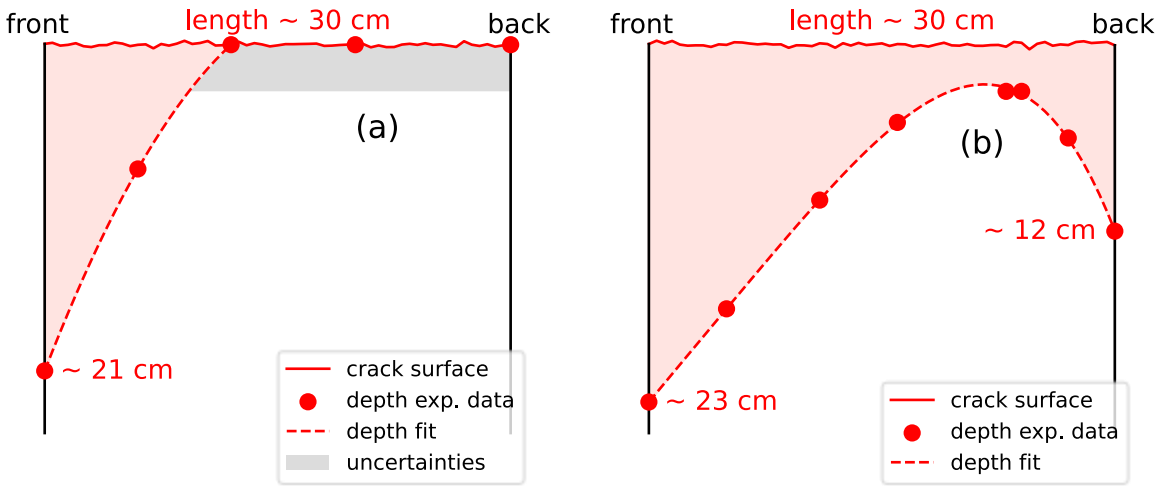

Fig. 77 Crack depth estimation. (a) Left-side and (b) right-side crack depth estimations based on several punctual depth measurements along the crack lengths. The left-side crack first three experimental data and the right-side crack experimental data were fitted with polynomial laws.

3.5. Conclusion on the degradation at the sculpture scale

Carrara marble degradation at the sculpture scale was investigated by means of acoustic tomography coupled to photogrammetry. The objects under study were two archaeological pieces, the Apollo altar and the Augustus statue, exposed outdoors in the Roman theater of Arles for several centuries but with different degrees of exposure to weather conditions. Acoustic tomography and 3D photogrammetric models were combined to reconstruct 3D cartographies of ultrasound propagation velocity inside the sculptures in order to assess their inner degradation state and to evaluate the extent of some superficially visible alterations.

In this work, an innovative procedure is applied to locate the measurement points on the 3D photogrammetric models. Indeed, the photogrammetric models were directly projected onto the objects instead of using stickers. The measurement positions were tracked and saved on the models during the measurement campaigns. The direct projection of the 3D models is an adequate solution in cases in which markers cannot be sticked on the sculped objects.

The results of acoustic tomography show that both sculptures have a correct global cohesion state, although the Apollo altar exhibits a worse cohesion state than the Augustus statue. The difference in the degradation state of both objects corroborates the

visual inspections of both sculptures and is in agreement with their degrees of exposure to weather conditions in Roman times. Indeed, due to their respective location in the Roman theater, the Apollo altar was more subjected to weather conditions than the Augustus statue. The previous chapter highlighted the significant impact of thermal and thermo-hygric weathering on Carrara marble degradation state. Here, the Apollo altar was more subjected to insolation, rain and wind than the Augustus statue which was partially protected in a niche. The Apollo altar is also the more degraded of the two sculptures. The repeated exposure to thermal variations and to rain could thus be responsible for the worse global cohesion state of the Apollo altar compared to the Augustus statue.

3D imaging of the propagation velocity enabled to identify some more degraded areas at the back of the Apollo altar and in the front and upper parts of the Augustus statue. The front part of the statue was, like the altar, more subjected to weather fluctuations than its other parts. Moreover, several breakages and the presence of a thick vein can explain the worse degradation state of the upper half of the statue. Regarding the cohesion state of the back of the altar, it does not coincidence with the areas the most exposed to weather conditions. Therefore, the local cohesion variations within the altar could be explained by other events occurring in its mostly unknown history.

Depth profiles of the Apollo altar cracks were estimated independently of the 3D imaging of the propagation velocity. The left-side crack is mostly superficial except at the very front of the altar. Therefore, the estimated profiles confirmed that the most worrying crack is the right-side one as the curators thought. Nevertheless, the right-side crack has not yet crossed the altar along all its height, and the middle and lateral parts of the altar still hold together. The two cracks were not detected in the 3D imaging, which could come from averaging effects during reconstruction and interpolation, from ill-adapted tomography procedures, or from a too small impact of these cracks on the mechanical integrity of the altar.

The acoustic tomography procedures could be improved in future works by using higher frequency transducers and by exploring curved ray tracing strategies. Further work is also needed to link the inner cohesion state reconstructed by acoustic tomography to surface defects. Moreover, photogrammetric and tomographic data could be reused in complementary numerical simulations. Such simulations could help evaluate risks of crack propagation or of mechanical failure associated with sculpture displacement, for instance.

General conclusion and perspectives

Carrara marble is widely used in built and statuary cultural heritage, in ancient and recent works. Yet, it can develop various forms of alteration over time, which can result in cracks, deformation, loss of mechanical strength. One of the alteration factors responsible for these deteriorations are weather conditions. For instance, marble is known to be extremely sensitive to thermal variations. The identification and comprehension of marble alterations is essential to provide adequate conservation and restoration of marble artefacts.

In this context, this thesis aimed at characterizing and imaging Carrara marble degradation at multiple scales by means of acoustic techniques which have the advantage of being non-destructive and therefore of meeting the requirements of the field of cultural heritage conservation. Among all alteration forms, this work focused on Carrara marble weathering, and particularly on exposure to thermal and hygric variations, by investigating both artificially weathered laboratory samples and naturally weathered sculptures.

The thermo-hygric weathering of Carrara marble was first studied in laboratory experiments on artificially weathered samples. Their mechanical decay was monitored by nonlinear resonant ultrasound spectroscopy (NRUS) through the evolution of the resonant frequency f_0 and of the nonlinear parameter α. These evolutions were linked to an increasing porosity, a widening of intergranular spaces and a loss of mechanical strength occurring in Carrara marble upon thermal weathering. This study indicated that thermal alteration impact is measurable in Carrara marble after only one heating cycle up to a temperature as low as 40 °C which is commonly reached at marble surface under natural outdoor exposure. Besides, Carrara marble decay is mainly impacted by the first stages of exposure to thermal or thermo-hygric fluctuations. Thermal alteration is able to completely disintegrate marble at temperatures close to 500 °C, whereas hygric variations alone do not induce permanent weakening in this material regardless of its thermal damage degree. Finally, thermo-hygric cycling has a greater impact on Carrara marble damage than thermal cycling alone. These results highlight the vulnerability of Carrara marble to outdoor exposure and the difficulties to preserve Carrara marble artefacts from the early stages of decay due to environmental temperature and humidity variations. These climatic variations are able to weaken marble mechanical properties by widening intergranular spaces and could make possible the action of more harmful degradation agents such as acid rain, salt crystallization, micro-organisms, etc. Climate change and global warming could worsen such phenomena in the future. For instance, the risk of Carrara marble thermal weathering is predicted to increase in some parts of the world such as in the Mediterranean area.

The NRUS method is not traditionally employed in the field of cultural heritage conservation but has proved to efficiently monitor mechanical properties of marble samples during cycling. The nonlinear parameter α exhibits a greater sensitivity to marble decay than linear parameters such as the resonant frequency f_0 or the ultrasonic pulse velocity. Moreover, thanks to the nonlinear parameter α, NRUS provides information on the material microcracking state, in addition to classically studied information on stiffness brought by the resonant frequency f_0.

Regarding the perspectives for future laboratory studies, NRUS could be applied to the investigation of other conservation issues to overcome problems of sample scarcity and of stone property variability from one sample to another. The two NRUS parameters could bring insights on the thermo-hygric behavior of other cultural heritage stones and on other conservation issues such as the durability and effectiveness of consolidation treatments, or the effects of soluble salt crystallization-dissolution cycles.

Carrara marble decay was then investigated on two archaeological sculptures from the Roman theater of Arles. A non-destructive diagnosis was implemented by coupling acoustic tomography and 3D photogrammetric imaging of the sculptures. Contrary to other similar studies, the 3D photogrammetric models were directly projected onto the objects under study to locate measurement positions as the measurement campaign progressed. The results showed different degradation degrees in the two archaeological pieces, which coincidences with their dissimilar exposure to weather conditions for several centuries in the Roman theater. However, some superficial defects with inner extension could not be identified in the 3D imaging of the propagation velocity.

Therefore, the tomography procedures could be optimized in future works in order to link inner velocity variations to surface defects. The study of inner alterations on sculpted objects thanks to tomography coupled to photogrammetry will be investigated further during the DEMOS project, supported by the *Fondation des Sciences du Patrimoine* (FSP) and led by the *Centre Interdisciplinaire de Conservation et de Restauration du Patrimoine* (CICRP), the MAP-Gamsau laboratory and the *Laboratoire de Mécanique et d'Acoustique* (LMA). The project will be an opportunity to optimize the acquisition and reconstruction protocols (acquisition at other frequencies, straight or curved-ray strategies, reconstruction algorithms) and to explore the potential of the use of lasers for tomography. Indeed, a proof of concept in laboratory on very small sculpted samples is planned to study the ability of generating and receiving wave by lasers without damaging the stone. The use of laser instead of contact transducers could enable wave amplitude to be measured and reconstructed in addition to propagation velocity, and both parameters could be combined and correlated. Ultimately, these techniques could be decision-support tools for curators and could also provide explanatory media for the public.

Bibliography

[1] E.M. Winkler, Stone in Architecture, Springer Berlin Heidelberg, Berlin, Heidelberg, 1997. https://doi.org/10.1007/978-3-662-10070-7.

[2] J.W. Anthony, R.A. Bideaux, K.W. Bladh, M.C. Nichols, Eds., Handbook of Mineralogy, Mineralogical Society of America, Chantilly, VA 20151-1110, USA, n.d. http://www.handbookofmineralogy.org/.

[3] T. Weiss, P.N.J. Rasolofosaon, S. Siegesmund, Ultrasonic wave velocities as a diagnostic tool for the quality assessment of marble, Geol. Soc. Lond. Spec. Publ. 205 (2002) 149–164. https://doi.org/10.1144/GSL.SP.2002.205.01.12.

[4] S. Siegesmund, T. Weiss, E.K. Tschegg, Control of marble weathering by thermal expansion and rock fabrics, in: Proc. 9th Int. Congr. Deterioration Conserv. Stone, Venice, 2000: pp. 205–213. https://doi.org/10.1016/B978-044450517-0/50102-1.

[5] S. Siegesmund, J. Ruedrich, A. Koch, Marble bowing: comparative studies of three different public building facades, Environ. Geol. 56 (2008) 473–494. https://doi.org/10.1007/s00254-008-1307-z.

[6] M. Meccheri, G. Molli, P. Conti, P. Blasi, L. Vaselli, The Carrara Marbles (Alpi Apuane, Italy): a geological and economical updated review, Z. Dtsch. Ges. Für Geowiss. 158 (2007) 719–736. https://doi.org/10.1127/1860-1804/2007/0158-0719.

[7] P. Primavori, Carrara Marble: a nomination for 'Global Heritage Stone Resource' from Italy, Geol. Soc. Lond. Spec. Publ. 407 (2015) 137–154. https://doi.org/10.1144/SP407.21.

[8] ICOMOS-ISCS, Illustrated glossary on stone deterioration patterns - Glossaire illustré sur les formes d'altération de la pierre, Paris, 2008.

[9] A.Z. Miller, P. Sanmartín, L. Pereira-Pardo, A. Dionísio, C. Saiz-Jimenez, M.F. Macedo, B. Prieto, Bioreceptivity of building stones: A review, Sci. Total Environ. 426 (2012) 1–12. https://doi.org/10.1016/j.scitotenv.2012.03.026.

[10] C.M. Ek, La dissolution du carbonate de calcium, Bull. Société Géographique Liège 9 (1973) 55–87.

[11] X. Cai, Z. Zhou, K. Liu, X. Du, H. Zang, Water-Weakening Effects on the Mechanical Behavior of Different Rock Types: Phenomena and Mechanisms, Appl. Sci. 9 (2019) 4450. https://doi.org/10.3390/app9204450.

[12] R. Bugini, M.L. Tabasso, M. Realini, Rate of formation of black crusts on marble. A case study, J. Cult. Herit. 1 (2000) 111–116. https://doi.org/10.1016/S1296-2074(00)00161-8.

[13] F. Wang, Y. Fu, D. Li, Y. Huang, S. Wei, Study on the mechanism of the black crust formation on the ancient marble sculptures and the effect of pollution in Beijing area, Heliyon 8 (2022) e10442. https://doi.org/10.1016/j.heliyon.2022.e10442.

[14] P. Maravelaki-Kalaitzaki, Black crusts and patinas on Pentelic marble from the Parthenon and Erechtheum (Acropolis, Athens): characterization and origin, Anal. Chim. Acta 532 (2005) 187–198. https://doi.org/10.1016/j.aca.2004.10.065.

[15] D. Mitsos, V. Kantarelou, E. Palamara, A.G. Karydas, N. Zacharias, E. Gerasopoulos, Characterization of black crust on archaeological marble from the Library of Hadrian in Athens and inferences about contributing pollution sources, J. Cult. Herit. 53 (2022) 236–243. https://doi.org/10.1016/j.culher.2021.12.003.

[16] A. Chabas, D. Jeannette, Weathering of marbles and granites in marine environment: petrophysical properties and special role of atmospheric salts, Environ. Geol. 40 (2001) 359–368. https://doi.org/10.1007/s002540000157.
[17] L.C. Jerwood, D.A. Robinson, R.B.G. Williams, Experimental frost and salt weathering of chalk—II, Earth Surf. Process. Landf. 15 (1990) 699–708. https://doi.org/10.1002/esp.3290150804.
[18] D.A. Lienhart, The Geographic Distribution of Intensity and Frequency of Freeze-Thaw Cycles, Environ. Eng. Geosci. xxv (1988) 465–469. https://doi.org/10.2113/gseegeosci.xxv.4.465.
[19] S. Taber, Frost Heaving, J. Geol. 37 (1929) 428–461. https://doi.org/10.1086/623637.
[20] T. Han, J. Shi, Y. Chen, X. Cao, Physical and Mechanical Properties of Marble under the Combined Effects of Chemical Solutions and Freeze–Thaw Cycles, Geotech. Test. J. 40 (2017) 1057–1070. https://doi.org/10.1520/GTJ20160225.
[21] X. Luo, S. Zhou, B. Huang, N. Jiang, M. Xiong, Effect of Freeze–Thaw Temperature and Number of Cycles on the Physical and Mechanical Properties of Marble, Geotech. Geol. Eng. 39 (2021) 567–582. https://doi.org/10.1007/s10706-020-01513-0.
[22] J. Ondrasina, D. Kirchner, S. Siegesmund, Freeze-thaw cycles and their influence on marble deterioration: a long-term experiment, Geol. Soc. Lond. Spec. Publ. 205 (2002) 9–18. https://doi.org/10.1144/GSL.SP.2002.205.01.02.
[23] B. Vasarhelyi, K. Ledniczky, Influence of water-saturation and weathering on mechanical properties of Sivac marble, in: Paris, France, 1999: pp. 691–694.
[24] K. Malaga-Starzec, U. Åkesson, J.E. Lindqvist, B. Schouenborg, Microscopic and macroscopic characterization of the porosity of marble as a function of temperature and impregnation, Constr. Build. Mater. 20 (2006) 939–947. https://doi.org/10.1016/j.conbuildmat.2005.06.016.
[25] S. Siegesmund, K. Ullemeyer, T. Weiss, E.K. Tschegg, Physical weathering of marbles caused by anisotropic thermal expansion, Int. J. Earth Sci. 89 (2000) 170–182. https://doi.org/10.1007/s005310050324.
[26] B. Grelk, P. Goltermann, B. Schouenborg, A. Koch, L. Alneas, The laboratory testing of potential bowing and expansion of marble, in: Proc. Int. Conf. Dimens. Stone, Taylor & Francis Group plc, A.A. Balkerma Publische, Prague, Czech Republic, 2004: pp. 253–259.
[27] A. Zeisig, S. Siegesmund, T. Weiss, Thermal expansion and its control on the durability of marbles, Geol. Soc. Lond. Spec. Publ. 205 (2002) 65–80. https://doi.org/10.1144/GSL.SP.2002.205.01.06.
[28] A.M. Ferrero, M. Migliazza, A. Spagnoli, Theoretical modelling of bowing in cracked marble slabs under cyclic thermal loading, Constr. Build. Mater. 23 (2009) 2151–2159. https://doi.org/10.1016/j.conbuildmat.2008.12.015.
[29] Y. Mahmutoglu, Mechanical Behaviour of Cyclically Heated Fine Grained Rock, Rock Mech. Rock Eng. 31 (1998) 169–179. https://doi.org/10.1007/s006030050017.
[30] Y. Mahmutoğlu, The effects of strain rate and saturation on a micro-cracked marble, Eng. Geol. 82 (2006) 137–144. https://doi.org/10.1016/j.enggeo.2005.09.001.
[31] A.M. Ferrero, P. Marini, Experimental Studies on the Mechanical Behaviour of two Thermal Cracked Marbles, Rock Mech. Rock Eng. 34 (2001) 57–66. https://doi.org/10.1007/s006030170026.
[32] E. Sassoni, E. Franzoni, Influence of porosity on artificial deterioration of marble and limestone by heating, Appl. Phys. A 115 (2014) 809–816. https://doi.org/10.1007/s00339-013-7863-4.

[33] B. Sena Da Fonseca, A.P. Ferreira Pinto, S. Piçarra, B. Caldeira, M.F. Montemor, Consolidating efficacy of diammonium hydrogen phosphate on artificially aged and naturally weathered coarse-grained marble, J. Cult. Herit. 51 (2021) 145–156. https://doi.org/10.1016/j.culher.2021.08.003.
[34] B. Schouenborg, B. Grelk, K. Malaga, K. Hoigard, M. Scheffler, S.W. Dean, Testing and Assessment of Marble and Limestone (TEAM)—Important Results from a Large European Research Project on Cladding Panels, J. ASTM Int. 4 (2007) 100855. https://doi.org/10.1520/JAI100855.
[35] H.A. Viles, Microclimate and weathering in the central Namib Desert, Namibia, Geomorphology 67 (2005) 189–209. https://doi.org/10.1016/j.geomorph.2004.04.006.
[36] K. Malaga, J.E. Lindqvist, B. Schouenborg, Experimental study on the variation in porosity of marble as a function of temperature, Geol. Soc. Lond. Spec. Publ. 205 (2002) 81–88. https://doi.org/10.1144/GSL.SP.2002.205.01.07.
[37] T. Waragai, Influence of thermal cycling in the mild temperature range on the physical properties of cultural stones, J. Cult. Herit. 59 (2023) 171–180. https://doi.org/10.1016/j.culher.2022.12.001.
[38] B. Grelk, C. Christiansen, B. Schouenborg, K. Malaga, K. Hoigard, M. Scheffler, S.W. Dean, Durability of Marble Cladding—A Comprehensive Literature Review, J. ASTM Int. 4 (2007) 100857. https://doi.org/10.1520/JAI100857.
[39] U. Åkesson, J.E. Lindqvist, B. Schouenborg, B. Grelk, Relationship between microstructure and bowing properties of calcite marble claddings, Bull. Eng. Geol. Environ. 65 (2006) 73–79. https://doi.org/10.1007/s10064-005-0026-x.
[40] A. Koch, S. Siegesmund, The combined effect of moisture and temperature on the anomalous expansion behaviour of marble, Environ. Geol. 46 (2004). https://doi.org/10.1007/s00254-004-1037-9.
[41] P. Marini, R. Bellopede, Bowing of marble slabs: Evolution and correlation with mechanical decay, Constr. Build. Mater. 23 (2009) 2599–2605. https://doi.org/10.1016/j.conbuildmat.2009.02.010.
[42] P. Marini, R. Bellopede, The Influence of the Climatic Factors on the Decay of Marbles: an Experimental Study, Am. J. Environ. Sci. 3 (2007) 143–150. https://doi.org/10.3844/ajessp.2007.143.150.
[43] D.W. Kessler, Physical and chemical tests on the commercial marbles of the United States, Department of Commerce, 1919.
[44] E. Sassoni, G. Graziani, G. Ridolfi, M.C. Bignozzi, E. Franzoni, Thermal behavior of Carrara marble after consolidation by ammonium phosphate, ammonium oxalate and ethyl silicate, Mater. Des. 120 (2017) 345–353. https://doi.org/10.1016/j.matdes.2017.02.040.
[45] J. Peng, G. Rong, Z. Tang, S. Sha, Microscopic characterization of microcrack development in marble after cyclic treatment with high temperature, Bull. Eng. Geol. Environ. 78 (2019) 5965–5976. https://doi.org/10.1007/s10064-019-01494-2.
[46] K.S.W. Sing, Reporting physisorption data for gas/solid systems with special reference to the determination of surface area and porosity (Recommendations 1984), Pure Appl. Chem. 57 (1985) 603–619. https://doi.org/10.1351/pac198557040603.
[47] D.A. Rose, Water movement in porous materials: Part 2 - The separation of the components of water movement, Br. J. Appl. Phys. 14 (1963) 491–496. https://doi.org/10.1088/0508-3443/14/8/310.
[48] J. Berthonneau, Rôle des minéraux argileux dans la dégradation de la pierre. Application à la conservation de la “Pierre du Midi” en termes de durabilité et compatibilité des matériaux en oeuvre, Aix-Marseille Université, 2013.

[49] B. Rousset Tournier, Transferts par capillarité et évaporation dans des roches - Rôle des structures de porosité, Université Louis Pasteur - Strasbourg I, 2001.
[50] K.S.W. Sing, R.T. Williams, Physisorption Hysteresis Loops and the Characterization of Nanoporous Materials, Adsorpt. Sci. Technol. 22 (2004) 773–782. https://doi.org/10.1260/0263617053499032.
[51] K.E.-A. Van Den Abeele, Influence of water saturation on the nonlinear elastic mesoscopic response in Earth materials and the implications to the mechanism of nonlinearity, J. Geophys. Res. 107 (2002) 2121. https://doi.org/10.1029/2001JB000368.
[52] Y. Zeng, C. Fan, D.D. Do, D. Nicholson, Evaporation from an Ink-Bottle Pore: Mechanisms of Adsorption and Desorption, Ind. Eng. Chem. Res. 53 (2014) 15467–15474. https://doi.org/10.1021/ie500215x.
[53] P. Phadungbut, D.D. Do, D. Nicholson, On the microscopic origin of the hysteresis loop in closed end pores – Adsorbate restructuring, Chem. Eng. J. 285 (2016) 428–438. https://doi.org/10.1016/j.cej.2015.10.008.
[54] F. Cherblanc, J. Berthonneau, P. Bromblet, Role of hydro-mechanical coupling in the damage process of limestones used in historical buildings, in: Glasgow, United-Kingdom, 2016.
[55] J. Berthonneau, P. Bromblet, F. Cherblanc, E. Ferrage, J.-M. Vallet, O. Grauby, The spalling decay of building bioclastic limestones of Provence (South East of France): From clay minerals swelling to hydric dilation, J. Cult. Herit. 17 (2016) 53–60. https://doi.org/10.1016/j.culher.2015.05.004.
[56] S. Siegesmund, R. Snethlage, eds., Stone in Architecture: Properties, Durability, Springer Berlin Heidelberg, Berlin, Heidelberg, 2014. https://doi.org/10.1007/978-3-642-45155-3.
[57] E. Ilin, M. Marchevsky, I. Burkova, M. Pak, A. Bezryadin, Nanometer-Scale Deformations of Berea Sandstone Under Moisture-Content Variations, Phys. Rev. Appl. 13 (2020) 024043. https://doi.org/10.1103/PhysRevApplied.13.024043.
[58] M.L. Lin, F.S. Jeng, L.S. Tsai, T.H. Huang, Wetting weakening of tertiary sandstones—microscopic mechanism, Environ. Geol. 48 (2005) 265–275. https://doi.org/10.1007/s00254-005-1318-y.
[59] X. Li, K. Peng, J. Peng, D. Hou, Experimental investigation of cyclic wetting-drying effect on mechanical behavior of a medium-grained sandstone, Eng. Geol. 293 (2021) 106335. https://doi.org/10.1016/j.enggeo.2021.106335.
[60] H. Li, Y. Qiao, R. Shen, M. He, T. Cheng, Y. Xiao, J. Tang, Effect of water on mechanical behavior and acoustic emission response of sandstone during loading process: phenomenon and mechanism, Eng. Geol. 294 (2021) 106386. https://doi.org/10.1016/j.enggeo.2021.106386.
[61] E. Verstrynge, R. Adriaens, J. Elsen, K. Van Balen, Multi-scale analysis on the influence of moisture on the mechanical behavior of ferruginous sandstone, Constr. Build. Mater. 54 (2014) 78–90. https://doi.org/10.1016/j.conbuildmat.2013.12.024.
[62] F. Cherblanc, J. Berthonneau, P. Bromblet, V. Huon, Influence of Water Content on the Mechanical Behaviour of Limestone: Role of the Clay Minerals Content, Rock Mech. Rock Eng. 49 (2016) 2033–2042. https://doi.org/10.1007/s00603-015-0911-y.
[63] S. Taibi, A. Duperret, J.-M. Fleureau, The effect of suction on the hydro-mechanical behaviour of chalk rocks, Eng. Geol. 106 (2009) 40–50. https://doi.org/10.1016/j.enggeo.2009.02.012.
[64] Á. Török, B. Vásárhelyi, The influence of fabric and water content on selected rock mechanical parameters of travertine, examples from Hungary, Eng. Geol. 115 (2010) 237–245. https://doi.org/10.1016/j.enggeo.2010.01.005.

[65] Á. Rabat, M. Cano, R. Tomás, Effect of water saturation on strength and deformability of building calcarenite stones: Correlations with their physical properties, Constr. Build. Mater. 232 (2020) 117259. https://doi.org/10.1016/j.conbuildmat.2019.117259.
[66] Á. Rabat, R. Tomás, M. Cano, Evaluation of mechanical weakening of calcarenite building stones due to environmental relative humidity using the vapour equilibrium technique, Eng. Geol. 278 (2020) 105849. https://doi.org/10.1016/j.enggeo.2020.105849.
[67] S. Yasar, Long term wetting characteristics and saturation induced strength reduction of some igneous rocks, Environ. Earth Sci. 79 (2020) 353. https://doi.org/10.1007/s12665-020-09105-0.
[68] E.M. Van Eeckhout, The mechanisms of strength reduction due to moisture in coal mine shales, Int. J. Rock Mech. Min. Sci. Geomech. Abstr. 13 (1976) 61–67. https://doi.org/10.1016/0148-9062(76)90705-1.
[69] J. Zhu, J. Deng, F. Chen, Y. Huang, Z. Yu, Water Saturation Effects on Mechanical and Fracture Behavior of Marble, Int. J. Geomech. 20 (2020) 04020191. https://doi.org/10.1061/(ASCE)GM.1943-5622.0001825.
[70] S. Siegesmund, J. Menningen, V. Shushakova, Marble decay: towards a measure of marble degradation based on ultrasonic wave velocities and thermal expansion data, Environ. Earth Sci. 80 (2021) 395. https://doi.org/10.1007/s12665-021-09654-y.
[71] Yu.V. Yastrebov, V.V. Kostyleva, V.A. Nikolaev, M.S. Barilko, Practical application of UWB georadar technique for investigations of cultural heritage objects, in: 2010 5th Int. Confernce Ultrawideband Ultrashort Impulse Signals, IEEE, Sevastopol, Ukraine, 2010: pp. 171–173. https://doi.org/10.1109/UWBUSIS.2010.5609152.
[72] N.P. Avdelidis, A. Moropoulou, Applications of infrared thermography for the investigation of historic structures, J. Cult. Herit. 5 (2004) 119–127. https://doi.org/10.1016/j.culher.2003.07.002.
[73] E.T. Delegou, M. Krokida, N.P. Avdelidis, A. Moropoulou, Assessment of cleaning interventions on marble surfaces using pulsed thermography, in: Emerg. Technol. Non-Destr. Test. V, Taylor&Francis Group, CRC Press, London, 2012: pp. 31–36.
[74] K. Mouhoubi, V. Detalle, J.-M. Vallet, J.-L. Bodnar, Improvement of the Non-Destructive Testing of Heritage Mural Paintings Using Stimulated Infrared Thermography and Frequency Image Processing, J. Imaging 5 (2019) 72. https://doi.org/10.3390/jimaging5090072.
[75] N. Ludwig, E. Rosina, A. Sansonetti, Evaluation and monitoring of water diffusion into stone porous materials by means of innovative IR thermography techniques, Measurement 118 (2018) 348–353. https://doi.org/10.1016/j.measurement.2017.09.002.
[76] Y. Peng, Q. Lin, M. He, C. Zhu, H. Zhang, P. Guo, Experimental Study on Infrared Temperature Characteristics and Failure Modes of Marble with Prefabricated Holes under Uniaxial Compression, Energies 14 (2021) 713. https://doi.org/10.3390/en14030713.
[77] W. Köhler, Untersuchungen zu Verwitterungsvorgängen an Carrara-Marmor in Potsdam-Sanssouci, Berichte Zu Forsch. Prax. Denkmalpfl. Dtschl. Steinschäden-Steinkonservierung 2 (1991) 50–53.
[78] G. Pascale, A. Lolli, Crack assessment in marble sculptures using ultrasonic measurements: Laboratory tests and application on the statue of David by Michelangelo, J. Cult. Herit. 16 (2015) 813–821. https://doi.org/10.1016/j.culher.2015.02.005.
[79] S. Fais, G. Casula, F. Cuccuru, P. Ligas, M.G. Bianchi, An innovative methodology for the non-destructive diagnosis of architectural elements of ancient historical buildings, Sci. Rep. 8 (2018) 4334. https://doi.org/10.1038/s41598-018-22601-5.

[80] J. Ruedrich, C. Knell, J. Enseleit, Y. Rieffel, S. Siegesmund, Stability assessment of marble statuaries of the Schlossbrücke (Berlin, Germany) based on rock strength measurements and ultrasonic wave velocities, Environ. Earth Sci. 69 (2013) 1451–1469. https://doi.org/10.1007/s12665-013-2246-x.
[81] C. Colombero, P. Dabove, N. Grasso, F. Khosro Anjom, F. Pace, S. Aicardi, Microgeophysics and geomatics data integration reveals the internal fracturing conditions of the statue of Ramses II (Museo Egizio, Torino, Italy), Sci. Rep. 12 (2022) 9933. https://doi.org/10.1038/s41598-022-14300-z.
[82] A. Migliori, J.L. Sarrao, Resonant ultrasound spectroscopy: applications to physics, materials measurements, and nondestructive evaluation, Wiley, New York, 1997.
[83] M.C. Remillieux, T.J. Ulrich, C. Payan, J. Rivière, C.R. Lake, P.-Y. Le Bas, Resonant ultrasound spectroscopy for materials with high damping and samples of arbitrary geometry: RUS FOR ARBITRARY SHAPE AND HIGH DAMPING, J. Geophys. Res. Solid Earth 120 (2015) 4898–4916. https://doi.org/10.1002/2015JB011932.
[84] T. Ulrich, K.R. McCall, R.A. Guyer, Determination of elastic moduli of rock samples using resonant ultrasound spectroscopy, J. Acoust. Soc. Am. 111 (2002) 1667–1674. https://doi.org/10.1121/1.1463447.
[85] C. Payan, T.J. Ulrich, P.Y. Le Bas, T. Saleh, M. Guimaraes, Quantitative linear and nonlinear resonance inspection techniques and analysis for material characterization: Application to concrete thermal damage, J. Acoust. Soc. Am. 136 (2014) 537–546. https://doi.org/10.1121/1.4887451.
[86] S.-J. Park, H.J. Yim, H.-G. Kwak, Nonlinear resonance vibration method to estimate the damage level on heat-exposed concrete, Fire Saf. J. 69 (2014) 36–42. https://doi.org/10.1016/j.firesaf.2014.07.003.
[87] K. Van Den Abeele, J. De Visscher, Damage assessment in reinforced concrete using spectral and temporal nonlinear vibration techniques, Cem. Concr. Res. 30 (2000) 1453–1464. https://doi.org/10.1016/S0008-8846(00)00329-X.
[88] K. Van Den Abeele, P.Y. Le Bas, B. Van Damme, T. Katkowski, Quantification of material nonlinearity in relation to microdamage density using nonlinear reverberation spectroscopy: Experimental and theoretical study, J. Acoust. Soc. Am. 126 (2009) 963–972. https://doi.org/10.1121/1.3184583.
[89] K.E.-A. Van Den Abeele, J. Carmeliet, J.A. Ten Cate, P.A. Johnson, Nonlinear Elastic Wave Spectroscopy (NEWS) Techniques to Discern Material Damage, Part II: Single-Mode Nonlinear Resonance Acoustic Spectroscopy, Res. Nondestruct. Eval. 12 (2000) 31–42. https://doi.org/10.1080/09349840009409647.
[90] M.-L. Chavazas, P. Bromblet, J. Berthonneau, J. Hénin, C. Payan, Impact of relative humidity variations on Carrara marble mechanical properties investigated by nonlinear resonant ultrasound spectroscopy, Constr. Build. Mater. 431 (2024) 136529. https://doi.org/10.1016/j.conbuildmat.2024.136529.
[91] M.-L. Chavazas, P. Bromblet, J. Berthonneau, J. Hénin, C. Payan, Progressive thermal decohesion in Carrara marble monitored with nonlinear resonant ultrasound spectroscopy, Bull. Eng. Geol. Environ. 83 (2024). https://doi.org/10.1007/s10064-024-03875-8.
[92] P.A. Johnson, B. Zinszner, P. Rasolofosaon, F. Cohen-Tenoudji, K. Van Den Abeele, Dynamic measurements of the nonlinear elastic parameter α in rock under varying conditions: NONLINEAR ELASTIC PARAMETER IN ROCK, J. Geophys. Res. Solid Earth 109 (2004). https://doi.org/10.1029/2002JB002038.
[93] R.A. Guyer, P.A. Johnson, Nonlinear Mesoscopic Elasticity: Evidence for a New Class of Materials, Phys. Today 52 (1999) 30–36. https://doi.org/10.1063/1.882648.
[94] P. Johnson, A. Sutin, Slow dynamics and anomalous nonlinear fast dynamics in diverse solids, J. Acoust. Soc. Am. 117 (2005) 124–130. https://doi.org/10.1121/1.1823351.

[95] L.A. Ostrovsky, P.A. Johnson, Dynamic nonlinear elasticity in geomaterials, Riv. Nuovo Cimento 24 (2001) 1–46. https://doi.org/10.1007/BF03548898.
[96] P. Rasolofosaon, B. Zinszner, P.A. Johnson, Propagation des ondes élastiques dans les matériaux non linéaires Aperçu des résultats de laboratoire obtenus sur les roches et des applications possibles en géophysique, Rev. Inst. Fr. Pétrole 52 (1997) 585–608. https://doi.org/10.2516/ogst:1997061.
[97] S. Maier, J.-Y. Kim, M. Forstenhäusler, J.J. Wall, L.J. Jacobs, Noncontact nonlinear resonance ultrasound spectroscopy (NRUS) for small metallic specimens, NDT E Int. 98 (2018) 37–44. https://doi.org/10.1016/j.ndteint.2018.04.003.
[98] S.M. Hogg, B.E. Anderson, P.-Y. Le Bas, M.C. Remillieux, Nonlinear resonant ultrasound spectroscopy of stress corrosion cracking in stainless steel rods, NDT E Int. 102 (2019) 194–198. https://doi.org/10.1016/j.ndteint.2018.12.007.
[99] S. Haupert, S. Guérard, F. Peyrin, D. Mitton, P. Laugier, Non Destructive Characterization of Cortical Bone Micro-Damage by Nonlinear Resonant Ultrasound Spectroscopy, PLoS ONE 9 (2014) e83599. https://doi.org/10.1371/journal.pone.0083599.
[100] M. Muller, A. Sutin, R. Guyer, M. Talmant, P. Laugier, P.A. Johnson, Nonlinear resonant ultrasound spectroscopy (NRUS) applied to damage assessment in bone, J. Acoust. Soc. Am. 118 (2005) 3946–3952. https://doi.org/10.1121/1.2126917.
[101] M. Meo, U. Polimeno, G. Zumpano, Detecting Damage in Composite Material Using Nonlinear Elastic Wave Spectroscopy Methods, Appl. Compos. Mater. 15 (2008) 115–126. https://doi.org/10.1007/s10443-008-9061-7.
[102] Q. Wei, L. Zhu, J. Zhu, L. Zhuo, W. Hao, W. Xie, Characterization of impact fatigue damage in CFRP composites using nonlinear acoustic resonance method, Compos. Struct. 253 (2020) 112804. https://doi.org/10.1016/j.compstruct.2020.112804.
[103] R.A. Guyer, K.R. McCall, G.N. Boitnott, Hysteresis, Discrete Memory, and Nonlinear Wave Propagation in Rock: A New Paradigm, Phys. Rev. Lett. 74 (1995) 3491–3494. https://doi.org/10.1103/PhysRevLett.74.3491.
[104] R.A. Guyer, K.R. McCall, G.N. Boitnott, L.B. Hilbert, T.J. Plona, Quantitative implementation of Preisach-Mayergoyz space to find static and dynamic elastic moduli in rock, J. Geophys. Res. Solid Earth 102 (1997) 5281–5293. https://doi.org/10.1029/96JB03740.
[105] K.R. McCall, R.A. Guyer, Equation of state and wave propagation in hysteretic nonlinear elastic materials, J. Geophys. Res. Solid Earth 99 (1994) 23887–23897. https://doi.org/10.1029/94JB01941.
[106] L.A. Ostrovsky, P.A. Johnson, Nonlinear dynamics of rock: Hysteretic behavior, Radiophys. Quantum Electron. 44 (2001) 450–464. https://doi.org/10.1023/A:1017953331645.
[107] J.A. TenCate, P.A. Johnson, Nonlinear Resonant Ultrasound Spectroscopy: Assessing Global Damage, in: T. Kundu (Ed.), Nonlinear Ultrason. Vibro-Acoust. Tech. Nondestruct. Eval., Springer International Publishing, Cham, 2019: pp. 89–101. https://doi.org/10.1007/978-3-319-94476-0_2.
[108] K.E.-A. Van Den Abeele, A. Sutin, J. Carmeliet, P.A. Johnson, Micro-damage diagnostics using nonlinear elastic wave spectroscopy (NEWS), NDT E Int. 34 (2001) 239–248. https://doi.org/10.1016/S0963-8695(00)00064-5.
[109] V. Genovés, A. Carrión, D. Escobar, J. Gosálbez, J. Monzó, M.V. Borrachero, J. Payá, Nonlinear Acoustic Spectroscopy and Frequency Sweep Ultrasonics: Case on Thermal Damage Assessment in Mortar, J. Nondestruct. Eval. 38 (2019) 61. https://doi.org/10.1007/s10921-019-0599-0.
[110] L. Gao, P. Shokouhi, J. Rivière, Effect of Grain Shape and Relative Humidity on the Nonlinear Elastic Properties of Granular Media, Geophys. Res. Lett. 50 (2023) e2023GL103245. https://doi.org/10.1029/2023GL103245.

[111] L. Gao, P. Shokouhi, J. Rivière, Effect of relative humidity on the nonlinear elastic response of granular media, J. Appl. Phys. 131 (2022) 055101. https://doi.org/10.1063/5.0073967.
[112] V.S. Averbakh, V.V. Bredikhin, A.V. Lebedev, S.A. Manakov, Nonlinear acoustic spectroscopy of carbonate rocks, Acoust. Phys. 63 (2017) 346–358. https://doi.org/10.1134/S1063771017030022.
[113] M.C. Remillieux, R.A. Guyer, C. Payan, T.J. Ulrich, Decoupling Nonclassical Nonlinear Behavior of Elastic Wave Types, Phys. Rev. Lett. 116 (2016) 115501. https://doi.org/10.1103/PhysRevLett.116.115501.
[114] C. Mechri, M. Scalerandi, M. Bentahar, Separation of Damping and Velocity Strain Dependencies using an Ultrasonic Monochromatic Excitation, Phys. Rev. Appl. 11 (2019) 054050. https://doi.org/10.1103/PhysRevApplied.11.054050.
[115] M. Muller, J.A. Tencate, T.W. Darling, A. Sutin, R.A. Guyer, M. Talmant, P. Laugier, P.A. Johnson, Bone micro-damage assessment using non-linear resonant ultrasound spectroscopy (NRUS) techniques: A feasibility study, Ultrasonics 44 (2006) e245–e249. https://doi.org/10.1016/j.ultras.2006.06.043.
[116] F. Bouchaala, C. Payan, V. Garnier, J.P. Balayssac, Carbonation assessment in concrete by nonlinear ultrasound, Cem. Concr. Res. 41 (2011) 557–559. https://doi.org/10.1016/j.cemconres.2011.02.006.
[117] M. Bentahar, H. El Aqra, R. El Guerjouma, M. Griffa, M. Scalerandi, Hysteretic elasticity in damaged concrete: Quantitative analysis of slow and fast dynamics, Phys. Rev. B 73 (2006) 014116. https://doi.org/10.1103/PhysRevB.73.014116.
[118] M. Lott, M.C. Remillieux, V. Garnier, T.J. Ulrich, P.-Y. Le Bas, A. Deraemaeker, C. Dumoulin, C. Payan, Fracture processes imaging in concrete using nonlinear ultrasound, NDT E Int. 120 (2021) 102432. https://doi.org/10.1016/j.ndteint.2021.102432.
[119] J. Chen, A.R. Jayapalan, J.-Y. Kim, K.E. Kurtis, L.J. Jacobs, Rapid evaluation of alkali–silica reactivity of aggregates using a nonlinear resonance spectroscopy technique, Cem. Concr. Res. 40 (2010) 914–923. https://doi.org/10.1016/j.cemconres.2010.01.003.
[120] D.N. Fahse, K.M. Scott Levy, J.-Y. Kim, L.J. Jacobs, Comparison of changes in nonclassical (α) and classical (β) acoustic nonlinear parameters due to thermal aging of 9Cr–1Mo ferritic martensitic steel, NDT E Int. 110 (2020) 102226. https://doi.org/10.1016/j.ndteint.2020.102226.
[121] T. Ohtani, Y. Ishii, Nonlinear Resonant Ultrasound Spectroscopy (NRUS) applied to fatigue damage evaluation in a pure copper, in: Tokyo, Japan, 2012: pp. 203–206. https://doi.org/10.1063/1.4749331.
[122] J. Jin, P. Shokouhi, Nonlinear Resonant Ultrasonic Spectroscopy (NRUS) for Monitoring Fatigue Crack Growth in Aluminum, Res. Nondestruct. Eval. 33 (2022) 4–16. https://doi.org/10.1080/09349847.2021.2017530.
[123] C. Payan, V. Garnier, J. Moysan, Effect of water saturation and porosity on the nonlinear elastic response of concrete, Cem. Concr. Res. 40 (2010) 473–476. https://doi.org/10.1016/j.cemconres.2009.10.021.
[124] J.A. Ten Cate, T.J. Shankland, Slow dynamics in the nonlinear elastic response of Berea sandstone, Geophys. Res. Lett. 23 (1996) 3019–3022. https://doi.org/10.1029/96GL02884.
[125] J. Rivière, P. Shokouhi, R.A. Guyer, P.A. Johnson, A set of measures for the systematic classification of the nonlinear elastic behavior of disparate rocks, J. Geophys. Res. Solid Earth 120 (2015) 1587–1604. https://doi.org/10.1002/2014JB011718.

[126] J.A. Ten Cate, J. Duran, T.J. Shankland, Nonlinear and Slow Dynamics in Rocks: Response to Changes of Temperature and Humidity, in: Nonlinear Acoust. Begin. 21st Century, Moscow, Russia, 2002: pp. 767–770.
[127] J.A. TenCate, D. Pasqualini, S. Habib, K. Heitmann, D. Higdon, P.A. Johnson, Nonlinear and Nonequilibrium Dynamics in Geomaterials, Phys. Rev. Lett. 93 (2004) 065501. https://doi.org/10.1103/PhysRevLett.93.065501.
[128] D. Pasqualini, K. Heitmann, J.A. TenCate, S. Habib, D. Higdon, P.A. Johnson, Nonequilibrium and nonlinear dynamics in Berea and Fontainebleau sandstones: Low-strain regime, J. Geophys. Res. Solid Earth 112 (2007) 2006JB004264. https://doi.org/10.1029/2006JB004264.
[129] G. Renaud, J. Rivière, P. -Y. Le Bas, P.A. Johnson, Hysteretic nonlinear elasticity of Berea sandstone at low-vibrational strain revealed by dynamic acousto-elastic testing, Geophys. Res. Lett. 40 (2013) 715–719. https://doi.org/10.1002/grl.50150.
[130] K. Malaga-Starzec, I. Panas, J.E. Lindqvist, O. Lindqvist, Efflorescence on thin sections of calcareous stones, J. Cult. Herit. 4 (2003) 313–318. https://doi.org/10.1016/j.culher.2003.09.002.
[131] J. Menningen, E. Sassoni, R. Sobott, S. Siegesmund, Constraints of the durability of inorganic and organic consolidants for marble, Environ. Earth Sci. 80 (2021) 370. https://doi.org/10.1007/s12665-021-09664-w.
[132] R.J. Menningen, Ultrasonic tomography for the characterization of the weathering state of marble: A systematic study about influencing parameters, Georg-August-Universität Göttingen, 2020.
[133] G.F. Royer-Carfagni, On the thermal degradation of marble, Int. J. Rock Mech. Min. Sci. 36 (1999) 119–126. https://doi.org/10.1016/S0148-9062(98)00169-7.
[134] Météo-France, Marignane meteorological data, (n.d.). https://public.opendatasoft.com/explore/dataset/donnees-synop-essentielles-omm (accessed March 15, 2023).
[135] P.A. Johnson, Nonlinear Elastic Wave NDE I. Nonlinear Resonant Ultrasound Spectroscopy and Slow Dynamics Diagnostics, in: AIP Conf. Proc., AIP, Golden, Colorado (USA), 2005: pp. 377–384. https://doi.org/10.1063/1.1916701.
[136] J.A. Tencate, J. Duran, T.J. Shankland, Nonlinearity and Slow Dynamics in Rocks: Response to Changes of Temperature and Humidity, Nonlinear Acoust. Begin. 21st Century 2 (2002) 767–770.
[137] H. Yiming, D. Jianhui, Z. Jun, An Experimental Investigation of Moisture-Induced Softening Mechanism of Marble Based on Quantitative Analysis of Acoustic Emission Waveforms, Appl. Sci. 9 (2019) 446. https://doi.org/10.3390/app9030446.
[138] Climate Change 2023: Synthesis Report, Summary for Policymarkers, Intergovernmental Panel on Climate Change (IPCC), 2023.
[139] E. Sesana, A.S. Gagnon, C. Ciantelli, J. Cassar, J.J. Hughes, Climate change impacts on cultural heritage: A literature review, WIREs Clim. Change 12 (2021) e710. https://doi.org/10.1002/wcc.710.
[140] P. Capizzi, P.L. Cosentino, Electromagnetic and ultrasonic investigations on a Roman marble slab, J. Geophys. Eng. 8 (2011) S117–S125. https://doi.org/10.1088/1742-2132/8/3/S11.
[141] P. Capizzi, P.L. Cosentino, S. Schiavone, Some tests of 3D ultrasonic traveltime tomography on the Eleonora d'Aragona statue (F. Laurana, 1468), J. Appl. Geophys. 91 (2013) 14–20. https://doi.org/10.1016/j.jappgeo.2013.01.012.
[142] E. Cardarelli, R. De Nardis, Seismic refraction, isotropic anisotropic seismic tomography on an ancient monument (Antonino and Faustina temple AD 141), Geophys. Prospect. 49 (2001) 228–240. https://doi.org/10.1046/j.1365-2478.2001.00251.x.

[143] V. Di Pietra, E. Donadio, D. Picchi, L. Sambuelli, A. Spanò, MULTI-SOURCE 3D MODELS SUPPORTING ULTRASONIC TEST TO INVESTIGATE AN EGYPTIAN SCULPTURE OF THE ARCHAEOLOGICAL MUSEUM IN BOLOGNA, Int. Arch. Photogramm. Remote Sens. Spat. Inf. Sci. XLII-2/W3 (2017) 259–266. https://doi.org/10.5194/isprs-archives-XLII-2-W3-259-2017.
[144] L. Sambuelli, G. Bohm, P. Capizzi, E. Cardarelli, P. Cosentino, Comparison between GPR measurements and ultrasonic tomography with different inversion algorithms: an application to the base of an ancient Egyptian sculpture, J. Geophys. Eng. 8 (2011) S106–S116. https://doi.org/10.1088/1742-2132/8/3/S10.
[145] L. Sambuelli, G. Böhm, C. Colombero, A. Filipello, Photogrammetry and 3-D Ultrasonic Tomography to Estimate the Integrity of Two Sculptures of the Egyptian Museum of Turin, in: European Association of Geoscientists & Engineers, Turin, Italy, 2015. https://doi.org/10.3997/2214-4609.201413675.
[146] F. Vagnon, C. Comina, M.C. Canepa, A. Bovero, G. Giraudo, Experiences and preliminary results of geophysical methods on historical statues, IOP Conf. Ser. Earth Environ. Sci. 1124 (2023) 012132. https://doi.org/10.1088/1755-1315/1124/1/012132.
[147] E. Cardarelli, 3D tomography of some pillard of the Coliseum, Boll. Geofis. Teor. Ed Appl. 37 (1995) 257–265.
[148] E. Cardarelli, U. Mascia, A. Neri, S. Puledda, Seismic 3D-tomography with statistical constraints on pillars of the Coliseum, Rome, Boll. Geofis. Teor. Ed Appl. 37 (1995) 267–275.
[149] M. Zielińska, M. Rucka, Non-Destructive Assessment of Masonry Pillars using Ultrasonic Tomography, Materials 11 (2018) 2543. https://doi.org/10.3390/ma11122543.
[150] E. Cardarelli, R. De Nardis, The use of 3-D and 2-D seismic tomography for assessing the physical integrity of building panels, Eur. J. Environ. Eng. Geophys. 3 (1999) 131–142.
[151] M. Bagnéris, F. Cherblanc, P. Bromblet, E. Gattet, L. Gügi, N. Nony, V. Mercurio, A. Pamart, A complete methodology for the mechanical diagnosis of statue provided by innovative uses of 3D model. Application to the imperial marble statue of Alba-la-Romaine (France), J. Cult. Herit. 28 (2017) 109–116. https://doi.org/10.1016/j.culher.2017.05.002.
[152] Musée Départemental Arles Antique, Press Kit, (n.d.).
[153] F. Botton, Le théâtre antique d'Arles, Monumental (2009) 63–68.
[154] C. Carrier, Sculptures augustéennes du théâtre d'Arles, Rev. Archéologique Narbonnaise 38 (2005) 365–396. https://doi.org/10.3406/ran.2005.1164.
[155] V. Eggert, Arles - Tour de Roland (théâtre antique), ADLFI Archéologie Fr. - Inf. (2007). http://journals.openedition.org/adlfi/6413 (accessed April 21, 2024).
[156] Climate and annual weather averages in Arles, France, (n.d.). https://fr.weatherspark.com/y/50260/M%C3%A9t%C3%A9o-moyenne-%C3%A0-Arles-France-tout-au-long-de-l'ann%C3%A9e (accessed September 3, 2024).
[157] Museum label for "Autel d'Apollon", Musée Départemental Arles Antique, Arles, France, (n.d.).
[158] Museum label for "Statue d'Auguste", Musée Départemental Arles Antique, Arles, France, (n.d.).
[159] J. McCarthy, Multi-image photogrammetry as a practical tool for cultural heritage survey and community engagement, J. Archaeol. Sci. 43 (2014) 175–185. https://doi.org/10.1016/j.jas.2014.01.010.
[160] P. Grussenmeyer, K. Hanke, Architectural Photogrammetry: Basic theory, Procedures, Tools, in: Corfu, Greece, 2002.

[161] P. Waldhäusl, C.L. Ogleby, Lerma J. L., A. Georgopoulos, 3 x 3 rules for simple photogrammetric documentation of architecture, (2013). https://www.cipaheritagedocumentation.org/wp-content/uploads/2017/02/CIPA__3x3_rules__20131018.pdf (accessed June 3, 2024).
[162] T. Lindeberg, Scale Invariant Feature Transform, Scholarpedia 7 (2012) 10491. https://doi.org/10.4249/scholarpedia.10491.
[163] T.S. Douglas, Image processing for craniofacial landmark identification and measurement: a review of photogrammetry and cephalometry, Comput. Med. Imaging Graph. 28 (2004) 401–409. https://doi.org/10.1016/j.compmedimag.2004.06.002.
[164] R. Jiang, D.V. Jáuregui, K.R. White, Close-range photogrammetry applications in bridge measurement: Literature review, Measurement 41 (2008) 823–834. https://doi.org/10.1016/j.measurement.2007.12.005.
[165] P. Sapirstein, Accurate measurement with photogrammetry at large sites, J. Archaeol. Sci. 66 (2016) 137–145. https://doi.org/10.1016/j.jas.2016.01.002.
[166] T. Cavaleri, S. Legnaioli, F. Lozar, C. Comina, F. Poole, C. Pelosi, A. Spoladore, D. Castelli, V. Palleschi, A Multi-Analytical Study of an Ancient Egyptian Limestone Stele for Knowledge and Conservation Purposes: Recovering Hieroglyphs and Figurative Details by Image Analysis, Heritage 4 (2021) 1193–1207. https://doi.org/10.3390/heritage4030066.
[167] P.C. Hansen, J.S. Jørgensen, AIR Tools II: algebraic iterative reconstruction methods, improved implementation, Numer. Algorithms 79 (2018) 107–137. https://doi.org/10.1007/s11075-017-0430-x.
[168] P.C. Hansen, M. Saxild-Hansen, AIR Tools — A MATLAB package of algebraic iterative reconstruction methods, J. Comput. Appl. Math. 236 (2012) 2167–2178. https://doi.org/10.1016/j.cam.2011.09.039.
[169] F. Jalinoos, L. D. Olson, M. F. Aouad, Ultrasonic Crosshole And Crossmedium Tomography For The Detection Of Defects In Structural Concrete, in: 8th EEGS Symp. Appl. Geophys. Eng. Environ. Probl., European Association of Geoscientists & Engineers, Orlando, Florida, Canada, 1995. https://doi.org/10.3997/2214-4609-pdb.206.1995_005.
[170] M.P. Schuller, R.H. Atkinson, Evaluation of Concrete using Acoustic Tomography, in: D.O. Thompson, D.E. Chimenti (Eds.), Rev. Prog. Quant. Nondestruct. Eval., Springer US, Boston, MA, 1995: pp. 2215–2222. https://doi.org/10.1007/978-1-4615-1987-4_283.
[171] V.G. Haach, F.C. Ramirez, Qualitative assessment of concrete by ultrasound tomography, Constr. Build. Mater. 119 (2016) 61–70. https://doi.org/10.1016/j.conbuildmat.2016.05.056.
[172] L.P. Perlin, R.C.A. Pinto, Tomografia ultrassônica em concreto, Rev. IBRACON Estrut. E Mater. 6 (2013) 246–269. https://doi.org/10.1590/S1983-41952013000200006.
[173] W. Wei, Y. Biwen, W. Jiexian, Application of a simultaneous iterations reconstruction technique for a 3-D water vapor tomography system, Geod. Geodyn. 4 (2013) 41–45. https://doi.org/10.3724/SP.J.1246.2013.01041.
[174] Sanzhi Liu, Jiexian Wang, Junqiang Gao, Inversion of Ionospheric Electron Density Based on a Constrained Simultaneous Iteration Reconstruction Technique, IEEE Trans. Geosci. Remote Sens. 48 (2010) 2455–2459. https://doi.org/10.1109/TGRS.2010.2040829.
[175] M. Zielińska, M. Rucka, Detection of debonding in reinforced concrete beams using ultrasonic transmission tomography and hybrid ray tracing technique, Constr. Build. Mater. 262 (2020) 120104. https://doi.org/10.1016/j.conbuildmat.2020.120104.

[176] J. Martin, K.J. Broughton, A. Giannopolous, M.S.A. Hardy, M.C. Forde, Ultrasonic tomography of grouted duct post-tensioned reinforced concrete bridge beams, NDT E Int. 34 (2001) 107–113. https://doi.org/10.1016/S0963-8695(00)00035-9.
[177] O. Büyüköztürk, Imaging of concrete structures, NDT E Int. 31 (1998) 233–243. https://doi.org/10.1016/S0963-8695(98)00012-7.
[178] B. Abayowa, display_obj, (2008). https://www.mathworks.com/matlabcentral/fileexchange/20307-display_obj (accessed November 3, 2023).
[179] B. Abayowa, readObj, (2008). https://www.mathworks.com/matlabcentral/fileexchange/18957-readobj (accessed November 3, 2023).
[180] A. Luthfian, dispObj, (2018). https://www.mathworks.com/matlabcentral/fileexchange/66275-david-laserscanner-wavefront-obj-file-reader-plotter-volume-and-surface-area-calculator (accessed May 23, 2024).
[181] A. Ahmad, M. Pamplona, S. Simon, Ultrasonic testing for the investigation and characterization of stone – a non-destructive and transportable tool, Stud. Conserv. 54 (2009) 43–53. https://doi.org/10.1179/sic.2009.54.Supplement-1.43.

ANNEXES

A. Optical microscope observations

Optical microscope images of thin sections of Carrara marble samples heated at different temperatures are presented below. All images are taken at magnification x25 under plane polarized light. Widths of the observed intergranular spaces are given in red. The heating temperature of the sample is indicated on the top right corner of each image.

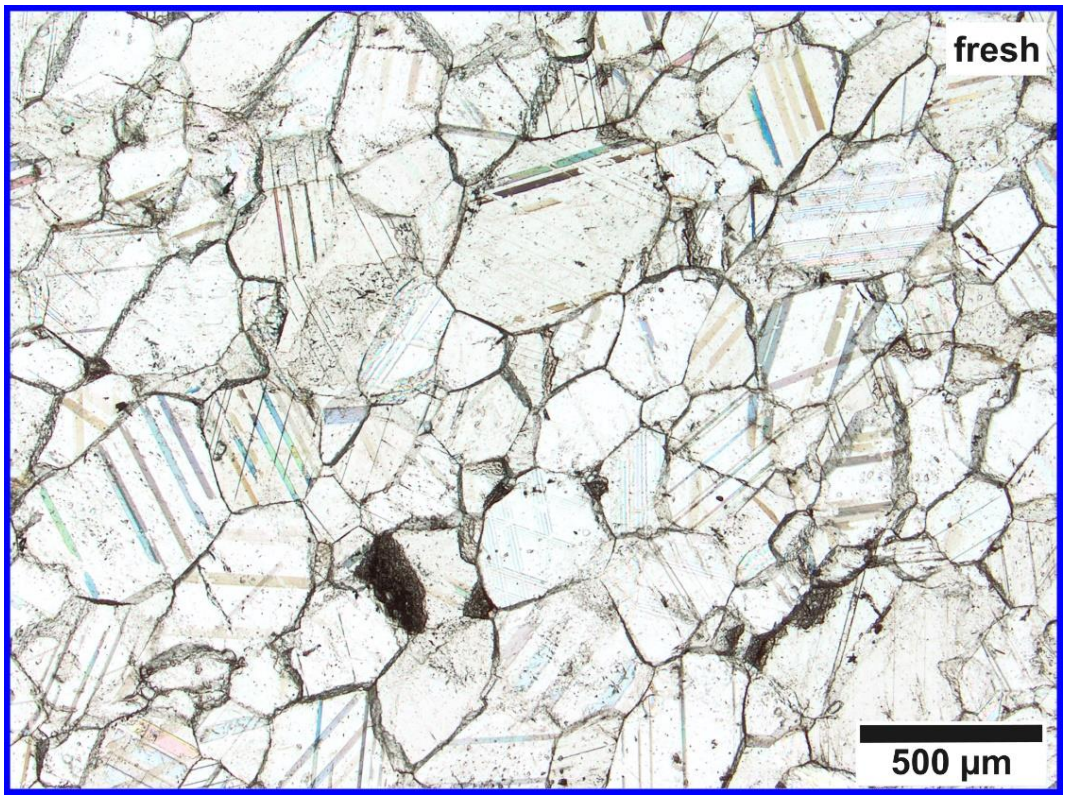

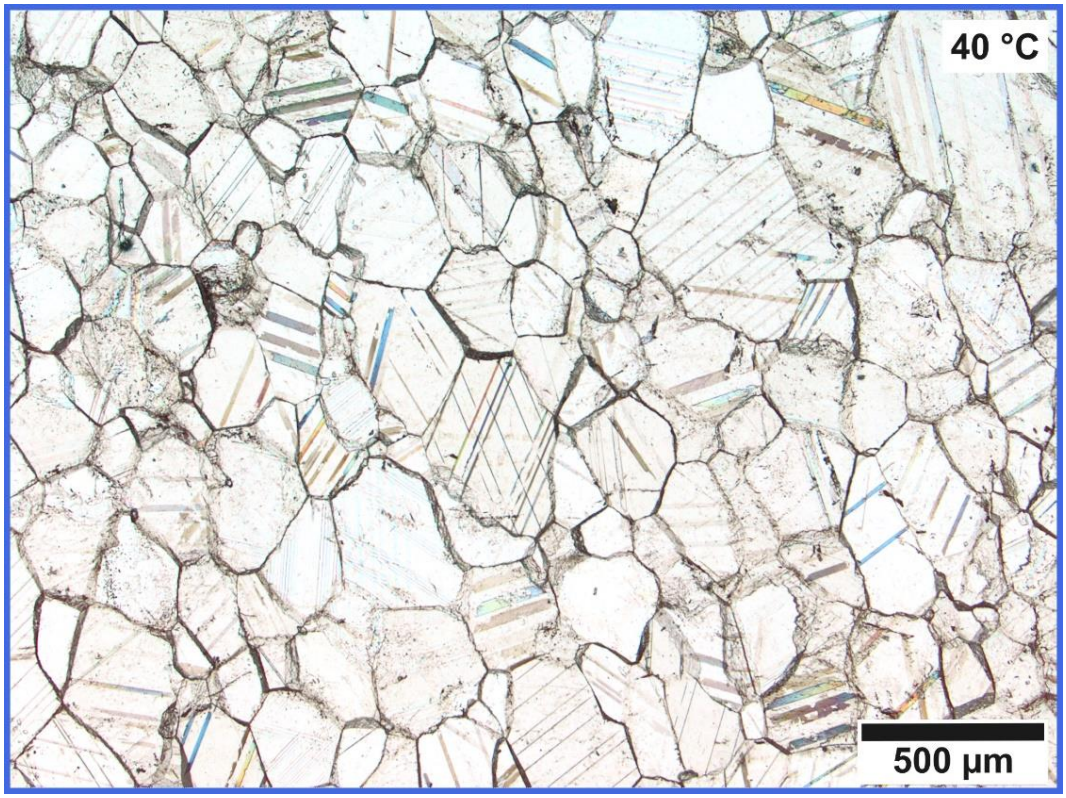
40 °C
500 µm

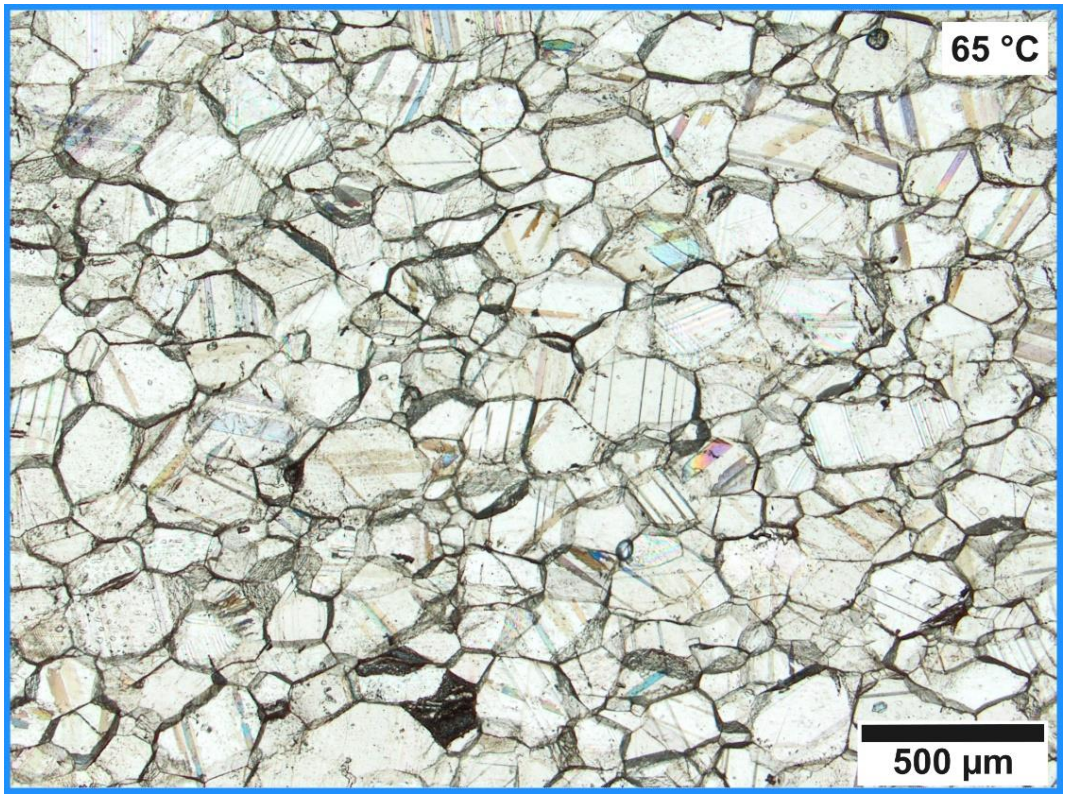
65 °C
500 µm

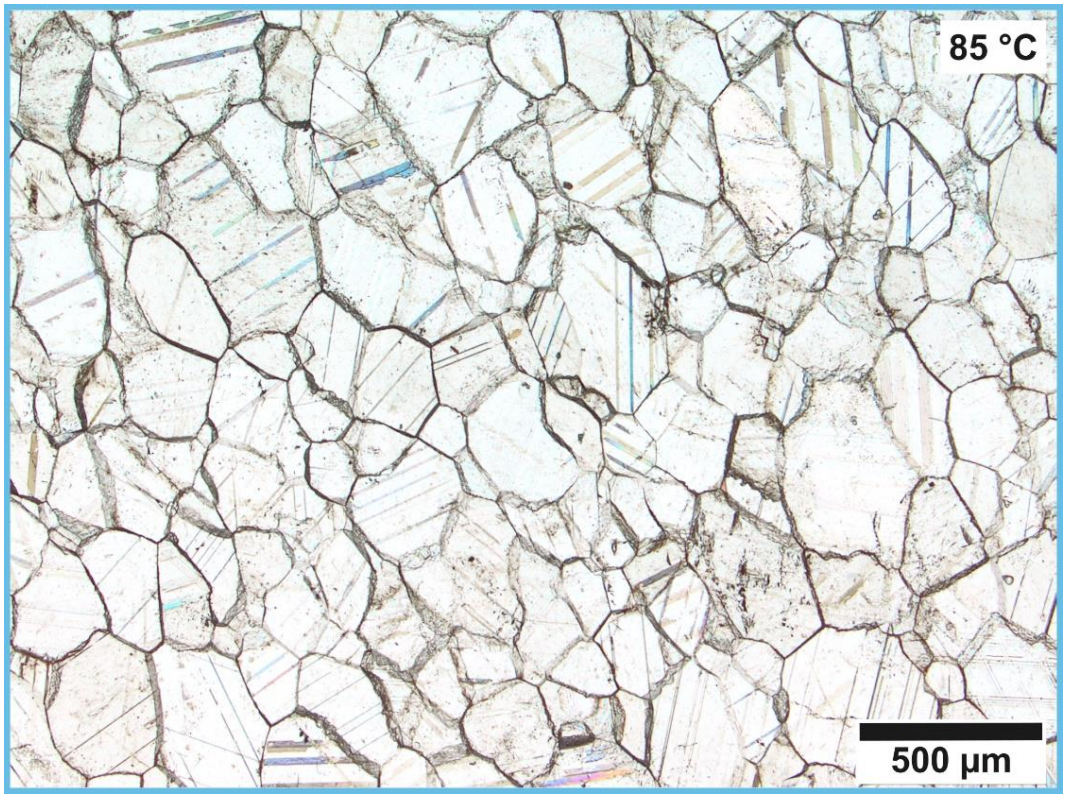
85 °C
500 µm

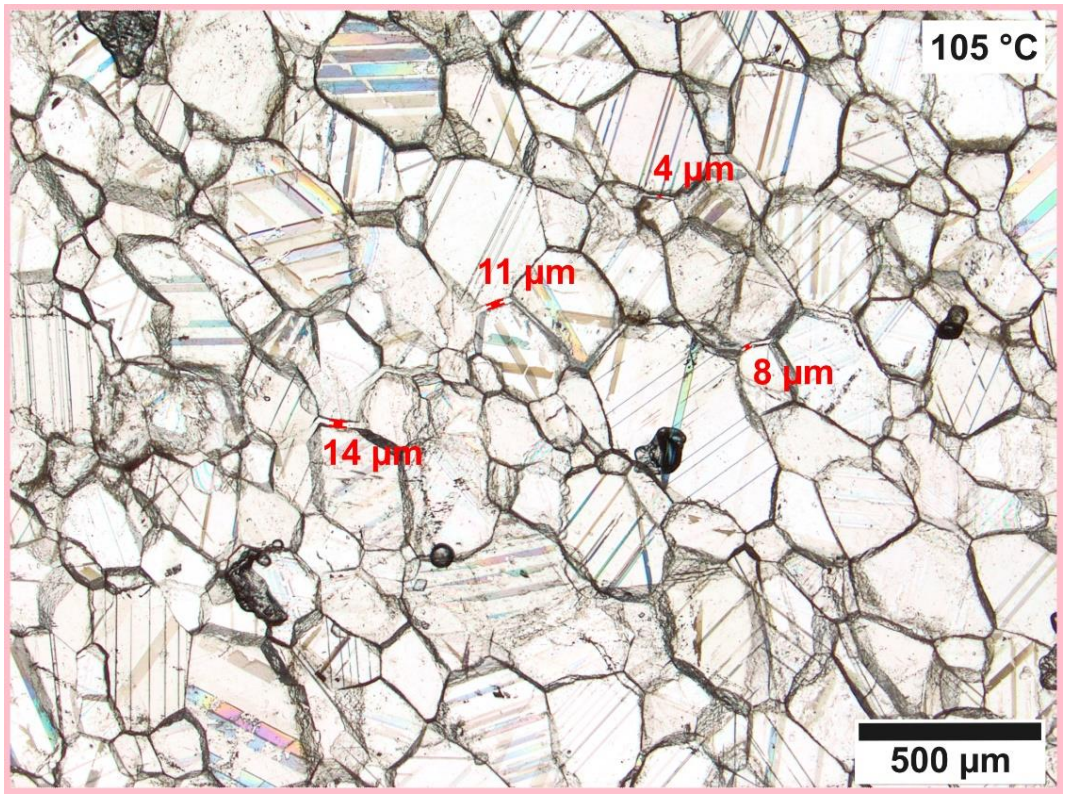
105 °C
4 µm
11 µm
8 µm
14 µm
500 µm

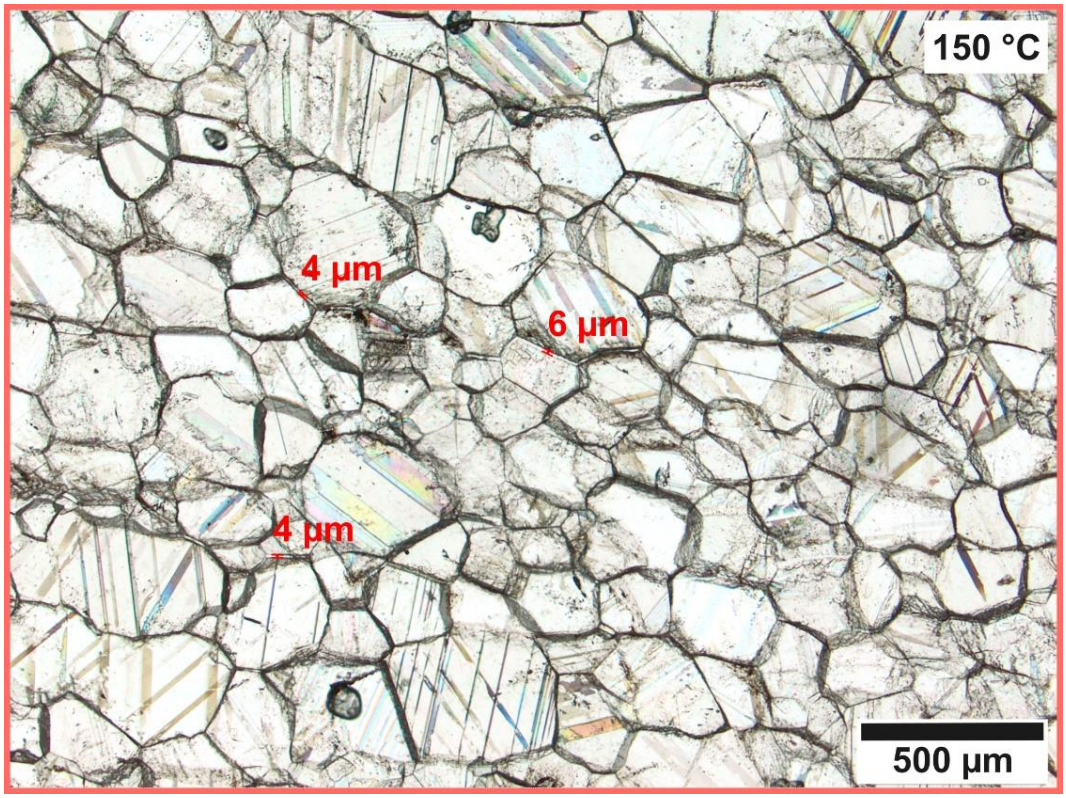
150 °C
4 µm
6 µm
4 µm
500 µm

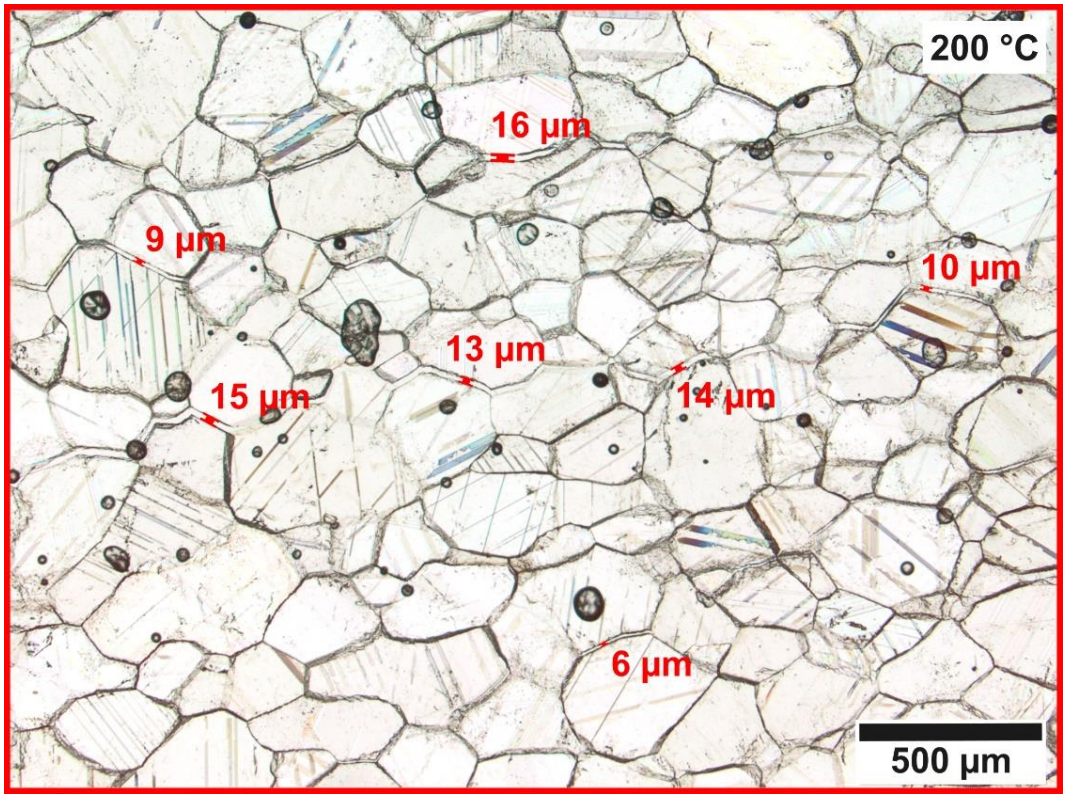
200 °C
16 µm
9 µm
10 µm
13 µm
15 µm
14 µm
6 µm
500 µm

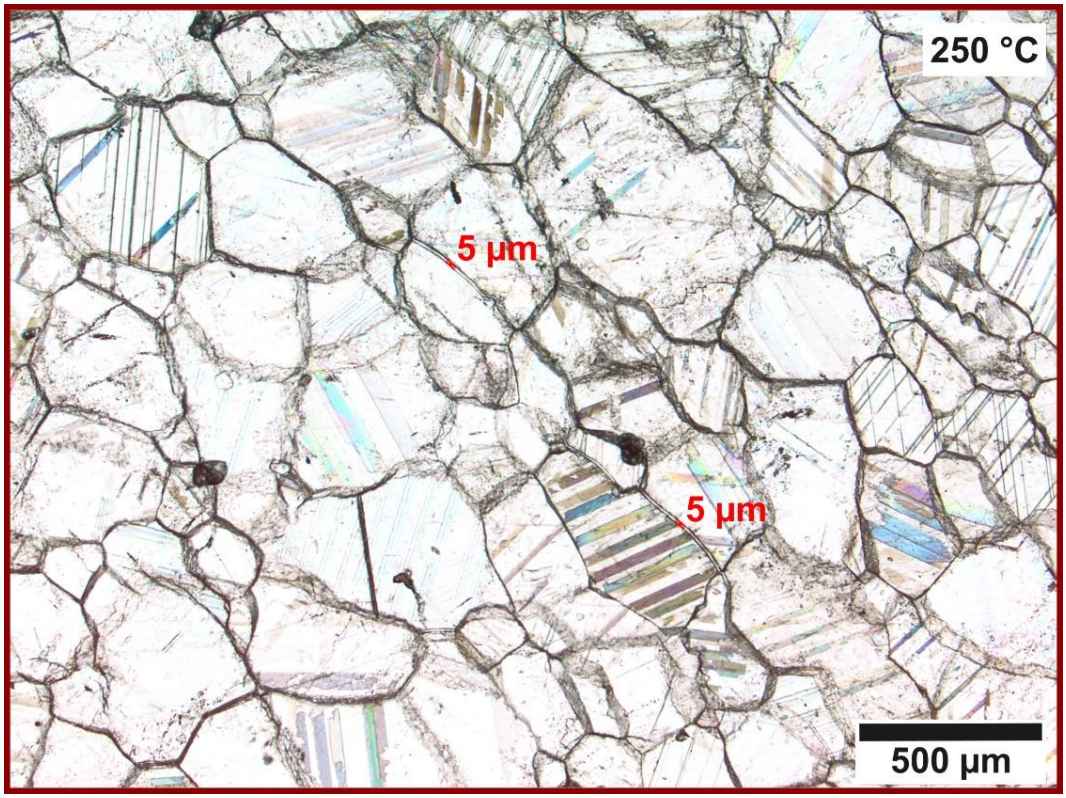
250 °C
5 µm
5 µm
500 µm

B. Article published in *Construction and Building Materials*

Article published in *Construction and Building Materials*, volume 431, 14 June 2024.
DOI: 10.1016/j.conbuildmat.2024.136529
Accepted version below.

Impact of relative humidity variations on Carrara marble mechanical properties investigated by Nonlinear Resonant Ultrasound Spectroscopy

Marie-Laure Chavazas[1, 2] *, Philippe Bromblet[2], Jérémie Berthonneau[2], Jérémy Hénin[3], Cédric Payan[1]

[1] Aix Marseille Univ, CNRS, Centrale Marseille, LMA UMR 7031, Marseille, France
4, impasse Nikola Tesla CS 40006 13 453 Marseille cedex 13 France

[2] Centre Interdisciplinaire de Conservation et de Restauration du Patrimoine, Marseille, France
21, rue Guibal 13 003 Marseille France

[3] Ministère de la Culture, Laboratoire de Recherche des Monuments Historiques
29, rue de Paris 77 420 Champs-sur-Marne France

* Corresponding author:
e-mail: chavazas@lma.cnrs-mrs.fr
full postal address: Marie-Laure Chavazas CICRP 21, rue Guibal 13 003 Marseille France

E-mail addresses:
- Philippe Bromblet: philippe.bromblet@cicrp.fr
- Jérémie Berthonneau: jeremie.berthonneau@cicrp.fr
- Jérémy Hénin: jeremy.henin@culture.gouv.fr
- Cédric Payan: cedric.payan@univ-amu.fr

Abstract

Like many other stones, marble mechanical properties can be significantly changed in presence of water. Water most often induces a weakening which can lead to marble degradation when coupled to temperature variations. Yet, marble artefacts are more frequently subjected to relative humidity (RH) variations than episodes of water imbibition and/or drastic temperature variations. Thus, one could wonder how do variations of RH alone impact marble mechanical state. In this study, Carrara Gioia marble samples are subjected to adsorption-desorption cycles. They were previously thermally-damaged between 40 and 105 °C, and their microstructure was characterized for each heating temperature. The evolution of their mechanical properties is monitored non-destructively with two parameters measured by Nonlinear Resonant Ultrasound Spectroscopy. The resonant frequency decreases weakly with increasing RH, indicating a diminution in sample stiffness due to low moisture-induced softening. The nonlinear parameter increases strongly, probably due to higher capillary pressure associated to a capillary condensation increase with RH. However, these phenomena are reversible: during adsorption-desorption cycling both parameters remain quite constant for a given RH. Therefore, while a RH increase impacts the mechanical properties of Carrara marble, adsorption-desorption cycling shows a reversible behavior which does not induce any permanent change in mechanical properties.

Keywords: Carrara marble, nonlinear resonant ultrasound, relative humidity, adsorption-desorption cycles

Highlights

- No permanent weakening of Carrara marble under relative humidity cycling
- Moisture-induced softening noticeable at low water content (0.01 – 0.18 wt. %)
- Great sensitivity of nonlinearity to relative humidity but reversible behavior
- Variations of linear and nonlinear parameters not linked to thermal damage degree

1 Introduction

Outdoor exposure can result in various deterioration patterns on built and statuary heritage made of stone [1]. More specifically, weather condition variations can be damaging for this type of material. For instance, stone artefacts exposed outdoors are subjected to frequent changes in temperature and relative humidity (RH) (day-night and seasonal variations). These cyclical fluctuations can lead to considerable damage. As an example, marble slabs can be affected by a bowing phenomenon when exposed to temperatures variations and moisture [1–4].

The presence of water alone can also significantly impact stone artefacts. Indeed, stone are porous materials that can be greatly affected by water molecules (in liquid or gaseous state) migrating within the pore spaces. As a consequence, the mechanical properties of various stone types, such as sandstones [5–8], limestones [9–14], igneous rocks [15], shales [16], are significantly changed in presence of water. Various mechanisms can be at stake depending on stone type: fracture energy reduction, capillary tension decrease, pore pressure increase, frictional reduction, chemical and corrosive deterioration [16,17]. Marble is also mechanically affected by the presence of water molecules. Mahmutoğlu (2006) shows that peak strength of Muğla marble diminishes between dry and saturated samples subjected to the same strain rate [18]. Vásárhelyi *et al.* (1999) find that Young's modulus decreases by 4%, compressive strength by 7% and tensile strength by 1% between air-dry and saturated samples of Sivac marble [19]. In Zhu *et al.* (2020), Chinese white marble exhibits a 29% reduction in average uniaxial compressive strength and a 23% reduction in average Young's modulus between dry and water-saturated samples [20]. Therefore, the influence of water saturation on the mechanical properties of different marble types have been extensively investigated. However, stone artefacts are not only subjected to water imbibition but also often to RH variations. Therefore, the impact of exposure to different RH levels and to cyclical RH fluctuations on marble mechanical properties is also important to study.

Destructive mechanical tests have their limitations to monitor mechanical properties of marble samples during adsorption-desorption cycling as they do not allow following the same sample all along the cycling process. Ultrasonic pulse velocity can overcome this restraint as it is a non-destructive technique [21]. However, this tool is ill-adapted for probing the influence of RH variations on marble samples. Indeed, Siegesmund *et al.* (2021) show on Blanco Macael marble that changes in RH levels do not significantly affect ultrasonic pulse velocity [22]. On the contrary, Nonlinear Resonant Ultrasound Spectroscopy (NRUS) is sensitive to any change occurring at the microstructural scale, including ones due to RH fluctuations. It is a resonance method which allows monitoring the mechanical state of materials non-destructively. It is well-suited to stones in which nonlinear phenomena occur when the excitation amplitude increases, since stones are part of the nonclassical nonlinear class of materials which is characterized by hysteresis, slow dynamics, end-point memory [23–27]. So far, the influence of water saturation and RH on the nonlinear responses has been investigated in a few studies on glass bead, sand, limestone and sandstone [23,26,28–31] but not on marble. Besides, to the authors' knowledge, the impact of RH changes on the NRUS response of rocks with different damage degrees has not been yet investigated.

This work thus aims at evaluating the impact of exposure to cyclical RH fluctuations on Carrara marble, as well as the effect of the coupling between thermal damage and exposure to RH fluctuations. First, microstructural characterizations (mercury intrusion porosimetry, SEM) were conducted on the studied fresh and thermally-damaged marble samples. The influence of RH changes on the decay of Carrara Gioia marble was then monitored using NRUS. Resonant frequency and nonclassical nonlinear parameter were measured at different RH levels during adsorption and desorption on marble samples with different thermal weathering degrees. They were then also measured as samples underwent adsorption-desorption cycles between 12% and 96% RH to simulate cyclical variations. The evolution of the NRUS parameters are eventually discussed in light of marble sample microstructures.

2 Materials and methods

2.1 Sample preparation

Five core samples of Carrara Gioia marble of 20 cm in height and 4 cm in diameter were studied. They were drilled from a fresh block of Carrara Gioia marble (provided by Logica SRL, Carrara, Italy), which is a calcitic white veined marble and has a granoblastic equigranular-polygonal microstructure. The sample faces were polished to ensure flat and parallel surfaces for measurement. Four of the samples underwent a thermal treatment at respectively 40, 65, 85 and 105 °C, and one sample remained unheated. The heating rate of the oven was set to 1 °C·min^{-1} to allow the homogeneous heating of the material [22,32,33], the setpoint temperature was maintained for 6 h [22] and the cooling down to room temperature was left free. All five samples were then stored at 23 °C in temperature-controlled oven.

2.2 Microstructural characterization

Microstructural analyses were carried out on core samples drilled from the same marble block and having undergone the same thermal treatments. Marble porous network was characterized with mercury intrusion porosimetry using an AutoPore IV 9500 (Micromeritics) working with a maximal pressure of 210 MPa, thus probing pores between 0.01 and 360 µm. Mercury intrusion was measured at 111 increasing pressure points. Freshly cut fragments of thermally-damaged marble samples were also characterized under a Scanning Electron Microscope (SEM, ZEISS EVO 15).

Vapor sorption behavior was characterized along adsorption for all the samples using the 8 supersaturated salt solutions listed in section 2.3. Measurements were carried out on cylindrical slices of 4 cm in diameter and of about 1 cm in thickness. The experiment was done at 23 °C, in a temperature-controlled oven. One slice was used per sample. The dry masses were measured after the slices were under 3% RH (controlled by silica gel). The experimental points were fitted with the GAB theoretical modeling.

2.3 Experimental set-up

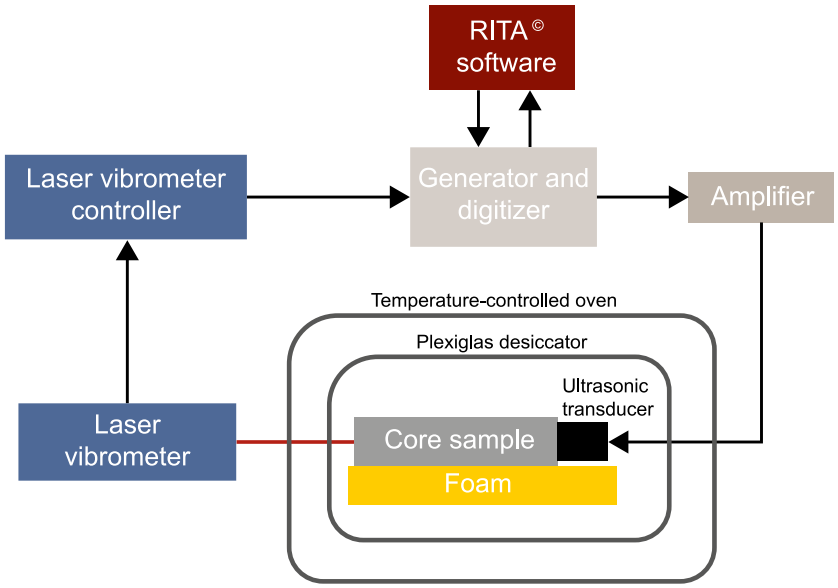

Fig. 1 (Color online) Scheme of the experimental set-up.

Fig. 2 (Color online) Sample disposition in the experimental set-up. This picture corresponds to the temperature-controlled oven and laser vibrometer part of the scheme of Fig. 1.

Fig. 1 illustrates the experimental set-up for the NRUS experiments, and Fig. 2 specifically shows sample disposition in the experimental set-up. The signal generation is managed by RITA© software coupled with a generator (NI PXIe-5406) and an amplifier (NF Electronic Instruments 4005 High Speed). The vibrations are generated in the core sample thanks to a piezoelectric transducer (Beijing Ultrasonic, resonant frequency of 40 kHz) which is permanently glued to one sample extremity with epoxy Araldite® 2020. The piezoelectric devices and the unsheathed wires are wrapped in stretch film to avoid deterioration due to high humidity levels. Samples are placed on the two middle racks of a four-level desiccator cabinet (no. 1 in Fig. 2). They are put on foam to minimize the attenuation or modification of the vibration modes due to the rigid support. On the lowest and highest racks of the desiccator, two containers with supersaturated salt solutions (no. 2 in Fig. 2) are placed to control RH inside the desiccator. The following salts are used throughout the experiments (equilibrium humidity is bracketed): LiCl (12%), $MgCl_2$ (33%), K_2CO_3 (44%), $Mg(NO_3)_2$ (52%), $NaNO_2$ (66%), NaCl (76%), KCl (86%) and K_2SO_4 (96%). The desiccator cabinet is itself placed in a temperature-controlled oven maintained at 23 °C (no. 3 in Fig. 2). This configuration was maintained during the NRUS testing: the samples were not taken out of the desiccator cabinet nor of the oven for the NRUS tests. Indeed, the out-of-plane velocity is measured at the sample extremity opposite to the piezoelectric transducer with a Polytec laser vibrometer (no. 4 in Fig. 2) (OFV-505 Single Point Sensor Head and OFV-5000 Controller, $\lambda = 633$ nm (He-Ne), power < 1 mW), which allows carrying out measurements through the interior glass door of the temperature-controlled oven and through the Plexiglas wall of the desiccator. The exterior steel doors of the temperature-controlled oven are left open during measurements to allow the laser going through. The signal acquisition is managed by RITA© software coupled with a digitizer (NI PXIe-5122). The NRUS measurements were made after the samples had been exposed under a specific RH for at least 48 h to ensure stabilization of equilibrium humidity inside the desiccator (controlled by an iButton® temperature-humidity logger). At least three NRUS tests were performed on each sample at each ambient RH, waiting at least 3 h between two scans on the same sample in order to avoid slow dynamic processes influence [24,26,27,34].

2.4 Nonlinear Resonant Ultrasound Spectroscopy (NRUS)

NRUS is a resonance technique in which a sample is excited at different increasing amplitudes to study the evolution of its resonant modes. Marble belongs to the nonclassical nonlinear class of materials, which means that its modulus K is in the form [25–28]:

$$K = K_0[1 + \beta\varepsilon + \delta\varepsilon^2 + \cdots + \alpha(\Delta\varepsilon, \dot{\varepsilon})] \quad (1)$$

where K_0 is the elastic modulus, β and δ are the classical nonlinear coefficients and α is the nonclassical nonlinear parameter. As marble is a nonlinear material, its resonant frequency for a given mode is shifted towards low frequencies as the drive amplitude increases. This phenomenon can be observed on the NRUS scan for the unheated Carrara Gioia marble sample under 12% RH displayed on Fig. 3. Relative shift frequency is proportional to the strain amplitude $\Delta\varepsilon$ of the sample, with the nonclassical nonlinear parameter α as the proportionality coefficient [35,36]:

$$\Delta f / f_0 = \alpha \, \Delta\varepsilon \qquad (2)$$

where $\Delta f = f_0 - f$ with f_0 the linear resonant frequency (obtained for the lowest drive amplitude) and f the resonant frequency for higher drive amplitudes. In this study, only the first longitudinal mode of marble samples is investigated. The strain $\Delta\varepsilon$ reached at resonance peaks is evaluated from the out-of-plane particle velocity amplitude A recorded by the vibrometer at resonance:

$$\Delta\varepsilon = A/(2 * L * f_0) \qquad (3)$$

where L is the sample length and f_0 is the low amplitude resonant frequency.

Therefore, NRUS provides two useful parameters to characterize any nonclassical nonlinear material such as marble:

- The resonant frequency f_0 (linear resonant frequency extracted for the lowest drive amplitude) which is related to the stiffness and density of the macroscopic sample,
- The nonlinear parameter α which is highly sensitive to any change at the microstructural scale, such as microcracks, capillary effects, friction, contacts, dislocations [23,37–39].

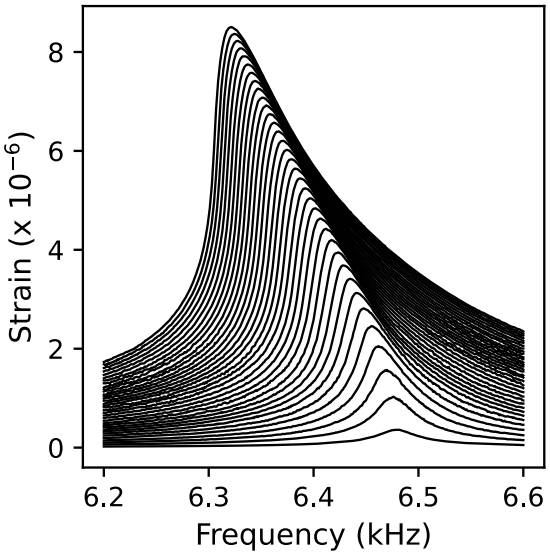

Fig. 3 NRUS curves obtained for the unheated Carrara Gioia marble sample under 12% RH. Resonant frequency f_0 is of 6479.9 ± 0.7 Hz and nonlinear parameter α of (3.5 ± 0.5) × 10^3. One single curve corresponds to one drive amplitude level. The resonant frequency shift towards low frequencies is noticeable, as well as its proportionality with the strain reached at resonance for the highest drive amplitudes.

3 Results

3.1 Microstructural impact of thermal treatment

The evolutions of total porosity and pore size distribution with setpoint temperature of thermal treatment are respectively displayed on Fig. 4 and Fig. 5, and are summarized in Table 1. One can note

the global increase in porosity with heating temperature, from 0.81% for the unheated sample to 2.59% for the sample heated at 105 °C (Fig. 4). Fig. 5 shows an increase in the radius of pore access with heating temperature. Indeed, the contribution of pores with access radius between 0.01 and 1 µm diminishes for the benefit of wider pores (> 1 µm) as heating temperature increases.

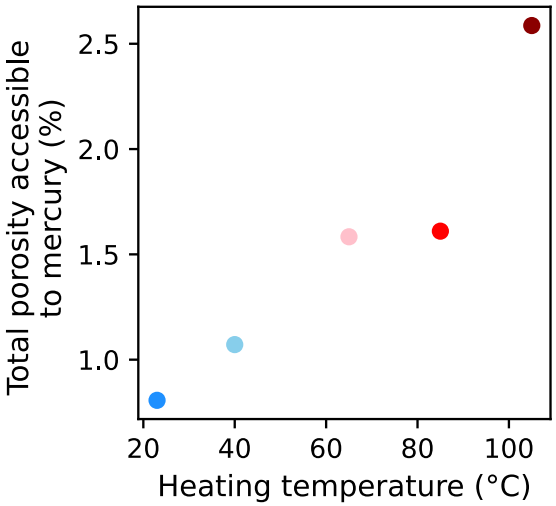

Fig. 4 (Color online) Total porosity (accessible to mercury) of Carrara marble samples heated at different temperatures.

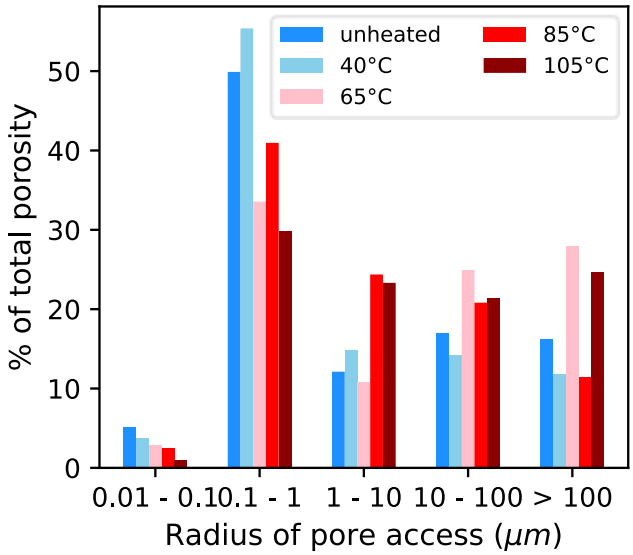

Fig. 5 (Color online) Porosity classes for Carrara marble samples heated at different temperatures. Contribution of five porosity classes (radius of pore access between 0.01 and 0.1 µm, between 0.1 and 1 µm, between 1 and 10 µm, between 10 and100 µm, and above 100 µm) to the global porosity of Carrara marble samples.

Fig. 6 shows SEM images of pores for the unheated sample and the sample heated at 85 °C. It highlights the presence of intergranular spaces even in unheated Carrara marble samples, and their widening due to heating.

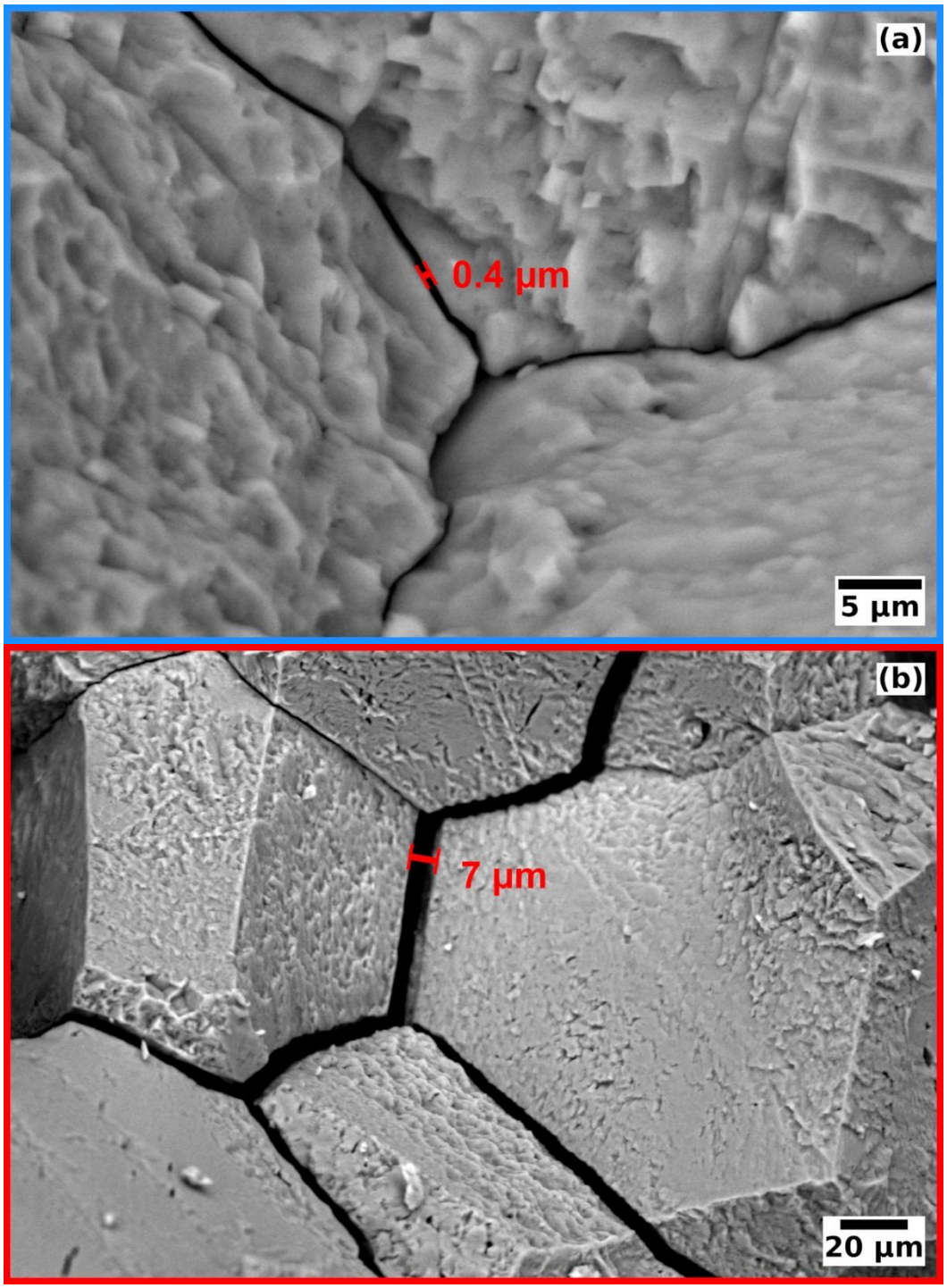

Fig. 6 (Color online) SEM images (magnification (a) x2000, (b) x400) on fracture plans of Carrara Gioia marble for (a) unheated sample and (b) sample heated at 85 °C. Indications of the width of the intergranular spaces is given in red.

Sorption isotherms are displayed on Fig. 7. The water uptake is the lowest for the sample heated at 105 °C and the highest for the unheated sample and the sample heated at 40 °C with the samples heated at 65 and 85 °C in between. The increase in water content with RH at a given heating temperature can be explained by the capillary condensation occurring at highest RH. One can note that, for a given value of RH, water content tends to decrease with heating temperature. It can be linked to the widening of pores access radius (Fig. 5, Fig. 6) when heating temperature increases, as less small pores are available for capillary condensation to occur.

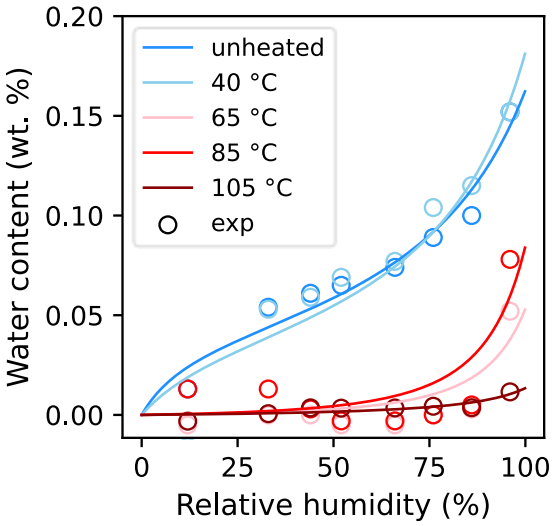

Fig. 7 (Color online) Sorption isotherms for the Carrara marble samples heated at different temperatures.

3.2 Impact of relative humidity: adsorption

The five Carrara marble samples were exposed to the relative humidities listed in section 2.3 in increasing order (from 12% to 96%). Fig. 8 (a) and (b) present for each sample the evolution of its resonant frequency f_0 and of its nonlinear parameter α with RH. A data point corresponds to the average value of the studied parameter for all NRUS scans performed at a given RH on the sample. The uncertainties (shaded areas in Fig. 8) correspond to one standard deviation. The data spread is very low for the resonant frequency f_0 and higher for the nonlinear parameter α. Relative changes in resonant frequency f_0 and nonlinear parameter α for each sample are shown in Fig. 9, the reference value being the parameter value at 12% RH. In Fig. 10, the relative changes are also given as a function of the relative changes in sample water content (reference value is the value at 12% RH for both axes).

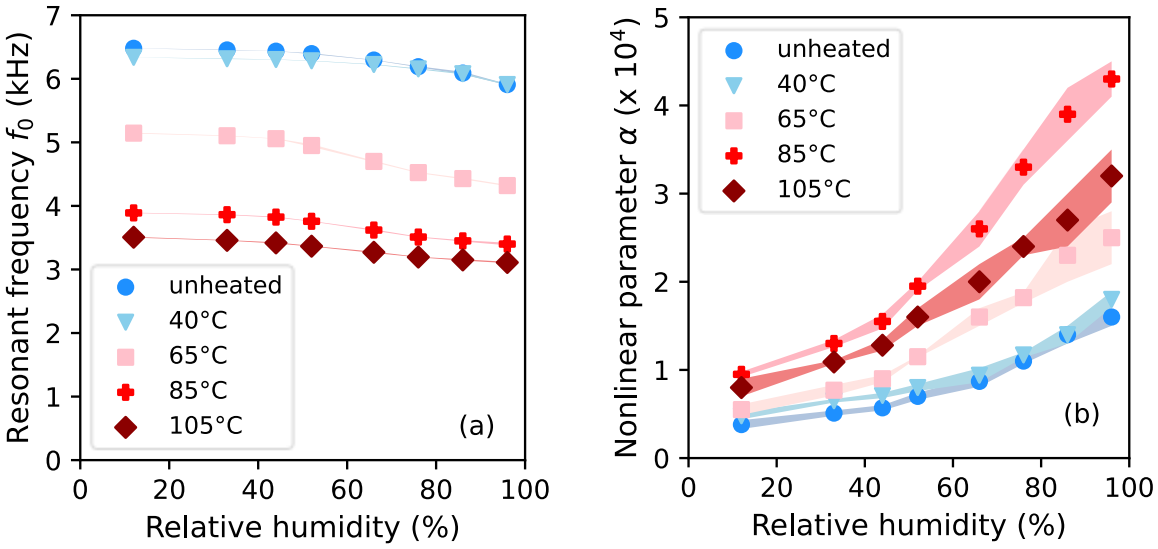

Fig. 8 (Color online) Evolution of the NRUS parameters during adsorption. (a) Resonant frequency f_0 and (b) nonlinear parameter α as a function of RH for Carrara Gioia marble samples previously heated at various temperatures. Shaded areas denote one standard deviation.

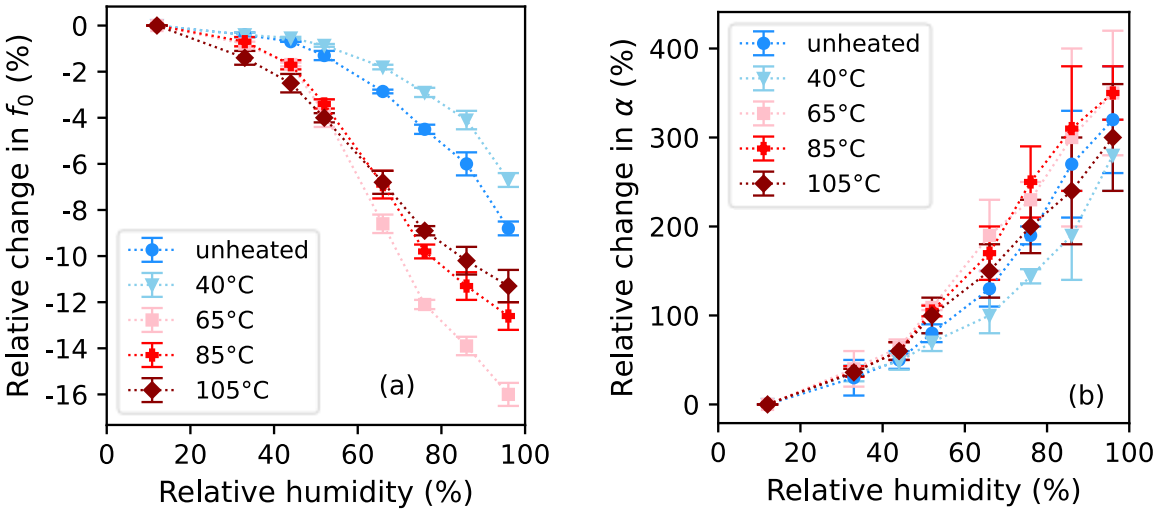

Fig. 9 (Color online) Variation of the NRUS parameters during adsorption. Relative change in (a) resonant frequency f_0 and (b) nonlinear parameter α with RH during adsorption for Carrara marble samples previously heated at various temperatures.

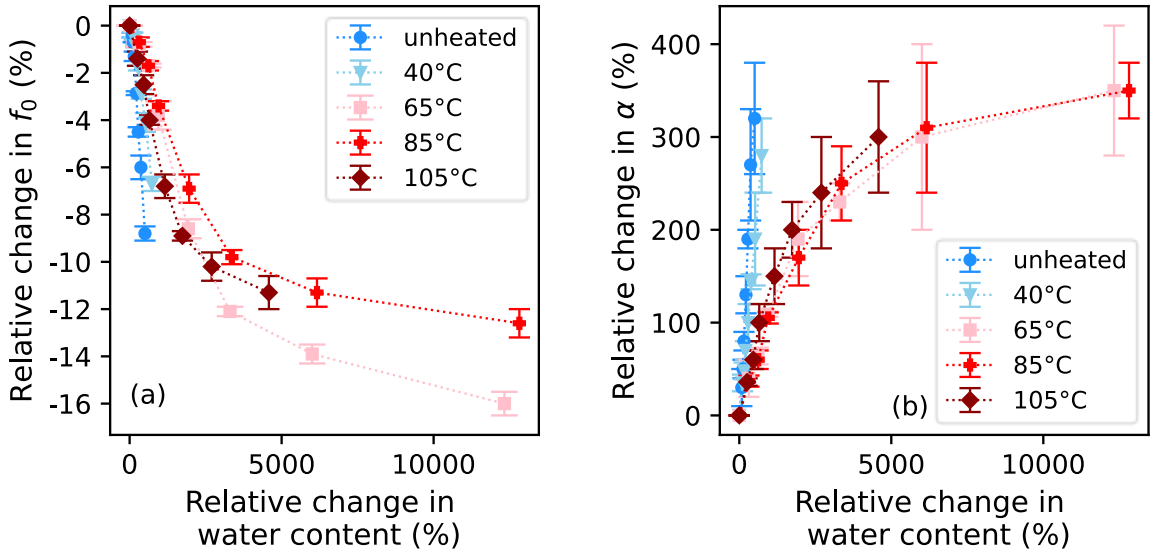

Fig. 10 (Color online) Variation of the NRUS parameters during adsorption. Relative change in (a) resonant frequency f_0 and (b) nonlinear parameter α as a function of the relative change in water content during adsorption for Carrara marble samples previously heated at various temperatures.

For all the samples, the resonant frequency f_0 tends to slightly decrease as RH increases (Fig. ***8***). For a given air humidity, the resonant frequency f_0 is always the highest for the unheated and the 40 °C heated samples, then it gradually diminishes for samples heated at 65, 85 and 105°C. For the unheated sample, the resonant frequency f_0 reduces from 6.4801 ± 0.0007 kHz at 12% RH to 5.909 ± 0.008 kHz at 96% RH. For the sample heated at 105°C, it decreases from 3.507 ± 0.006 kHz at 12% RH to 3.11 ± 0.01 kHz at 96% RH. Between 12% and 96% RH, the resonant frequency f_0 globally decreases by 9%, 7%, 16%, 13% and 11%, respectively for the unheated sample and the samples heated at 40, 65, 85 and 105°C (Fig. 9). For a given increase in water content, samples exhibit comparable relative changes in resonant frequency f_0 (Fig. 10).

The nonlinear parameter α increases with increasing RH for all the samples (Fig. 8). For a specific RH, the highest value of nonlinear parameter α is always reached for the sample heated at 85°C and the lowest is reached for the unheated sample. Between them two, the value of the nonlinear parameter α increases in this order: samples heated at 40, 65 and 105°C. For the unheated sample, at 12% RH the nonlinear parameter α is evaluated at $(3.8 \pm 0.5) \times 10^3$ and reaches $(16 \pm 1) \times 10^3$ at 96% RH. Between 12% and 96% RH, the nonlinear parameter α of the sample heated at 85°C rises from $(9.5 \pm 0.3) \times 10^3$ to $(43 \pm 2) \times 10^3$. Between 12% RH and 96%, the nonlinear parameter α globally increases by 320%, 280%, 350%, 350% and 300%, respectively for the unheated sample and the samples heated at 40, 65, 85 and 105°C (Fig. 9). Samples do not reach the same levels of increase in nonlinear parameter α at a given increase in water content: the highest is reached for the unheated sample and the sample heated at 40 °C, followed by the samples heated at 65, 85 and 105 °C (Fig. 10).

3.3 Adsorption-desorption cycles

The evolution of the NRUS parameters was also investigated during desorption for the unheated and 85 °C heated samples to study a complete adsorption-desorption cycle. The samples were exposed to the relative humidities listed in section 2.3 in decreasing order (from 96% to 12%). The results are presented in Fig. 11. Fig. 11 (a) and (b) display the evolution of the resonant frequency f_0 and of the nonlinear parameter α with RH during adsorption (empty black circles) and desorption (filled blue circles) for the unheated sample. The same evolutions are presented for the sample heated at 85 °C in Fig. 11 (c) and (d) (empty black crosses for adsorption, filled red crosses for desorption). For a given RH level, the resonant frequency values are extremely similar during adsorption and desorption phases for the two samples. They only differ at 12% and 33% RH for the sample heated at 85 °C. In contrast, the nonlinear parameter values do not coincide during the two phases for intermediate relative humidities for none of the samples.

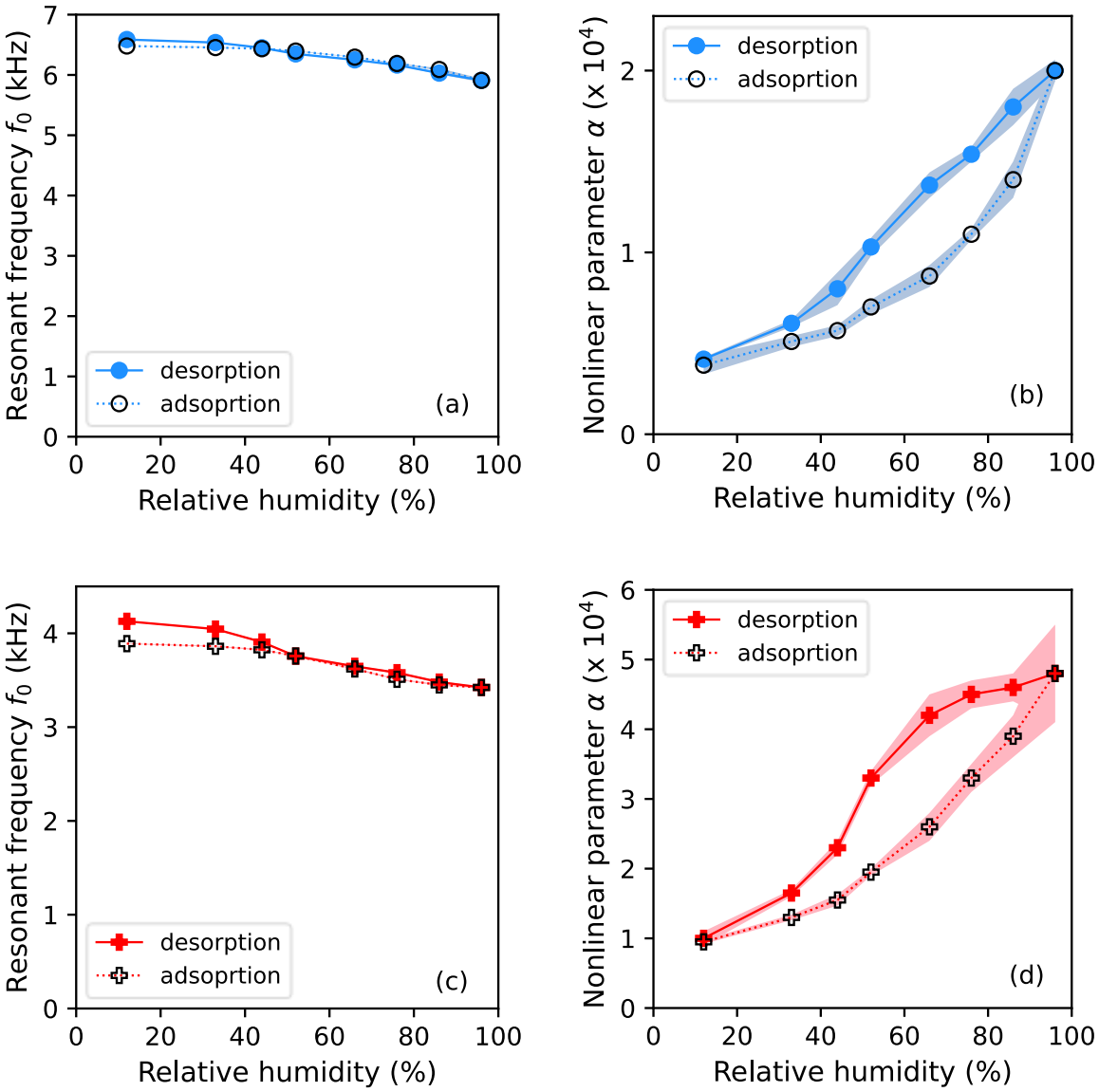

Fig. 11 (Color online) Adsorption-desorption cycle. Evolution of the resonant frequency f_0 (on the left) and of the nonlinear parameter α (on the right) with RH during adsorption (empty symbols) and desorption (filled symbols) for the (a, b) unheated (blue circles) and (c, d) 85 °C heated (red crosses) samples. Shaded areas denote one standard deviation.

The evolution of the NRUS parameters at 12% and 96% RH was also followed during 10 adsorption-desorption cycles for the five samples to verify whether the effects of RH changes on the resonant frequency f_0 and the nonlinear parameter α could be reversible. The results are displayed on Fig. 12. Fig. 12 (a) and (b) present the evolution of the resonant frequency f_0 and of the nonlinear parameter α at 12% RH during 10 adsorption-desorption cycles. Fig. 12 (c) and (d) present the same evolutions at 96% RH. Dashed lines correspond to average values of the NRUS parameters over the 10 cycles. Data for the second cycle lack for samples heated at 40, 65 and 105 °C because they were not measured. The resonant frequency f_0 slightly increases at 12% RH over the 10 cycles and remains steady at 96% RH. At 12% and 96% RH, the nonlinear parameter α varies around the average but without exhibiting an overall tendency to increase or decrease during cycling.

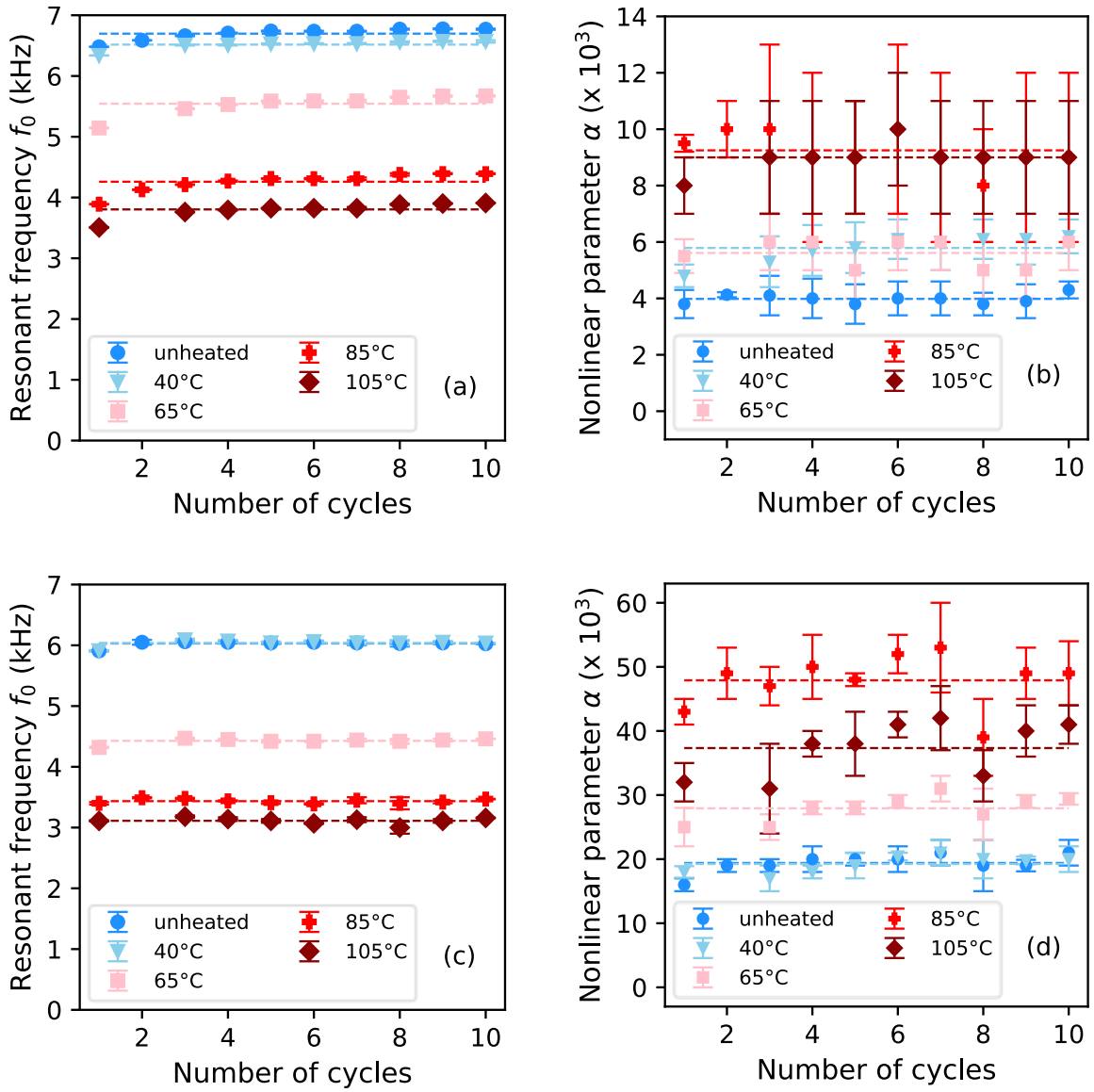

Fig. 12 (Color online) Adsorption-desorption cycling. Evolution of the resonant frequency f_0 (on the left) and of the nonlinear parameter α (on the right) at (a, b) 12% RH and (c, d) 96% RH during 10 adsorption-desorption cycles for marble samples previously heated at various temperatures. Dashed lines correspond to average values of the parameter over the 10 cycles and are given for information.

4 Discussion

Marble artefacts undergo various deterioration patterns when exposed to cyclical thermo-hygric variations. Yet, the sole impact of RH fluctuations remained unknown. Its influence has thus been investigated with NRUS and the results show the role of moisture-induced softening and capillary condensation. They also show that RH cycling does not lead to permanent deterioration in Carrara marble regardless of its damage state.

One can first note the difference in the sensitivity of the resonant frequency f_0 and the nonlinear parameter α to RH changes (Fig. 8, Fig. 9). This observation is consistent with previous studies on granular materials. In Siegesmund *et al.* (2021), the influence of air humidity on ultrasonic velocity in marble is found to be low [22]. Compressional wave velocity V_P is closely linked to the resonant frequency f_0 of the longitudinal mode: $V_P = 2 * L * f_0$, L being the sample length. Moreover,

Ostrovsky and Johnson (2001) emphasize that the nonlinear parameter α is more dependent on water presence than linear parameters in geomaterials [23]. It is also in agreement with findings on a medium made of glass beads in which linear wave velocity is not affected by RH changes while all the nonlinear parameters (α, β, γ) increase with increasing RH [31].

The resonant frequency f_0 of Carrara marble samples decreases by between 7 and 16% as RH increases between 12% and 96% whatever the heating temperature (Fig. 9 (a)). This decrease of the resonant frequency f_0 could be explained by the moisture-induced softening of stones: the reduction of their mechanical strength in presence of water [40]. Studies have shown that mechanical properties (Young's modulus, compressive and tensile strength) of marble are reduced when the samples are water saturated [18–20]. While generally considered as a result of liquid water, this work shows that this reduction occurs even along RH changes corresponding to very low water content (between 0.01 and 0.18 wt. %). This diminution of the resonant frequency f_0 at low water content could correspond to the onset of moisture-induced softening in Carrara marble: water inside pores can weaken friction between grains, thus inducing sliding between them and reducing mechanical properties.

Regarding the nonlinear parameter α, it can first be noticed that this parameter is affected by a hysteresis phenomenon during adsorption-desorption cycles. Indeed, values reached during the desorption phase do not correspond to the ones of the adsorption phase (Fig. 11). Hysteresis loops during an adsorption-desorption cycle are well-known in sorption isotherms and are due to different mechanisms occurring during adsorption and desorption, such as a reduction of contact angle from adsorption to desorption, delay in meniscus formation, condensate trapped in ink bottle pores [41]. These different mechanisms occurring at the microscopic scale could also affect the nonlinear parameter α and lead to the presence of a hysteresis loop between adsorption and desorption phases. Therefore, values of the nonlinear parameter α measured at a given RH depend on the sample history regarding moisture uptake or release.

Besides, the nonlinear parameter α exhibits a significant increase with increasing RH: by between 280% and 350% from 12% to 96% RH. This increase corroborates observations made on other granular materials. In Johnson *et al.* (2004), the nonlinear parameter α increases with water saturation in St. Pantaleon limestone. In Meule sandstone, it increases for saturations below 30% and then slowly decreases [26]. Averbakh *et al.* (2017) show that the nonlinear parameter α of longitudinal mode increases with increasing water saturation for an unspecified limestone [29]. Van Den Abeele *et al.* (2002) find that the nonlinear parameter α first increases with increasing water saturation in Lavoux limestone and Berea and Meule sandstones, and then levels off at highest saturations [28]. Gao *et al.* (2023) find that the nonlinear parameter α increases with RH in glass beads but not in sand where it remains constant [30]. Authors hypothesize that this difference in behavior comes from more grain interlocking in sand which prevents adsorbed water from weakening/dilating the sample, unlike in glass beads [30]. Van Den Abeele *et al.* (2002) explain the increase in nonlinearity with increasing water saturation by the presence of capillary condensation. Capillary condensation does not appear simultaneously in the whole pore network as it depends on the pore radius via Kelvin's law. Therefore, menisci are formed at the interfaces of air and liquid water and these menisci are subjected to microscopic capillary pressure because of the difference between the pressure in air and in liquid water. Microscopic capillary pressure results in a microscopic contraction pressure in the solid matrix where the menisci are formed. These microscopic forces occurring in the pore network can lead to an additional nonlinearity when samples are subjected to an increasing RH. Microscopic forces due to capillary condensation could also explain the increase of nonlinearity with RH in this work as water molecules can penetrate the intergranular spaces which are present in all the studied samples (Fig. 6).

However, it can be noted on Fig. 9 that relative changes in nonlinear parameter α (and in resonant frequency f_o) do not seem correlated with the total amount of porosity in sample (Fig. 4), pore size distribution (Fig. 5, Fig. 6), or water content (Fig. 7). Relative changes are of the same order of magnitude for all the samples whereas one could have expected that some of the samples exhibit more relative variations of nonlinearity than others due to their different pore network (Fig. 4, Fig. 5, Fig. 6). As capillary condensation is conditioned by Kelvin's law, a study of pore proportion below and above Kelvin's radius in the studied marble samples could have been insightful. Unfortunately, for water as the fluid and at 25 °C, Kelvin's radius ranges from 4.95×10^{-4} to 2.57×10^{-2} µm for RH between 12% and 96%, which is below the pore radius detected by mercury intrusion porosimetry on

the studied samples. The sorption isotherms can still give a first insight (Fig. 7). They highlight that less capillary condensation occurs in the samples heated at 65, 85 and 105 °C than in those unheated and heated at 40 °C, even though all these samples display similar increase of nonlinearity. Therefore, for the same water content, the relative changes in the nonlinear parameter α (and in the resonant frequency f_0) are extremely dissimilar between each samples. Nonetheless, Fig. 10 shows that more comparable increases of the nonlinear parameter α and very similar decreases of the resonant frequency f_0 are reached for a given relative change in water content. Therefore, the NRUS parameters could be more affected by water content variations than by the absolute water content amount within the samples.

After one adsorption-desorption cycle, changes caused in the resonant frequency f_0 and in the nonlinear parameter α by RH fluctuations seem reversible as similar values for the nonlinear parameter α are reached at 12% RH at the beginning and at the end of the adsorption-desorption cycle (Fig. 11). The evolutions of the resonant frequency f_0 and of the nonlinear parameter α were therefore followed during 10 adsorption-desorption cycles (Fig. 12) to verify this hypothesis on a longer-term experiment. Overall, the results tend to validate the hypothesis of reversibility (Fig. 12). The resonant frequency f_0 at 12% RH displays a slight increase during cycling (up to 13% for the sample heated at 85 °C). However, it remains constant at 96% RH for all the samples. The nonlinear parameter α at 12% and 96% RH does not remain completely steady during cycling. Nevertheless, it does not exhibit any overall tendency to increase or decrease. It varies around the average value while remaining within the uncertainty range. Therefore, the nonlinear parameter α does not seem permanently affected by RH variation: same values are reached when returning to the initial RH level. Thus, fresh as well as thermally-damaged marble samples exhibit a reversible behavior with RH variations. Therefore, climatic RH fluctuations alone do not seem able to lead to a permanent weakening or deformation of Carrara Gioia marble.

5 Conclusions

The effects of RH variations on Carrara Gioia marble were investigated with NRUS through the evolution of the resonant frequency f_0 and of the nonlinear parameter α during single and multiple adsorption-desorption cycles. The impact of the coupling between thermal damage and exposure to RH fluctuations is also investigated as Carrara marble samples were previously thermally-damaged by heating between 40 and 105 °C.

The decrease of the resonant frequency f_0 with increasing RH could reflect the onset of moisture-induced softening. The nonlinear parameter α is extremely sensitive to RH changes and is affected by hysteretic phenomena occurring during adsorption-desorption cycle. The increase in nonlinearity with RH could be due to capillary condensation occurring in pore network. The intensity of NRUS parameters variation seems more linked to water content variation than to thermal damage degree (and therefore total amount of porosity) or to absolute water content.

Nonetheless, adsorption-desorption cycling does not lead to an overall significant decrease or increase of the resonant frequency f_0 or of the nonlinear parameter α. Therefore, under stable temperature conditions, microstructural phenomena at stake in Carrara Gioia samples subjected to RH variations could be reversible. This work shows that exposure to cyclical RH fluctuations alone cannot lead to permanent weakening/deformation of Carrara marble. This reversibility is observed for five increasing degrees of thermal deterioration, meaning that RH cycling does not permanently impact Carrara marble no matter its degradation state. Nevertheless, RH variations could play a role to initiate or enhance some alterations when they are coupled to other agents (salt crystallizations, thermal variations, etc.).

Author contributions

Conceptualization, P.B., J.B., C.P.; supervision, P.B., J.B., C.P.; investigation, M.L.C., J.H.; visualization, M.L.C.; writing – original draft, M.L.C.; writing – review & editing, M.L.C., P.B., J.B., C.P.

Competing interests statement

The authors declare that they have no known competing financial interests or personal relationships that could have appeared to influence the work reported in this paper.

Funding sources

This research did not receive any specific grant from funding agencies in the public, commercial, or not-for-profit sectors.

Acknowledgements

Authors wish to thank Alain Tonetto and Louis Godaert (PRATIM, Aix Marseille Univ, France) for their help with the SEM observations.

References

[1] ICOMOS-ISCS, Illustrated glossary on stone deterioration patterns - Glossaire illustré sur les formes d'altération de la pierre, Paris, 2008.

[2] B. Grelk, P. Goltermann, B. Schouenborg, A. Koch, L. Alneas, The laboratory testing of potential bowing and expansion of marble, in: Proceedings of the International Conference on Dimension Stone, Taylor & Francis Group plc, A.A. Balkerma Publische, Prague, Czech Republic, 2004: pp. 253–259.

[3] A. Koch, S. Siegesmund, The combined effect of moisture and temperature on the anomalous expansion behaviour of marble, Env Geol 46 (2004). https://doi.org/10.1007/s00254-004-1037-9.

[4] S. Siegesmund, J. Ruedrich, A. Koch, Marble bowing: comparative studies of three different public building facades, Environ Geol 56 (2008) 473–494. https://doi.org/10.1007/s00254-008-1307-z.

[5] M.L. Lin, F.S. Jeng, L.S. Tsai, T.H. Huang, Wetting weakening of tertiary sandstones—microscopic mechanism, Environ Geol 48 (2005) 265–275. https://doi.org/10.1007/s00254-005-1318-y.

[6] X. Li, K. Peng, J. Peng, D. Hou, Experimental investigation of cyclic wetting-drying effect on mechanical behavior of a medium-grained sandstone, Engineering Geology 293 (2021) 106335. https://doi.org/10.1016/j.enggeo.2021.106335.

[7] H. Li, Y. Qiao, R. Shen, M. He, T. Cheng, Y. Xiao, J. Tang, Effect of water on mechanical behavior and acoustic emission response of sandstone during loading process: phenomenon and mechanism, Engineering Geology 294 (2021) 106386. https://doi.org/10.1016/j.enggeo.2021.106386.

[8] E. Verstrynge, R. Adriaens, J. Elsen, K. Van Balen, Multi-scale analysis on the influence of moisture on the mechanical behavior of ferruginous sandstone, Construction and Building Materials 54 (2014) 78–90. https://doi.org/10.1016/j.conbuildmat.2013.12.024.

[9] J. Berthonneau, P. Bromblet, F. Cherblanc, E. Ferrage, J.-M. Vallet, O. Grauby, The spalling decay of building bioclastic limestones of Provence (South East of France): From clay minerals swelling to hydric dilation, Journal of Cultural Heritage 17 (2016) 53–60. https://doi.org/10.1016/j.culher.2015.05.004.
[10] F. Cherblanc, J. Berthonneau, P. Bromblet, V. Huon, Influence of Water Content on the Mechanical Behaviour of Limestone: Role of the Clay Minerals Content, Rock Mech Rock Eng 49 (2016) 2033–2042. https://doi.org/10.1007/s00603-015-0911-y.
[11] S. Taibi, A. Duperret, J.-M. Fleureau, The effect of suction on the hydro-mechanical behaviour of chalk rocks, Engineering Geology 106 (2009) 40–50. https://doi.org/10.1016/j.enggeo.2009.02.012.
[12] Á. Török, B. Vásárhelyi, The influence of fabric and water content on selected rock mechanical parameters of travertine, examples from Hungary, Engineering Geology 115 (2010) 237–245. https://doi.org/10.1016/j.enggeo.2010.01.005.
[13] Á. Rabat, M. Cano, R. Tomás, Effect of water saturation on strength and deformability of building calcarenite stones: Correlations with their physical properties, Construction and Building Materials 232 (2020) 117259. https://doi.org/10.1016/j.conbuildmat.2019.117259.
[14] Á. Rabat, R. Tomás, M. Cano, Evaluation of mechanical weakening of calcarenite building stones due to environmental relative humidity using the vapour equilibrium technique, Engineering Geology 278 (2020) 105849. https://doi.org/10.1016/j.enggeo.2020.105849.
[15] S. Yasar, Long term wetting characteristics and saturation induced strength reduction of some igneous rocks, Environ Earth Sci 79 (2020) 353. https://doi.org/10.1007/s12665-020-09105-0.
[16] E.M. Van Eeckhout, The mechanisms of strength reduction due to moisture in coal mine shales, International Journal of Rock Mechanics and Mining Sciences & Geomechanics Abstracts 13 (1976) 61–67. https://doi.org/10.1016/0148-9062(76)90705-1.
[17] X. Cai, Z. Zhou, K. Liu, X. Du, H. Zang, Water-Weakening Effects on the Mechanical Behavior of Different Rock Types: Phenomena and Mechanisms, Applied Sciences 9 (2019) 4450. https://doi.org/10.3390/app9204450.
[18] Y. Mahmutoğlu, The effects of strain rate and saturation on a micro-cracked marble, Engineering Geology 82 (2006) 137–144. https://doi.org/10.1016/j.enggeo.2005.09.001.
[19] B. Vasarhelyi, K. Ledniczky, Influence of water-saturation and weathering on mechanical properties of Sivac marble, in: Paris, France, 1999: pp. 691–694.
[20] J. Zhu, J. Deng, F. Chen, Y. Huang, Z. Yu, Water Saturation Effects on Mechanical and Fracture Behavior of Marble, Int. J. Geomech. 20 (2020) 04020191. https://doi.org/10.1061/(ASCE)GM.1943-5622.0001825.
[21] T. Waragai, Influence of thermal cycling in the mild temperature range on the physical properties of cultural stones, Journal of Cultural Heritage 59 (2023) 171–180. https://doi.org/10.1016/j.culher.2022.12.001.
[22] S. Siegesmund, J. Menningen, V. Shushakova, Marble decay: towards a measure of marble degradation based on ultrasonic wave velocities and thermal expansion data, Environ Earth Sci 80 (2021) 395. https://doi.org/10.1007/s12665-021-09654-y.
[23] L.A. Ostrovsky, P.A. Johnson, Dynamic nonlinear elasticity in geomaterials, Riv. Nuovo Cim. 24 (2001) 1–46. https://doi.org/10.1007/BF03548898.
[24] J.A. Ten Cate, T.J. Shankland, Slow dynamics in the nonlinear elastic response of Berea sandstone, Geophys. Res. Lett. 23 (1996) 3019–3022. https://doi.org/10.1029/96GL02884.
[25] R.A. Guyer, P.A. Johnson, Nonlinear Mesoscopic Elasticity: Evidence for a New Class of Materials, Physics Today 52 (1999) 30–36. https://doi.org/10.1063/1.882648.
[26] P.A. Johnson, B. Zinszner, P. Rasolofosaon, F. Cohen-Tenoudji, K. Van Den Abeele, Dynamic measurements of the nonlinear elastic parameter α in rock under varying conditions: NONLINEAR ELASTIC PARAMETER IN ROCK, J. Geophys. Res. 109 (2004). https://doi.org/10.1029/2002JB002038.
[27] P. Johnson, A. Sutin, Slow dynamics and anomalous nonlinear fast dynamics in diverse solids, The Journal of the Acoustical Society of America 117 (2005) 124–130. https://doi.org/10.1121/1.1823351.

[28] K.E.-A. Van Den Abeele, Influence of water saturation on the nonlinear elastic mesoscopic response in Earth materials and the implications to the mechanism of nonlinearity, J. Geophys. Res. 107 (2002) 2121. https://doi.org/10.1029/2001JB000368.
[29] V.S. Averbakh, V.V. Bredikhin, A.V. Lebedev, S.A. Manakov, Nonlinear acoustic spectroscopy of carbonate rocks, Acoust. Phys. 63 (2017) 346–358. https://doi.org/10.1134/S1063771017030022.
[30] L. Gao, P. Shokouhi, J. Rivière, Effect of Grain Shape and Relative Humidity on the Nonlinear Elastic Properties of Granular Media, Geophysical Research Letters 50 (2023) e2023GL103245. https://doi.org/10.1029/2023GL103245.
[31] L. Gao, P. Shokouhi, J. Rivière, Effect of relative humidity on the nonlinear elastic response of granular media, Journal of Applied Physics 131 (2022) 055101. https://doi.org/10.1063/5.0073967.
[32] T. Weiss, P.N.J. Rasolofosaon, S. Siegesmund, Ultrasonic wave velocities as a diagnostic tool for the quality assessment of marble, Geological Society, London, Special Publications 205 (2002) 149–164. https://doi.org/10.1144/GSL.SP.2002.205.01.12.
[33] E. Sassoni, G. Graziani, G. Ridolfi, M.C. Bignozzi, E. Franzoni, Thermal behavior of Carrara marble after consolidation by ammonium phosphate, ammonium oxalate and ethyl silicate, Materials & Design 120 (2017) 345–353. https://doi.org/10.1016/j.matdes.2017.02.040.
[34] P.A. Johnson, Nonlinear Elastic Wave NDE I. Nonlinear Resonant Ultrasound Spectroscopy and Slow Dynamics Diagnostics, in: AIP Conference Proceedings, AIP, Golden, Colorado (USA), 2005: pp. 377–384. https://doi.org/10.1063/1.1916701.
[35] M.C. Remillieux, R.A. Guyer, C. Payan, T.J. Ulrich, Decoupling Nonclassical Nonlinear Behavior of Elastic Wave Types, Phys. Rev. Lett. 116 (2016) 115501. https://doi.org/10.1103/PhysRevLett.116.115501.
[36] C. Mechri, M. Scalerandi, M. Bentahar, Separation of Damping and Velocity Strain Dependencies using an Ultrasonic Monochromatic Excitation, Phys. Rev. Applied 11 (2019) 054050. https://doi.org/10.1103/PhysRevApplied.11.054050.
[37] L.A. Ostrovsky, P.A. Johnson, Nonlinear dynamics of rock: Hysteretic behavior, Radiophysics and Quantum Electronics 44 (2001) 450–464. https://doi.org/10.1023/A:1017953331645.
[38] C. Payan, T.J. Ulrich, P.Y. Le Bas, T. Saleh, M. Guimaraes, Quantitative linear and nonlinear resonance inspection techniques and analysis for material characterization: Application to concrete thermal damage, The Journal of the Acoustical Society of America 136 (2014) 537–546. https://doi.org/10.1121/1.4887451.
[39] P. Rasolofosaon, B. Zinszner, P.A. Johnson, Propagation des ondes élastiques dans les matériaux non linéaires Aperçu des résultats de laboratoire obtenus sur les roches et des applications possibles en géophysique, Rev. Inst. Fr. Pét. 52 (1997) 585–608. https://doi.org/10.2516/ogst:1997061.
[40] H. Yiming, D. Jianhui, Z. Jun, An Experimental Investigation of Moisture-Induced Softening Mechanism of Marble Based on Quantitative Analysis of Acoustic Emission Waveforms, Applied Sciences 9 (2019) 446. https://doi.org/10.3390/app9030446.
[41] K.S.W. Sing, R.T. Williams, Physisorption Hysteresis Loops and the Characterization of Nanoporous Materials, Adsorption Science & Technology 22 (2004) 773–782. https://doi.org/10.1260/0263617053499032.

Table 1 Impact of heating temperature on Carrara Gioia marble microstructure probed by mercury intrusion porosimetry.

Heating temperature	Total porosity (%)	Pore size distribution (% of total porosity)				
		0.01 – 0.1 μm	0.1 – 1 μm	1 – 10 μm	10 – 100 μm	> 100 μm
unheated	0.81	5.11	49.9	12.12	16.90	16.21
40 °C	1.07	3.78	55.38	14.81	14.14	11.77
65 °C	1.58	2.84	33.56	10.78	24.94	27.88
85 °C	1.61	2.46	40.96	24.37	20.82	11.40
105 °C	2.59	0.97	29.79	23.32	21.34	24.59

Supplementary material: NRUS data

Tables of the NRUS results for the different hygric states.

Table 1 Resonant frequency values during the first adsorption-desorption cycle

Resonant frequency f_0 (Hz) during adsorption (1st cycle)								
RH	12%	33%	44%	52%	66%	76%	86%	96%
unheated	6480.1 ± 0.7	6454 ± 4	6434.8 ± 0.4	6396 ± 7	6295 ± 3	6190 ± 7	6090 ± 20	5909 ± 8
40 °C	6337.5 ± 0.3	6315 ± 4	6303 ± 2	6283 ± 3	6225 ± 4	6156 ± 7	6080 ± 10	5910 ± 10
65 °C	5145 ± 6	5104 ± 5	5058 ± 3	4950 ± 20	4700 ± 10	4524 ± 7	4430 ± 10	4320 ± 10
85 °C	3890 ± 4	3862 ± 5	3824 ± 7	3758 ± 4	3620 ± 10	3510 ± 6	3450 ± 10	3400 ± 20
105 °C	3507 ± 6	3458 ± 5	3418 ± 9	3366 ± 5	3270 ± 10	3195 ± 4	3150 ± 10	3110 ± 10
Resonant frequency f_0 (Hz) during desorption (1st cycle)								
RH	12%	33%	44%	52%	66%	76%	86%	96%
unheated	6587 ± 2	6537 ± 7	6450 ± 10	6349 ± 5	6250 ± 10	6164 ± 5	6030 ± 20	5910 ± 30
85 °C	4128 ± 4	4045 ± 7	3907 ± 9	3757 ± 5	3648 ± 9	3580 ± 10	3480 ± 10	3423 ± 9

Table 2 Nonlinear parameter values during the first adsorption-desorption cycle

Nonlinear parameter α (x 10^3) during adsorption (1st cycle)								
RH	12%	33%	44%	52%	66%	76%	86%	96%
unheated	3.8 ± 0.5	5.1 ± 0.3	5.7 ± 0.3	7.0 ± 0.4	8.7 ± 0.6	11.0 ± 0.3	14 ± 1	16 ± 1
40 °C	4.8 ± 0.4	6.5 ± 0.2	7.1 ± 0.3	8.0 ± 0.4	9.4 ± 0.8	11.7 ± 0.3	14 ± 1	18.0 ± 0.9
65 °C	5.5 ± 0.6	7.7 ± 0.6	9.0 ± 0.4	11.5 ± 0.1	16 ± 1	18.2 ± 0.6	23 ± 3	25 ± 3
85 °C	9.5 ± 0.3	13.0 ± 0.4	15.5 ± 0.8	19.5 ± 0.5	26 ± 2	33 ± 2	39 ± 3	43 ± 2
105 °C	8 ± 1	10.9 ± 0.2	12.8 ± 0.6	16 ± 1	20 ± 2	24 ± 1	27 ± 3	32 ± 3
Nonlinear parameter α (x 10^3) during desorption (1st cycle)								
RH	12%	33%	44%	52%	66%	76%	86%	96%
unheated	4.13 ± 0.09	6.1 ± 0.2	8.0 ± 0.9	10.3 ± 0.5	13.7 ± 0.7	15.4 ± 0.4	18 ± 1	20 ± 0.6
85 °C	10 ± 1	16.5 ± 0.5	23 ± 1	33 ± 1	42 ± 3	45 ± 2	46 ± 2	48 ± 7

Table 3 Resonant frequency values during 10 adsorption-desorption cycles

Resonant frequency f_0 (Hz) during adsorption-desorption cycling											
Number of cycles		1	2	3	4	5	6	7	8	9	10
unheated	12% RH	6480.1 ± 0.7	6587 ± 2	6662 ± 7	6706 ± 7	6740 ± 7	6737 ± 8	6737 ± 7	6771 ± 9	6776 ± 8	6770 ± 10
	96% RH	5909 ± 8	6050 ± 40	6060 ± 10	6050 ± 20	6040 ± 20	6050 ± 20	6040 ± 40	6030 ± 50	6040 ± 20	6026 ± 5
40 °C	12% RH	6337.5 ± 0.3	/	6508 ± 7	6510 ± 8	6529 ± 8	6533 ± 8	6533 ± 10	6560 ± 10	6570 ± 10	6570 ± 20
	96% RH	5910 ± 10	/	6090 ± 20	6070 ± 20	6040 ± 20	6060 ± 20	6040 ± 30	6040 ± 40	6050 ± 20	6038 ± 4
65 °C	12% RH	5145 ± 6	/	5462 ± 6	5530 ± 10	5588 ± 8	5590 ± 10	5590 ± 20	5650 ± 10	5670 ± 10	5672 ± 9
	96% RH	4320 ± 10	/	4470 ± 10	4450 ± 10	4420 ± 20	4420 ± 10	4440 ± 20	4420 ± 40	4440 ± 20	4461 ± 2
85 °C	12% RH	3890 ± 4	4128 ± 4	4212 ± 5	4270 ± 10	4313 ± 2	4310 ± 10	4310 ± 20	4380 ± 20	4393 ± 9	4392 ± 7
	96% RH	3400 ± 20	3491 ± 9	3480 ± 10	3440 ± 8	3410 ± 20	3390 ± 10	3450 ± 50	3400 ± 100	3420 ± 20	3469 ± 4
105 °C	12% RH	3507 ± 6	/	3761 ± 1	3796 ± 9	3824 ± 3	3824 ± 9	3820 ± 20	3887 ± 8	3901 ± 4	3910 ± 3
	96% RH	3110 ± 10	/	3180 ± 20	3140 ± 30	3110 ± 30	3070 ± 10	3130 ± 40	3000 ± 100	3110 ± 30	3159 ± 5

Table 4 Nonlinear parameter values during 10 adsorption-desorption cycles

Nonlinear parameter α (x 10^3) during adsorption-desorption cycling											
Number of cycles		1	2	3	4	5	6	7	8	9	10
unheated	12% RH	3.8 ± 0.5	4.13 ± 0.09	4.1 ± 0.7	4.0 ± 0.7	3.8 ± 0.7	4.0 ± 0.6	4.0 ± 0.6	3.8 ± 0.4	3.9 ± 0.6	4.3 ± 0.03
	96% RH	16 ± 1	19 ± 1	19 ± 1	20 ± 2	20 ± 1	20 ± 2	21 ± 2	19 ± 4	19.0 ± 0.9	21 ± 2
40 °C	12% RH	4.8 ± 0.4	/	5.3 ± 0.9	5.7 ± 0.9	5.8 ± 0.9	6.1 ± 0.7	6 ± 1	6.1 ± 0.7	6.1 ± 0.9	6.2 ± 0.6
	96% RH	18.0 ± 0.9	/	17 ± 2	18 ± 1	19 ± 2	20.4 ± 0.6	21 ± 2	20 ± 3	19.8 ± 0.6	20 ± 2
65 °C	12% RH	5.5 ± 0.6	/	6 ± 1	6 ± 1	5 ± 1	6 ± 1	6 ± 1	5 ± 1	5 ± 1	6 ± 1
	96% RH	25 ± 3	/	25 ± 2	28 ± 1	28 ± 1	29 ± 1	31 ± 2	27 ± 4	29 ± 1	29.4 ± 0.9
85 °C	12% RH	9.5 ± 0.3	10 ± 1	10 ± 3	9 ± 3	9 ± 2	10 ± 3	9 ± 3	8 ± 2	9 ± 3	9 ± 3
	96% RH	43 ± 2	49 ± 4	47 ± 3	50 ± 5	48 ± 1	52 ± 3	53 ± 7	39 ± 6	49 ± 4	49 ± 5
105 °C	12% RH	8 ± 1	/	9 ± 2	9 ± 2	8 ± 2	10 ± 2	9 ± 2	9 ± 2	9 ± 2	9 ± 2
	96% RH	32 ± 3	/	31 ± 7	38 ± 2	38 ± 5	41 ± 2	42 ± 5	33 ± 4	40 ± 4	41 ± 3

C. Article published in the *Bulletin of Engineering Geology and the Environment*

Article published in the Bulletin of Engineering Geology and the Environment, volume 83, number 383, 06 September 2024.
DOI: 10.1007/s10064-024-03875-8
Accepted version below.

Progressive Thermal Decohesion in Carrara Marble Monitored with Nonlinear Resonant Ultrasound Spectroscopy

Marie-Laure Chavazas[1, 2] *, Philippe Bromblet[2], Jérémie Berthonneau[2], Jérémy Hénin[3], Cédric Payan[1]

[1] Aix Marseille Univ, CNRS, Centrale Marseille, LMA UMR 7031, Marseille, France

[2] Centre Interdisciplinaire de Conservation et de Restauration du Patrimoine, Marseille, France

[3] Ministère de la Culture, Laboratoire de Recherche des Monuments Historiques

* Corresponding author. E-mail: chavazas@lma.cnrs-mrs.fr. ORCID: 0000-0003-2680-5563

ORCID contributing authors: Philippe Bromblet: 0000-0002-8735-1481 / Jérémie Berthonneau: 0000-0003-2354-5567

Acknowledgements

Authors wish to thank Alain Tonetto and Louis Godaert (PRATIM, Aix Marseille Univ, France) for their help with the SEM observations, Nathalie Gandolfo (CICRP, Marseille, France) for the thin section preparation, and Laurent Sabatier and Sophie Steinlin (LMA, Marseille, France) for their help with the uniaxial compressive strength tests.

Author contributions

Cédric Payan, Philippe Bromblet and Jérémie Berthonneau contributed to the study conception and design. Material preparation, data collection and analysis were performed by Marie-Laure Chavazas and Jérémy Hénin. The first draft of the manuscript was written by Marie-Laure Chavazas and all authors commented on previous versions of the manuscript. All authors read and approved the final manuscript.

Abstract

Marble has been used in sculpture and architecture since Antiquity. When exposed outdoors, it is subjected to physical, chemical, or biological weathering. Studies have shown that some deterioration (bowing, microcrack generation, thermal damage) can result from the exposure to cyclical thermal variations, but the actual temperature range triggering these phenomena remains unknown. Specifically, it is not yet understood if these phenomena are activated at a certain threshold temperature or by prolongated cyclic temperature exposure . In this work, the evolution of the mechanical state of Carrara Gioia marble samples under thermal stress is followed by means of Nonlinear Resonant Ultrasound Spectroscopy (NRUS). The results show, on the one hand, a progressive decrease of the linear parameter (resonant frequency) with heating temperature. This evolution agrees with results from previous works and with the consequent evolution of the microstructure. The (nonclassical) nonlinear parameter, on the other hand, exhibits an increase in the mild temperature range (40 – 85°C), followed by a decrease for the highest temperatures (85 – 250°C). This evolution of the NRUS parameters, as well as microstructural observations, depicts mild temperature induced degradation in Carrara marble. Carrara marble decohesion starts at the mesoscopic scale as evidenced by the initial increase in the nonlinear parameter, and then progressively expands to the macroscopic scale as highlighted by the resonant frequency evolution.

Keywords: Carrara marble; thermal weathering; nonlinear resonant ultrasound; nondestructive testing

1 Introduction

Carrara marble is a well-appreciated and well-known marble variety used in sculpture and architecture since Antiquity (Primavori 2015). It can undergo diverse deteriorations during its aging such as sugaring, thermal damage, bowing, microcrack generation, loss of mechanical resistance. Many studies have shown the significant role of temperature variations in marble degradation (Kessler 1919; Lord Rayleigh 1934; Mahmutoglu 1998; Ferrero and Marini 2001; Siegesmund et al. 2008; Peng et al. 2019; Sena Da Fonseca et al. 2021). The sensitivity of marble to thermal weathering is generally explained by the anisotropy of the thermal dilation coefficient of calcite, the main mineralogical component of calcitic marble (Siegesmund et al. 2000a; Grelk et al. 2004; Malaga-Starzec et al. 2006). The anisotropic expansion/contraction of calcite crystals during heating/cooling cycles generates intergranular decohesion between calcite grains. Such phenomenon has classically been recreated in laboratories by applying artificial weathering on fresh marble by means of thermal degradation between 100 and 500 °C (Ferrero and Marini 2001; Koch and Siegesmund 2004; Sassoni et al. 2017; Sena Da Fonseca et al. 2021). Yet, the study of thermal weathering induced by exposure to mild temperatures is particularly relevant as these temperatures are often recorded on the surface of marble exposed outdoors. From an onsite monitoring campaign and a comprehensive literature review, Schouenborg et al. (2007) concluded that the maximum temperature reached on white Carrara marble surface was about 60 °C. Besides, the environmental monitoring made on marble in the central Namib desert for three years by Viles (2005) showed that marble surface temperature reaches 55 °C, with a maximum air temperature of 37 °C. Some studies already indicate marble deterioration in the mild temperature range (Malaga et al. 2002; Schouenborg et al. 2007; Gherardi et al. 2019; Waragai 2023). For instance, Schouenborg et al. (2007) recommended to condition marble at 40 °C rather than 70 °C since a considerable loss of mechanical strength was observed for temperatures lower than 70 °C. Besides, Malaga et al. (2002) suggested that intergranular decohesion could occur between 40 and 50 °C for some marble varieties, based on porosity measurements on calcitic and dolomitic marbles heated between 40 and 200 °C.

The evolution of marble thermal degradation can be monitored by various techniques. Mechanical properties are usually evaluated by destructive testing: Brazilian test, uniaxial compression test, flexural strength test (Mahmutoglu 1998; Ferrero and Marini 2001; Marini and Bellopede 2007, 2009; Siegesmund et al. 2008). Due to their destructive nature, these tests do not allow following the evolution of damage in one sample during thermal weathering. However, mechanical properties can also be probed using nondestructive methods. For example, ultrasound-based techniques have been developed to characterize marble degradation. Ultrasonic pulse velocity allows monitoring the deterioration of the same sample all along the ageing process (Weiss et al. 2002; Malaga-Starzec et al. 2006; Marini and Bellopede 2007, 2009; Siegesmund et al. 2021; Zhang et al. 2022; Wu et al. 2023; Sáez-Pérez et al. 2024). Ultrasound tomography can provide a mapping of the inner degradation state of samples without damaging them during the experiment (Siegesmund et al. 2021). Resonance methods also enable probing and monitoring the mechanical state of materials. In fact, Resonant Ultrasound Spectroscopy (RUS) method (Migliori and Sarrao 1997) was developed in the early 2000s and successfully applied for characterization of rocks (Ulrich et al. 2002; Remillieux et al. 2015). The Nonlinear Resonant Ultrasound Spectroscopy (NRUS) method was also developed in the same period when it was found that noticeable nonlinear phenomena occurred in rocks when increasing vibration amplitude. Rocks and geomaterials fall in the nonclassical class of nonlinear media which exhibit features such as hysteresis, slow dynamics, end-point memory (Ten Cate and Shankland 1996; Guyer and Johnson 1999; Ostrovsky and Johnson 2001a; Johnson et al. 2004; Johnson and Sutin 2005). These nonlinear phenomena are found to be highly sensitive to any change (microcracks, relative humidity, etc.) at the microstructural scale. Nonclassical nonlinearity has been investigated in diverse rock types such as sandstone (Ten Cate and Shankland 1996; Van Den Abeele 2002; Johnson et al. 2004; Rivière et al. 2015) and carbonate rocks like marble, limestone and chalk (Van Den Abeele 2002; Johnson et al. 2004; Johnson and Sutin 2005; Averbakh et al. 2017).

However, specific studies on the impact of marble heating on its NRUS response are very limited and present very few data. Johnson et al. (2004) studied the nonclassical nonlinearity in a white Asian marble

(from Turkey) under varying conditions. In their work the nonlinear parameter was first measured in ambient conditions, then after the sample was heated at 200 °C. The 44% drop of the nonlinear parameter value (from 27,006 to 15,251) was interpreted by the authors as an ability of Asian marble to heal itself during the heating process. Yet, no other studies have supported this hypothesis so far and the temperature at which such mechanism may be triggered is unknown, especially within the mild temperatures (40 – 85 °C). The impact of exposure to mild temperatures can be critical for marble artefact preservation. However, this temperature range has not yet been investigated by NRUS even though this technique can bring further information on the underlying degradation mechanisms compared to traditional techniques such as destructive mechanical tests and ultrasonic pulse velocity. Indeed, NRUS does not only probe the macroscopic scale of materials as traditional methods but also the mesoscopic scale, and accounts for other phenomena.

This work aims at investigating further the impact of thermal damage on the NRUS response of Carrara marble, especially at mild temperatures and until its complete granular disintegration, and thus linking the evolution of the NRUS parameters to the changes occurring in marble microstructure. To this end, Carrara marble samples are heated at different temperatures between 40 and 500 °C. Their degradation is then evaluated with NRUS by following the evolution of linear (resonant frequency) and nonlinear (nonclassical parameter) parameters. The nonclassical nonlinear parameter exhibits an unexpected evolution with thermal damage compared to other granular materials. Microstructural and mechanical characterizations are also carried out to investigate the evolution of marble microstructure due to thermal damage.

2 Materials and methods

2.1 Carrara marble samples

A block (45 cm x 45 cm x 20 cm) of fresh Carrara Gioia marble (provided by Logica SRL, Carrara, Italy), a calcitic white veined marble, was used in this study. This variety of Carrara marble was chosen since it has a granoblastic equigranular-polygonal microstructure (Malaga-Starzec et al. 2003; Siegesmund et al. 2008, 2021; Menningen 2020; Menningen et al. 2021). Marbles with this microstructure are expected to be more sensitive to thermal weathering (Royer-Carfagni 1999; Grelk et al. 2004; Åkesson et al. 2006). The microstructure of the studied block is illustrated in Fig. 1. This marble is mainly composed of equigranular monocrystals of calcite (calcium carbonate, $CaCO_3$). The average size of the calcite grains is ca. 300 µm and the grain boundaries are mostly straight.

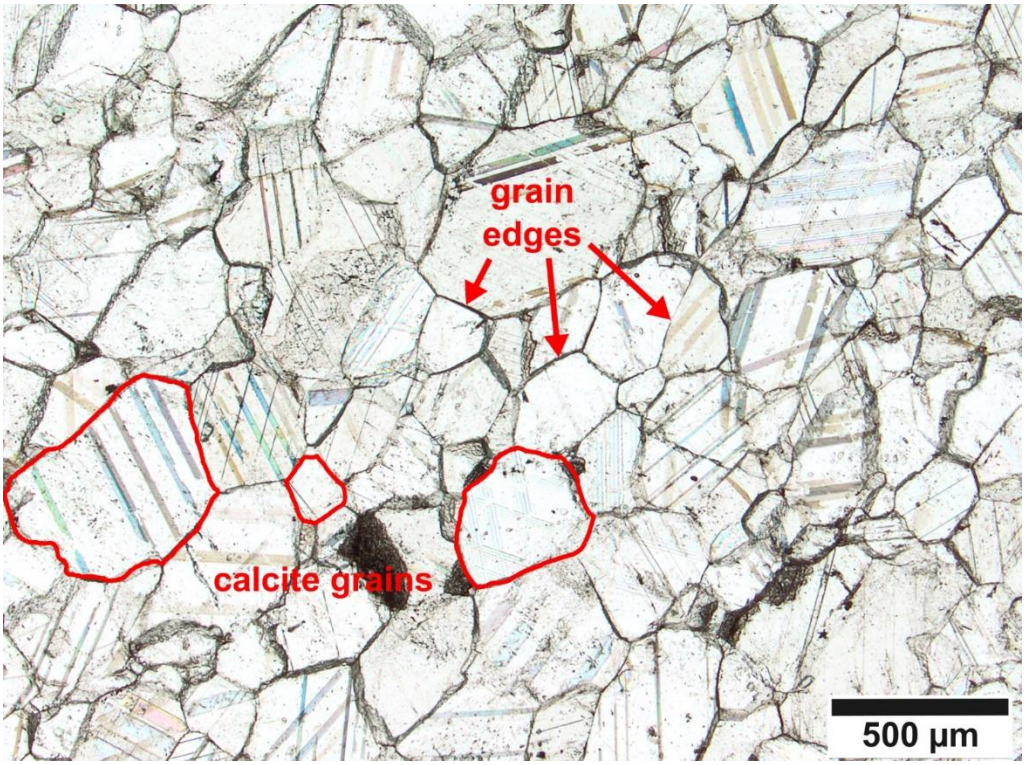

Fig. 1 (Color online) Optical microscope image of a sample of fresh Carrara Gioia marble, magnification x25, plane light. Some calcite grains are circled in red, and some calcite grain edges are indicated by red arrows

The condition and isotropy of the marble block were first checked by measuring ultrasonic pulse velocity. Core samples of 20 cm in height and 4 cm in diameter were then drilled from the block. At this point, reference NRUS measurements (see section 2.2 for details on this technique) were made on each core sample before they undergo any thermal treatment.

To evaluate the influence of temperature on marble weathering, samples were heated in an oven up to various setpoint temperatures. The heating rate was set to 1 °C.min^{-1} to allow the homogeneous heating of the material (Weiss et al. 2002; Sassoni et al. 2017; Siegesmund et al. 2021). The setpoint temperature was maintained for 6 h as in Siegesmund et al. (2021). The cooling down to room temperature was left free. After heating, the samples were stored in a temperature-controlled oven maintained at 23 °C, and they also remained in this oven during the NRUS testing. The setpoint temperatures were the following: 40, 65, 85, 105, 150, 200, 250 and 500 °C. Four core samples were heated per setpoint temperature, and four unheated samples (stocked at 23 °C) were used as references. This temperature set was chosen to explore the impact of natural (40 – 85 °C) (Viles 2005; Schouenborg et al. 2007) as well as artificial (105 – 500 °C) (Ferrero and Marini 2001; Koch and Siegesmund 2004; Sassoni et al. 2017; Sena Da Fonseca et al. 2021) weathering conditions. The interval between each temperature point was first set low to study the influence of several natural heating conditions to evaluate the impact of exposure to climatic conditions on marble alteration. The temperature point at 105 °C was preferred to 100 °C to go beyond the water evaporation point. The highest temperatures (105 – 500 °C) enabled to continue a progressive artificial alteration of marble until its complete granular disintegration (500 °C).

2.2 Nonlinear Resonant Ultrasound Spectroscopy (NRUS)

NRUS consists in exciting a sample at several increasing drive amplitudes to study the evolution of the resonant modes. For linear materials the resonant frequency of a given mode remains constant as the drive

amplitude increases, whereas for nonlinear media a shift towards the low frequencies is observed. Geomaterials, such as marble, exhibit a nonclassical nonlinear behavior. Their modulus K is expressed as (Guyer and Johnson 1999; Van Den Abeele 2002; Johnson et al. 2004; Johnson and Sutin 2005):

$$K = K_0[1 + \beta\varepsilon + \delta\varepsilon^2 + \cdots + \alpha(\Delta\varepsilon, \dot{\varepsilon})] \quad (1)$$

where K_0 is the elastic modulus, β and δ are the classical nonlinear coefficients and α is the nonclassical nonlinear parameter. In nonclassical nonlinear materials, the relative shift in frequency is proportional to the strain amplitude $\Delta\varepsilon$ of the sample:

$$\Delta f / f_0 = \alpha \, \Delta\varepsilon \quad (2)$$

where $\Delta f = f_0 - f$ with f_0 the linear resonant frequency obtained for the lowest drive amplitude and f the resonant frequency for higher drive amplitudes. In this work, only the first longitudinal resonant mode of the core samples is studied. The detection of this mode is facilitated by the sample geometry (cylinders with a large height over diameter ratio). Fig. 2 shows an example of an NRUS scan, obtained for an unheated core sample of Carrara Gioia marble with a resonant frequency f_0 of 6.42 ± 0.03 kHz and a nonlinear parameter α of (5.0 ± 0.4) × 10^3.

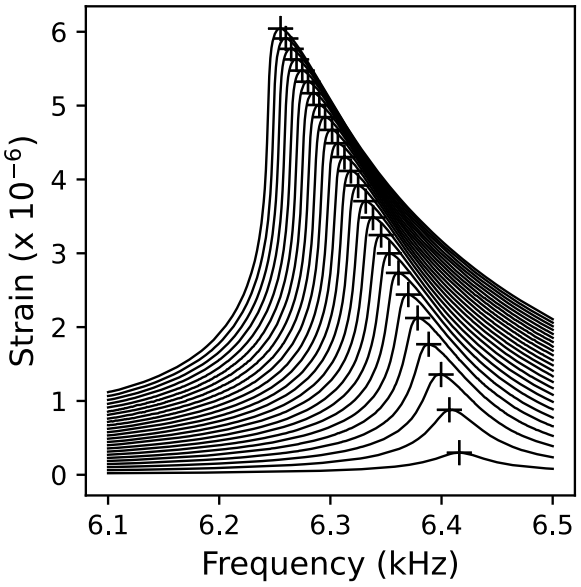

Fig. 2 NRUS curves obtained for an unheated sample of Carrara Gioia marble with a resonant frequency f_0 of 6.42 ± 0.03 kHz and a nonlinear parameter α of (5.0 ± 0.4) × 10^3

Linear and nonlinear parameters extracted from NRUS scans provide information on the mechanical state of a sample. The resonant frequency (linear resonant frequency extracted for the lowest drive amplitude) is related to the stiffness and density of the macroscopic sample. The nonlinear parameter α finds its origin in nonlinear phenomena occurring at the mesoscopic scale of the material, such as opening/closing of microcracks, capillary effects, friction, contacts, dislocations, etc. (Rasolofosaon et al. 1997; Ostrovsky and Johnson 2001a, b; Payan et al. 2014). Therefore, the mesoscopic scale is ranging between the grain contacts and the grain assemblage. Thus, the two parameters account for different phenomena occurring at different scales in the material.

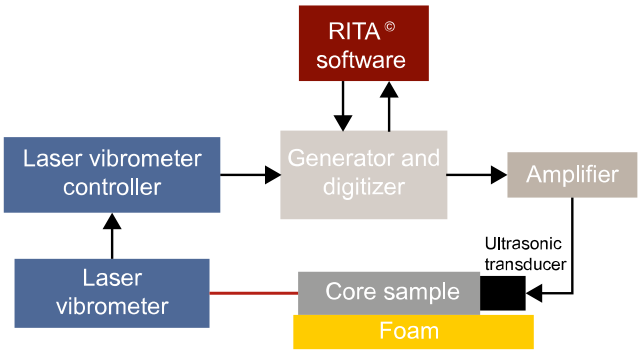

Fig. 3 (Color online) Scheme of the experimental set-up used for the NRUS tests

Fig. 3 illustrates the experimental set-up for the NRUS experiments. The signal generation is managed by RITA© software coupled with a generator (NI PXIe-5406) and an amplifier (NF Electronic Instruments 4005 High Speed). The vibrations are generated in the core sample thanks to an ultrasonic piezoelectric transducer (Beijing Ultrasonic, resonant frequency of 40 kHz) placed at one sample extremity. The piezoelectric transducer was non-permanently glued with phenyl salicylate (also called salol) and unglued between each NRUS scan. The out-of-plane velocity is measured at the other sample extremity with a Polytec laser vibrometer (OFV-505 Single Point Sensor Head and OFV-5000 Controller, $\lambda = 633$ nm (He-Ne), power < 1 mW). The signal acquisition is also managed by RITA© software coupled with a digitizer (NI PXIe-5122). During the signal recording, the tested sample was placed on foam to minimize the attenuation or modification of the vibration modes due to the rigid support. As shown by Fig. 2, the resonant frequency f_0 is directly accessible from the output signal data provided by the laser vibrometer. However, to calculate the nonlinear parameter α by means of Eq. (2), amplitude strain $\Delta\varepsilon$ reached at resonance must be evaluated from the out-of-plane particle velocity amplitude A recorded by the vibrometer at resonance. It is calculated as follows (Remillieux et al. 2016; Mechri et al. 2019):

$$\Delta\varepsilon = \frac{A}{2 * L * f_0} \qquad (3)$$

where L is the sample length and f_0 is the (low amplitude) resonant frequency.

2.3 Microstructural and mechanical characterizations

For each setpoint temperature, two 8 cm long cylinders and centimetric fragments were extracted from one core sample. One fragment was used to characterize marble microstructure with Mercury Intrusion Porosimetry (MIP) using a AutoPore IV 9500 (Micromeritics) working with a maximal pressure of 210 MPa, thus probing pores between 0.01 and 360 µm. Mercury intrusion was measured at 111 increasing pressure points. Another fragment was used to prepare thin sections to perform a petrographic description using a polarized light microscope (Olympus BX-51). The thin sections as well as the remaining freshly cut fragments were also characterized under a Scanning Electron Microscope (SEM, ZEISS EVO 15). The two 8 cm long cylinders were used to measure Uniaxial Compressive Strength (UCS). Uniaxial compression tests were performed on a MTS 809 Axial / Torsional Test System, at a constant displacement rate of 0.24 $mm.min^{-1}$. Two discs of Teflon™ of 1 mm thick and 5.4 cm in diameter were placed on the top and bottom of the sample to correct the lack of strict parallelism of the sample faces and limit edge effect.

3 Results

3.1 Degradation state and variability in the fresh Carrara marble block

Ultrasonic pulse velocity was measured on the whole Carrara marble block, at different points, in the three orthogonal directions. The mean velocities were 3.9 ± 0.1 km.s^{-1}, 4.4 ± 0.2 km.s^{-1} and 3.8 ± 0.4 km.s^{-1}, respectively along the X, Y and Z directions. Based on these values, the block may be considered as a class I marble (Köhler 1991). All core samples were drilled along the same direction (Z).

A first set of NRUS measurements was performed on the drilled core samples before any heating (temperature of 23 ± 0.1°C). The results show some variability among the samples in both resonant frequency f_0 and nonlinear parameter α values. The minimum and maximum values for the resonant frequency f_0 are 4.5 ± 0.2 kHz and 6.9 ± 0.2 kHz, respectively. For the nonlinear parameter α, the minimum and maximum values are $(4.4 \pm 0.7) \times 10^3$ and $(10 \pm 4) \times 10^3$, respectively. The NRUS parameters values acquired at 23 °C are displayed in Fig. 4. The grid is a scheme of the top view of the marble block with each square corresponding to the original sample position. One can note that the resonant frequency value tends to decrease along the X-axis, and that the nonlinear parameter α also exhibits some variability. This variability in the NRUS parameters values does not, however, seem to follow any pattern across the marble block. Nonetheless, the drilled core samples were randomly assigned to the setpoint temperatures to account for this variability and avoid any influence of their original location in the marble block.

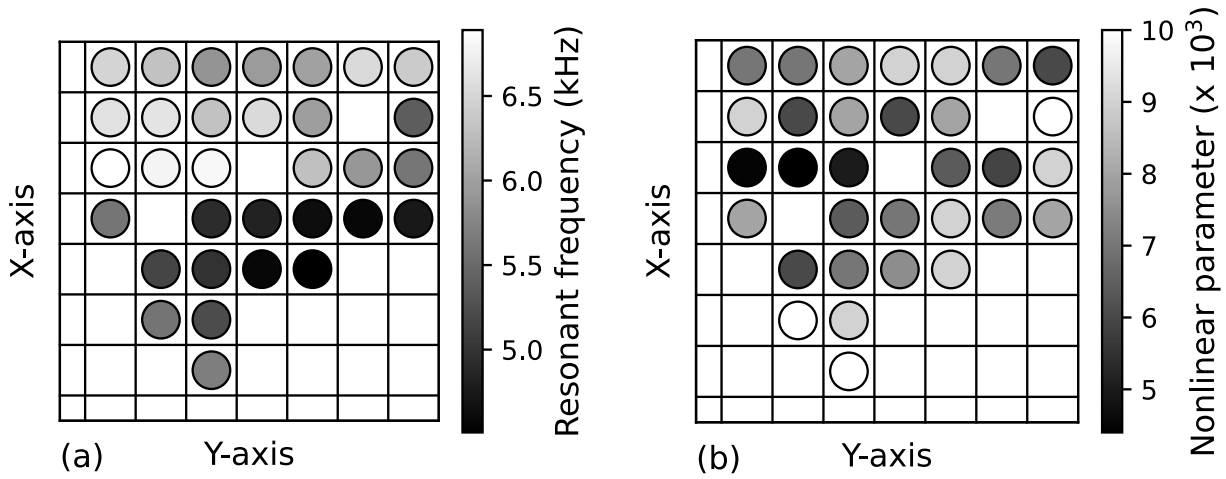

Fig. 4 (a) Resonant frequency and (b) nonlinear parameter values of the tested Carrara samples prior to their heating. The grid schematizes the top view of the marble block. Each square corresponds to the initial position of a core sample in the block

3.2 Influence of heating temperature

32 core samples were used to study the influence of thermal damage on the NRUS response of Carrara marble. 4 samples remained unheated to be used as reference. The other 28 samples were heated up to7 different setpoint temperatures (4 samples heated at each temperature of 40, 65, 85, 105, 150, 200 and 250 °C). All samples were then stored and tested with NRUS in a temperature-controlled oven maintained at 23 ± 0.1 °C. At least three NRUS scans were acquired per sample removing and reattaching the transducer on the sample (using phenyl salicylate) each time. 4 samples were also heated at 500 °C but suffered complete disintegration after the heating, therefore they could not be scanned with NRUS.

The resulting evolutions of the resonant frequency f_0 and of the nonlinear parameter α with heating temperature are displayed in Fig. 5 (a) and (b), respectively. Each point shown on Fig. 5 corresponds to the average value for all NRUS measurements made on all four samples heated at a given temperature. The uncertainties displayed in these figures (shaded areas) correspond to one standard deviation.

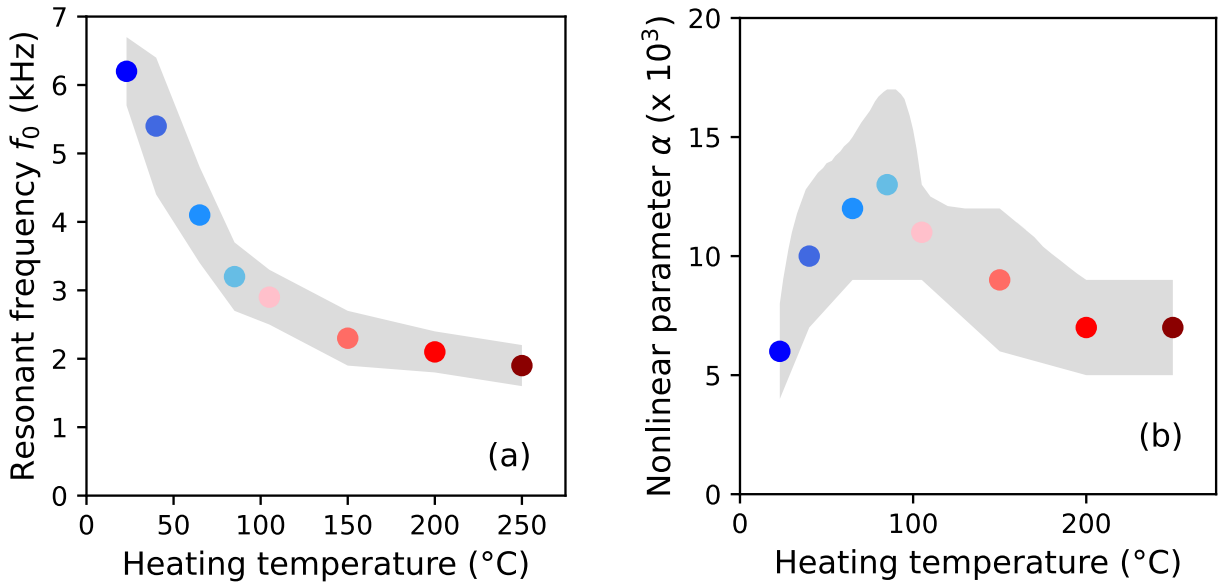

Fig. 5 (Color online) Evolutions of (a) resonant frequency f_0 and of (b) nonlinear parameter α with heating temperature for Carrara Gioia marble. Filled circles correspond to average values of the NRUS parameters. Shaded areas denote one standard deviation

Fig. 5 (a) clearly shows that the resonant frequency f_0 decreases with increasing heating temperature. This parameter ranges from an average of 6.2 ± 0.5 kHz for the unheated samples to an average of 1.9 ± 0.3 kHz for the samples heated at 250 °C, thus exhibiting a global decrease of 69%.

The evolution of the nonlinear parameter α with heating temperature (Fig. 5 (b)) differs from the resonant frequency evolution. For heating temperature between 23 and 85 °C, the nonlinear parameter α increases from an average of $(6 \pm 2) \times 10^3$ to an average of $(13 \pm 4) \times 10^3$. Then, it decreases down to an average of $(7 \pm 2) \times 10^3$ for the samples heated at 250 °C.

Aside from these general trends, the collected data display significant uncertainties, especially for the nonlinear parameter α (Fig. 5 (b)). This could be explained by diverse factors such as the significant variation in the nonlinear parameter values between samples (even prior to thermal treatment as shown on Fig. 4), the reattachment of the piezoelectric transducers on the samples between each NRUS scan with the use of a reversible glue (phenyl salicylate), or by the fact that air relative humidity was not controlled during the

NRUS scans. Nonetheless, the measured variations are still greater than the uncertainties, and the global tendencies are thus robust.

3.3 Microstructural and mechanical evolutions

Microstructural and mechanical characterizations were then performed on the samples to understand the evolution of the NRUS parameters with heating temperature. First, the evolution of porosity and pore size distribution with temperature was probed through Mercury Intrusion Porosimetry (MIP). Fig. 6 presents the total porosity accessible to mercury as a function of the heating temperature of the sample. Fig. 7 indicates the contribution of different porosity classes to the total porosity of each sample.

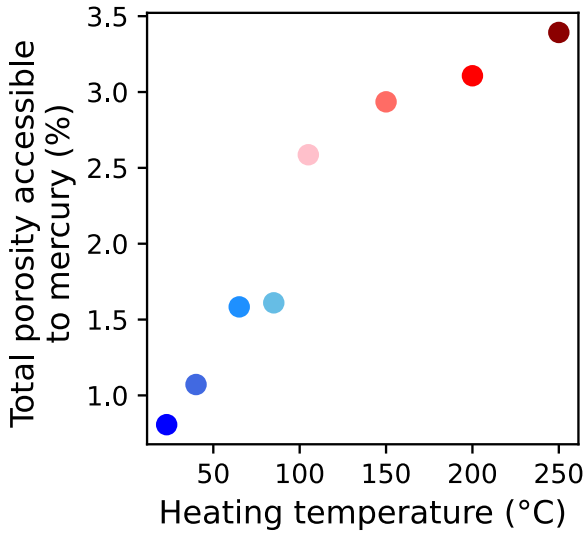

Fig. 6 (Color online) Total porosity (accessible to mercury) of Carrara marble samples heated at different temperatures

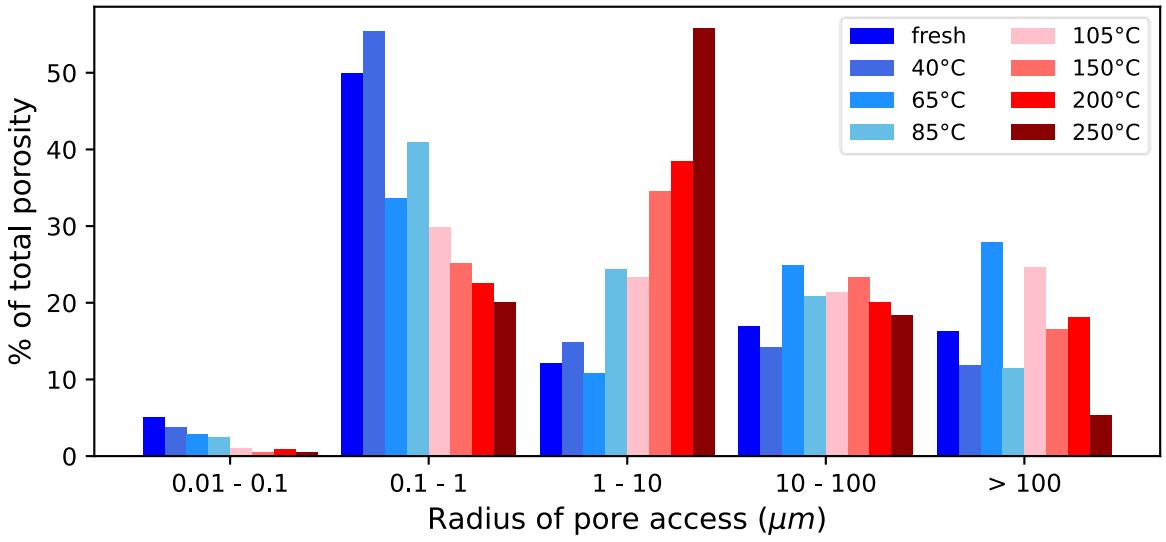

Fig. 7 (Color online) Porosity classes for Carrara marble samples heated at different temperatures

The total porosity accessible to mercury increases with heating temperature, from 0.81% for the unheated sample to 3.39% for the sample heated at 250 °C (Fig. 6). The contribution of five porosity classes to the total porosity was analyzed: radius of pore access between 0.01 and 0.1 µm, between 0.1 and 1 µm, between 1 and 10 µm, between 10 and 100 µm, and above 100 µm. The porosity class with radius of pore access between 0.01 and 1 µm exhibits a tendency to decrease as heating temperature increases whereas the porosity class between 1 and 10 µm tends to increase with heating temperature. The contribution of pore access with a radius between 10 and 100 µm is relatively steady from heating temperature of 65 °C and is lower for the unheated and 40 °C heated samples. The contribution of pores with access radius above 100 µm is quite variable with heating temperature but does not show a clear evolution pattern.

SEM observations were then performed on thin sections and fracture plans to follow the evolution of intergranular spaces. Fig. 8 presents images of fracture plans for the unheated sample and the sample heated at 85 °C, at magnification x100. One can note the widening of the intergranular spaces between the unheated sample and the sample heated at 85 °C. Fig. 9 presents a SEM image of a thin section of marble heated at 150 °C, at magnification x400. It shows that localized microcracking can be found along some grain edges.

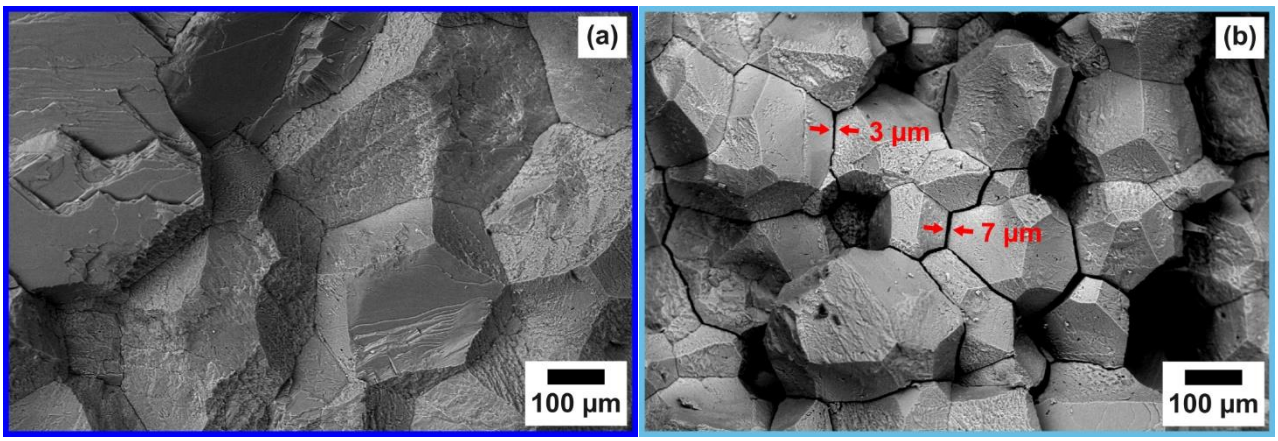

Fig. 8 (Color online) SEM images (magnification x100) on fracture plans of Carrara Gioia for (a) the unheated sample and for (b) the sample heated at 85 °C. Some cracks are indicated between red arrows, along with their width

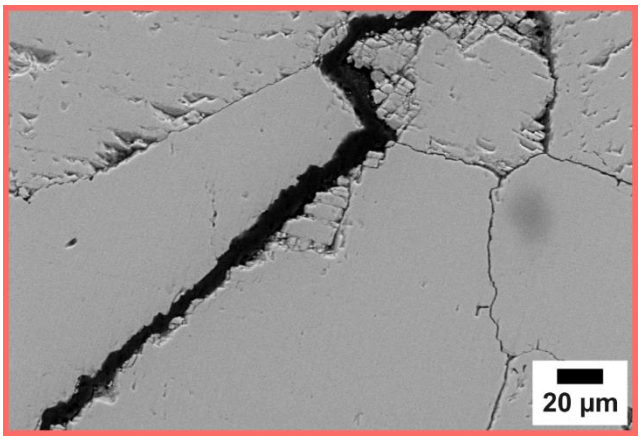

Fig. 9 SEM image (magnification x400) on a thin section of Carrara Gioia marble heated at 150 °C: localized microcracking along grain edges is visible at the center and at the top right of the image

Eventually, mechanical properties of marble samples were destructively probed through uniaxial compression tests. Fig. 10 shows the evolution of Uniaxial Compressive Strength (UCS) with heating temperature. Empty circle data points correspond to the UCS values extracted from two measurements at each heating temperature. The data points were linearly fitted: the linear trend is shown as the dashed line and the fitting parameters are given in the figure. UCS exhibits an overall tendency to decrease with heating

temperature, from 57 MPa at 23 °C to 45 MPa at 250 °C in average. Only one of the two measurements made on the sample heated at 85 °C does not follow the linear trend. No specific reason for this behavior was found: NRUS measurements on this sample did not give scattered values of linear or nonlinear parameters compared to the three other samples heated at 85 °C.

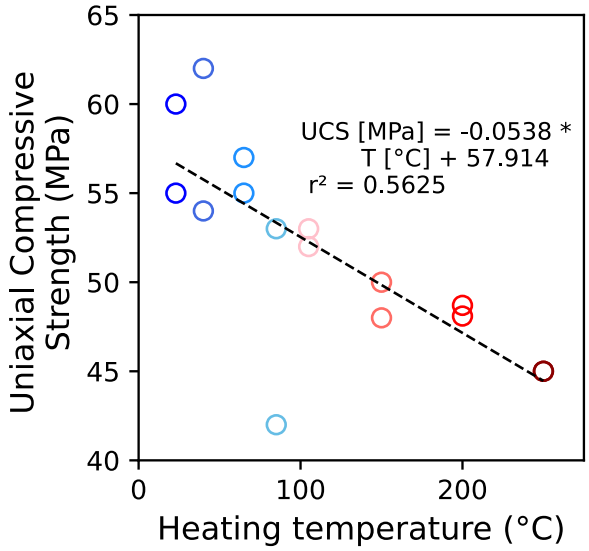

Fig. 10 (Color online) Values of the two UCS measurements (empty circles) made on Carrara marble samples heated at different temperatures, and their linear trend (dashed line)

4 Discussion

Calcite crystals have a strongly anisotropic thermal dilation coefficient: 26×10^{-6} K^{-1} parallel to the crystallographic c-axis and -6×10^{-6} K^{-1} perpendicular to c-axis (Siegesmund et al. 2000b; Grelk et al. 2004). This anisotropy of the thermal dilation coefficient has long been shown to result in the development of intergranular decohesion when calcitic marble is subjected to temperature variations (Siegesmund et al. 2000a; Grelk et al. 2004; Malaga-Starzec et al. 2006). This mechanism could well explain the progressive decrease of resonant frequency f_0 found along this study (Fig. 5), as this parameter is linked to the material stiffness. Indeed, Fig. 11 (a) shows that the resonant frequency f_0 decreases with increasing porosity which reflects the widening of intergranular spaces. This widening is also noticeable in Fig. 7 as the proportion of pores with access radius between 0.01 and 1 µm decreases with heating temperature for the benefit of pores with access radius between 1 and 10 µm. Waragai (2023) found a similar shift in pore access radius of Carrara marble between untreated samples and samples subjected to five thermal cycles between 4 and 84 °C. The progressive loss of cohesion in marble samples as heating temperature increases is also supported by UCS measurements: Fig. 11 (b) shows that the resonant frequency f_0 decreases as the mechanical strength of marble samples diminishes. SEM observations also show that the intergranular spaces widen as heating temperature increases, and that they affect the sample more and more homogenously. Fig. 8 illustrates this phenomenon on a fracture plan for the unheated sample and the sample heated at 85 °C. In addition to microcracks, areas with localized microcracking is visible along some grain edges, as it is shown on Fig. 9. This may be explained by the fact that, during the heating of marble, calcite grains expand parallel to c-axis and thus neighbor grains could enter in contact and undergo friction from shear stress as they do not have the same orientations. Such

friction could be responsible for the localized microcracking on the grain edges. Conversely, during the cooling, calcite grains contract parallel to c-axis and intergranular spaces are created. They result in a loss of cohesion between grains, leading to a loss of stiffness at the macroscopic scale.

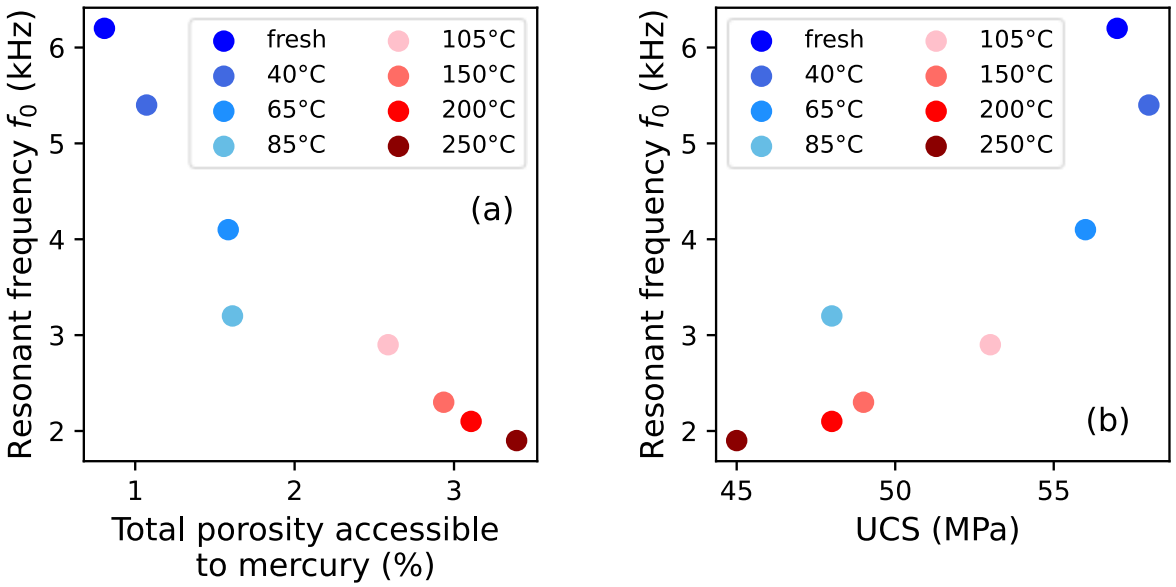

Fig. 11 (Color online) Evolution of resonant frequency f_0 with (a) total porosity accessible to mercury and with (b) UCS in marble samples heated at different temperatures

Even before its heating, the fresh quarried block of Carrara Gioia marble was already exhibiting relatively high levels of nonlinearity. Indeed, the nonlinear parameter α of core samples ranged between $(4.4 \pm 0.7) \times 10^3$ and $(10 \pm 4) \times 10^3$ before heating (see section 3.1 and Fig. 4). Values of the same order are found for Asian white marble in Johnson et al. (2004) (α = 27,006 for ambient conditions). However in other studies, values can be significantly lower, e.g. 149 ± 45 for Carrara marble in Johnson and Sutin (2005). Values measured on this fresh marble block correspond to relatively high levels of nonlinearity and lead to think that numerous features of nonclassical nonlinearity (linked to the quality of grain contacts) are present in the fresh marble block even before thermal weathering.

The nonlinear parameter α is sensitive to deterioration at the mesoscopic scale, i.e., between the size of the grain contacts and the grain assemblage. It is sensitive to very local phenomena occurring at grain contacts such as opening/closing of microcracks or friction (Van Den Abeele et al. 2000; Ostrovsky and Johnson 2001a; Johnson 2005; Johnson and Sutin 2005; Payan et al. 2014). For some granular materials, the nonlinear parameter α exhibits an increase with thermal damage. That is the case for concrete (Payan et al. 2012, 2014), mortar (Genovés et al. 2019) and sandstone (Johnson et al. 2004) for instance. Unlike other granular materials, marble is composed of only one mineral (calcite) and has no cemented material in between grains, which can result in a different nonlinear behavior.

In this study, the nonlinear parameter α increases for heating temperatures between 23 and 85 °C (mild temperature range), and then keeps diminishing for heating temperatures between 85 and 250 °C (Fig. 5 (b)). The initial increase could be explained by the phenomena occurring at intergranular contacts between calcite grains such as the closing/opening of the intergranular spaces created by heating (Fig. 8) and the friction between adjacent grains (Fig. 9). A hypothesis for the subsequent diminution of the nonlinear parameter α is the loss of these intergranular contacts. Indeed, intergranular spaces between calcite grains widen as heating temperature increases, and contacts between adjacent grains are thus gradually lost and with them the local nonlinear phenomena occurring at grain contacts. The porosimetry data support this hypothesis as the total porosity jumps from 1.6% to 2.6% between 85 and 105 °C, and as the radius of pore access is

shifted from between 0.01 and 1 µm to between 1 and 10 µm with increasing heating temperature (Fig. 6 and Fig. 7). This hypothesis thus allows decoupling the thermal degradation affecting Carrara Gioia marble at the mesoscopic scale for the mild heating temperatures (40 – 85 °C), and at progressively higher scale (macroscopic) above 85 °C. Above 85 °C, granular decohesion caused by thermal weathering is so large that nonlinear phenomena at grain contacts are lost. The nonclassical nonlinearity thus provides a helpful alert tool for the detection of the damage initiation.

The transition point between 85 and 105 °C for the change in the nonlinear parameter behavior could also suggest that water content plays a role in the nonlinear parameter variations since it corresponds to water phase change. Indeed, water saturation level influences the nonlinear parameter measurements (Van Den Abeele 2002; Gao et al. 2022, 2023). Nevertheless, we do not think that change in water content linked to evaporation above 100 °C is responsible for the transition point between 85 and 105 °C since months after heating the nonlinear parameter α is still greater for the sample heated at 85 °C than for other samples.

Overall, the results presented here are not consistent with an ability of marble to heal itself during the heating process. This hypothesis, presented by Johnson et al. (2004) to explain a diminution of the nonlinear parameter α between measurements at ambient temperature and after heating at 200 °C for Asian white marble, fall short to explain the decrease of the resonant frequency f_0 (Fig. 5), the microstructural evolution (Fig. 6), mechanical tests (Fig. 10) and observations made previously. Specifically, more porosity is created (Fig. 6) in the form of microcracks visible in SEM (Fig. 8 and Fig. 9) when heating temperature increases, which invalidates the idea of a healing of the grain contacts during the heating process. On the contrary, this study evidences a progressive decohesion of marble until complete disintegration occurring at 500 °C with sample breakage.

Along this trend, the nonlinear parameter α exhibits a significant increase for temperatures ranging between 40 and 85 °C. This illustrates that weathering already appears in Carrara marble in the mild temperature range. This is consistent with the studies of Malaga et al. (2002) and Schouenborg et al. (2007). The evolution of the nonlinear parameter α with heating temperature confirms from laboratory testing that exposure to temperatures as low as 40 °C can initiate damage at marble microscopic scale. In situ monitoring on buildings and stones shows that this temperature range can be reached on marble exposed outdoors (Viles 2005; Schouenborg et al. 2007). This extreme sensitivity of marble to thermal alteration could therefore easily affect marble heritage subjected to climatic variations.

5 Conclusions

The application of NRUS on Carrara Gioia marble samples heated at various temperatures allows monitoring thermal degradation at macroscopic (resonant frequency) and mesoscopic (nonlinear parameter) scales. In brief, the results clearly show that the resonant frequency gradually decreases with thermal damage. The evolution of porosity and pore access as the heating temperature rises could well explain this progressive loss of stiffness. The nonlinear parameter which increases up to 85 °C as it could be expected, decreases onward. This could result from the progressive loss of intergranular contacts as decohesion between marble grains increases.

The evolution of both parameters (resonant frequency and nonlinear parameter) indicates that thermal damage of Carrara Gioia marble already starts at temperatures as low as 40 °C. Such temperatures are often reached on facades or objects exposed outdoors even in the temperate climatic area. The induced increasing porosity and loss of stiffness make this originally non-porous, compact and hard material much more sensitive to any degradation processes which are responsible for stone degradation: chemical dissolution, sulphation, soluble salt crystallizations, freezing-thaw cycles, etc. Only an efficient protection against insolation or even

an indoor exposure could be able to preserve Carrara Gioia marble artworks of the first stages of intergranular decohesion.

After this introductive work dealing with thermal damage, future works will be focused on simulating outdoor exposure conditions to study their effects on Carrara marble: samples will undergo thermo-hygric cycles at mild temperatures. Such cycling will allow investigating the fatigue effects on marble. NRUS that has proved to be an appropriate and accurate non-destructive technique, will be used for the long-term monitoring of marble samples ageing. Supplemental studies would also be necessary to see whether results presented here can be extended to other marble varieties and other rock types.

Declarations

Conflict of Interest The authors have no relevant financial or non-financial interests to disclose.

References

Åkesson U, Lindqvist JE, Schouenborg B, Grelk B (2006) Relationship between microstructure and bowing properties of calcite marble claddings. Bull Eng Geol Environ 65:73–79. https://doi.org/10.1007/s10064-005-0026-x

Averbakh VS, Bredikhin VV, Lebedev AV, Manakov SA (2017) Nonlinear acoustic spectroscopy of carbonate rocks. Acoust Phys 63:346–358. https://doi.org/10.1134/S1063771017030022

Ferrero AM, Marini P (2001) Experimental Studies on the Mechanical Behaviour of two Thermal Cracked Marbles. Rock Mechanics and Rock Engineering 34:57–66. https://doi.org/10.1007/s006030170026

Gao L, Shokouhi P, Rivière J (2023) Effect of Grain Shape and Relative Humidity on the Nonlinear Elastic Properties of Granular Media. Geophysical Research Letters 50:e2023GL103245. https://doi.org/10.1029/2023GL103245

Gao L, Shokouhi P, Rivière J (2022) Effect of relative humidity on the nonlinear elastic response of granular media. Journal of Applied Physics 131:055101. https://doi.org/10.1063/5.0073967

Genovés V, Carrión A, Escobar D, et al (2019) Nonlinear Acoustic Spectroscopy and Frequency Sweep Ultrasonics: Case on Thermal Damage Assessment in Mortar. J Nondestruct Eval 38:61. https://doi.org/10.1007/s10921-019-0599-0

Gherardi F, Kapridaki C, Roveri M, et al (2019) The deterioration of Apuan white marble in contemporary architectural context. Journal of Cultural Heritage 35:297–306. https://doi.org/10.1016/j.culher.2018.06.008

Grelk B, Goltermann P, Schouenborg B, et al (2004) The laboratory testing of potential bowing and expansion of marble. In: Proceedings of the international conference on dimension stone. Taylor & Francis Group plc, A.A. Balkerma Publische, Prague, Czech Republic, pp 253–259

Guyer RA, Johnson PA (1999) Nonlinear Mesoscopic Elasticity: Evidence for a New Class of Materials. Physics Today 52:30–36. https://doi.org/10.1063/1.882648

Johnson P, Sutin A (2005) Slow dynamics and anomalous nonlinear fast dynamics in diverse solids. The Journal of the Acoustical Society of America 117:124–130. https://doi.org/10.1121/1.1823351

Johnson PA (2005) Nonlinear Elastic Wave NDE I. Nonlinear Resonant Ultrasound Spectroscopy and Slow Dynamics Diagnostics. In: AIP Conference Proceedings. AIP, Golden, Colorado (USA), pp 377–384

Johnson PA, Zinszner B, Rasolofosaon P, et al (2004) Dynamic measurements of the nonlinear elastic parameter α in rock under varying conditions: NONLINEAR ELASTIC PARAMETER IN ROCK. J Geophys Res 109:. https://doi.org/10.1029/2002JB002038

Kessler DW (1919) Physical and chemical tests on the commercial marbles of the United States. Department of Commerce

Koch A, Siegesmund S (2004) The combined effect of moisture and temperature on the anomalous expansion behaviour of marble. Env Geol 46:. https://doi.org/10.1007/s00254-004-1037-9

Köhler W (1991) Untersuchungen zu Verwitterungsvorgängen an Carrara-Marmor in Potsdam-Sanssouci. Berichte zu Forschung und Praxis der Denkmalpflege in Deutschland, Steinschäden-Steinkonservierung 2:50–53

Lord Rayleigh (1934) The Bending of Marble. Proceedings of the Royal Society of London Series A, Containing Papers of a Mathematical and Physical Character 144:266–279

Mahmutoglu Y (1998) Mechanical Behaviour of Cyclically Heated Fine Grained Rock. Rock Mechanics and Rock Engineering 31:169–179. https://doi.org/10.1007/s006030050017

Malaga K, Lindqvist JE, Schouenborg B (2002) Experimental study on the variation in porosity of marble as a function of temperature. Geological Society, London, Special Publications 205:81–88. https://doi.org/10.1144/GSL.SP.2002.205.01.07

Malaga-Starzec K, Åkesson U, Lindqvist JE, Schouenborg B (2006) Microscopic and macroscopic characterization of the porosity of marble as a function of temperature and impregnation. Construction and Building Materials 20:939–947. https://doi.org/10.1016/j.conbuildmat.2005.06.016

Malaga-Starzec K, Panas I, Lindqvist JE, Lindqvist O (2003) Efflorescence on thin sections of calcareous stones. Journal of Cultural Heritage 4:313–318. https://doi.org/10.1016/j.culher.2003.09.002

Marini P, Bellopede R (2009) Bowing of marble slabs: Evolution and correlation with mechanical decay. Construction and Building Materials 23:2599–2605. https://doi.org/10.1016/j.conbuildmat.2009.02.010

Marini P, Bellopede R (2007) The Influence of the Climatic Factors on the Decay of Marbles: an Experimental Study. American J of Environmental Sciences 3:143–150. https://doi.org/10.3844/ajessp.2007.143.150

Mechri C, Scalerandi M, Bentahar M (2019) Separation of Damping and Velocity Strain Dependencies using an Ultrasonic Monochromatic Excitation. Phys Rev Applied 11:054050. https://doi.org/10.1103/PhysRevApplied.11.054050

Menningen J, Sassoni E, Sobott R, Siegesmund S (2021) Constraints of the durability of inorganic and organic consolidants for marble. Environ Earth Sci 80:370. https://doi.org/10.1007/s12665-021-09664-w

Menningen RJ (2020) Ultrasonic tomography for the characterization of the weathering state of marble: A systematic study about influencing parameters. Georg-August-Universität Göttingen

Migliori A, Sarrao JL (1997) Resonant ultrasound spectroscopy: applications to physics, materials measurements, and nondestructive evaluation. Wiley, New York

Ostrovsky LA, Johnson PA (2001a) Dynamic nonlinear elasticity in geomaterials. Riv Nuovo Cim 24:1–46. https://doi.org/10.1007/BF03548898

Ostrovsky LA, Johnson PA (2001b) Nonlinear dynamics of rock: Hysteretic behavior. Radiophysics and Quantum Electronics 44:450–464. https://doi.org/10.1023/A:1017953331645

Payan C, Ulrich TJ, Le Bas PY, et al (2014) Quantitative linear and nonlinear resonance inspection techniques and analysis for material characterization: Application to concrete thermal damage. The Journal of the Acoustical Society of America 136:537–546. https://doi.org/10.1121/1.4887451

Payan C, Ulrich TJ, Le Bas PY, Guimaraes M (2012) Quantitative linear and nonlinear resonant inspection techniques for characterizing thermal damage in concrete. In: Proceedings of the Acoustics 2012 Nantes Conference. Nantes, France, pp 2587–2592

Peng J, Rong G, Tang Z, Sha S (2019) Microscopic characterization of microcrack development in marble after cyclic treatment with high temperature. Bull Eng Geol Environ 78:5965–5976. https://doi.org/10.1007/s10064-019-01494-2

Primavori P (2015) Carrara Marble: a nomination for 'Global Heritage Stone Resource' from Italy. Geological Society, London, Special Publications 407:137–154. https://doi.org/10.1144/SP407.21

Rasolofosaon P, Zinszner B, Johnson PA (1997) Propagation des ondes élastiques dans les matériaux non linéaires Aperçu des résultats de laboratoire obtenus sur les roches et des applications possibles en géophysique. Rev Inst Fr Pét 52:585–608. https://doi.org/10.2516/ogst:1997061

Remillieux MC, Guyer RA, Payan C, Ulrich TJ (2016) Decoupling Nonclassical Nonlinear Behavior of Elastic Wave Types. Phys Rev Lett 116:115501. https://doi.org/10.1103/PhysRevLett.116.115501

Remillieux MC, Ulrich TJ, Payan C, et al (2015) Resonant ultrasound spectroscopy for materials with high damping and samples of arbitrary geometry: RUS FOR ARBITRARY SHAPE AND HIGH DAMPING. J Geophys Res Solid Earth 120:4898–4916. https://doi.org/10.1002/2015JB011932

Rivière J, Shokouhi P, Guyer RA, Johnson PA (2015) A set of measures for the systematic classification of the nonlinear elastic behavior of disparate rocks. J Geophys Res Solid Earth 120:1587–1604. https://doi.org/10.1002/2014JB011718

Royer-Carfagni GF (1999) On the thermal degradation of marble. International Journal of Rock Mechanics and Mining Sciences 36:119–126. https://doi.org/10.1016/S0148-9062(98)00169-7

Sáez-Pérez MP, Durán-Suárez JA, Castro-Gomes J (2024) Study of the correlation of the mechanical resistance properties of Macael white marble using destructive and non-destructive techniques. Construction and Building Materials 418:135400. https://doi.org/10.1016/j.conbuildmat.2024.135400

Sassoni E, Graziani G, Ridolfi G, et al (2017) Thermal behavior of Carrara marble after consolidation by ammonium phosphate, ammonium oxalate and ethyl silicate. Materials & Design 120:345–353. https://doi.org/10.1016/j.matdes.2017.02.040

Schouenborg B, Grelk B, Malaga K, et al (2007) Testing and Assessment of Marble and Limestone (TEAM)—Important Results from a Large European Research Project on Cladding Panels. J ASTM Int 4:100855. https://doi.org/10.1520/JAI100855

Sena Da Fonseca B, Ferreira Pinto AP, Piçarra S, et al (2021) Consolidating efficacy of diammonium hydrogen phosphate on artificially aged and naturally weathered coarse-grained marble. Journal of Cultural Heritage 51:145–156. https://doi.org/10.1016/j.culher.2021.08.003

Siegesmund S, Menningen J, Shushakova V (2021) Marble decay: towards a measure of marble degradation based on ultrasonic wave velocities and thermal expansion data. Environ Earth Sci 80:395. https://doi.org/10.1007/s12665-021-09654-y

Siegesmund S, Ruedrich J, Koch A (2008) Marble bowing: comparative studies of three different public building facades. Environ Geol 56:473–494. https://doi.org/10.1007/s00254-008-1307-z

Siegesmund S, Ullemeyer K, Weiss T, Tschegg EK (2000a) Physical weathering of marbles caused by anisotropic thermal expansion. International Journal of Earth Sciences 89:170–182. https://doi.org/10.1007/s005310050324

Siegesmund S, Weiss T, Tschegg EK (2000b) Control of marble weathering by thermal expansion and rock fabrics. In: Proceedings of the 9th International Congress on Deterioration and Conservation of Stone. Venice, pp 205–213

Ten Cate JA, Shankland TJ (1996) Slow dynamics in the nonlinear elastic response of Berea sandstone. Geophys Res Lett 23:3019–3022. https://doi.org/10.1029/96GL02884

Ulrich T, McCall KR, Guyer RA (2002) Determination of elastic moduli of rock samples using resonant ultrasound spectroscopy. The Journal of the Acoustical Society of America 111:1667–1674. https://doi.org/10.1121/1.1463447

Van Den Abeele KE-A (2002) Influence of water saturation on the nonlinear elastic mesoscopic response in Earth materials and the implications to the mechanism of nonlinearity. J Geophys Res 107:2121. https://doi.org/10.1029/2001JB000368

Van Den Abeele KE-A, Carmeliet J, Ten Cate JA, Johnson PA (2000) Nonlinear Elastic Wave Spectroscopy (NEWS) Techniques to Discern Material Damage, Part II: Single-Mode Nonlinear Resonance Acoustic Spectroscopy. Research in Nondestructive Evaluation 12:31–42. https://doi.org/10.1080/09349840009409647

Viles HA (2005) Microclimate and weathering in the central Namib Desert, Namibia. Geomorphology 67:189–209. https://doi.org/10.1016/j.geomorph.2004.04.006

Waragai T (2023) Influence of thermal cycling in the mild temperature range on the physical properties of cultural stones. Journal of Cultural Heritage 59:171–180. https://doi.org/10.1016/j.culher.2022.12.001

Weiss T, Rasolofosaon PNJ, Siegesmund S (2002) Ultrasonic wave velocities as a diagnostic tool for the quality assessment of marble. Geological Society, London, Special Publications 205:149–164. https://doi.org/10.1144/GSL.SP.2002.205.01.12

Wu Q, Li B, Jiang X (2023) Triaxial Test Study on Energy Evolution of Marble after Thermal Cycle. Minerals 13:428. https://doi.org/10.3390/min13030428

Zhang Y, Ta X, Qin S (2022) Effect of heat treatment on physico-mechanical behaviour of a natural building stone: Laizhou dolomite marble. Journal of Building Engineering 47:103885. https://doi.org/10.1016/j.jobe.2021.1038